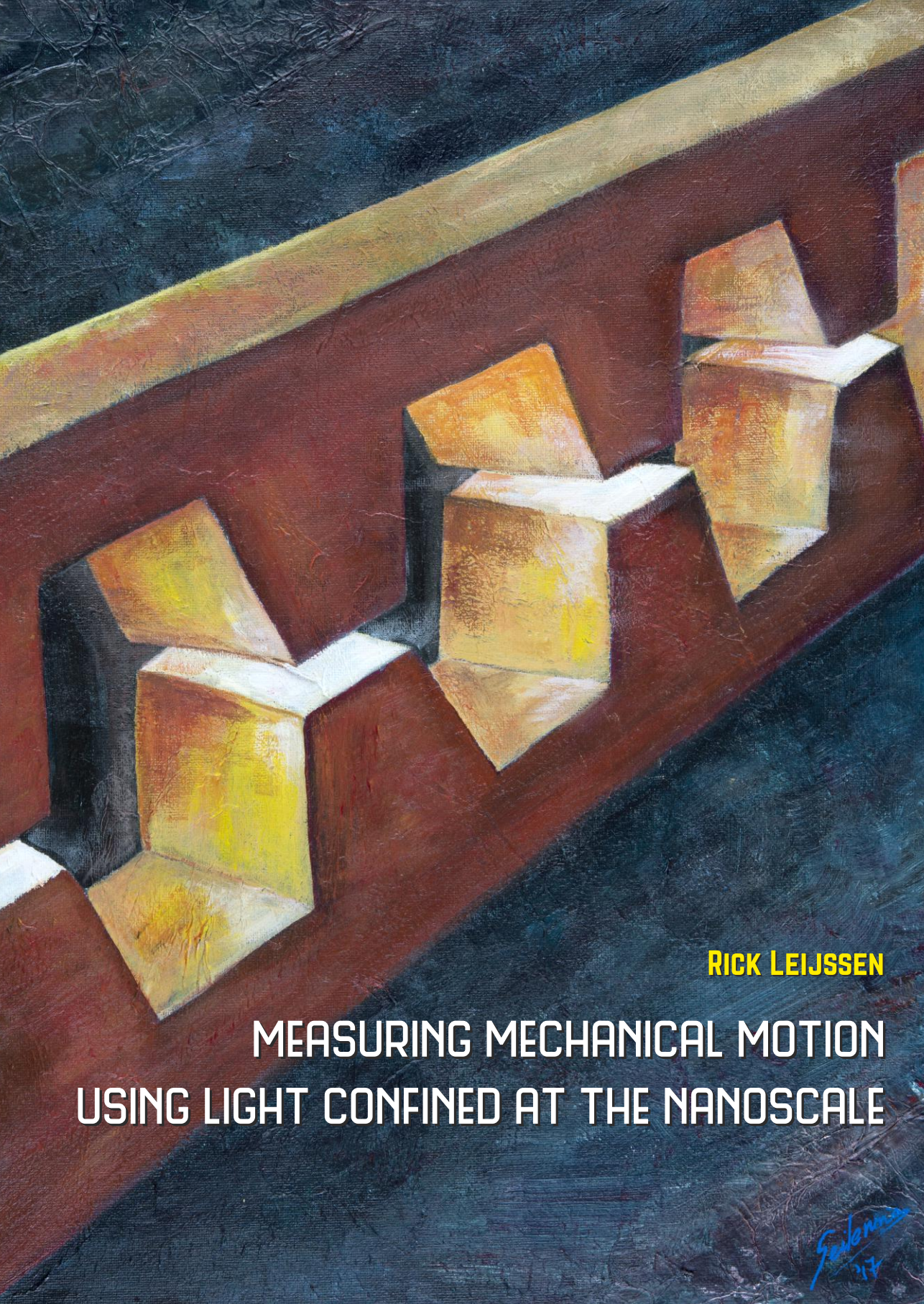

Rick Leijssen

# MEASURING MECHANICAL MOTION USING LIGHT CONFINED AT THE NANOSCALE

# Measuring mechanical motion using light confined at the nanoscale

Rick Leijssen

The cover shows an artist impression of the *sliced nanobeam* design featured in chapters 3 to 6 of this thesis. Image by Annelies Leijssen-Rietjens.

ISBN 978-94-92323-14-9

Printed by: GVO Drukkers & Vormgevers B.V.

The work described in this thesis was performed at AMOLF, Science Park 104, 1098 XG Amsterdam, The Netherlands.
This work is part of the Netherlands Organisation for Scientific Research (NWO).

More information about the *Photonic Forces* group at AMOLF can be found at `http://www.optomechanics.nl`.

An electronic version of this thesis is available at `https://amolf.nl/publications` and `http://repository.tue.nl`.

# Measuring mechanical motion using light confined at the nanoscale

PROEFSCHRIFT

ter verkrijging van de graad van doctor aan de Technische Universiteit Eindhoven, op gezag van de rector magnificus prof.dr.ir. F.P.T. Baaijens, voor een commissie aangewezen door het College voor Promoties, in het openbaar te verdedigen op donderdag 19 oktober 2017 om 16:00 uur

door

Rick Johannes Maria Leijssen

geboren te Weert

Dit proefschrift is goedgekeurd door de promotoren en de samenstelling van de promotiecommissie is als volgt:

| | |
|---|---|
| Voorzitter: | prof. dr. ir. G.M.W. Kroesen |
| 1e promotor: | prof. dr. E. Verhagen |
| 2e promotor: | prof. dr. A. Fiore |
| leden: | prof. dr. M. Lončar (Harvard University) |
| | prof. dr. Y.M. Blanter (TU Delft) |
| | prof. dr. J. Gómez Rivas |
| | prof. dr. ir. O.J. Luiten |

*Het onderzoek dat in dit proefschrift wordt beschreven is uitgevoerd in overeenstemming met de TU/e Gedragscode Wetenschapsbeoefening.*

# Contents

# 1

# Introduction

We use measurements to gain information about the world. In everyday life, we mostly use our senses to observe. Additionally, in our modern society, we interact with many measurement devices directly, such as with clocks, thermometers, or speedometers, and indirectly, such as with the GPS system in many of our smartphones. Scientific researchers employ ever more sensitive measurement devices, for example to understand the building blocks of matter, to determine the structure of cells in living organisms, or to study the universe as we can observe it from Earth. Measurements are at the basis of scientific and technological progress.

In quantum mechanics, which describes physical processes at small scales, measurements play a pivotal role [1, 2]. Quantum states correspond to probability amplitudes, which one can use to predict the outcome of a future measurement in a probabilistic way. At the same time, a measurement always changes the state of the system, for example by disturbing the conjugate variable of the observed quantity as described by the Heisenberg uncertainty principle. This leads to fundamental limits to the sensitivity of certain measurements, as we discuss later in this chapter. It also provides the interesting possibility of measurement-based state preparation, where measurements are used to manipulate the quantum state of a system [2].

Using optical measurements is often an effective strategy to reach high sensitivity, since light can carry information while adding only a minimal amount of noise. Optical measurements of mechanical motion are at the heart of the atomic force microscope, where the deflection of a small cantilever that is in contact with a surface provides a probe of the forces exerted on the cantilever [3]. Likewise, the recently reported first detection of gravitational waves by the LIGO collaboration [4] was made possible by extremely sensitive optical interferometric distance measurements.

Light can also exert a force on objects and can therefore be used to control mechanical motion. This optical force was first observed by Kepler [5], who noticed that comets have a tail which always points away from the sun. It has found

application in so-called “optical tweezers”, where the optical forces are used to trap a small transparent bead in the focus of a laser beam, as first demonstrated by Ashkin [6].

## 1.1. Cavity optomechanics

The field of cavity optomechanics studies the interaction between an optical cavity and the motion of a mechanical resonator coupled to it [7]. The optical cavity enhances the effects of the interaction by storing the light in time and confining it in space. This enables extremely sensitive optical measurements of mechanical motion as well as optical control of the motion of the resonator. A wide range of different implementations of cavity optomechanical systems have been reported, which span many orders of magnitude in scale (see the review by Aspelmeyer, Kippenberg & Marquardt [7] for an overview). Examples include Fabry-Pérot cavities with suspended mirrors in a large range of sizes [8–10], microdisk [11, 12] or microtoroid [13] whispering gallery mode cavities, capacitive drum resonators coupled to a resonant microwave circuit [14], photonic crystal cavities [15–21], and coupled plasmonic antennas [22]. Here we list some of the milestones that have been reached in the field of cavity optomechanics in recent years. Optical measurements of displacement with an imprecision smaller than that at the standard quantum limit (see section 1.5) were demonstrated in several systems [14, 23], which was enabled by the development of miniaturized systems with large optomechanical coupling rates and low losses. Direct observation of the radiation pressure shot noise driving the mechanical resonator strongly enough to overcome its thermal motion was reported both for the motion of a cloud of cold atoms [24] and with a thin semiconductor membrane [25]. The optical forces can provide damping of the mechanical resonator, such that its thermal motion is decreased—effectively cooling the resonator. Optical cooling of a mechanical resonator to near its ground state of motion using sideband cooling was shown around 2011 [13, 15, 26]. In this process, the cavity naturally provides damping of the motion when driven by an off-resonance laser beam (see section 1.4.2). Cooling can also be achieved with active feedback, using sensitive measurements of the motion of the resonator. This technique was first implemented in the optical domain in 1999 [8], and while finite measurement efficiencies have so far precluded cooling below the level of a single phonon, recent experiments have reached measurement rates that exceed the thermal decoherence rate [27]. The optomechanical interaction has also been used to demonstrate quantum squeezing of the light field [17, 28, 29] and of the mechanical zero-point fluctuations [30–32]. The coupling between the radiation field and the motion of the resonator is coherent, which has enabled experiments that show entanglement [33] and state transfer [34, 35] between them. Finally, several recent experiments have studied nonclassical correlations in optomechanical systems [36–39].

A major goal that remains in the field of cavity optomechanics is the creation, manipulation and observation of nonclassical states of motion, beyond the Gaussian states that have now been demonstrated. Preparing such states using the optomechanical interaction is in principle possible, but it requires either transferring

a nonclassical state of the light field to the mechanical resonator, or increasing the optomechanical coupling rate to be larger than both the optical and mechanical loss rates of the system. Before reaching this so-called single-photon strong coupling regime, increasing the optomechanical coupling rate helps to improve the sensitivity of measurements, lower the minimum temperature that can be achieved with optical cooling, and lower the power or bandwidth requirements for many effects using the optomechanical interaction. In this thesis, we develop and study optomechanical systems in which the optomechanical coupling rate is especially large. In this introductory chapter, the model used to describe the cavity optomechanical system is introduced, focusing on measurement and back-action in systems with relatively large optical linewidths. We will then introduce the measurement techniques we employ. An outline of the other chapters in this thesis is given in section 1.6.

## 1.2. Optomechanical model system

Cavity optomechanics describes an optical cavity that is coupled to a mechanical resonator. In the following sections we will introduce the theoretical formalism used to describe such systems. For a more exhaustive description, we refer the reader to the review by Aspelmeyer, Kippenberg & Marquardt [7] or the textbook by Bowen & Milburn [40].

### 1.2.1. Hamiltonian and equations of motion

A simple example of an optomechanical system is a Fabry-Pérot cavity, shown in fig. 1.1a, which consists of two highly reflective mirrors, where one of the mirrors is mounted on a spring. The spring-mounted mirror can be described as a harmonic oscillator with resonance frequency $\Omega_\mathrm{m}$. The displacement $x$ of this mechanical resonator modulates the length of the Fabry-Pérot cavity, which changes the optical resonance frequency $\omega_\mathrm{c}$. The same description can be used for optomechanical systems which have very different geometries, such as the sliced nanobeam system we describe in this thesis. Figure 1.1b shows the simulated profiles of the mechanical resonator and optical cavity modes in such a nanobeam, with the model parameters that we use to describe them.

In general, we can expand the cavity frequency $\omega_\mathrm{c}$ around its equilibrium value $\omega_0$ for small displacements $x$ as

$$\omega_\mathrm{c} = \omega_0 + \frac{\partial \omega_\mathrm{c}}{\partial x} x + \frac{1}{2}\frac{\partial^2 \omega_\mathrm{c}}{\partial x^2} x^2 + \dots , \tag{1.1}$$

where for the Fabry-Pérot cavity and for the structures we consider in this thesis, the term linear in $x$ is the only term that contributes significantly. For convenience, we define a coupling rate $G \equiv -\partial\omega_\mathrm{c}/\partial x$.

We describe both the optical mode and the mechanical mode as harmonic oscillators, which yields the Hamiltonian

$$\hat{H} = \hbar\omega_\mathrm{c}\left(\hat{a}^\dagger\hat{a} + \frac{1}{2}\right) + \hbar\Omega_\mathrm{m}\left(\hat{b}^\dagger\hat{b} + \frac{1}{2}\right). \tag{1.2}$$

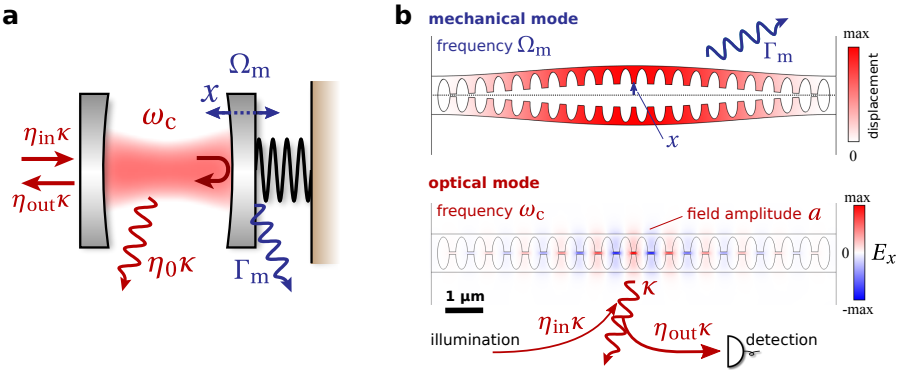


Figure 1.1: (a) Optomechanical model system, consisting of a Fabry-Pérot optical cavity where one of the mirrors is mounted on a spring. The optical cavity mode has frequency $\omega_c$ and total loss rate $\kappa$, which is the sum of the intrinsic loss rate $\eta_0\kappa$ and the coupling rate $\eta_{in}\kappa = \eta_{out}\kappa$ to the mode used for excitation and detection. The mechanical resonator has a frequency of $\Omega_m$ and total loss rate $\Gamma_m$. (b) Sliced photonic crystal nanobeam system, which can be described using the same model parameters as the Fabry-Pérot cavity shown in (a), despite the fact that the system looks completely different. The simulated mechanical and optical resonances of the nanobeam are shown separately in the interest of clarity. One important difference in the model parameters is that we no longer assume the modes used for excitation and detection are one and the same mode, thus $\eta_{in}$ and $\eta_{out}$ can be different (see section 1.3.1). We still define an intrinsic loss rate $\eta_0\kappa$, with $\eta_0 \equiv 1 - \eta_{in}$.

Here $\hat{a}$ and $\hat{b}$ are the lowering operators for the optical and mechanical degrees of freedom, respectively. For the mechanical resonator, it is sometimes more convenient to use the displacement operator $\hat{x} = x_{zpf}(\hat{b} + \hat{b}^\dagger)$, where

$$x_{zpf} = \sqrt{\frac{\hbar}{2m\Omega_m}} \tag{1.3}$$

describes the zero-point fluctuations of the mechanical resonator with frequency $\Omega_m$ and motional mass $m$. In the following, we will not include the ground-state energy given by the extra terms of $1/2$ in eq. (1.2), since they only provide a constant offset and do not affect the dynamics of the system. We can now substitute $\omega_c = \omega_0 - G\hat{x}$ into eq. (1.2) and obtain the Hamiltonian interaction term

$$\hat{H}_{int} = -\hbar g_0 \hat{a}^\dagger \hat{a}(\hat{b} + \hat{b}^\dagger) = -\hbar g_0 \hat{a}^\dagger \hat{a}\hat{x}/x_{zpf}, \tag{1.4}$$

where we defined the optomechanical photon-phonon coupling rate $g_0 \equiv G x_{zpf}$.

We will now write down the equations of motion for the cavity field amplitude $\hat{a}$ and the mechanical amplitude $\hat{b}$ in the Heisenberg picture. While we left out the damping and driving terms in the Hamiltonian description above, we include them here. The mechanical resonator is coupled to a thermal bath with fluctuations $\hat{b}_{in}$ at a rate $\Gamma_m$, which therefore also characterizes the damping of the energy in the resonator. The optical cavity is damped at a rate $\kappa$. It is coupled to an input channel $\hat{s}_{in}$ at a rate $\eta_{in}\kappa$, where $\eta_{in}$ is called the incoupling efficiency,

and to a bath of vacuum fluctuations $\hat{f}_{\mathrm{in}}$ via the remainder of its damping rate $\eta_0\kappa \equiv (1-\eta_{\mathrm{in}})\kappa$. The quantum Langevin equations of motion are

$$\dot{\hat{a}} = i(\Delta + G\hat{x})\hat{a} - \frac{\kappa}{2}\hat{a} + \sqrt{\eta_{\mathrm{in}}\kappa}\hat{s}_{\mathrm{in}} + \sqrt{\eta_0\kappa}\hat{f}_{\mathrm{in}}, \tag{1.5}$$

$$\dot{\hat{b}} = -i\Omega_{\mathrm{m}}\hat{b} - \frac{\Gamma_{\mathrm{m}}}{2}\hat{b} + ig_0\hat{a}^\dagger\hat{a} + \sqrt{\Gamma_{\mathrm{m}}}\hat{b}_{\mathrm{in}}. \tag{1.6}$$

Here we chose a frame rotating at the laser frequency $\omega_{\mathrm{L}}$ and introduced the laser detuning $\Delta \equiv \omega_{\mathrm{L}} - \omega_{\mathrm{c}}$. In addition to the usual terms in the equation of motion for a cavity using the input-output formalism, a coupling term appears in both equations due to the interaction term of the Hamiltonian.

The classical equations of motion of the field amplitude $a$ and the displacement $x$ can be found from eqs. (1.5) and (1.6) by calculating the expectation value of the quantum operators $\hat{a}$ and $\hat{x}$, respectively. Note that with this definition, the field $a$ is normalized such that $|a|^2$ gives the number of photons in the cavity. The resulting equations of motion are

$$\dot{a} = \left(i(\Delta + Gx) - \frac{\kappa}{2}\right)a + \sqrt{\eta_{\mathrm{in}}\kappa}s_{\mathrm{in}}, \tag{1.7}$$

$$\ddot{x} = -\Omega_{\mathrm{m}}^2 x - \Gamma_{\mathrm{m}}\dot{x} + \frac{\hbar G|a|^2}{m} + \frac{F_{\mathrm{ext}}}{m}. \tag{1.8}$$

Equation (1.8) is written here in terms of the displacement $x$, and we introduced the external driving force $F_{\mathrm{ext}}$. Note that we have written the mechanical equation of motion as a second-order differential equation here. This means that it is in principle generally valid, unlike eq. (1.6), which approximates the mechanical response as Lorentzian and only describes the dynamics for a weakly damped resonator at frequencies close to $\Omega_{\mathrm{m}}$. We will use these equations as the basis for discussing the cavity response in absence of coupling to a mechanical resonator ($G = 0$) in section 1.3.1 and the mechanical resonator's response to the optical force in section 1.4.

### 1.2.2. Linearization

The interaction Hamiltonian in eq. (1.4) is nonlinear, since it involves three operators, which leads to terms in the equations of motion that contain products of two operators. However, often we can linearize the interaction. We write the cavity field operator as $\hat{a} = \bar{\alpha} + \delta\hat{a}$, with an average coherent amplitude $\bar{\alpha}$ and small fluctuations $\delta\hat{a}$. Substituting this in eq. (1.4), we obtain four terms. The term proportional to $|\bar{\alpha}|^2$ describes an average radiation pressure force, which can be dealt with by incorporating the resulting shift into a new equilibrium position and cavity resonance frequency (see section 1.4.1). The term proportional to $\delta\hat{a}^\dagger\delta\hat{a}\hat{x}$ can be neglected if we assume $\delta\hat{a} \ll \bar{\alpha}$. While this captures many of the interactions encountered in this thesis, in chapter 5 we describe a regime where this assumption breaks down. In the regime where the approximation is valid, keeping only the terms linear in $\bar{\alpha}$ leads to the linearized Hamiltonian

$$\hat{H}_{\mathrm{int}} = -\hbar g_0\bar{\alpha}(\delta\hat{a} + \delta\hat{a}^\dagger)(\hat{b} + \hat{b}^\dagger) = -\hbar g_0\bar{\alpha}(\delta\hat{a} + \delta\hat{a}^\dagger)\hat{x}/x_{\mathrm{zpf}}. \tag{1.9}$$

The corresponding linearized Langevin equations of motion are

$$\delta\dot{\hat{a}} = i(\Delta + \bar{\alpha}G\hat{x})\delta\hat{a} - \frac{\kappa}{2}\delta\hat{a} + \sqrt{\eta_{\text{in}}\kappa}\delta\hat{s}_{\text{in}} + \sqrt{\eta_0\kappa}\hat{f}_{\text{in}}, \tag{1.10}$$

$$\dot{\hat{b}} = -i\Omega_{\text{m}}\hat{b} - \frac{\Gamma_{\text{m}}}{2}\hat{b} + i\bar{\alpha}g_0(\delta\hat{a} + \delta\hat{a}^\dagger) + \sqrt{\Gamma_{\text{m}}}\hat{b}_{\text{in}}. \tag{1.11}$$

In contrast to the nonlinear versions (eqs. (1.5) and (1.6)), the linearized equations of motion can be solved analytically.

### 1.2.3. Bad-cavity limit

The ratio between the optical linewidth $\kappa$ and the mechanical resonance frequency $\Omega_{\text{m}}$ can often be used to simplify calculations describing optomechanical interactions. When $\Omega_{\text{m}} \gg \kappa$, the system is said to be in the *resolved sideband regime*. In this regime, the mechanical modulation of the cavity creates sidebands which are spectrally resolved with respect to the cavity linewidth. In eq. (1.9), the spectral separation means that only some of the terms are resonant with the cavity when driven at a detuning of $\Delta \approx \pm\Omega_{\text{m}}$, leading to efficient dynamical backaction (see section 1.4.2), that is, optical cooling or parametric amplification.

For all the experiments presented in this thesis, we work in the opposite regime ($\kappa \gg \Omega_{\text{m}}$), which is called the *bad-cavity limit* or sometimes *Doppler* or *stationary regime*. In this case, the cavity responds to the mechanical motion on a timescale much shorter than the mechanical resonance period. In describing the optomechanical interaction, the assumption that the cavity responds instantaneously corresponds to using the steady-state solution for the cavity field as a function of the displacement. In this regime, dynamical backaction effects are strongly reduced and cooling of the mechanical resonator can be more effectively implemented using feedback [41]. The fast cavity response also allows pulsed optical measurements of the displacement in a time shorter than the mechanical resonance period (see chapter 6).

### 1.2.4. Nanoscale systems

Both factors in the optomechanical coupling rate $g_0 = Gx_{\text{zpf}}$ can reach their largest values in miniaturized systems. The mechanical zero-point fluctuations (eq. (1.3)) are increased for systems with low mass, and the optical dependence on displacement $G = -\partial\omega_{\text{c}}/\partial x$ is larger if the light is confined more to a small volume where it is affected by the mechanical motion (see section 2.2.1). Indeed, the highest values of $g_0$ to date have been achieved in micrometer-size devices such as photonic crystal cavities [15–17, 19, 20, 42, 43] or disk resonators [11, 12], with reported values ranging up to about $g_0/2\pi \approx 1\,\text{MHz}$ [12, 44].

There are a few notable differences between miniaturized systems and more macroscopic systems. The optical force associated with the coupling term in the equation of motion for the mechanical resonator (eq. (1.6)) often includes near-field effects such as the gradient force, while in the Fabry-Pérot cavity it can be described by only considering the momentum transfer upon reflection. In terms of the system design and parameters, stronger confinement of the light often means

higher losses, such that it is more difficult to reach the resolved sideband regime, if desired. Finally, the stronger confinement of the light can also lead to stronger nonlinear effects in the optical cavity response (see section 1.3.2 and appendix A), which ultimately limit the maximum optical power that can be used in the experiment.

## 1.3. Cavity response

In this thesis, we use optical reflection measurements to probe the response of the optical cavity. In this section we describe the expected cavity response. In the equations of motion in the previous section, we have only included the linear optical response of the cavity, which we further explore here. We also briefly estimate for which power nonlinear effects start playing a role.

### 1.3.1. Linear response

To write down the optical equation of motion eq. (1.5), we have used the input-output formalism to describe the field of a cavity coupled to a single input channel [45]. Here we will use the equation of motion for the classical field amplitude $a$ given in eq. (1.7), for a cavity which is not coupled to a mechanical resonator ($G = 0$). The steady-state solution to this equation of motion can be found by setting $\dot{a} = 0$, which yields

$$a = \frac{\sqrt{\eta_{\text{in}}\kappa}s_{\text{in}}}{-i\Delta + \kappa/2} = \frac{2\sqrt{\eta_{\text{in}}/\kappa}s_{\text{in}}}{1 - iu}. \tag{1.12}$$

In the second step we have expressed the detuning dependence of the cavity in terms of the unitless relative detuning parameter $u \equiv 2\Delta/\kappa$. In this thesis, we express most detuning dependencies as a function of $u$, since the resulting expressions explicitly reveal the scaling with the cavity linewidth $\kappa$. We note that although this eq. (1.12) is derived with $G = 0$, in the bad-cavity limit ($\kappa \gg \Omega_{\text{m}}$, see section 1.2.3) one can use it also for $G \neq 0$ by substituting $\Delta \to \Delta + Gx$. This is essentially based on the assumption that the cavity can reach this steady-state amplitude so fast with respect to the mechanical motion that any transients or delay can be neglected.

The incoupling rate $\eta_{\text{in}}\kappa$ describes the coupling of the cavity to the optical mode we use for illumination. We describe the detection of light escaping from the cavity as an output channel, coupled to the cavity with the rate $\eta_{\text{out}}\kappa$, where $\eta_{\text{out}}$ is the outcoupling efficiency. If the input and output channels both describe the same optical mode, for example when the cavity is coupled to a single-mode waveguide, then $\eta_{\text{in}} = \eta_{\text{out}}$. In a free-space setup with a miniaturized optical cavity, the emission profile of the cavity does not necessarily coincide with the Gaussian profile of the input laser beam, so the two rates can be different. In general, the total loss rate of the cavity cannot be calculated from the in- and outcoupling rates (for example by addition), since the input and output channel can have an arbitrary amount of overlap. We note that the emission profile of the cavity can be represented as a linear combination of modes in a suitable basis,

for example the Hermite-Gaussian modes [46]. In principle, it is possible to use spatial filtering to reduce the contribution of higher-order components, at the expense of reduced detection efficiency.

In addition to the resonant channel via the cavity, light can also directly couple from the input channel to the output channel. For a Fabry-Pérot cavity with highly reflective mirrors, this coupling is just the reflection from the front mirror, in which case the off-resonant reflection coefficient is equal to $1$. This leads to the input-output relation

$$s_{\text{out}}^{\text{FP}} = s_{\text{in}} - \sqrt{\eta_{\text{out}}\kappa}a, \tag{1.13}$$

where the phase relation between the two terms, represented by the minus sign, is enforced by energy conservation [46]. In our nanobeam cavities, the nonresonant coupling between the output and input channel is due to broadband light scattering at the nanobeam—the planar interface of the substrate is out of focus, and in most of our experiments we further suppress this reflection by polarization filtering. We represent this term by $ce^{i\varphi}$, with the amplitude $c$ and phase $\varphi$ chosen to be real, which yields

$$\begin{aligned} s_{\text{out}} &= ce^{i\varphi}s_{\text{in}} - \sqrt{\eta_{\text{out}}\kappa}a \\ &= \left(ce^{i\varphi} - \frac{2\sqrt{\eta_{\text{in}}\eta_{\text{out}}}}{1-iu}\right)s_{\text{in}}. \end{aligned} \tag{1.14}$$

From eq. (1.14), it follows that the reflection $R = |s_{\text{out}}|^2/|s_{\text{in}}|^2$ of the cavity is

$$R = \left|ce^{i\varphi} - \frac{2\sqrt{\eta_{\text{in}}\eta_{\text{out}}}}{1-iu}\right|^2. \tag{1.15}$$

This equation describes a Fano lineshape, which reduces to a Lorentzian lineshape for $\varphi = k\pi$, an integer number $k$ times $\pi$. For different values of the phase, the Fano lineshape is asymmetric. In fig. 1.2, three reflection spectra are plotted using eq. (1.15) with different parameters. From the structure of eq. (1.15), it is apparent that the origin of the variations in the shape of the reflection spectrum is the interference between the nonresonant scattering, which has a constant phase $\varphi$, and the cavity response, which has a rapidly varying phase as a function of the relative detuning $u$.

The Fano lineshape is often written in a different way, for example by Galli *et al.* [47], as

$$R = A + F\frac{(q+u)^2}{1+u^2}, \tag{1.16}$$

which is closer to the original form derived by Fano [48]. Here $q$ is an asymmetry parameter, such that the equation describes a Lorentzian lineshape for $q = 0$ and $q \to \pm\infty$. The parameters for this expression for the Fano lineshape can be

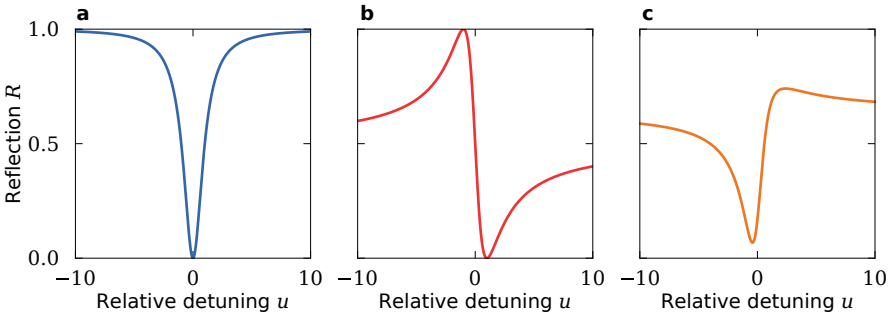


Figure 1.2: Reflection spectra (eq. (1.15)) with different parameters $c$, $\varphi$ and $\eta \equiv \sqrt{\eta_{\text{in}}\eta_{\text{out}}}$. (a) $ce^{i\varphi} = 1$, yielding a Lorentzian lineshape, with $\eta = 0.5$. (b) $c = 1/\sqrt{2}, \varphi = \pi/4, \eta = 0.5$, which yields a perfectly antisymmetric lineshape. (c) $c = 0.8, \varphi = -\pi/6, \eta = 0.3$, which represents a general asymmetric lineshape.

obtained from the parameters of eq. (1.15) via the rather cumbersome expressions

$$q = \frac{-\eta + c\cos\varphi \pm \sqrt{\eta^2 + c^2 - 2\eta c\cos\varphi}}{c\sin\varphi}, \tag{1.17}$$

$$F = \frac{-2c\eta\sin\varphi}{q}, \tag{1.18}$$

$$A = c^2 - F. \tag{1.19}$$

Here we defined $\eta \equiv \sqrt{\eta_{\text{in}}\eta_{\text{out}}}$ in the interest of compactness. In this thesis, we choose to use eq. (1.15) directly, whose parameters offer more insight into the underlying physical mechanism.

### 1.3.2. Nonlinear response

In addition to the linear cavity response described above, at higher optical powers, nonlinear effects can play a role. Due to the small mode volumes and high quality factors that can be achieved in photonic crystal cavities, the optical intensity inside the cavity is enhanced. This leads to the amplification of intensity-dependent effects which ultimately limit the optical power that can be used. The main processes that occur in silicon photonic crystal cavities at wavelengths near $1500\,\text{nm}$ were modeled by Barclay, Srinivasan & Painter [49], who showed that free carriers in the silicon, generated by two-photon absorption, account for most of the increased absorption observed at higher optical powers. Additionally, the absorbed light leads to local heating of the cavity, which in turn shifts the cavity frequency since the refractive index of the material depends on temperature. In appendix A, we estimate the size of these effects in a silicon photonic crystal cavity with a small mode volume and a quality factor of $10^4$, and find that none of these effects modify the resonant frequency or linewidth by more than $10\,\%$ of the linewidth when the average photon occupancy of the cavity is less than $\sim 10^3$ photons.

1

## 1.4. Optical forces

In the equation of motion for the mechanical resonator (eq. (1.8)) the coupling term shows that there is an optical force $F_{\text{opt}} = \hbar G|a|^2$. This force can lead to a shift of the equilibrium displacement, tuning of the mechanical resonance frequency, as well as damping or amplification of the motion. In this section, we briefly discuss the expected effects of these forces in our measurements. Additionally, the temperature gradients caused by local heating due to absorption of light can drive mechanical motion through a photo-thermo-elastic force. We discuss these forces and their description in appendix A.3.

### 1.4.1. Optomechanical tuning

A constant energy in the cavity of $U = \hbar\omega_{\text{L}}|a|^2$ leads to a force of $F_{\text{opt}} = GU/\omega_{\text{L}}$. The mechanical resonator with resonance frequency $\Omega_{\text{m}}$ and motional mass $m$ has an effective spring constant $k_{\text{eff}} = m\Omega_{\text{m}}^2$, so the resulting displacement is

$$\Delta x = \frac{-\hbar G|a|^2}{m\Omega_{\text{m}}^2} = \frac{-GU}{m\Omega_{\text{m}}^2\omega_{\text{L}}}. \tag{1.20}$$

This leads to a shift of the optical resonance frequency of

$$\Delta\omega_{\text{c}} = -G\Delta x = \frac{G^2U^2}{m\Omega_{\text{m}}^2\omega_{\text{L}}}. \tag{1.21}$$

This effect has the same characteristic power dependence as thermo-optic tuning (see appendix A.2). Like the thermo-optic effect, it leads to a nonlinear response and exhibits bistable behavior at higher powers.

Here we calculate the energy in the cavity which will lead to a shift of $10\,\%$ of the linewidth of the cavity, which we also use as a criterion in appendix A in the case of thermal effects. We take the same cavity with wavelength $1.5\,\mu\text{m}$ and $Q = 10^4$. For the mechanical resonator, we take a mass $m = 1.5\,\text{pg}$ and frequency $\Omega_{\text{m}}/2\pi = 5\,\text{MHz}$, and we set the coupling to $G/2\pi = 500\,\text{GHz}\,\text{nm}^{-1}$. These are all realistic values, which we will encounter later in this thesis. We find that $\Delta\omega_{\text{c}} \leq 0.1\kappa$ for cavity occupancies $U/\hbar\omega_{\text{L}} \leq 18$ photons. Evidently, for these parameters, the optomechanical tuning is expected to be more than ten times stronger than the thermo-optic tuning. This effect can therefore become a limiting factor for the amount of optical power we can use in our experiments, for example if we want to avoid bistable operation or just want to avoid distorting the detuning dependence of the cavity response.

### 1.4.2. Dynamical backaction

The detuning dependence of $|a|^2$ makes the optical force detuning-dependent as well. Since the mechanical motion modulates the cavity frequency, the optical force reacts to the mechanical motion, setting up a feedback loop. This is often referred to as dynamical backaction. If the force reacts instantaneously to the motion, it is opposed to, or aligned with the mechanical restoring force, depending

on the laser detuning. Thus it effectively changes the spring constant of the harmonic oscillator and therefore the resonance frequency. This is called the *optical spring effect*. The finite lifetime of the cavity introduces a delay of a fraction $\Omega_{\mathrm{m}}/\kappa$ of the mechanical period. The out-of-phase component of this delayed force can cause damping or amplification of the motion.

To discuss this in a quantitative way, we use the linearized version of the classical equations of motion (eqs. (1.7) and (1.8)), which read

$$\delta\dot{a} = \left(i\Delta - \frac{\kappa}{2}\right)\delta a + iG\bar{\alpha}x, \tag{1.22}$$

$$\ddot{x} = -\Omega_{\mathrm{m}}^2 x - \Gamma_{\mathrm{m}}\dot{x} + \frac{\hbar G\bar{\alpha}}{m}(\delta a + \delta a^*) + \frac{\delta F_{\mathrm{ext}}}{m}. \tag{1.23}$$

To find the effect of the linearized optical force $\delta F_{\mathrm{opt}} = \hbar G\bar{\alpha}(\delta a + \delta a^*)$, we take the Fourier transform of these equations, which yields

$$-i\Omega\delta a = \left(i\Delta - \frac{\kappa}{2}\right)\delta a + iG\bar{\alpha}x, \tag{1.24}$$

$$-\Omega^2 x = -\Omega_{\mathrm{m}}^2 x + i\Omega\Gamma_{\mathrm{m}}x + \frac{\delta F_{\mathrm{opt}}}{m} + \frac{\delta F_{\mathrm{ext}}}{m}. \tag{1.25}$$

From eq. (1.24), we find

$$\delta a = \frac{-G\bar{\alpha}x}{\Delta + \Omega + i\kappa/2}, \tag{1.26}$$

$$\delta a^* = \frac{-G\bar{\alpha}x}{\Delta - \Omega - i\kappa/2}, \tag{1.27}$$

where we used $(\delta a(\Omega))^* = \delta a^*(-\Omega)$. Using eqs. (1.26) and (1.27), we obtain

$$\delta F_{\mathrm{opt}} = -\hbar G^2\bar{\alpha}^2 x\left(\frac{1}{\Delta + \Omega + i\kappa/2} + \frac{1}{\Delta - \Omega - i\kappa/2}\right) \tag{1.28}$$

We now define $\Sigma_{\mathrm{opt}} \equiv -\delta F_{\mathrm{opt}}/x$, such that the equation of motion for the mechanical motion becomes

$$\left(m\left[\Omega_{\mathrm{m}}^2 - \Omega^2 - i\Omega\Gamma_{\mathrm{m}}\right] + \Sigma_{\mathrm{opt}}\right)x = \delta F_{\mathrm{ext}}. \tag{1.29}$$

This equation shows that the real part of $\Sigma_{\mathrm{opt}}$ can be associated with a change of the resonance frequency $\Omega_{\mathrm{m}}$. This is due to the in-phase component of the optical force, which acts as an additional spring force. The imaginary part of $\Sigma_{\mathrm{opt}}$ can be associated with a change of the loss rate $\Gamma_{\mathrm{m}}$, which corresponds to the out-of-phase component of the optical force, which provides damping or amplification. We use $(\Omega_{\mathrm{m}} + \delta\Omega_{\mathrm{m}})^2 \approx \Omega_{\mathrm{m}}^2 + 2\Omega_{\mathrm{m}}\delta\Omega_{\mathrm{m}}$, which is a good approximation for $\delta\Omega_{\mathrm{m}} \ll \Omega_{\mathrm{m}}$, and find

$$\delta\Omega_{\mathrm{m}} = \frac{\mathrm{Re}(\Sigma_{\mathrm{opt}})}{2m\Omega_{\mathrm{m}}}, \tag{1.30}$$

$$\delta\Gamma_{\mathrm{m}} = \frac{-\mathrm{Im}(\Sigma_{\mathrm{opt}})}{m\Omega_{\mathrm{m}}}. \tag{1.31}$$

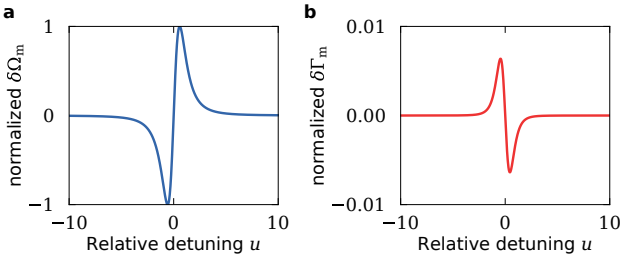


Figure 1.3: (a) Detuning dependence of the optical spring effect, where the optical force shifts the mechanical resonance frequency, with constant optical input power (see eq. (1.35)), normalized to the maximum frequency shift. (b) Detuning dependence for the optical damping and amplification, with constant optical input power (see eq. (1.36)). The scale is the same as in panel (a), normalized to the maximum frequency shift $\delta\Omega_m$. We used $\Omega_m/\kappa = 10^{-3}$, which determines the size of this effect with respect to the frequency shift (see eq. (1.34)).

We combine eq. (1.28) with eqs. (1.30) and (1.31) and use $G = g_0/x_{zpf}$ to rewrite $\hbar G^2 = 2m\Omega_m g_0^2$. In the bad-cavity limit ($\kappa \gg \Omega_m$), we then arrive at the expressions

$$\delta\Omega_m = \frac{4g_0^2\bar{\alpha}^2}{\kappa}\frac{u}{1+u^2}, \tag{1.32}$$

$$\delta\Gamma_m = \frac{-32g_0^2\bar{\alpha}^2\Omega_m}{\kappa^2}\frac{u}{(1+u^2)^2}, \tag{1.33}$$

with $u \equiv 2\Delta/\kappa$ like before. From eqs. (1.32) and (1.33), the ratio between the changes of mechanical frequency and linewidth in the bad-cavity limit is seen to be

$$\frac{\delta\Omega_m}{\delta\Gamma_m} = \frac{-8\Omega_m/\kappa}{1+u^2}, \tag{1.34}$$

which reveals that the optical damping and amplification are weaker than the frequency tuning by approximately a factor of $\Omega_m/\kappa$, which is $10^{-3}$ or smaller for all structures used in this thesis.

Finally, we substitute the cavity occupancy $\bar{\alpha} = |s_{in}|^2 4\eta_{in}/(\kappa(1+u^2))$ (see eq. (1.12)) to obtain the detuning dependency with constant input laser power of $P_{in} = \hbar\omega_L|s_{in}|^2$, which yields

$$\delta\Omega_m = \frac{16g_0^2\eta_{in}|s_{in}|^2}{\kappa^2}\frac{u}{(1+u^2)^2}, \tag{1.35}$$

$$\delta\Gamma_m = \frac{-128g_0^2\Omega_m\eta_{in}|s_{in}|^2}{\kappa^3}\frac{u}{(1+u^2)^3}. \tag{1.36}$$

Figure 1.3 shows the detuning dependence of the optical spring effect and of the optical damping and amplification as given by eqs. (1.35) and (1.36). Note that since these effects are dependent on the optical power in the cavity, the optically-induced frequency shift and linewidth broadening and narrowing are

only sensitive to the input coupling efficiency $\eta_{\text{in}}$ and not to the output coupling efficiency $\eta_{\text{out}}$—in contrast to the measurement sensitivity, as we will show below (see section 1.5).

At the blue side of the optical resonance ($u > 0$), the decrease of the mechanical linewidth predicted by eq. (1.36) corresponds to parametric amplification of the motion. At high optical power, the optical amplification can overcome the intrinsic damping rate, such that the total damping rate $\Gamma_{\text{tot}} = \Gamma_{\text{m}} + \delta\Gamma_{\text{m}}$ becomes negative. This corresponds to gain, which will amplify random fluctuations until nonlinear effects limit further growth of the amplitude of motion. This self-oscillation, or parametric instability, can be a limiting factor for operation of optomechanical systems, especially those with low-loss optical cavities—although eq. (1.36) is derived in the bad-cavity limit, the effect also occurs in the resolved-sideband regime, albeit with a different detuning dependence.

## 1.5. Optical measurement of displacement

Through the coupling between the displacement $x$ and the cavity frequency $\omega_{\text{c}}$, the mechanical motion is transduced to the light field reflected by the cavity. Detecting this light field therefore allows measuring the mechanical displacement. Measurements are always associated with noise, which limits the precision with which we obtain a result. In fact, for a continuous displacement measurement, there is a fundamental lower limit to the amount of added noise associated with the measurement, called the standard quantum limit [1, 50]. This is a manifestation of the Heisenberg uncertainty principle, since a measurement of the displacement at time $t_1$ provides information about the momentum of the resonator at time $t_2 = t_1 + T_{\text{m}}/4$, a quarter of its oscillation period later. In the case of optical measurements of displacements, it arises due to the optical shot noise, which limits the precision of the measurement of the light field. When we use higher optical powers for the measurement, this imprecision is reduced, but the randomly fluctuating force due to the optical shot noise increasingly drives the resonator, disturbing its motion. The standard quantum limit is reached when these two effects are balanced and the measurement is $100\,\%$ efficient.

In this section, we discuss the standard quantum limit as a consequence of the Heisenberg uncertainty limit. We then introduce the concept of spectral density and find the standard quantum limit in terms of spectral density, which reveals the role of optical shot noise. After that, we derive expressions for the transduction of motion to the detected signal in the case of a direct reflection measurement, which we use in chapters 2 and 4, and in the case of a balanced homodyne interferometer, which we use in chapters 5 and 6.

### 1.5.1. Standard quantum limit of continuous displacement measurement

For an object with position $x$ and momentum $p$, the familiar form of the Heisenberg uncertainty relation states that the product of the uncertainties $\Delta x$ and $\Delta p$

has a minimum value [1],

$$\Delta x \Delta p \geq \frac{\hbar}{2}. \tag{1.37}$$

In a harmonic oscillator with mass $m$ and resonance frequency $\Omega_{\mathrm{m}}$ with no damping and no external force acting on it, the displacement $x(t)$ is related to the displacement and momentum at time $t = 0$ as

$$x(t) = x(0)\cos\Omega_{\mathrm{m}}t + \frac{p(0)}{m\Omega_{\mathrm{m}}}\sin\Omega_{\mathrm{m}}t, \tag{1.38}$$

such that the added uncertainty of the position after a time $t$ from the uncertainty in momentum at $t = 0$ is

$$\Delta x(t) = \frac{\Delta p(0)}{m\Omega_{\mathrm{m}}}\sin\Omega_{\mathrm{m}}t. \tag{1.39}$$

Combining this with eq. (1.37), the product of uncertainties $\Delta x$ at different times $t$ is

$$\Delta x(t)\Delta x(t') \geq \frac{\hbar}{2m\Omega_{\mathrm{m}}}\sin(\Omega_{\mathrm{m}}|t - t'|), \tag{1.40}$$

which leads to the minimum uncertainty for a continuous measurement (where the displacement uncertainty $\Delta x(t)$ is the same for all times $t$) of

$$\Delta x_{\mathrm{SQL}} \geq \sqrt{\frac{\hbar}{2m\Omega_{\mathrm{m}}}}. \tag{1.41}$$

The label "SQL" indicates that this uncertainty is the standard quantum limit for a continuous position measurement. The right-hand side of eq. (1.41) is equal to $x_{\mathrm{zpf}}$ (eq. (1.3)), the ground-state uncertainty of the displacement of the oscillator.

### 1.5.2. Spectral density

In chapter 6 we discuss direct measurements of the displacement $x$, but in most of this thesis we instead measure the spectrum of displacement fluctuations. We present these using the power spectral density (see the appendices of review by Clerk, Marquardt & Jacobs [51]). According to the Wiener-Khinchin theorem, the spectral density is equal to the Fourier transform of the autocorrelation function,

$$S_{xx}(\Omega) = \int \langle x(t)x(0)\rangle e^{i\Omega t}dt. \tag{1.42}$$

Here the assumption was made that the autocorrelation of $x$ only depends on the time difference (the fluctuations $x(t)$ are produced by a *stationary* process), which allows the substitution $\langle x(t - t')x(t)\rangle = \langle x(t)x(0)\rangle$. The autocorrelation can often be calculated from theoretical considerations, for example by assuming delta-correlated noise processes to describe thermal or ground-state motion. For a classical variable $x$, the spectral density is symmetric for positive and negative

frequencies: $S_{xx}(\Omega) = S_{xx}(-\Omega)$. Therefore the concepts of a single-sided spectral density $S_x(\Omega) \equiv 2S_{xx}(\Omega)$, and the symmetrized spectral density $\overline{S}_{xx}(\Omega) \equiv \frac{1}{2}(S_{xx}(\Omega) + S_{xx}(-\Omega))$, with $\Omega \geq 0$, are sometimes useful.

Experimentally, we measure an optical power $P(t)$ during a finite measurement time $t_{\mathrm{M}}$. The spectral content in such a trace is given by the gated Fourier transform

$$P_{t_{\mathrm{M}}}(\Omega) = \frac{1}{\sqrt{t_{\mathrm{M}}}} \int_{-t_{\mathrm{M}}/2}^{t_{\mathrm{M}}/2} P(t) e^{i\Omega t} dt, \tag{1.43}$$

where the normalization makes the statistical properties of $P_{t_{\mathrm{M}}}(\Omega)$ independent of the measurement time $t_{\mathrm{M}}$ if the latter is sufficiently large with respect to the correlation time of the fluctuations in $P(t)$. The spectral density is then given by the ensemble average of $|P_{t_{\mathrm{M}}}(\Omega)|^2$,

$$S_{PP}(\Omega) = \lim_{t_{\mathrm{M}} \to \infty} \langle |P_{t_{\mathrm{M}}}(\Omega)|^2 \rangle. \tag{1.44}$$

In the case of displacement measurements of a harmonic oscillator with damping rate $\Gamma_{\mathrm{m}}$, the correlation time of its motion driven by thermal fluctuations is given by the damping time $2/\Gamma_{\mathrm{m}}$. Therefore we need $t_{\mathrm{M}} \geq 2/\Gamma_{\mathrm{m}}$. To obtain the ensemble average, we average in time over a total acquisition time $N t_{\mathrm{M}}$. By doing this, we implicitly assume that the displacement at time $t$ is not correlated with the displacement at a time $t + t'$ if $t' > 2/\Gamma_{\mathrm{m}}$, which is valid for motion that is dominated by thermal fluctuations.

The units of the spectral density for the displacement, $S_{xx}(\Omega)$, are $\mathrm{m}^2\,\mathrm{Hz}^{-1}$. In the literature, it is not uncommon to encounter the square root of the spectral density, $\sqrt{S_{xx}(\Omega)}$, which has units of $\mathrm{m}\,\mathrm{Hz}^{-1/2}$, just like a gated Fourier transform of $x(t)$ would have (as defined in eq. (1.43), replacing $P(t)$ with $x(t)$).

The spectral density also has the property that its integral gives the variance:

$$\int S_{xx}(\Omega) \frac{\mathrm{d}\Omega}{2\pi} = \langle x^2 \rangle. \tag{1.45}$$

**Transfer function and electronic spectrum analyzer signal**

If two variables $U$ and $V$ are linearly related through $V(\Omega) = g(\Omega)U(\Omega)$, their spectral densities are also linearly related

$$S_{VV}(\Omega) = |g(\Omega)|^2 S_{UU}(\Omega), \tag{1.46}$$

where $|g(\Omega)|^2$ is called the transfer function.

The optical power $P$ is transformed by the detector to a voltage $V$, which is fed to an electronic spectrum analyzer (ESA). Here we discuss the relation between the output of this device and the optical power spectral density $S_{PP}(\Omega)$. The ESA measures the power in the electrical signal over a load of $R = 50\,\Omega$ within its resolution bandwidth (RBW), as a function of frequency. We consider here the case that the resolution bandwidth is smaller than the bandwidth of the features in $S_{PP}(\Omega)$, which for fluctuations induced by a mechanical resonator with damping

rate $\Gamma_{\mathrm{m}}$ corresponds to RBW $< \Gamma_{\mathrm{m}}$. In this regime, the ESA signal $P_{\mathrm{ESA}}(\Omega)$ is proportional to the voltage spectral density $S_{VV}(\Omega)$ through

$$P_{\mathrm{ESA}}(\Omega) = \frac{2\mathrm{RBW}}{R} S_{VV}(\Omega) = \frac{2\mathrm{RBW}\xi_{\mathrm{det}}^2}{R} S_{PP}(\Omega), \tag{1.47}$$

and it has units of W. For the second step, we used that the voltage $V$ is directly proportional to the optical power $P$ with the conversion efficiency of the detector $\xi_{\mathrm{det}}$ in $\mathrm{V\,W^{-1}}$. With proper calibration, we can convert $P_{\mathrm{ESA}}(\Omega)$ to $S_{PP}(\Omega)$. In this thesis, we have sometimes omitted such a calibration step, instead opting to display the electrical power spectral density directly (usually labeled "PSD"). In those cases, we have defined

$$\mathrm{PSD}(\Omega) = \frac{P_{\mathrm{ESA}}(\Omega)}{\mathrm{RBW}}, \tag{1.48}$$

which has units of $\mathrm{W\,Hz^{-1}}$.

**Displacement spectral density**

The proportionality constant that connects the displacement response of the mechanical resonator to an external force is the susceptibility $\chi_{\mathrm{m}}(\Omega)$, defined by $x(\Omega) = \chi_{\mathrm{m}}(\Omega) F_{\mathrm{ext}}(\Omega)$. It can be derived from eq. (1.8) and was already implicitly used in section 1.4.2. The susceptibility is given by

$$\chi_{\mathrm{m}}(\Omega) = \frac{1}{m(\Omega_{\mathrm{m}}^2 - \Omega^2) - im\Gamma_{\mathrm{m}}\Omega}. \tag{1.49}$$

The fluctuation-dissipation theorem links the dissipative part of the susceptibility to the displacement spectral density in thermal equilibrium. The quantum version of this theorem is given by

$$S_{xx}(\Omega) = \frac{2\hbar}{1 - \exp(-\hbar\Omega/k_{\mathrm{B}}T)} \operatorname{Im} \chi_{\mathrm{m}}(\Omega). \tag{1.50}$$

For large temperature ($k_{\mathrm{B}}T \gg \hbar\Omega$), this reduces to

$$\begin{aligned} S_{xx}^{\mathrm{th}}(\Omega) &= 2\frac{k_{\mathrm{B}}T}{\Omega} \operatorname{Im} \chi_{\mathrm{m}}(\Omega) \\ &= \frac{k_{\mathrm{B}}T}{m} \frac{2\Gamma_{\mathrm{m}}}{(\Omega_{\mathrm{m}}^2 - \Omega^2)^2 + \Gamma_{\mathrm{m}}^2\Omega^2} \\ &\approx 2x_{\mathrm{zpf}}^2 \bar{n}_{\mathrm{th}} \frac{\Gamma_{\mathrm{m}}/2}{(\Omega_{\mathrm{m}} - \Omega)^2 + \Gamma_{\mathrm{m}}^2/4}, \end{aligned} \tag{1.51}$$

where we have defined the average phonon occupancy $\bar{n}_{\mathrm{th}} \equiv k_{\mathrm{B}}T/(\hbar\Omega_{\mathrm{m}})$. The approximation in the last line is valid near resonance ($\Omega \approx \Omega_{\mathrm{m}}$) for weak damping ($\Gamma_{\mathrm{m}} \ll \Omega_{\mathrm{m}}$), in which case the spectrum has a Lorentzian lineshape. Integrating this expression yields the displacement variance due to thermal motion

$$\langle x^2 \rangle_{\mathrm{th}} = 2x_{\mathrm{zpf}}^2 \bar{n}_{\mathrm{th}}. \tag{1.52}$$

Using eq. (1.50) at $T = 0$, one can find the spectral density of the zero-point fluctuations [7], given in symmetrized form by

$$\overline{S}_{xx}^{\text{zpf}}(\Omega) = \hbar |\operatorname{Im} \chi_{\text{m}}(\Omega)|, \tag{1.53}$$

such that $\overline{S}_{xx}^{\text{th}}/\overline{S}_{xx}^{\text{zpf}} \approx 2\bar{n}_{\text{th}}$. The peak spectral density of the zero-point fluctuations at $\Omega \approx \Omega_{\text{m}}$ is given by $\overline{S}_{xx}^{\text{zpf}}(\Omega_{\text{m}}) = 2x_{\text{zpf}}^2/\Gamma_{\text{m}}$, and integrating yields the ground-state variance of the displacement $\langle x^2 \rangle_{\text{zpf}} = x_{\text{zpf}}^2$, as expected.

### 1.5.3. Standard quantum limit in terms of spectral densities

The Heisenberg uncertainty relation for continuous measurement can be expressed in terms of spectral densities as [1, 50]

$$\overline{S}_{xx}^{\text{imp}}(\Omega)\overline{S}_{FF}(\Omega) \geq \frac{\hbar^2}{4}, \tag{1.54}$$

where $S_{xx}^{\text{imp}}(\Omega)$ represents the imprecision noise density, the spectral density in displacement associated with the measurement uncertainty, and $S_{FF}(\Omega)$ is the spectral density of the force acting on the mechanical resonator due to the measurement, which is called the backaction force. The total added noise as inferred from the measurement output is given by the sum of these two noise terms, where the displacement noise due to the backaction force can be calculated via the mechanical susceptibility $\chi_{\text{m}}(\Omega)$ (see eq. (1.49)), which yields

$$\overline{S}_{xx}^{\text{add}}(\Omega) = \overline{S}_{xx}^{\text{imp}}(\Omega) + \overline{S}_{FF}(\Omega)|\chi_{\text{m}}(\Omega)|^2. \tag{1.55}$$

For a measurement in which the equality in eq. (1.54) is realized, the minimum added noise corresponds to $\overline{S}_{FF}(\Omega) = \hbar/(2|\chi_{\text{m}}|)$, such that both contributions are equal and we obtain

$$\overline{S}_{xx}^{\text{add}} \geq \hbar|\chi_{\text{m}}(\Omega)| \geq \overline{S}_{xx}^{\text{zpf}}(\Omega), \tag{1.56}$$

where the second step follows from eq. (1.53). This inequality is the standard quantum limit for weak continuous measurement of displacement, expressed in terms of spectral density.

#### Imprecision and backaction with optical measurements

For an optical measurement of displacement, the imprecision noise and backaction noise can be found by considering the optical shot noise in the laser beam used for the measurement [7, 50]. The imprecision noise arises due to the shot noise at the detector, which induces noise in the measurement of the light field quadrature which carries information about the displacement. The expression for the imprecision noise for an optimal measurement at resonance with the optical cavity, which has in- and outcoupling efficiencies $\eta_{\text{in}}$ and $\eta_{\text{out}}$, is

$$\overline{S}_{xx}^{\text{imp}}(\Omega) = \frac{\kappa}{16G^2\eta_{\text{out}}|a|^2} = \frac{\kappa^2\hbar\omega_{\text{c}}}{64G^2\eta_{\text{in}}\eta_{\text{out}}P_{\text{in}}}, \tag{1.57}$$

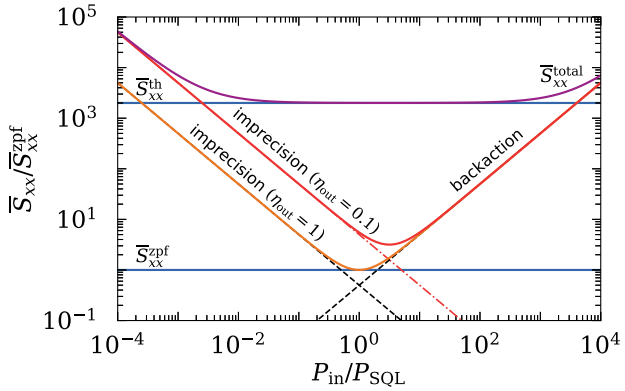


Figure 1.4: Displacement spectral density contributions as a function of optical input power $P_{\text{in}}$. The imprecision noise $\overline{S}_{xx}^{\text{imp}}$ is shown both for outcoupling efficiency $\eta_{\text{out}} = 1$ (black dashed line) and $\eta_{\text{out}} = 0.1$ (red dash-dotted line). The horizontal lines represent the ground-state fluctuations $\overline{S}_{xx}^{\text{zpf}}$ and the thermal motion $\overline{S}_{xx}^{\text{th}}$ with $\overline{n}_{\text{th}} = 10^3$. The orange and red solid lines show the added noise due to the measurement $\overline{S}_{xx}^{\text{add}}$ which is the sum of the imprecision and backaction noise (see eq. (1.55)). The purple solid line indicates the total measured spectral density for a resonator in thermal motion (assuming optical shot noise dominates the imprecision), which is given by $\overline{S}_{xx}^{\text{total}} = \overline{S}_{xx}^{\text{th}} + \overline{S}_{xx}^{\text{add}}$.

where the second step substitutes the cavity occupancy at resonance $|a|^2 = 4\eta_{\text{in}}P_{\text{in}}/(\kappa\hbar\omega_{\text{c}})$. Note that this expression does not include the fact that the cavity acts as a low pass filter, which suppresses frequencies $\Omega > \kappa$ in its output and therefore effectively increases the imprecision at those higher frequencies. In this thesis, we only consider devices in the bad-cavity limit ($\kappa \gg \Omega_{\text{m}}$) so we can safely ignore this contribution. In fig. 1.4, the imprecision noise is the dominant noise source for low input power $P_{\text{in}}$.

The origin of the backaction noise force is that random fluctuations of the radiation pressure force acting on the mechanical resonator due to shot noise in the cavity. Its spectral density at resonance with the optical cavity is given by

$$\overline{S}_{FF}(\Omega) = \frac{4\hbar^2G^2|a|^2}{\kappa} = \frac{16\hbar^2G^2\eta_{\text{in}}P_{\text{in}}}{\kappa^2\hbar\omega_{\text{c}}}. \tag{1.58}$$

In fig. 1.4, the backaction noise dominates for high input power $P_{\text{in}}$. We note that for most systems, actually observing this "radiation pressure shot noise" requires relatively high optical powers, especially since one does not just need $P_{\text{in}} > P_{\text{SQL}}$, an input power higher than the power at which the SQL is reached, but the backaction noise should actually overcome the thermal noise of the resonator. This is indicated with the upper horizontal line in fig. 1.4.

From eqs. (1.57) and (1.58), it follows that the standard quantum limit can only be reached if $\eta_{\text{out}} = 1$. Any extra losses or inefficiencies in the detection process will similarly increase the total added noise. We note that with $\eta_{\text{out}} < 1$, by increasing the optical power $P_{\text{in}} > P_{\text{SQL}}$ it is still possible to decrease the imprecision noise level to the imprecision noise at the standard quantum

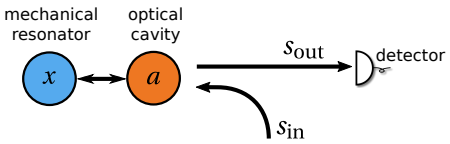


Figure 1.5: Schematic diagram of a simple reflection measurement. The optical input field $s_{\text{in}}$ interacts with the cavity and the power of the reflected field $s_{\text{out}}$ is measured with a detector.

limit, $\overline{S}_{xx}^{\text{imp}}(\Omega) = \frac{1}{2}\overline{S}_{xx}^{\text{zpf}}(\Omega)$ (see the red dash-dotted line in fig. 1.4). However, this will correspond to a backaction force that is larger than that at the SQL, $\overline{S}_{FF}(\Omega)|\chi_{\text{m}}(\Omega)|^2 > \frac{1}{2}\overline{S}_{xx}^{\text{zpf}}(\Omega)$.

### 1.5.4. Reflection measurement

In this section, we derive the effect that a small frequency modulation of the intracavity field has on the output of a cavity. This allows us to set up a model that describes the transduction of thermal motion to optical intensity modulation that can be detected. This derivation follows the calculation by Gorodetsky *et al.* [52], with the important difference that we include the nonresonant contribution in the reflection spectrum that leads to a Fano lineshape (see eq. (1.15)).

We start from the classical equations of motion given by eqs. (1.7) and (1.8). As described in section 1.4.2, the frequency $\Omega_{\text{m}}$ and damping rate $\Gamma_{\text{m}}$ of the mechanical resonator are influenced by the number of photons in the cavity $|a|^2$, an effect we neglect in the following by assuming a low input power. This simplification is motivated by the fact that we seek to predict the amplitude of the mechanically-induced light modulation, not the frequency of such modulations. Moreover, dynamical backaction affecting mechanical linewidth is small in devices that have large $\kappa/\Omega_{\text{m}}$. We consider a small harmonic oscillation of the mechanical resonator $x(t) = x_0\cos(\Omega_{\text{m}}t)$, which causes a modulation of the cavity frequency with amplitude $x_0G$, or a modulation of the optical intracavity phase with amplitude $x_0G/\Omega_{\text{m}}$. If the modulation is small ($x_0G \ll \kappa$), this yields

$$\begin{aligned} a_x =& \frac{2s_{\text{in}}\sqrt{\eta_{\text{in}}}\,\mathcal{L}(0)}{\sqrt{\kappa}}\left(1 - \frac{ix_0G}{\kappa}\left[\mathcal{L}(\Omega_{\text{m}})e^{-i\Omega_{\text{m}}t} + \mathcal{L}(-\Omega_{\text{m}})e^{i\Omega_{\text{m}}t}\right]\right), \\ \mathcal{L}(\Omega) =& \frac{1}{1 - i(u + 2\Omega/\kappa)}. \end{aligned} \tag{1.59}$$

The cavity is coupled to the output $s_{\text{out}}$ with the coupling rate $\eta_{\text{out}}\kappa$. The output field is given by eq. (1.14), which reads $s_{\text{out}} = ce^{i\varphi}s_{\text{in}} - \sqrt{\eta_{\text{out}}\kappa}a_x$, where the first term represents nonresonant scattering from the input to the output.

In the experiment, we measure the reflected power $P_{\text{out}} = \hbar\omega_{\text{L}}|s_{\text{out}}|^2$ corresponding to an input power $P_{\text{in}} = \hbar\omega_{\text{L}}|s_{\text{in}}|^2$ (see fig. 1.5). We then feed the reflected power signal to a spectrum analyzer, which yields the single-sided spectrum of the signal. Since we are interested in the strength of the spectral component at the mechanical oscillation frequency $\Omega_{\text{m}}$, we highlight the time depen-

dence here:

$$\begin{aligned}|s_{\text{out}}(t)|^2 =& c^2|s_{\text{in}}|^2 + \eta_{\text{out}}\kappa|a_x(t)|^2 \\ &- c\sqrt{\eta_{\text{out}}\kappa}\left[e^{i\varphi}s_{\text{in}}a_x^*(t) + e^{-i\varphi}s_{\text{in}}^*a_x(t)\right].\end{aligned} \tag{1.60}$$

The first term is constant so it does not contribute to a signal at $\Omega_{\text{m}}$. Substituting $a_x$ into the other two terms, and discarding any terms not oscillating at $\pm\Omega_{\text{m}}$ yields

$$\begin{aligned}\left.\frac{|s_{\text{out}}(t)|^2}{|s_{\text{in}}|^2}\right|_{\pm\Omega_{\text{m}}} &= \frac{2x_0G\sqrt{\eta_{\text{in}}\eta_{\text{out}}}}{\kappa} \\ &\times\left[\frac{4\sqrt{\eta_{\text{in}}\eta_{\text{out}}}}{\kappa}|\,\mathcal{L}(0)|^2\left(\left\{ie^{i\Omega_{\text{m}}t}\left[\mathcal{L}^*(\Omega_{\text{m}}) - \mathcal{L}(-\Omega_{\text{m}})\right]\right\} + \text{c.c.}\right)\right. \\ &\left. - c\left(\left\{ie^{i\Omega_{\text{m}}t}\left[e^{i\varphi}\,\mathcal{L}^*(0)\,\mathcal{L}^*(\Omega_{\text{m}}) - e^{-i\varphi}\,\mathcal{L}(0)\,\mathcal{L}(-\Omega_{\text{m}})\right]\right\} + \text{c.c.}\right)\right].\end{aligned} \tag{1.61}$$

Here we used "c.c." to denote the complex conjugate of the preceding term (enclosed in braces {}). This expression scales linearly with the modulation amplitude $x_0G$. In our experiment, we compare the variance of the modulation to the known variance of the mechanical thermal motion $\langle x^2\rangle_{\text{th}} = 2x_{\text{zpf}}^2\bar{n}_{\text{th}}$. Therefore we calculate the variance of $P_{\text{out}} = \hbar\omega_L|s_{\text{out}}|^2$ due to the modulation at $+\Omega_{\text{m}}$ and $-\Omega_{\text{m}}$, which will both contribute to the signal at $+\Omega_{\text{m}}$ in the single-sided spectrum. We can write $P_{\text{out}}\big|_{\pm\Omega_{\text{m}}} = Ae^{i\Omega_{\text{m}}t} + A^*e^{-i\Omega_{\text{m}}t}$, which leads to $\langle|P_{\text{out}}|^2\rangle_{\Omega_{\text{m}}} = 2|A|^2$. After some algebra, we arrive at

$$\begin{aligned}\langle|P_{\text{out}}|^2\rangle_{\Omega_{\text{m}}} &= \frac{32P_{\text{in}}^2x_0^2G^2\eta_{\text{in}}\eta_{\text{out}}}{\kappa^2(1+u^2)^2(1+(u+2\Omega_{\text{m}}/\kappa)^2)(1+(u-2\Omega_{\text{m}}/\kappa)^2)} \\ &\times\left\{4u^2\eta_{\text{in}}\eta_{\text{out}} + 4uc\sqrt{\eta_{\text{in}}\eta_{\text{out}}}\left[-2u\cos\varphi + (1-u^2)\sin\varphi\right]\right. \\ &\quad + c^2\left[u^2((2\Omega_{\text{m}}/\kappa)^2+4)\cos^2\varphi\right. \\ &\qquad + (u^4 - 2u^2 + (2\Omega_{\text{m}}/\kappa)^2 + 1)\sin^2\varphi \\ &\qquad\quad \left.\left. + 2u(2u^2 - (2\Omega_{\text{m}}/\kappa)^2 - 2)\cos\varphi\sin\varphi\right]\right\}.\end{aligned} \tag{1.62}$$

If we evaluate this expression in the bad-cavity limit ($\Omega_{\text{m}} \ll \kappa$), we find it is directly related to the derivative of the Fano lineshape in eq. (1.15),

$$\begin{aligned}\langle|P_{\text{out}}|^2\rangle_{\Omega_{\text{m}}} &= \frac{32P_{\text{in}}^2x_0^2G^2\eta_{\text{in}}\eta_{\text{out}}}{\kappa^2(1+u^2)^4} \\ &\quad\times\left[2u\sqrt{\eta_{\text{in}}\eta_{\text{out}}} - 2uc\cos\varphi + (1-u^2)c\sin\varphi\right]^2 \\ &= \frac{2P_{\text{in}}^2x_0^2G^2}{\kappa^2}\left(\frac{\partial R}{\partial u}\right)^2.\end{aligned} \tag{1.63}$$

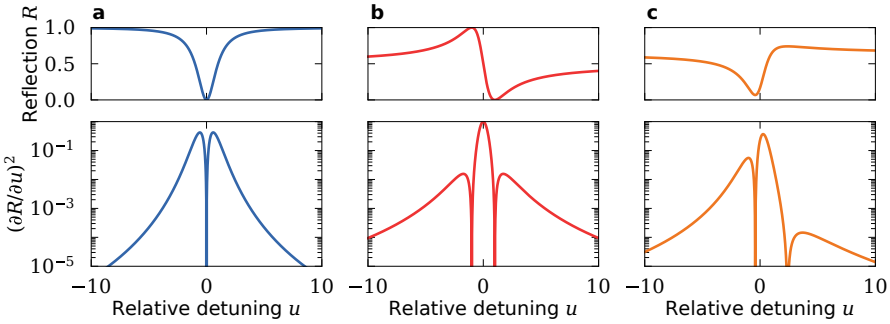


Figure 1.6: Detuning dependence of the transduction of motion to reflected optical intensity, given by $(\partial R/\partial u)^2$ (see eq. (1.64)). The corresponding reflection spectrum $R(u)$ is shown at the top of the panels. The parameters are the same as in fig. 1.2: (a) $ce^{i\varphi} = 1, \eta = 0.5$; (b) $c = 1/\sqrt{2}, \varphi = \pi/4, \eta = 0.5$; (c) $c = 0.8, \varphi = -\pi/6, \eta = 0.3$.

To relate this variance due to a small harmonic modulation $x_0$ to the transduction of any mechanical spectral density $S_{xx}$, we substitute the variance of our modulation $\langle x^2 \rangle = x_0^2/2$. Since the variance is given by the integral over the spectral density, the relation between the variances is equal to the relation between the spectral densities. We obtain

$$S_{PP} = \frac{4G^2 P_{\text{in}}^2}{\kappa^2} \left( \frac{\partial R}{\partial u} \right)^2 S_{xx}. \tag{1.64}$$

Figure 1.6 shows the squared derivative $(\partial R/\partial u)^2$ as a function of detuning, for the different Fano lineshapes shown in fig. 1.2 (repeated here at the top of the figure).

We note that a measurement efficiency $h < 1$, for example due to imperfect transmission of the optics between the sample and the detector, can be incorporated by considering the detected power $P_{\text{det}} = hP_{\text{out}}$, such that $\langle P_{\text{det}}^2 \rangle = h^2 \langle P_{\text{out}}^2 \rangle$ (and similar for the spectral density). Finally, the expected variance in the output signal due to the thermal motion of the mechanical resonator can be found by using the variance of the thermal mechanical motion, which is $\langle x^2 \rangle_{\text{th}} = 2x_{\text{zpf}}^2 \bar{n}_{\text{th}}$, such that

$$\langle P_{\text{out}}^2 \rangle_{\text{th}} = \frac{8\bar{n}_{\text{th}} g_0^2 P_{\text{in}}^2}{\kappa^2} \left( \frac{\partial R}{\partial u} \right)^2. \tag{1.65}$$

### 1.5.5. Balanced homodyne interferometer measurement

The balanced homodyne interferometer is an important tool in the field of quantum optics, as it allows quantum-limited detection of the quadratures of a light field (see for example the review by Lvovsky & Raymer [53] and references therein). It has several advantages over the direct reflection measurement described in the previous section. The most important disadvantage of the direct reflection measurement described in the previous section is that the amount of

optical power at the detector is directly linked to the amount of light at the cavity. This means that if we need to limit $P_{\text{in}}$ to decrease the influence of nonlinear effects, the relative importance of the electronic noise in the detector increases. Electronic noise in detectors based on photodiodes is typically dominated by their dark current, which is mostly independent of the power incident on the detector. Interfering the reflected light field with a strong reference beam (usually called the "local oscillator") boosts the signal at the detector, thus allowing the noise level of the light to overcome the electronic noise. If the noise level in the laser beam is dominated by the shot noise, and this noise level is also the dominant source of noise in the measurement, quantum-limited detection of the quadratures of the light field is achieved.

An additional advantage to measurements using an interferometer is that the phase of the light field can be measured. For cavities where the direct reflection (or transmission) follows a Lorentzian lineshape, the derivative $\partial R/\partial u$ vanishes at resonance ($u = 0$), which means displacement measurements using a measurement of the reflected (transmitted) intensity are only possible at non-zero detuning. In an interferometer, the local oscillator beam provides a phase reference, which allows displacement measurements at any detuning. In principle, the local oscillator can be at a different frequency than the signal beam, in which case the two quadratures of the light field in the signal arm can both be detected at the beat frequency. This method is called heterodyne detection. When the light field in both arms of the interferometer has the same frequency, it is called homodyne detection. In this case only one quadrature is detected, selected by the optical path length difference between the two arms of the interferometer.

In a balanced homodyne interferometer, the two outputs of the beamsplitter at which the local oscillator and the signal field are overlapped are detected using two photodiodes, whose photocurrents are subtracted. This balanced detection scheme ensures that all of the light in the signal arm reaches the detector, as opposed to detecting only at a single output of the beamsplitter. Moreover, classical intensity noise in the local oscillator beam is subtracted, suppressing the influence of such noise on the measurement.

The detection efficiency of both the direct intensity measurements and the balanced homodyne measurements depends on the quantum efficiency of the photodiode-based detector and on transmission of light in the optical setup. In the homodyne detector, an additional factor is the spatio-temporal mode overlap between the local oscillator and signal arm. Optimizing this factor requires careful alignment of the two beams, as well as matching their polarization and wavefront profiles. This can also be interpreted as a mode filter, such that the measurement is only sensitive to the component of the signal beam which overlaps with the local oscillator mode. Experimentally, the overlap factor can be determined by observing the fringe visibility [54].

**Balanced homodyne interferometer signal**

A schematic diagram of a balanced homodyne interferometer is shown in fig. 1.7. At the $50:50$ beamsplitter, the field in the signal arm $s_{\text{out}}$, which has interacted with the cavity, interferes with the field in the local oscillator arm $s_{\text{LO}}$.

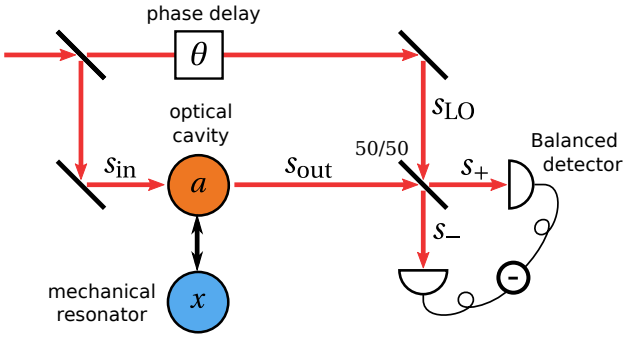


Figure 1.7: Schematic diagram of a balanced homodyne interferometer. An input laser beam is split into a signal arm and a reference "local oscillator" arm. A phase delay $\theta$ is introduced in the local oscillator arm. The field in the signal arm interacts with the cavity and the resulting field $s_{\text{out}}$ interferes with the local oscillator field at the $50:50$ beamsplitter. Finally, the powers of the two outputs $s_+$ and $s_-$ are detected and subtracted by the balanced detector.

The resulting fields at the $(+)$ and $(-)$ ports of the balanced detector are $s_+ = \frac{1}{\sqrt{2}}(s_{\text{LO}} + is_{\text{out}})$ and $s_- = \frac{1}{\sqrt{2}}(s_{\text{out}} + is_{\text{LO}})$. To obtain the full expression for the output signal, we assume the cavity reacts sufficiently fast to the mechanical motion that we can use the steady-state cavity response (eq. (1.14)) with a detuning $\Delta = \Delta_0 + Gx$ modified by the mechanically induced frequency shift $\delta\omega_{\text{c}} = -G\delta x$. This assumption is valid in the bad-cavity limit, with $\kappa \gg \Omega_{\text{m}}$. The cavity response is then given by eq. (1.14), where we will use $\eta \equiv \sqrt{\eta_{\text{in}}\eta_{\text{out}}}$ as the overall coupling efficiency of the cavity. Note that if the interferometer is well-aligned, the interference with the Gaussian local oscillator beam provides a mode filter such that both the input and output mode of the cavity consist of the same Gaussian beam. In that case, $\eta_{\text{in}} = \eta_{\text{out}} = \eta$. Conversely, $\eta_{\text{out}}$ might have a different value for interferometric detection than for the direct detection method described in section 1.5.4. We take the input to the cavity, $s_{\text{in}}$, to be real-valued, and describe the local oscillator, which has a phase delay of $\theta$, as $s_{\text{LO}} = |s_{\text{LO}}|e^{i\theta}$. This phase delay is important, essentially selecting the quadrature of the light field $s_{\text{out}}$ that is detected. The subtracted output of the detector is proportional to a virtual optical power $P_{\text{H}}/\hbar\omega_{\text{L}} = |s_+|^2 - |s_-|^2$. Substituting $s_+$ and $s_-$, we obtain

$$\begin{aligned}\frac{P_{\text{H}}}{\hbar\omega_{\text{L}}} &= \left|\frac{i}{\sqrt{2}}s_{\text{out}} + \frac{1}{\sqrt{2}}s_{\text{LO}}\right|^2 - \left|\frac{i}{\sqrt{2}}s_{\text{LO}} + \frac{1}{\sqrt{2}}s_{\text{out}}\right|^2 \\ &= i(s_{\text{LO}}s_{\text{out}}^* - s_{\text{LO}}^* s_{\text{out}}) \\ &= |s_{\text{LO}}||s_{\text{in}}|\left(2c\sin(\theta-\phi) + \frac{4\eta\,(u\cos\theta - \sin\theta)}{1+u^2}\right).\end{aligned} \tag{1.66}$$

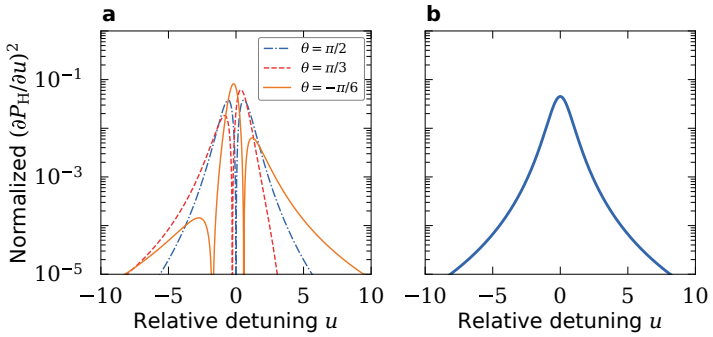


Figure 1.8: (a) Detuning dependence of the transduction of motion to the detected homodyne signal, given by $(\partial P_{\mathrm{H}}/\partial u)^2$ (see eq. (1.69)). The scale is normalized to the maximum achieved value at $\theta = 0, u = 0, \eta = 1$. The plotted values were calculated using $\eta = 0.3$, corresponding to fig. 1.2c and fig. 1.6c. The different lines correspond to different choices for the interferometer phase $\theta$, indicated in the legend. (b) Detuning dependence of the transduction of motion to the detected homodyne signal for phase-averaged operation (see eq. (1.70)). In this case, the detuning dependence follows the square of a Lorentzian lineshape, for any choice of parameters $c$ and $\varphi$. The line shown here was calculated using $\eta = 0.3$, like in panel (a).

**Transduction of motion**

To find the transduction of motion to the homodyne signal, we use eq. (1.46), in this case

$$S_{PP} = \left(\frac{\partial P_{\mathrm{H}}}{\partial x}\right)^2 S_{xx}. \tag{1.67}$$

Since $u = 2\Delta/\kappa = (2/\kappa)(\Delta_0 + Gx)$, to find the transduction of motion to the homodyne signal we can use eq. (1.66) and take the first term of its Taylor expansion around $u_0 = 2\Delta_0/\kappa$,

$$P_{\mathrm{H}}(u) = P_{\mathrm{H}}(u_0) + \frac{\partial P_{\mathrm{H}}}{\partial u} u. \tag{1.68}$$

The derivative of $P_{\mathrm{H}}$ can be found from eq. (1.66) to be

$$\frac{\partial P_{\mathrm{H}}}{\partial u} = 4\eta\sqrt{P_{\mathrm{LO}} P_{\mathrm{in}}} \frac{(1-u^2)\cos\theta + 2u\sin\theta}{(1+u^2)^2}, \tag{1.69}$$

where we used $P_{\mathrm{LO}} = \hbar\omega_{\mathrm{L}}|s_{\mathrm{LO}}|^2$ and likewise for $P_{\mathrm{in}}$. This result shows that the transduction of motion to our signal will depend strongly on the interferometer phase $\theta$, for example at resonance with the cavity ($u_0 = 0$), the derivative is a constant prefactor times $\cos\theta$. Figure 1.8a illustrates this by showing the detuning dependence of $(\partial P_{\mathrm{H}}/\partial u)^2$ for different values of $\theta$.

In practice, $\theta$ might have a detuning dependence if there is an arm length difference in the interferometer, for example of a few wavelengths. Moreover, it will fluctuate in time due to acoustical vibrations and variations in the refractive index in the optical path, which can be caused by small temperature fluctuations. Therefore a common mode of operation is to use feedback to lock the homodyne interferometer to a certain phase. For cavities where the cavity response has a

Lorentzian lineshape, which corresponds to a phase $\varphi = k\pi$ of the nonresonant response that is an integer number $k$ times $\pi$, eq. (1.66) shows that at resonance ($u_0 = 0$) the point $\theta = 0$ coincides with $P_{\mathrm{H}} = 0$. For the more general case, the relation is not so straightforward, and a more complex approach is needed to obtain a lock at the desired phase. For example, one could determine the resonance frequency of the cavity by using the detuning of the mechanical resonance frequency $\delta\Omega_{\mathrm{m}}$ due to the optical spring effect (eq. (1.35)), and then maximize the transduced signal to find the correct set point for the feedback loop. An additional complication is that the exact behavior of the nonresonant term $ce^{i\varphi}$ can depend on the alignment of the laser beam to the cavity structure.

**Phase-averaged homodyne operation**

To avoid the complex dependence on the alignment-sensitive parameters $c$ and $\varphi$, we can also average over the interferometer phase $\theta$, which essentially corresponds to averaging over the quadratures of the field $s_{\mathrm{out}}$. In the experiments, we accomplish this by sweeping the position of a piezo-mounted mirror over a distance of more than a wavelength and averaging the measured spectra in time such that all phases between $0$ and $2\pi$ contribute to the signal. The quantity we are interested in to describe the transduction of motion in this mode of operation is the average transduction factor (see eq. (1.67)) written as $\langle(\partial P_{\mathrm{H}}/\partial x)^2\rangle_\theta$, where $\langle\rangle_\theta$ denotes averaging over $\theta$. Using $\langle\cos^2\theta\rangle_\theta = \langle\sin^2\theta\rangle_\theta = 1/2$ and $\langle\sin\theta\cos\theta\rangle_\theta = 0$, we can find

$$\left\langle \left(\frac{\partial P_{\mathrm{H}}}{\partial u}\right)^2 \right\rangle_\theta = \frac{1}{2}(4\eta)^2 P_{\mathrm{LO}} P_{\mathrm{in}} \frac{1}{(1+u^2)^2}, \tag{1.70}$$

which has a simple detuning dependency that follows the square of a Lorentzian lineshape, illustrated in Figure 1.8b. We substitute this result into eq. (1.67) using $u = (2/\kappa)(\Delta_0 + Gx)$, from which it follows that $\partial u/\partial x = 2G/\kappa$. We obtain

$$\begin{aligned} \langle S_{PP}\rangle_\theta &= \left\langle \left(\frac{2G}{\kappa}\frac{\partial P_{\mathrm{H}}}{\partial u}\right)^2 \right\rangle_\theta S_{xx} \\ &= \frac{32 P_{\mathrm{LO}} P_{\mathrm{in}} \left(G\eta/\kappa\right)^2}{(1+u^2)^2} S_{xx}. \end{aligned} \tag{1.71}$$

The maximum signal observed with this mode of operation is lower than the maximum possible signal without averaging, which is obtained with $\theta = 0$ at resonance with the cavity ($u_0 = 0$). By comparing eq. (1.70) to the square of eq. (1.69), we see that the signal averaged over the phase $\theta$ is up to a factor $2$ lower than the signal obtained with a fixed phase. We note that modulating the phase of the local oscillator beam is related to the concept of a heterodyne interferometer, where the local oscillator beam is at a different frequency than the signal beam. Like the phase-modulated homodyne detection we describe here, heterodyne detection provides information about both quadratures of the light at the expense of a small sensitivity decrease.

We can generalize the result of eq. (1.70) for higher-order derivatives $\partial^k/\partial u^k$, which will be useful when we extend this analysis to nonlinear transduction of

motion in chapters 4 and 5. To simplify the notation, we define

$$P_0 \equiv \frac{u\cos\theta - \sin\theta}{1+u^2}, \tag{1.72}$$

such that the derivatives of $P_{\mathrm{H}}$ can be related to those of $P_0$ as $\partial^k P_{\mathrm{H}}/\partial u^k = 4\eta\sqrt{P_{\mathrm{LO}}P_{\mathrm{in}}}(\partial^k P_0/\partial u^k)$. We additionally define $f \equiv u/(1+u^2)$ and $g \equiv 1/(1+u^2)$, such that $P_0 = f\cos\theta - g\sin\theta$. This leads to

$$\begin{aligned}\left\langle \left(\frac{\partial^k P_0}{\partial u^k}\right)\right\rangle_\theta &= \left\langle \left(\frac{\partial^k f}{\partial u^k}\cos\theta - \frac{\partial^k g}{\partial u^k}\sin\theta\right)^2\right\rangle_\theta \\ &= \frac{1}{2}\left(\frac{\partial^k f}{\partial u^k}\right)^2 + \frac{1}{2}\left(\frac{\partial^k g}{\partial u^k}\right)^2 \\ &= \frac{1}{2}\frac{\partial^k (f+ig)}{\partial u^k}\frac{\partial^k (f-ig)}{\partial u^k},\end{aligned} \tag{1.73}$$

where in the last line we used that both $f$ and $g$ are real-valued and that the derivative operator is linear. The derivatives of $f+ig$ are found to be

$$\frac{\partial^k (f+ig)}{\partial u^k} = \frac{\partial^k}{\partial u^k}\frac{u+i}{1+u^2} = \frac{\partial^k}{\partial u^k}\frac{1}{u-i} = \frac{(-1)^k k!}{(u-i)^{k+1}}, \tag{1.74}$$

while the derivatives of $f-ig$ are given by the complex conjugate of this. Substituting these derivatives into eq. (1.73), we find

$$\left\langle \left(\frac{\partial P_0}{\partial u^k}\right)\right\rangle_\theta = \frac{1}{2}\frac{(k!)^2}{(1+u^2)^{k+1}}. \tag{1.75}$$

For $k=1$, this indeed corresponds to eq. (1.70).

## 1.6. Outline of this thesis

In this thesis, we explore measurements of nanomechanical motion with light, using an optical cavity system whose resonant frequency is strongly dependent on the mechanical displacement of some freely moving part of the structure. To enhance the interaction between light and motion, we develop photonic crystal nanobeam cavities in which light is highly confined between two beams exhibiting flexural motion.

Chapter 2 introduces a waveguide-based model to compare the relative merits of horizontally and vertically coupled nanobeam cavities. We show optomechanical measurements of the thermal motion of a vertically coupled nanobeam system, which we fit with a model to obtain the parameters of the optomechanical system.

In chapter 3, we develop the design of a horizontally coupled nanobeam cavity system with a small gap along the middle, which we term the *sliced nanobeam*. Through finite-element simulation, we explore the effects of applying design strategies that minimize cavity radiation losses and identify general

design principles, trade-offs and key fabrication challenges to obtain both large optomechanical interactions and low optical losses.

We demonstrate the experimental implementation of the sliced nanobeam design in chapter 4. The optomechanical photon-phonon coupling rate is shown to be improved by an order of magnitude with respect to other state-of-the-art optomechanical systems, leading to sensitive detection of the mechanical motion even with a relatively large optical bandwidth.

When the design is altered to have lower optical losses, the devices enter a new regime where thermal fluctuations produce nonlinear effects. We analyze this in detail in chapter 5 by performing optomechanical measurements at various temperatures. We find that the optical cavity response is dominated by the mechanically induced frequency fluctuations over a wide range of temperatures. In this regime, the transduction of motion becomes highly nonlinear, which enables nonlinear measurements of the displacement.

Finally, in chapter 6 we present pulsed optomechanical measurements of our device. These measurements allow resolving the instantaneous position of the mechanical resonator in a duration much smaller than the mechanical period. As such, they evade measurement backaction and can potentially be used for measurement-based control of the resonator. We analyze the achieved measurement sensitivity, demonstrate squeezing of the thermal state of the resonator, and discuss opportunities and challenges for future work.

# 2

# Optomechanics with coupled nanobeams

*Photonic crystal nanobeams support localized optical modes with a small mode volume. They can strongly interact with low-mass flexural mechanical modes when coupling the optical fields of two nanobeams separated by nanoscale distances. We analyze the relative merits of using various waveguide geometries as the basis for the coupled nanobeam cavities, and find that the optimal choice depends on the minimum separation between the nanobeams that can be achieved. Subsequently, we show sensitive detection of thermal nanomechanical motion in a vertically coupled photonic crystal nanobeam made of GaAs. We find an optomechanical coupling rate* $g_0/2\pi = 1.7\,\mathrm{MHz}$*, which is larger than most other cavity optomechanics systems, even with a relatively large gap size of* $200\,\mathrm{nm}$*. The excellent optomechanical performance is especially promising since it can easily be combined with earlier demonstrated electro-mechanical tuning capability using essentially the same geometry, while the GaAs material platform can also provide relatively easy integration with active elements such as quantum dot emitters.*

## 2.1. Introduction

Optomechanical coupling can be especially strong in systems where the optical and mechanical modes are co-localized in a small volume [7, 55]. This can be understood by looking at the expression for the photon-phonon coupling rate, $g_0 = -x_{\mathrm{zpf}}\partial\omega_{\mathrm{c}}/\partial x$, and analyzing the optical and mechanical contributions separately: the sensitivity of the optical resonance frequency to motion is larger if a larger fraction of the light is contained in the region affected by the motion; and the mechanical zero-point fluctuations are larger for low motional masses, that is, when the motion only occurs in the region where the light is confined. In trying to optimize the optomechanical coupling rate, it is important to understand the mechanism(s) for the coupling. The most important mechanism is that the moving boundaries of the material rearrange the dielectric distribution that forms the potential for the light, thereby changing the optical resonance frequency [56]. In macroscopic systems such as Fabry-Pérot cavities or ring resonators, this is directly related to a change of the physical cavity length. Additionally, the photoelastic effect can play a role, especially for wavelength-scale systems with high-frequency mechanical modes in the gigahertz range, where the strain induced by the mechanical motion locally changes the refractive index of the material, which in turn changes the optical resonance frequency [57]. Depending on the geometry, these mechanisms can either enhance each other or (partially) cancel. In less stiff structures, the moving boundary effect typically dominates.

Based on the recognition that small feature size could lead to large optomechanical interactions, optomechanical structures were proposed that localize optical fields on the scale of the wavelength: based on photonic crystal membranes with a vertical gap [58–60], and based on nanoscale waveguides [61] or coupled cavity devices [62, 63], among other geometries (see Aspelmeyer, Kippenberg & Marquardt [7] for a more exhaustive overview). These ideas were first implemented around 2009 in waveguides [64–66], double ring resonators [67, 68] and coupled nanobeam cavities [16, 17, 42, 69, 70]. Later, the use of higher-frequency mechanical resonances confined to a smaller part of the nanobeams was demonstrated [15, 19, 20, 71]. Several demonstrations of optomechanical interactions with photonic crystal membranes, rather than nanobeams, have used in-plane motion by introducing a slot waveguide [72, 73] or even multiple small slots to create nanobeam resonators in the cavity region [74]. An alternative approach is to design an optomechanical (or “phoxonic”) crystal that supports simultaneous bandgaps for photons and phonons [18]. Photonic crystal membranes with optomechanical coupling to out-of-plane motion were demonstrated with a double-layer membrane in 2010 [75] and in a different geometry with only a single layer in 2011 [43], and recently again in a double-layer membrane which also supports tuning and readout functionalities [21]. However, most experimental effort has been focused on the in-plane geometries mentioned above, presumably because they are easier to fabricate.

Here, we compare the different design strategies in systems based on coupled nanobeams, and in particular we investigate the potential benefits of using vertically coupled nanobeam cavities in practical parameter regimes. We demon-

strate optomechanical coupling in such systems, using a fabrication technique developed for double-membrane photonic crystal cavities. This technique, which can provide electro-mechanical tuning of the cavity resonance wavelength [21, 76–79], was adapted to create tunable vertically stacked nanobeam cavities by Midolo *et al.* [80]. In the first part of this chapter (section 2.2), we explain the basic principle of optomechanical coupling through the moving boundary effect, and how this relates to the properties of the light field in nanobeam waveguides. We develop a model of a rectangular, slotted waveguide and use finite element modeling to discuss the relative merits of using particular guided modes as a starting point for device design. The second part of the chapter (section 2.3) shows optomechanical measurements of motion in an optomechanical system based on vertically coupled nanobeam cavities. We create a model for the optomechanical transduction to analyze the measurements, and find that these systems, originally optimized for tunability of the optical cavity, show optomechanical coupling rates that rival those of state-of-the-art optomechanical systems.



## 2.2. Slotted waveguides

As we will show in the next chapter, nanobeam photonic crystal cavities are created by introducing a defect in a periodically patterned waveguide. The defect creates a localized mode at a frequency where no guided modes (with the same symmetry) exist in the photonic crystal waveguide. This localized cavity mode is still closely related to the waveguide modes of the periodic structure, because the defect is typically chosen to be a relatively small and smooth change of the geometry, to reduce unwanted scattering. Studying waveguide dispersion can thus yield direct insight into nanobeam cavity performance. Coupled nanobeam cavities consist of two nanobeams separated by a gap, which can be much smaller than the free-space wavelength of the light. Optically, this resembles a single waveguide, with a slot in the middle: a slotted waveguide. For the related system of two slab waveguides separated by a small gap, the optical gradient forces were analyzed by Van Thourhout & Roels [55]. Coupled waveguides were also studied in the context of stimulated Brillouin scattering by Van Laer *et al.* [81]. To gain some basic understanding of the relative merits of various geometries we could choose for the initial waveguides to base our cavity design on, we investigate the optomechanical coupling in slotted waveguides.

### 2.2.1. Moving boundary effects

The main mechanism for optomechanical coupling in nanophotonic systems for mechanical resonances at megahertz frequencies is through the change in position of material boundaries. To calculate the effect of this on a mode frequency $\omega$, we can apply perturbation theory to Maxwell's equations [56], and write

$$\frac{\mathrm{d}\omega}{\mathrm{d}\xi} = -\frac{\omega^{(0)}}{2}\frac{\int \mathrm{d}V(\mathrm{d}\varepsilon/\mathrm{d}\xi)|\mathbf{E}^{(0)}|^2}{\int \mathrm{d}V\varepsilon|\mathbf{E}^{(0)}|^2}, \tag{2.1}$$

where $\xi$ parametrizes the change of the boundaries, $\mathrm{d}V$ indicates integration over volume, $\omega^{(0)}$ and $\mathbf{E}^{(0)}$ are the frequency and electric field profile of the unperturbed modes, and $\varepsilon$ is the dielectric index, which is a function of position: $\varepsilon = \varepsilon(\mathbf{r})$. To describe a boundary between materials, $\varepsilon$ is locally a step function, whose derivative is a Dirac delta function. This turns the volume integral in the numerator of eq. (2.1) into a surface integral, with an additional complication: since $E_\perp$ is discontinuous at the interface, the integrand is undefined. This can be solved by separating the parallel and perpendicular components and only using the continuous quantities $\mathbf{E}_\parallel$ and $D_\perp = \varepsilon E_\perp$, to get [56]

$$\begin{aligned}\int \mathrm{d}V \frac{\mathrm{d}\varepsilon}{\mathrm{d}\xi}\left|\mathbf{E}^{(0)}\right|^2 &= \int \mathrm{d}A \frac{\mathrm{d}x_\perp}{\mathrm{d}\xi}\left[(\varepsilon_1-\varepsilon_2)\left|\mathbf{E}_\parallel^{(0)}\right|^2 - (\varepsilon_1^{-1}-\varepsilon_2^{-1})\left|D_\perp^{(0)}\right|^2\right] \\ &\equiv \int \mathrm{d}A \frac{\mathrm{d}x_\perp}{\mathrm{d}\xi} W,\end{aligned} \tag{2.2}$$

where $\mathrm{d}A$ indicates surface integration, and we have defined the scalar quantity $W(\mathbf{r})$ on the surface. Here $\varepsilon_1, \varepsilon_2$ are the dielectric indices of the two materials between which the boundary is moving, and $x_\perp = x_\perp(\mathbf{r})$ is the local displacement of the boundary (perpendicular to the interface). To create a structure with large optomechanical coupling, we need to maximize this surface integral. This means we need the energy density $(\varepsilon|\mathbf{E}|^2)$ to be large at the moving interface; if some parts of the boundary are moving inwards $(x_\perp < 0)$ while other parts are moving outwards $(x_\perp > 0)$, the energy density should only be large at one of these parts, since otherwise the contributions at the two oppositely moving parts will cancel each other.

In a waveguide, we can create very high energy density at an interface by introducing a narrow low-index slot [82, 83]. For an infinitesimal slot width, we can assume that the overall distribution of $\mathbf{E}_\parallel$ and $D_\perp$ are unchanged. Therefore we can calculate the maximum contribution at the boundaries of the low-index slot to the surface integral of eq. (2.2) from the initial electric field $\mathbf{E}^{(0)}$. If we do this for the two cases when $\mathbf{E}^{(0)}$ is either completely parallel to the boundary, or completely perpendicular to it, the resulting integrands in eq. (2.2) become

$$W = \begin{cases} (\varepsilon_1-\varepsilon_2)\left|\mathbf{E}_\parallel^{(0)}\right|^2 = (\varepsilon_1-\varepsilon_2)\left|\mathbf{E}^{(0)}\right|^2 & (\mathbf{E}^{(0)} = \mathbf{E}_\parallel^{(0)}), \\ -(\varepsilon_1^{-1}-\varepsilon_2^{-1})\left|D_\perp^{(0)}\right|^2 = \dfrac{\varepsilon_1}{\varepsilon_2}(\varepsilon_1-\varepsilon_2)\left|\mathbf{E}^{(0)}\right|^2 & (\mathbf{E}^{(0)} = E_\perp^{(0)}). \end{cases} \tag{2.3}$$

In the second line, we used $D_\perp^{(0)} = \varepsilon_1 E_\perp^{(0)}$, since the initial electric fields are all in the high-index material with dielectric index $\varepsilon_1$. The extra factor $\varepsilon_1/\varepsilon_2$ in the second line shows that for an infinitesimal slot in a waveguide, the frequency change due to motion of the boundaries of the slot will be larger if the electric field of the mode is oriented perpendicular to the slot interfaces.

### 2.2.2. Numerical simulation of waveguide modes

For realistic gap sizes, the electric field will redistribute due to the introduction of a slot, so instead of relying on the result for infinitesimal slots shown

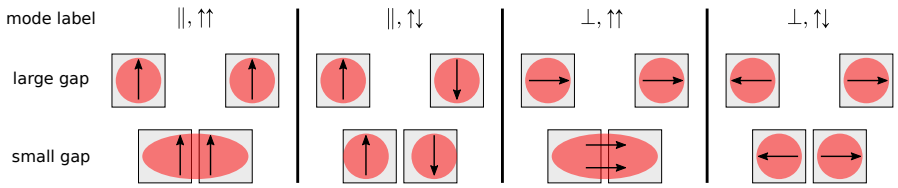


Figure 2.1: Schematic representation of the fundamental waveguide modes in a slotted rectangular waveguide, or equivalently, in two coupled rectangular waveguides. Here the two halves are drawn with a square cross section, but for the simulations we varied the height and width. The red shading represents the approximate energy density profile of the waveguide modes, while the arrows represent the dominant orientation of the electric field (at a particular point in the optical cycle).



in eq. (2.3), we perform a series of numerical simulations. For small gap sizes, we expect that the results from the numerical simulation will approach the prediction from eq. (2.3). For very large gap sizes, a better approximate description would be to consider the modes guided by the two halves of the waveguides separately, which will have mutual coupling. The coupling leads to hybridized modes where the electric fields in the two half-waveguides are either parallel or antiparallel with each other [42, 69, 80]. Figure 2.1 is a schematic representation of the fundamental waveguide modes for slotted waveguides, where we labeled the modes according to the direction of the electric field with respect to the gap ($\parallel$ or $\perp$), and whether the electric fields in the two half-waveguides are parallel or antiparallel ($\uparrow\uparrow$ or $\uparrow\downarrow$).

We perform finite element simulations in COMSOL Multiphysics to find the guided modes. We use a 2-dimensional model of the cross section of the waveguide, and specify a frequency of $200\,\mathrm{THz}$, corresponding to a free-space wavelength of $1500\,\mathrm{nm}$. We choose to simulate a waveguide made of silicon, which has a refractive index $n = 3.48$ at this frequency, surrounded by vacuum ($n = 1$). The simulation results in a set of waveguide modes at the specified frequency, which can be characterized by their effective mode index $n_{\mathrm{eff}}$ and the electromagnetic field distribution of the mode. The geometry is chosen such that several modes are guided at the chosen frequency (in other words, the effective index of the modes is larger than 1). While we choose a specific material and geometry here, we are mainly interested in the behavior with respect to the orientation of the electric field at the gap, which applies to other geometries and materials as well.

The simulated mode profiles are shown in fig. 2.2. In the pictured case, the two half-waveguides were $275 \times 550\,\mathrm{nm}$ in size, such that the overall structure forms a square waveguide of $550 \times 550\,\mathrm{nm}$ if the gap is absent. The color scale depicts the average energy density of the mode, while the arrows represent the in-plane components of the electric field, with the size of the vector proportional to $\log|\mathbf{E}|$. The most striking feature is the extreme concentration of the energy density in the gap of the mode $(\perp, \uparrow\uparrow)$, where the electric field is oriented across the gap, consistent with the expectation from eq. (2.3).

More quantitatively, we can look at the effective mode index $n_{\mathrm{eff}}$ as a function

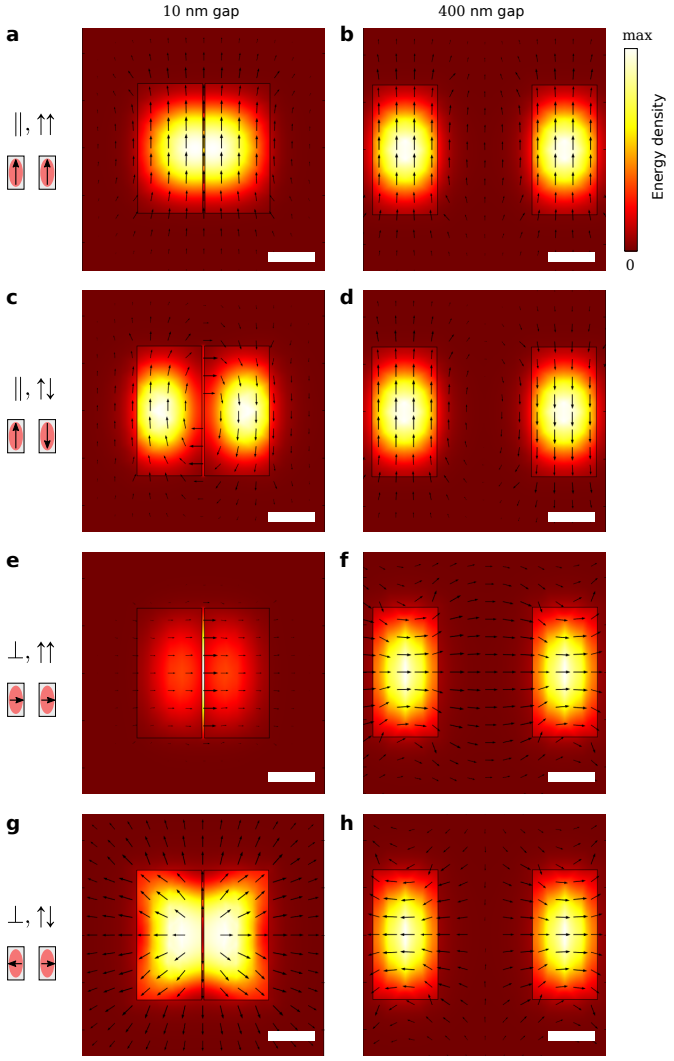


Figure 2.2: Simulated mode profiles of guided modes for a silicon waveguide at a free-space wavelength of $1500\,\mathrm{nm}$, in a waveguide with a base size (without gap) of $550 \times 550\,\mathrm{nm}$. The left and right columns correspond to gaps of $10\,\mathrm{nm}$ and $400\,\mathrm{nm}$, where every row corresponds to a particular mode, labeled on the left (see fig. 2.1). The scale bars are all $200\,\mathrm{nm}$. The color scale indicates the calculated average energy density $\langle \varepsilon |\mathbf{E}|^2 \rangle$, normalized to the maximum value in each panel. The arrows indicate the direction, and logarithm of the strength, of the electric field $\mathbf{E}$ at a particular point in the optical cycle.

of the gap width. The mode index connects the frequency and the length of the wavevector component along the direction of propagation $k$: whereas in vacuum, light propagates with the light speed $c$ and the dispersion is given by $\omega = ck$, for the guided mode at the chosen frequency, $\omega = ck/n_{\text{eff}}$. Figures 2.3a and 2.3b show the mode indices calculated in the simulations for the four modes depicted in figs. 2.1 and 2.2. The simulations shown here were carried out for rectangular half-waveguides of $275 \times 550\,\text{nm}$, placed side by side either with their short or long sides facing each other. The resulting combined waveguide, for the limit of vanishing gap size, would be either a square waveguide of $550 \times 550\,\text{nm}$ (fig. 2.3a) or a rectangular $1 : 4$ waveguide of $275 \times 1100\,\text{nm}$ (fig. 2.3b). As expected, for very large gap sizes, the parallel and antiparallel coupled modes are degenerate, resembling two uncoupled modes guided separately by the two half-waveguides. The point that most closely relates to the infinitesimal slot oriented parallel or perpendicular to the electric field, as described in eq. (2.3), is in the top left of the figure: for a square waveguide without a gap, the modes $(\parallel, \uparrow\uparrow)$ (dark blue triangles) and $(\perp, \uparrow\uparrow)$ (red diamonds) are degenerate. From the data at small gap sizes, it is evident that indeed, the dependence on the gap size is much larger for the mode where the electric field points across the gap (red diamonds). Another interesting feature is that the geometry where the high-index material is, on average, located further from the gap ($275 \times 1100\,\text{nm}$, fig. 2.3b) shows a smaller dependence on the gap size. This can be explained by the fact that the energy density is mostly concentrated in the high-index material, so less high-index material close to the gap means a lower energy density at the gap boundaries, which means the surface integral of eq. (2.2) yields a lower value.

Ultimately, we are interested in the frequency shift due to displacement $\partial\omega/\partial x$ for a photonic crystal cavity, where the periodicity of the structure selects the wavevector component $k$. Using the first-order Taylor expansion around the chosen frequency $\omega$, we find

$$\frac{\partial\omega}{\partial x} = \frac{\partial}{\partial x}\left(\frac{ck}{n_{\text{eff}}}\right) = \frac{-ck}{n_{\text{eff}}^2}\frac{\partial n_{\text{eff}}}{\partial x}, \tag{2.4}$$

where $c$ is the speed of light in vacuum. We can substitute $k$ in this equation as well, since that is determined by our choice of $\omega$ to be $k = \omega n_{\text{eff}}/c$, leading to

$$\frac{\partial\omega}{\partial x} = \frac{\omega}{n_{\text{eff}}}\frac{\partial n_{\text{eff}}}{\partial x}. \tag{2.5}$$

We determine $\partial n_{\text{eff}}/\partial x$ from the gradient of the data shown in figs. 2.3a and 2.3b, where in this case we take $x$ to be the gap size, and plot the resulting values of $\partial\omega/\partial x$ in figs. 2.3c and 2.3d. As expected, for very small gaps, the mode oriented perpendicular to the gap $(\perp, \uparrow\uparrow)$ performs best. However, for the wider slotted waveguide ($275 \times 1100\,\text{nm}$), the mode oriented parallel to the gap $(\parallel, \uparrow\uparrow)$ provides better performance already for gaps larger than $20\,\text{nm}$.

To draw a conclusion from these numerical simulations, we need to consider further steps in the device design. To create optical cavities with low losses, generally one tries to use an initial waveguide mode which has the lowest frequency

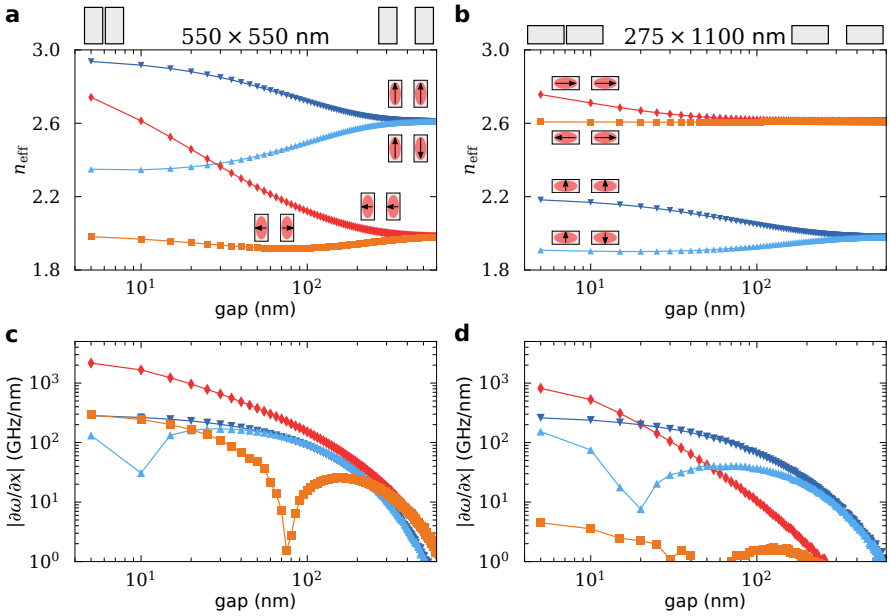


Figure 2.3: Simulated effective mode index for a simple silicon waveguide at a free-space wavelength of $1500\,\mathrm{nm}$. The waveguides of (a),(c) $550 \times 550\,\mathrm{nm}$ and (b),(d) $275 \times 1100\,\mathrm{nm}$ were split and the two halves were shifted outwards, such that the specified gap was formed between them. (a),(b) show the resulting effective mode indices, with the various modes schematically indicated (see fig. 2.1). (c),(d) show the numerically calculated derivative of the simulated effective mode indices, with the colors and symbols corresponding to (a),(b).

of all allowed modes at the wavevector values selected by the photonic crystal periodicity (which corresponds to the mode with the highest index $n_{\mathrm{eff}}$ at a chosen frequency). For the specific geometries shown in fig. 2.3, this is not the mode with the largest optomechanical response except for very small gaps in the wider waveguide (figs. 2.3b and 2.3d). Changing the geometry between the two cases in fig. 2.3, we can see that making the overall waveguide wider (moving from fig. 2.3a to fig. 2.3b) shifts the mode $(\perp, \uparrow\uparrow)$ to lower frequencies (higher $n_{\mathrm{eff}}$). At the same time, the absolute value of $\partial\omega/\partial x$ decreases, because high-index material is moving away from the gap. Another important factor is whether the desired waveguide geometry is easy to fabricate. The strategy for creating photonic crystal structures typically starts by choosing a slab of material of a thickness close to $\lambda/(2n)$ ($\sim 220\,\mathrm{nm}$ for silicon at a free-space wavelength $\lambda = 1550\,\mathrm{nm}$), such that it is easy to create waveguides which mainly support TE-like modes, where the electric field is oriented in the plane of the slab. Moreover, the typical anisotropic reactive ion etching techniques used to define the geometry work better for structures that have a low aspect ratio, in other words, structures that are wider than their height. Very broadly, we can say that structures resembling the square waveguide of figs. 2.3a and 2.3c (two waveguides of $1:2$ aspect ratio with

their long sides facing each other) are easier to fabricate with the gap horizontally, by creating a stack of layers with high and low index (or with layers used as sacrificial material), while structures resembling the wider waveguide in figs. 2.3b and 2.3d (two waveguides of $1:2$ aspect ratio with their short sides facing each other) are easier to create with the gap oriented vertically, by anisotropically etching the structure from a single layer of high-index material.

The guidelines for device design to optimize the optomechanical coupling $\partial\omega/\partial x$ we can distill from this discussion are:

- Minimize the gap size.
- Maximize the amount of high-index material close to the gap. This might lead to more difficult fabrication and a change in the relative frequencies of modes with the opposite symmetry ($\perp$ vs. $\parallel$).
- If it is necessary to compromise on gap size and/or geometry, the mode oriented parallel to the gap $(\parallel, \uparrow\uparrow)$ might offer more robust performance than the mode oriented across the gap $(\perp, \uparrow\uparrow)$, which is optimal for small gaps.



## 2.3. Vertically coupled nanobeams

Here we investigate the optomechanical interactions in a vertically coupled nanobeam cavity similar to the one used by Midolo *et al.* [80] to demonstrate electro-mechanical tuning of the resonance wavelength. For application in cavity optomechanics, such nanobeam devices offer a lower motional mass than membrane cavities, with comparable optical quality factors and mode volumes. This leads to larger $x_{\text{zpf}}$, zero-point fluctuations of mechanical modes, and therefore to larger photon-phonon coupling rates (see section 1.2.1). To minimize the necessity for re-optimization of the fabrication process, the design was not altered with respect to ref. [80] except for an overall scaling to shift the resonance wavelength to the range of the laser available for the measurements reported here. Most notably, the spacing between the two device layers was chosen to be quite large ($200\,\text{nm}$), since this eases fabrication and increases the electro-mechanical tuning range. These devices therefore represent a proof of principle of vertically coupled optomechanical nanobeam resonators, that could be further optimized for use as a cavity optomechanical system.

### 2.3.1. Design and fabrication

We briefly describe the device design and fabrication method. For details, we refer the reader to Midolo *et al.* [80], as well as the PhD thesis of Midolo [84] and the Master's thesis of Westendorp [85]. The overall geometry of the structure, as shown in fig. 2.4, consists of two suspended gallium arsenide (GaAs) nanobeams with identical photonic crystal patterning, vertically separated by a small gap. The refractive index of GaAs for optical frequencies around $200\,\text{THz}$ is $n = 3.38$, which means its optical properties are quite close to silicon ($n = 3.48$) in this frequency range. The design parameters are indicated in fig. 2.4a, consisting of

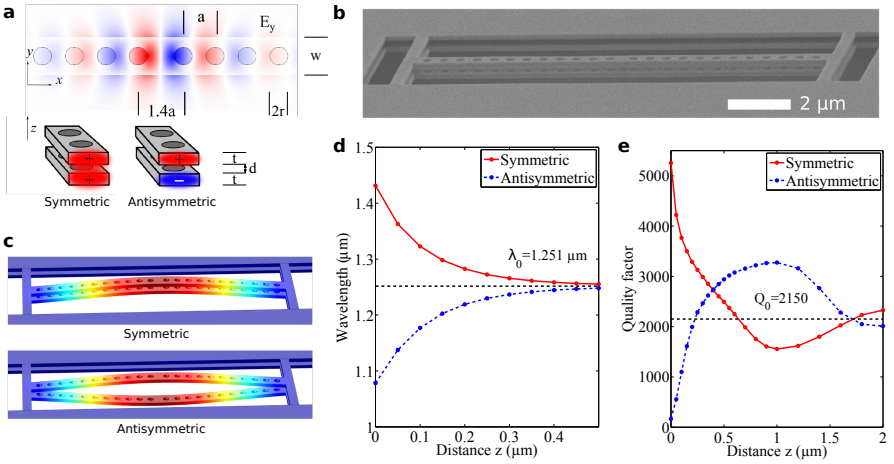


Figure 2.4: (a) Simulated horizontal field distribution of the optical cavity mode in the vertically coupled nanobeam, and schematic indication of the field in the top and bottom nanobeam for the two coupled modes. The structure parameters determining the design are indicated in the figure (see table 2.1). (b) Electron micrograph of a fabricated vertically coupled nanobeam with $a = 535\,\mathrm{nm}$, $l = l_3$ and $w = w_1$. (c) Simulated displacement profiles of the fundamental mechanical resonances of the structure. (d),(e) Simulated wavelengths and quality factors of the optical cavity modes of a vertically coupled nanobeam structure, as a function of the gap distance (here called $z$). (a) was adapted from, and (d),(e) reprinted from Midolo, "Electromechanical Tuning of Photonic Crystal Cavities" (2013)[84]. (b),(c) were reprinted from Westendorp, "Cavity optomechanics in vertically-coupled photonic crystal nanobeams and membranes" (2014)[85].

the layer thicknesses $t$ and gap size $d$, as well as the nanobeam length $l$ and width $w$, and finally the hole radius $r$ and periodicity $a$. The in-plane parameters $l$, $w$ and $r$ were defined in terms of the periodicity $a$ to facilitate scaling of the structures. The structure parameters that were used are shown in table 2.1.

The simulated fundamental mechanical resonances are shown in fig. 2.4c. Of these modes, only the antisymmetric mode is expected to couple to the optical cavity mode, since the optical resonance frequency is most sensitive to the gap distance between the nanobeams. The expected resonance frequencies for these modes are between $2.5$ and $3.5\,\mathrm{MHz}$, depending on the length and width of the structure.

In the middle of the nanobeam, the spacing between the holes is increased to $1.4a$, forming a defect in the periodic photonic crystal patterning which supports localized optical modes. The simulated field profile of the fundamental optical cavity mode is shown in fig. 2.4a. Like the rectangular slotted waveguides in the previous section, the optical modes of this structure are sensitive to the gap between the two nanobeams. Figures 2.4d and 2.4e show the simulated resonance wavelength and quality factor of the two fundamental modes for a structure with almost identical design (taken from Midolo *et al.* [80]), where *symmetric* and *antisymmetric* indicate modes with the electric field in the two cavities oriented paral-

Table 2.1: Parameters specifying the design of the vertically coupled nanobeams shown in this chapter. The meaning of the parameters is schematically indicated in fig. 2.4a. The main results of this chapter are reported for the structure A520L2W2, for which we explicitly list the design dimensions here.

| Parameter | Symbol | Definition | A520L2W2 (nm) |
|---|---|---|---|
| Thickness | $t$ | $160\,\mathrm{nm}$ | 160 |
| Gap | $d$ | $200\,\mathrm{nm}$ | 200 |
| Lattice period | $a$ | 360–535 nm (steps of $5\,\mathrm{nm}$) | 520 |
| Hole radius | $r$ | $0.28a$ | 145.6 |
| Width | $w$ | $w_1 = 1.31a$; $w_2 = 1.48a$; $w_3 = 1.55a$ | 769.6 |
| Length | $l$ | $l_1 = 20.96a$; $l_2 = 22.96a$; $l_3 = 24.96a$ | $11.94 \times 10^3$ |



lel (↑↑) or antiparallel (↑↓), respectively. From the geometry, we expect the cavity modes to resemble the waveguide modes oriented parallel to the gap, $(\parallel, \uparrow\uparrow)$ and $(\parallel, \uparrow\downarrow)$, in a structure which has two rectangular waveguides with their long sides facing each other ($550 \times 550\,\mathrm{nm}$, figs. 2.3a and 2.3c), and the wavelength dependence shown here indeed matches the results in fig. 2.3 qualitatively.

From fig. 2.4d, we determine the derivative of the tuning curve of the antisymmetric mode at a gap distance of $200\,\mathrm{nm}$ to estimate $\partial\omega_c/\partial x \approx 2\pi \times -109\,\mathrm{GHz\,nm^{-1}}$, where we now choose $x$ to be half of the gap distance, such that for the antisymmetric mode, it corresponds to the lab-frame displacement of a single nanobeam. If the structure would have a two times smaller gap distance of $100\,\mathrm{nm}$, the tuning curve yields $\partial\omega_c/\partial x \approx 2\pi \times -233\,\mathrm{GHz\,nm^{-1}}$, which is an improvement by about a factor 2. However, like the waveguide modes oriented parallel to the gap in fig. 2.3 (blue triangles), we don't see much increase of $\partial\omega/\partial x$ for gaps smaller than about $50\,\mathrm{nm}$. The effective motional mass for a slightly shorter nanobeam was simulated to be $3.2\,\mathrm{pg}$, which we can combine with $\partial\omega_c/\partial x$ and the expected mechanical resonance frequency $\Omega_m/2\pi \approx 3\,\mathrm{MHz}$ to get an order-of-magnitude estimate for the photon-phonon coupling rate (see section 1.2.1) of $g_0/2\pi \approx 3.2\,\mathrm{MHz}$, for the case with a gap size of $200\,\mathrm{nm}$.

**Fabricated devices**

The double nanobeam devices presented here were fabricated by Tian Xia at the Eindhoven University of Technology with a simplified version of the process developed for electro-mechanically tunable devices [80, 84]. A stack of layers was prepared by several steps of molecular beam epitaxy on a GaAs substrate, subsequently $1.4\,\mu\mathrm{m}$ $Al_{0.79}Ga_{0.21}As$, $160\,\mathrm{nm}$ GaAs, $200\,\mathrm{nm}$ $Al_{0.79}Ga_{0.21}As$, and $160\,\mathrm{nm}$ GaAs containing a thin layer of InAs quantum dots. Then a $400\,\mathrm{nm}$ SiN masking layer was deposited using plasma enhanced chemical vapor deposition, followed by a layer of e-beam resist. The nanobeam pattern was written using electron beam lithography (EBL) and transferred to the SiN mask layer by $CHF_3$ reactive ion etching (RIE), which was followed by a $Cl_2/N_2$ etching step to transfer the pattern to the GaAs layers. More SiN was deposited to support the nanobeams from the sides, followed by a $CHF_3/O_2$ RIE to open the holes in the nanobeam again.

The sacrificial $Al_{0.79}Ga_{0.21}As$ layers were removed using a solution of hydrochloric acid (HCl), and finally the remaining SiN was removed with a low power $CF_4$ plasma.

An electron microscope image of one of the fabricated double nanobeams is shown in fig. 2.4b. Photoluminescence spectroscopy was performed by Sybren Westendorp at the Eindhoven University of Technology [85] to characterize the devices with wavelength resonances near $1300\,\mathrm{nm}$ (in the emission band of the InAs quantum dots included in the top nanobeam). The devices showed strong luminescence enhancement for the antisymmetric mode $(\parallel, \uparrow\downarrow)$, with an average optical quality factor of $600$. The symmetric mode $(\parallel, \uparrow\uparrow)$ was either much weaker, or not visible at all in the measurements, which was ascribed to an asymmetry of the nanobeam thicknesses: the top beam is slightly thinner than the bottom beam due to the plasma etching steps in the fabrication process. This in turn could lead to the optical modes being distributed asymmetrically over the top and bottom nanobeam, as well as different outcoupling towards the collecting objective above the structure.

## 2.3.2. Direct reflection measurement

We measure the reflection from the nanobeams in the setup schematically depicted in fig. 2.5. The sample is placed inside a vacuum chamber with a pressure lower than $1 \times 10^{-3}\,\mathrm{mbar}$, to prevent air damping of the mechanical motion. Light from a tunable laser (New Focus Velocity 6728, wavelength tuning range between $1520\,\mathrm{nm}$ and $1570\,\mathrm{nm}$) is focused on the sample with an aspheric lens with a numerical aperture of $0.6$ (nominal focal length $2.97\,\mathrm{mm}$). We use a polarizing beamsplitter (PBS) to filter the directly reflected light, such that only light that interacts with the sample such that its polarization is changed will reach the detector (InGaAs photodiode, Femto HCA-S). For this purpose, the nanobeam cavities are oriented at $45°$ with respect to the incoming polarization. Because the optical cavity mode is dominantly polarized perpendicular to the nanobeam, as shown in fig. 2.4a, half of the light escaping from the cavity can be transmitted by the PBS, while in principle most of the directly reflected light will be filtered out. On a flat substrate, the direct reflection is indeed suppressed significantly below $1\,\%$, however if the laser beam is focused on these nanobeams, even if light is not resonant with the cavity, about $4\,\%$ of the input light reaches the detector despite the polarization filtering. Evidently, there is some broadband scattering process which rotates the polarization of the light.

To model the reflection from the cavity, we use the description introduced in sections 1.3.1 and 1.5.4. We recall that the dependence of the cavity reflectivity $R$ on the laser detuning $\Delta \equiv \omega_\mathrm{L} - \omega_\mathrm{c}$ can be written from eq. (1.15) as

$$R(\Delta) = \left| c e^{i\varphi} + \frac{\sqrt{\eta_\mathrm{in}\eta_\mathrm{out}}\kappa}{i\Delta - \kappa/2} \right|^2 , \tag{2.6}$$

where $\kappa$ is the cavity decay rate and $\eta_\mathrm{in}$ and $\eta_\mathrm{out}$ represent the fraction of light that couples into the cavity from the free-space input beam, and the fraction of the light escaping the cavity that passes the PBS, respectively. The first term describes

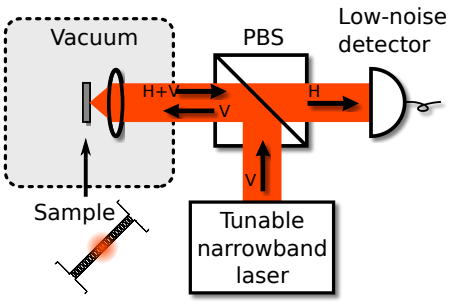


Figure 2.5: Schematic representation of the measurement setup. Light from a tunable laser is focused on a sample placed in a vacuum chamber. The reflection is measured using a low-noise photodetector. Due to interaction with the nanobeams placed at an angle of $45°$, some of the light rotates in polarization, which allows it to pass the polarizing beamsplitter (PBS), while directly reflected light will be filtered away. H,V: horizontally and vertically polarized light, respectively.



the nonresonant scattering process, with amplitude $c$ and phase $\varphi$. Thermal motion of a mechanical mode with mean occupancy $\bar{n}_{\text{th}}$ is transduced to optical power fluctuations $P$ at the detector with variance

$$\begin{aligned}\langle P^2 \rangle &= \left( h P_{\text{in}} \frac{\partial R}{\partial \omega_{\text{c}}} \frac{\partial \omega_{\text{c}}}{\partial x} \right)^2 2 x_{\text{zpf}}^2 \bar{n}_{\text{th}} \\ &= 2h^2 P_{\text{in}}^2 \bar{n}_{\text{th}} g_0^2 \left( \frac{\partial R}{\partial \omega_{\text{c}}} \right)^2 \end{aligned} \tag{2.7}$$

according to eq. (1.65), with the replacement $P \equiv P_{\text{det}} = h P_{\text{out}}$, where $h$ takes into account transmission losses between the PBS and the detector, and amounts to $95\,\%$ in our experiment.

We record the reflected optical power using an InGaAs photodiode detector, which has a high-gain AC-coupled output as well as a lower-gain DC-monitor output. We use a real-time spectrum analyzer to record the spectrum of the AC-coupled output around the mechanical resonance frequencies, and simultaneously record the voltage of the DC-monitor with an oscilloscope. We use a tunable external cavity diode laser with a tuning range between $1520\,\text{nm}$ and $1570\,\text{nm}$ to address the nanobeams. For these experiments, the laser wavelength is swept continuously using the built-in functionality of the laser controller, and the laser sweep, oscilloscope, and spectrum analyzer measurements are started at the same time using software triggering. This method could result in a small misalignment of the wavelength axis between the spectrum analyzer and oscilloscope measurements, due to uncertainties in timing.

### 2.3.3. Measurement results

Figure 2.6 shows the measured reflection spectrum $R(\omega_{\text{L}})$ as well as the simultaneously recorded spectrogram $S_{PP}(\omega_{\text{L}})$, for the structure A520L2W2D1 with design dimensions indicated in table 2.1 ('D1' in the structure name indicates a specific

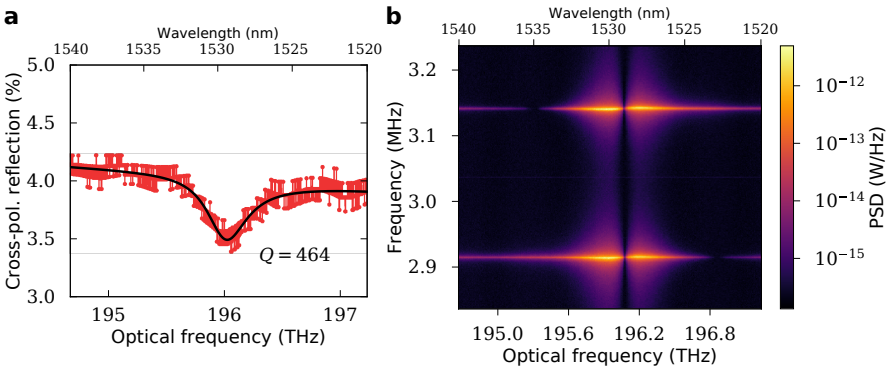


Figure 2.6: (a) Cross-polarized reflection spectrum of structure A520L2W2D1, with the sample placed at an angle of $45°$, recorded by sweeping the wavelength of the laser. The solid black line shows a fit of the red data points, with fitted optical quality factor $Q = 464$. (b) Spectrogram of mechanical fluctuation spectra, recorded simultaneously with the reflection spectrum shown in (a). Each vertical line is a spectrum measured by an electronic spectrum analyzer, with the color scale representing the electronic power spectral density (PSD) in the output of the photodetector.

dosage during the EBL fabrication step). The reflection spectrum shows a clear dip, slightly asymmetric in shape, which can be fit using a Fano lineshape. Using eq. (2.6) directly yields fit values for $\omega_c, \kappa, \eta \equiv \sqrt{\eta_{in}\eta_{out}}, c$ and $\varphi$. In this case, the optical resonance has a center frequency of $196\,\mathrm{THz}$, a width of $422\,\mathrm{GHz}$ (corresponding to a quality factor of $464$), and an overall coupling efficiency $\eta = 0.7\,\%$. Two peaks are visible in the spectrogram, corresponding to two mechanical resonances. The two resonances have quality factors of $1300$ and $1600$ and have nearly equal strength. This can be attributed to a slight asymmetry in the thicknesses of the two nanobeams, such that the two mechanical resonances are not the symmetric and antisymmetric mode shapes shown in fig. 2.4c, but rather the top and bottom nanobeam moving (nearly) independently of each other (see the discussion in section 3.2.3).

**Transduction of thermal motion**

We fit each individual spectrum in the spectrogram with two Lorentzian lineshapes. The resulting fit parameters can be analyzed as a function of detuning to study the optomechanical interaction. Figure 2.7 shows the fitted area, expressed as the band power associated with the peak, as a function of the laser frequency. Next, we fit this band power using eq. (2.7), where $\partial R/\partial\omega_c$ is determined by the fit parameters from the reflection spectrum, and only the optical resonance frequency and the overall scaling factor are used as free fitting parameters. From a separate calibration measurement, we determined the relation between the measured band power on the spectrum analyzer and the fluctuations of the optical power $P$ reaching the detector, such that we can indeed substitute known values for all parameters in eq. (2.7) except for $\omega_c$ and $g_0$. Combining this with the fit

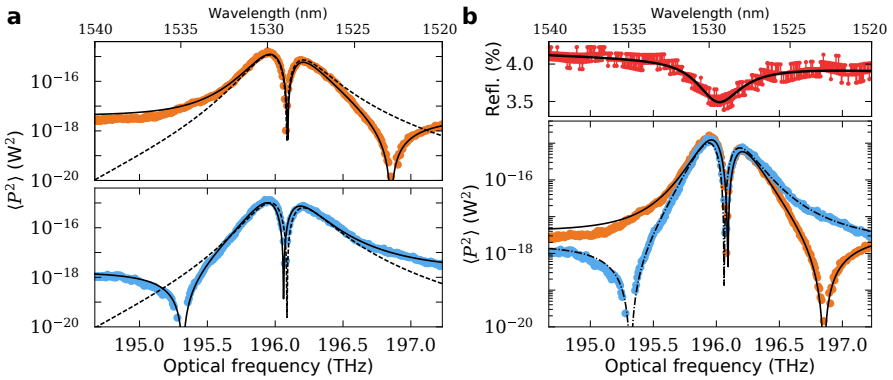


Figure 2.7: Measured transduced thermal motion in the structure A520L2W2D1. The top and bottom panels in (a) show the band power of the two peaks in the spectrogram shown in fig. 2.6 as a function of the laser frequency, calculated from their fitted areas. The dashed lines show fit functions that have the form of eq. (2.7), with only the overall scaling factor (corresponding to $g_0$) and the resonance frequency ($\omega_c$) as free fit parameters, with the other parameters known from the fit of the reflection spectrum and separate calibration measurements. The solid lines show fit functions where an extra term is included in the fit function, shown in eq. (2.9), such that there are 3 free parameters, corresponding to $\omega_c$, $g_0$ and $g_c$. This extra term accounts for a nonresonant scattering process that also transduces the mechanical motion. The bottom panel in (b) shows the same data with the fit functions that include the extra term (solid lines in (a)), with the reflection spectrum repeated in the top panel (fig. 2.6). There is a small horizontal offset between the features in the reflection spectrum and the corresponding features in the transduction of thermal motion, which is due to timing uncertainties in the experiment.

parameters of the fits shown with dashed lines in fig. 2.7a, we find the optomechanical coupling of the two mechanical resonances at $\Omega_m/2\pi = 2.90\,\mathrm{MHz}$ and $3.14\,\mathrm{MHz}$ to be $g_0/2\pi = 1.73\,\mathrm{MHz}$ and $1.69\,\mathrm{MHz}$, respectively.

**Nonresonant transduction**

While the fit close to the optical resonance is quite good, away from the resonance the two mechanical peaks show a frequency dependence that cannot be explained by eq. (2.7), with just the frequency dependence $\partial R/\partial\omega_c$. Most tellingly, the two mechanical peaks vanish at opposite sides of the optical resonance, while being stronger than predicted by the fit function on the other side. We also observe a broadband transduction of the mechanical motion over the entire tuning range of our laser ($1520\,\mathrm{nm}$ to $1570\,\mathrm{nm}$). To explain this, we hypothesize that the broadband, nonresonant scattering from the nanobeam structure, denoted by the term $ce^{i\varphi}$ in eq. (2.6), is influenced by the motion of the two beams. Far away from the cavity resonance, the phase $\varphi$ has no effect on the reflection $R(\Delta \gg \kappa) = |c|^2$, so in our model we assume $\partial c/\partial x \neq 0$. A possible origin of position dependence for broadband scattering is a gradient of optical intensity in the direction of motion, for instance the partial standing wave that is set up by the reflection from the substrate interface below the nanobeams. Previously, Ramos *et al.* [86] showed the interaction of such a partial standing wave with the resonant response of the cav-

ity to be the main mechanism of transduction for vertical motion in a side-coupled double nanobeam system.

Including the position dependence of $c$ leads to an extra term when we write down the derivative

$$\frac{\partial R}{\partial x} = \frac{\partial R}{\partial \omega_\mathrm{c}} \frac{\partial \omega_\mathrm{c}}{\partial x} + \frac{\partial R}{\partial c} \frac{\partial c}{\partial x}, \tag{2.8}$$

such that the total transduced signal due to the mechanical motion (see eq. (2.7)) becomes

$$\begin{aligned} \langle P^2 \rangle &= \left( h P_\mathrm{in} \left[ \frac{\partial R}{\partial \omega_\mathrm{c}} \frac{\partial \omega_\mathrm{c}}{\partial x} + \frac{\partial R}{\partial c} \frac{\partial c}{\partial x} \right] \right)^2 2 x_\mathrm{zpf}^2 \bar{n}_\mathrm{th} \\ &= 2h^2 P_\mathrm{in}^2 \bar{n}_\mathrm{th} \left( \frac{\partial R}{\partial \omega_\mathrm{c}} g_0 + \frac{\partial R}{\partial c} g_\mathrm{c} \right)^2, \end{aligned} \tag{2.9}$$

where we defined $g_c \equiv -x_\mathrm{zpf} \partial c / \partial x$ in analogy to $g_0$. From the equation we can readily see that it is possible for the transduction of motion to vanish, if the two terms in the parentheses are equally strong, but have opposite sign. The observation that this happens at opposite sides of the resonance for the two mechanical resonances is somewhat harder to explain: it requires that either $g_0$ or $g_c$ has a different sign for the two resonances. We define $x$ as half of the gap distance between the top and bottom nanobeams, such that $\partial \omega_\mathrm{c} / \partial x$ (and therefore also $g_0$) is the same, independently of which nanobeam is moving. However, this means that with respect to the incoming light (or the substrate), an increase of $x$ corresponds to different directions of movement for the top and bottom nanobeams. So if $c$ depends on the movement of the nanobeam with respect to the substrate, then $\partial c / \partial x$, and thus also $g_\mathrm{c}$, can have opposite sign for the two mechanical resonances.

The fits of the transduced thermal motion with eq. (2.9), including the extra term for the nonresonant transduction, are shown with solid lines in fig. 2.7a and again in fig. 2.7b. Like before, all the parameters in the derivatives of $R$ except $\omega_\mathrm{c}$ were kept fixed at the fitted values from the reflection spectrum (fig. 2.6). The only other fit parameters are $g_0$ and $g_c$, if we account for the overall scaling using the same calibration as before. The addition of this extra fit parameter allows the fit function to more closely match the measured values. We find slightly different values for the optomechanical coupling now, $g_0 / 2\pi = 1.68\,\mathrm{MHz}$ for both mechanical resonances. At the same time, we find $g_\mathrm{c} = -2.07 \times 10^{-9}$ and $g_\mathrm{c} = 2.61 \times 10^{-9}$, for the resonances at $2.90\,\mathrm{MHz}$ and $3.14\,\mathrm{MHz}$ respectively. As expected, there is an opposite sign for $g_\mathrm{c}$ between the two resonances. An order-of-magnitude estimate of the value of $\partial c / \partial x$, assuming the origin is a (partial) standing wave pattern, can be obtained by using the fitted value of $c = 0.20$ and the fringe spacing of a standing wave in free space, which is $\lambda/2 \approx 1530\,\mathrm{nm}/2$. This yields $\partial c / \partial x \approx c_\mathrm{fit} / \lambda = \pm 1.3 \times 10^5\,\mathrm{m}^{-1}$. Using the estimated $x_\mathrm{zpf} \approx 28\,\mathrm{fm}$, we arrive at an estimate of $g_\mathrm{c} \approx \pm 3.6 \times 10^{-9}$, which is the same order of magnitude as the fitted values. The values of $g_\mathrm{c}$ and $g_0$ can not be directly compared, since they are multiplied with the derivatives of $R$. However, the similar values we find for $g_0$, whether we include the extra fit parameter $g_\mathrm{c}$ or not, confirms that

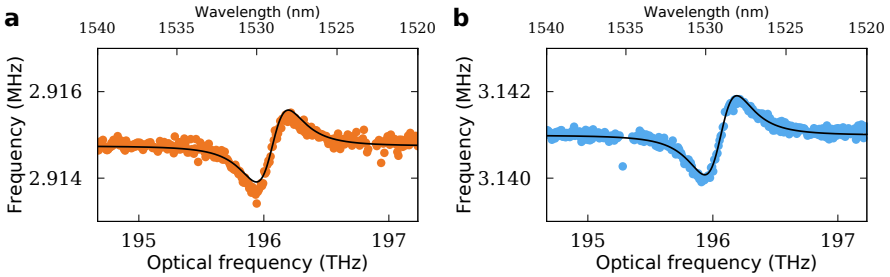


Figure 2.8: Measured optical spring effect in the structure A520L2W2D1. The two panels show the fitted center frequency of the two peaks in the spectrogram shown in fig. 2.6. The solid lines are fits with eq. (1.35).

the transduction near the optical resonance is well-explained by our model even without including the nonresonant transduction. From the figure we can also see the resonant transduction is at least three orders of magnitude stronger than the nonresonant readout, which dominates at large detunings.

**Optical spring effect**

While hardly visible on the scale of the spectrogram in fig. 2.6, the fitted center frequencies of the mechanical resonances are dependent on detuning, as shown in fig. 2.8. This is due to the radiation pressure force of the light in the cavity, interacting with the motion of the nanobeams [7] (see section 1.4.2). The figure also shows fits with the expression for the optical spring effect in the limit of a large cavity linewidth ($\kappa \gg \Omega_\mathrm{m}$), given by eq. (1.35). From the fits to the optical spring effect, we find independent values for the optical quality factor, in this case $442$ and $390$, which are slightly lower than the value from the fits to the optical reflection spectrum (fig. 2.6), which was $464$. Combining the fits with the previously obtained value for $g_0$ allows estimating $\eta_\mathrm{in} \approx 1.7\,\%$. This value is more than twice as large as the value for $\eta$ found from the fit of the reflection spectrum (fig. 2.6a), which would suggest that the detection path of our setup is suboptimal in some way. We would usually expect to find $\eta_\mathrm{out} \geq \eta_\mathrm{in}$ because the input beam has a Gaussian profile while in principle the detection is only limited by the field of view projected on the detector surface.

## 2.3.4. Discussion

In this chapter we presented the results from a representative single structure. In total we obtained results for $9$ structures with different period $a$, length $l$, and width $w$. We found mechanical quality factors between $1000$ and $2000$, optical quality factors between $430$ and $600$, and optomechanical coupling rates $g_0/2\pi$ between $1.0\,\mathrm{MHz}$ and $1.7\,\mathrm{MHz}$ from fits which did not include the extra $g_c$ term. Including the extra term for the nonresonant transduction yielded coupling rates in the range $1.0\,\mathrm{MHz}$ to $1.9\,\mathrm{MHz}$. This shows these vertically-coupled nanobeams provide a reliable platform for optomechanical experiments with a relatively large

optical bandwidth, with coupling rates that are on par with, or better than, the previously shown side-coupled nanobeam cavities ("zipper" cavities) [16, 17, 42, 69]. While the gap realized in that case was smaller, a larger amount of the high-index material was located away from the gap. As we showed for waveguide modes in fig. 2.3, the side-by-side geometry therefore leads to degraded performance especially for the mode oriented across the gap, which was used by the "zipper" cavities. We note that it should be possible to create devices with a much smaller gap than the $200\,\mathrm{nm}$ we show here. Since the control of layer thickness in molecular beam epitaxy is very good, the main limitation for how small the gap can be is the possibility of the two nanobeams sticking together [84]. With the SiN-supported wet etch technique used to create these devices, and careful engineering of the nanobeam support structure to release residual stress in the device layers, this problem can be avoided even for very small gaps. From fig. 2.3, as well as from fig. 2.4d, we determine we can expect at least a factor $2$ improvement in $\partial\omega_c/\partial x$ when going from $200\,\mathrm{nm}$ down to $100\,\mathrm{nm}$ gaps, but since we're using the mode oriented parallel to the gap ($\parallel, \updownarrow$), we don't expect much improvement for gap widths below $50\,\mathrm{nm}$.

In conclusion, we have shown that vertically-coupled photonic crystal nanobeam cavities are a promising platform for optomechanical experiments. This geometry has a large amount of high-index material near the gap, which increases the sensitivity of the waveguide modes to the gap size. Even with a relatively large gap of $200\,\mathrm{nm}$, the optomechanical coupling rate is larger than in many other cavity optomechanics systems, with $g_0/2\pi = 1.7\,\mathrm{MHz}$. In these proof-of-principle experiments, we find that the large optomechanical coupling allows us to measure the thermal motion of the nanobeam resonators even with relatively large optical bandwidths near $400\,\mathrm{GHz}$. The vertically-coupled nanobeams could be further optimized for sensitive optomechanical readout by decreasing the gap size for large optomechanical coupling, and by optimizing the photonic crystal cavity patterning for lower optical losses [87]. Additionally, the optical resonator can easily be made tunable with the previously demonstrated electro-mechanical tuning functionality [80, 84]. The recently reported realization of optomechanical coupling in a double-membrane structure, which also provides tuning functionality and integrated photodetection using quantum dot emitters in the cavity membrane by Zobenica *et al.* [21] shows the exciting possibilities of integrating these functionalities.

# 3

# Design and fabrication of sliced photonic crystal nanobeam cavities

*Systems in which optical and mechanical resonances are localized in a small volume can lead to large optomechanical interactions between light and motion in such a structure. Photonic crystal nanobeam cavities with small gaps can be designed such that the cavity field is confined strongly in the nanoscale gap. At the same time, such cavities can be engineered to have low optical losses. In this chapter, we introduce sliced photonic crystal nanobeam cavities, in which the optical cavity resonance couples to in-plane mechanical motion. We explore how the optomechanical coupling rate as well as the properties of the mechanical and optical resonances depend on the design parameters, resulting in guidelines for device design and several optimized designs with simulated optomechanical coupling rates that are more than an order of magnitude larger than previously demonstrated. We briefly describe the fabrication process used to realize these designs, as well as key challenges to creating the desired structures.*

## 3.1. Introduction

In section 1.2.4, we introduced the notion that optomechanical coupling is optimized when the optical and mechanical modes are co-localized in a small volume. This is due to the fact that small resonator mass results in large zero-point fluctuations $x_{\text{zpf}} = \sqrt{\hbar/2m_{\text{eff}}\Omega_{\text{m}}}$ and small cavity dimensions can lead to large optical frequency shift per unit displacement $G = -\partial\omega_{\text{c}}/\partial x$. In combination, these effects result in large values of the photon-phonon coupling rate $g_0 = Gx_{\text{zpf}}$. Here we wish to design a structure in which $g_0$ is as large as possible, while also keeping in mind the properties of the optical and mechanical resonances.

As established in the previous chapter, the optomechanical coupling rate depends on the electric fields at the moving boundaries of the structure, according to eqs. (2.1) and (2.2) [56]. In a slot waveguide geometry, the electric fields of the guided modes can be very high at the boundaries of the subwavelength gap, which results in large optical sensitivity to movement of those boundaries. The largest frequency shifts are predicted for the electric field oriented perpendicular to the dielectric material boundaries, across the gap, when the electric field is enhanced by the discontinuity at the interface (see eq. (2.3) and fig. 2.3) [82, 83]. The system we develop is therefore based on a silicon photonic crystal nanobeam, 'sliced' through the middle such that it mechanically resembles a pair of doubly clamped beams, coupled through the clamping points at the ends of the nanobeam. The optical cavity mode in this structure is derived from the guided mode of a slot waveguide, with a highly confined field oriented across the gap. While this geometry is similar to the "zipper" double nanobeam cavities [16, 17, 42, 69], an important difference is that the individual halves of the sliced nanobeam do not necessarily support low-loss optical cavity modes by themselves. Therefore we can follow the guideline, established in section 2.2.2, to maximize the amount of high-index material close to the gap by making the sliced nanobeam structures narrower than a "zipper" cavity, which leads to larger optical fields in the gap and incidentally also lowers the mass of the structure.

The mechanical mode that most strongly couples to the localized cavity mode is the fundamental flexural mode of the nanobeam. The changes to the local optical properties of the structure due to flexural motion are strongly localized at the silicon surface perpendicular to the motion, but extend over several micrometers along the beam. Therefore, it is most important to consider the transverse confinement of the light field in the cavity mode, while the optical mode profile along the beam has a much smaller effect on the optomechanical coupling. We create the optical cavity using photonic crystal design principles [87, 88], combining the established techniques to decrease optical losses with an optimization of the optomechanical coupling rate.

In this chapter, we describe the sliced nanobeam design and its mechanical and optical resonances. We use numerical finite-element simulations to optimize and characterize its theoretical performance, while later chapters show the implementation of the resulting structures. The last section of this chapter outlines the fabrication procedure and identifies the key challenges to overcome in order to create devices with the highest possible performance.

## 3.2. Mechanical resonances of sliced nanobeams

To evaluate whether the considered flexural modes are suitable for optomechanical experiments, in particular measurements of motion at the quantum level, we need to consider the parameters that determine the performance: the mechanical resonance frequency, the mechanical losses (or inversely, the resonator's quality factor), and the optomechanical coupling rate.

The *mechanical resonance frequency* $\Omega_\mathrm{m}$ of the fundamental flexural mode in silicon nanobeams with the dimensions we use (length $\sim 10\,\mu\mathrm{m}$, lateral dimensions $\sim 0.1$–$1\,\mu\mathrm{m}$) is typically a few $\mathrm{MHz}$. If the frequency drops, the initial thermal occupancy of the mechanical mode as well as the thermal decoherence increases, which decreases the feasibility of experiments in the quantum domain. This is quantified by the average phonon occupancy $\bar{n}_\mathrm{th}$, which for thermal occupancies well above $1$ is described by $\bar{n}_\mathrm{th} = k_\mathrm{B}T/\hbar\Omega_\mathrm{m}$. For a mode with a frequency of $\Omega_\mathrm{m}/2\pi = 5\,\mathrm{MHz}$, the occupancy at room temperature ($T \sim 300\,\mathrm{K}$) is $\bar{n}_\mathrm{th} = 1.25 \times 10^6$. Decreasing the influence of thermal fluctuations to below the single-quantum level would require cooling of the mode to $0.3\,\mathrm{mK}$, which could in principle be possible with a combination of cryogenic cooling of the environment and optical cooling of the mechanical mode, if the optomechanical coupling is strong enough. Quantitatively, the requirement to reach a thermal occupancy below $1$ through feedback cooling is to have a quantum cooperativity $C_\mathrm{q} = 4g_0^2 n_\mathrm{c}/(\kappa\Gamma_\mathrm{m}\bar{n}_\mathrm{th}) > 1/(9\zeta - 1)$ and $\zeta > 1/9$, where $n_\mathrm{c}$ is the number of photons in the cavity, $\Gamma_\mathrm{m}\bar{n}_\mathrm{th}$ is the thermal decoherence rate, and $\zeta$ is the total measurement efficiency [27, 41, 89].

The thermal decoherence rate $\Gamma_\mathrm{th} = \Gamma_\mathrm{m}\bar{n}_\mathrm{th}$ also scales with the *loss rate of the mechanical mode* $\Gamma_\mathrm{m}$. The loss rate additionally influences the sensitivity of continuous measurements: the lower the linewidth of the resonance, the higher the achievable signal-to-noise ratio of a measurement of the motion of the resonator at its resonance frequency. Often, the quality factor $Q_\mathrm{m} = \Omega_\mathrm{m}/\Gamma_\mathrm{m}$ is used instead, which quantifies the inverse of the fraction of the energy stored in the resonator that leaks out during one cycle. Another often-used figure of merit is the $Qf$-product of the resonator. Typically, silicon nanobeam resonators achieve quality factors of $10^3$–$10^4$ in vacuum at room temperature, with values up to $\sim 10^5$ at low temperatures ($T < 50\,\mathrm{K}$) [17, 90]. If the nanobeams are not operated in vacuum, displacement of the gas or liquid molecules provides extra damping mechanisms which decrease the quality factor by several orders of magnitude.

The *optomechanical coupling rate* $g_0 = -x_\mathrm{zpf}\partial\omega_\mathrm{c}/\partial x$ depends on the effective motional mass $m_\mathrm{eff}$ of the mechanical mode through the zero-point fluctuations $x_\mathrm{zpf}$. It is important to realize that the choice of the displacement coordinate $x$ is essentially arbitrary, and the effective mass of the mechanical modes can be defined to be consistent with any definition of $x$, as

$$m_\mathrm{eff} = \frac{1}{x^2}\int \mathbf{U}^2(\mathbf{r})\mathrm{d}m, \tag{3.1}$$

with $\mathbf{U}(\mathbf{r})$ the displacement of the mass element $\mathrm{d}m$ in the mechanical mode. For the eigenmodes of the sliced nanobeam, we choose $x \equiv (d - d_0)/2$, where $d$ is

the gap distance between the two halves of the nanobeam at the cavity position, and $d_0$ is the equilibrium distance. Intuitively, since this choice of $x$ closely corresponds to the gap distance in the slot waveguides of chapter 2, the term $\partial\omega_c/\partial x$ should be only weakly dependent on the mechanical mode shapes, as long as the displacement profile of the mode is relatively uniform along the optical cavity region of the nanobeam. Indeed, the value of $\partial\omega_c/\partial x$ can be obtained by calculating the integral of the optical energy density at the material boundaries, multiplied with the local displacement of the mechanical mode. On the other hand, choosing $x$ in this way leads to large differences in the effective mass between mechanical modes, depending on their mode shape: if a mechanical mode causes displacements which hardly change the gap distance between the half-beams, $x_{\text{zpf}}$ will be very small, corresponding to a dramatically increased $m_{\text{eff}}$ with respect to the physical mass of the structure. For modes that do change the gap distance, $x_{\text{zpf}}$ is largest if the displacement of the mode is maximum where $x$ is defined (in our case at the cavity position), and very little mass is moving elsewhere, leading to a small $m_{\text{eff}}$. We discuss this connection between mode shape and $x_{\text{zpf}}$ more quantitatively in section 3.2.3.



The resonance frequency $\Omega_{\text{m}}$ and zero-point fluctuations $x_{\text{zpf}}$ both depend on the effective spring constant $k_{\text{eff}}$ and the effective mass $m_{\text{eff}}$ of the mechanical mode, with $\Omega_{\text{m}} = \sqrt{k_{\text{eff}}/m_{\text{eff}}}$ and $x_{\text{zpf}} = [\hbar/(2m_{\text{eff}}\Omega_{\text{m}})]^{1/2} = [\hbar^2/(4k_{\text{eff}}m_{\text{eff}})]^{1/4}$. Therefore, the role of the resonance frequency in optomechanics is ambiguous, and it depends on the application which value of the frequency is desirable. For example, if one is interested in improving measurement sensitivity, an important figure of merit would be the inverse of $P_{\text{SQL}}$, the optical power necessary to reach the standard quantum limit (see section 1.5.3). By combining eqs. (1.57) and (1.58), we can find that in terms of the mechanical parameters, $P_{\text{SQL}}^{-1} \propto (m_{\text{eff}}\Gamma_{\text{m}}\Omega_{\text{m}})^{-1}$, which suggests that lower frequencies can be beneficial. On the other hand, to achieve control of the motion in the quantum regime, one needs to overcome the thermal decoherence. As mentioned above, an important figure of merit to optimize in this case is the quantum cooperativity, which in terms of mechanical parameters scales as $C_{\text{q}} \propto (m_{\text{eff}}\Gamma_{\text{m}})^{-1}$. For both of these figures of merit, we find decreasing the effective mass $m_{\text{eff}}$ is beneficial. Decreasing $\Omega_{\text{m}}$ through decreasing the effective spring constant $k_{\text{eff}}$ can also decrease the power to reach the standard quantum limit. We note that the achievable loss rate $\Gamma_{\text{m}}$ can be a function of frequency, which might increase the importance of manipulating $k_{\text{eff}}$ to achieve a desired frequency $\Omega_{\text{m}}$.

### 3.2.1. Mode shapes of uniform beams

The flexural modes of a sliced nanobeam can be approximated by the modes of a prismatic beam, that is, a beam that has a uniform cross section along its length. Since both ends of the sliced nanobeam are connected to the substrate, the boundary conditions are those of a doubly-clamped beam. The displacement profiles $\mathbf{U}_n(\mathbf{r})$ of the first four flexural modes of a doubly-clamped, prismatic beam are shown in fig. 3.1a. Such a displacement profile, combined with an amplitude $A_n$ and periodic motion at the resonance frequency $\Omega_n$ completely describes har-

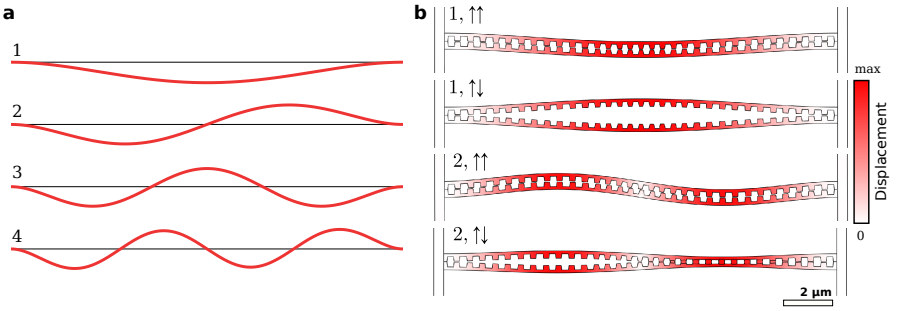


Figure 3.1: (a) Analytical solutions for the first four mode shapes of a uniform, doubly-clamped beam. The red solid lines show the displacement profile $\mathbf{U}(\mathbf{r})$, displaced from the equilibrium position indicated with the black solid lines. (b) Simulated mode profiles for a sliced nanobeam structure. The motion of the two identical half-beams couples to form common and differential normal modes where the two half-beams move either in phase (↑↑) or in antiphase (↑↓), respectively. The displacement profile $\mathbf{U}(\mathbf{r})$ with respect to the equilibrium position is shown both with the color scale and with an (exaggerated) deformation of the structure.



monic motion of the resonator due to the eigenmode with mode index $n$ as

$$\mathbf{V}_n(\mathbf{r},t) = A_n \mathbf{U}_n(\mathbf{r}) \cos(\Omega_n t + \phi), \tag{3.2}$$

where $\phi$ accounts for the phase of the motion at $t = 0$. The displacement profiles $\mathbf{U}_n(\mathbf{r})$ shown in fig. 3.1a follow the analytical expression [91]

$$\mathbf{U}_n(z) = \cos(\beta_n z/L) - \cosh(\beta_n z/L) - \alpha_n(\sin(\beta_n z/L) - \sinh(\beta_n z/L)), \tag{3.3}$$

where $n$ is the mode index, $z$ is the position along the beam, $L$ is the length of the beam, and the allowed values of the parameters $\beta_n$ and $\alpha_n$ are determined from the boundary conditions for doubly-clamped beams by

$$\cos\beta_n \cosh\beta_n - 1 = 0, \tag{3.4}$$

$$\alpha_n = \frac{\sin\beta_n - \sinh\beta_n}{\cos\beta_n - \cosh\beta_n}. \tag{3.5}$$

For the fundamental mode $n = 1$, we find $\beta_1 \approx 4.73$ and $\alpha_1 \approx 0.983$.

Knowledge of the displacement profile also allows evaluation of the effective mass (eq. (3.1)) in terms of the total mass $m_{\text{tot}} = \int \mathrm{d}m$. For beams that are uniform along their length, we find

$$\frac{m_{\text{eff}}}{m_{\text{tot}}} = \frac{\int \mathbf{U}^2(\mathbf{r})\mathrm{d}z}{Lx^2}, \tag{3.6}$$

which for the fundamental mode $n = 1$ yields $m_{\text{eff}} \approx 0.396 m_{\text{tot}}$.

For a rectangular beam with constant width $w$, oscillating in-plane, the resonance frequencies of the flexural modes are proportional to $\Omega_{\text{m}} \propto w/L^2$, independent of the thickness $t$. At the same time, the total mass of the beam is given by

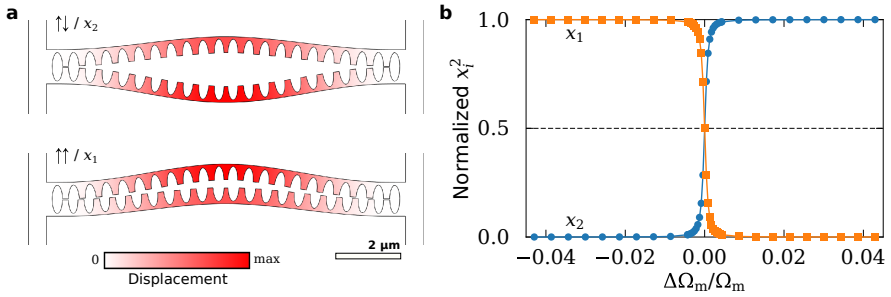


Figure 3.2: (a) Simulated mechanical displacement profiles of the two fundamental in-plane resonances of a sliced nanobeam structure, including disorder and compressive stress. The dimensions of the beam were matched to experimentally realized dimensions (see chapter 4) using measurements with a scanning electron microscope, including differences in hole and gap size along the beam. Compressive stress was introduced in the simulation by displacing one of the support pads by $10\,\mathrm{nm}$ along the direction of the beam. (b) Simulated squared displacement in the two half-beams for the fundamental mode of a sliced nanobeam structure (normalized to the maximum value). A frequency difference $\Delta\Omega_\mathrm{m}$ was introduced between the individual resonance frequencies of two identical half-beams by changing the density slightly. At $\Delta\Omega_\mathrm{m} = 0$ the modes hybridize to form the differential mode, while away from this point, the mode is dominated by motion in one of the individual half-beams.



$m_\mathrm{tot} = \rho w t L$, where $\rho$ is the density of the beam. This shows that to achieve large zero-point fluctuations without lowering the resonance frequency $\Omega_\mathrm{m}$, we can decrease the thickness $t$, while increasing the length $L$ or decreasing the width $w$ also increases $x_\mathrm{zpf}$ at the cost of decreasing $\Omega_\mathrm{m}$. In the sliced nanobeam structure, the periodic patterning provides additional design parameters. The narrow "rails" supporting the beam at the hole positions can be regarded as flexible hinges that connect the relatively inflexible "teeth". The width $s$ of these supporting rails (see figs. 3.4a and 3.4b) therefore provides a control parameter for the effective spring constant which has only a small effect on the effective mass, and vice versa for the size of the teeth.

### 3.2.2. Mode shapes for sliced nanobeams

The first few simulated modes of a sliced nanobeam structure are shown in fig. 3.1b. To obtain these figures, we perform numerical eigenmode simulations using the finite-element software COMSOL Multiphysics. The connection between the substrate and the support pads is modeled as a fixed boundary, while all other boundaries are kept free. The eigenmodes of the two identical half-beams couple to each other and form new normal modes where the half-beams move either in phase ($\uparrow\uparrow$) or in antiphase ($\uparrow\downarrow$) with each other. Of the four modes shown in the figure, only the fundamental differential mode $(1, \uparrow\downarrow)$ shows a substantial change in the gap size in the middle of the beam, where the optical mode is confined. It follows that this mode will be the one with the largest optomechanical coupling rate $g_0$.

The coupling between the two half-beams is quite weak. Therefore a small

amount of fabrication imperfection can stop the hybridization by breaking the symmetry, which shifts the frequencies of the two half-beams out of resonance with each other. Figure 3.2a shows the simulated mode shape for a sliced nanobeam structure with experimentally measured disorder (see chapter 4). Apart from the disorder, this simulation also includes compressive stress, which decreases the resonance frequencies, increases the difference between the two resonance frequencies, and also increases the asymmetry between the two mode shapes. The two mode shapes show the common and differential character described before, while also showing larger displacement values in one of the half-beams (labeled with $x_1$ and $x_2$ to indicate larger displacement in the upper or lower half-beam, respectively).

In fig. 3.2b, the squared displacements of the two half-beams in the simulated fundamental modes are shown as a function of the relative frequency difference of the uncoupled half-beams. These were obtained by changing the density of two identical half-beams slightly with respect to each other. The squared displacement is proportional to the energy of the resonator, so at $\Delta\Omega_{\mathrm{m}} = 0$, where the half-beams individually would have the same frequency, we find the modes hybridize and both half-beams contribute half of the total energy in the mode. With a difference between the half-beams equivalent to a relative frequency difference of $0.5\,\%$, the energy is already highly localized in one of the half-beams. Experimentally, we find relative frequency differences of up to a few percent, so this level of coupling is not enough to hybridize the mechanical modes reliably. Increasing the coupling between the half-beams could likely be achieved by changing the geometry at the ends of the beam, such that movement of one half-beam can more easily drive the motion of the other half-beam.



### 3.2.3. Imperfect hybridization and optomechanical coupling

The imperfect hybridization of the motion of the two half-beams discussed above has consequences for the values of $x_{\mathrm{zpf}}$, and therefore $g_0$, of the two modes [22], which we describe here. Harmonic motion of the two half-beams at a certain frequency $\Omega$ can be described as:

$$\begin{bmatrix} x_1(t) \\ x_2(t) \end{bmatrix} = \begin{bmatrix} \psi_1 \\ \psi_2 \end{bmatrix} \cos\Omega t \equiv \boldsymbol{\psi} \cos\Omega t, \text{ where } \boldsymbol{\psi} = \begin{bmatrix} \psi_1 \\ \psi_2 \end{bmatrix}. \tag{3.7}$$

Thus, $\psi_1$ and $\psi_2$ are the amplitudes of the oscillatory motion of the two individual half-beams, such that their variance is $\langle x_{1,2}^2 \rangle = \frac{1}{2}\psi_{1,2}^2$.

Our earlier choice of the displacement coordinate $x \equiv (d - d_0)/2$ becomes $x = (x_1 - x_2)/2$ in terms of the displacements of the individual half-beams. Since the optical response of the system is determined by the change in the distance $d$ between the beams, this choice leads to the same value of $G = -\partial\omega_{\mathrm{c}}/\partial x$ for both mechanical modes. Note that this choice of $x$ corresponds to the lab-frame displacement of the two beams for a purely differential mode ($\uparrow\downarrow$ in fig. 3.1b). The variance of $x$ due to harmonic motion described by $\boldsymbol{\psi}$ is then:

$$\langle x^2 \rangle_{\boldsymbol{\psi}} = \tfrac{1}{8}\left(\psi_1^2 + \psi_2^2 - 2\psi_1\psi_2\right). \tag{3.8}$$

The state vectors of the two normal modes can be written without loss of generality as

$$\boldsymbol{\psi}_\alpha = A_\alpha \begin{bmatrix} \cos\theta \\ \sin\theta \end{bmatrix}, \quad \boldsymbol{\psi}_\beta = A_\beta \begin{bmatrix} \sin\theta \\ -\cos\theta \end{bmatrix}. \tag{3.9}$$

For both of these modes, we can calculate the variance of $x$, denoted as $\langle x^2 \rangle_\alpha$ and $\langle x^2 \rangle_\beta$, respectively:

$$\begin{aligned} \langle x^2 \rangle_\alpha &= \frac{1}{8} A_\alpha^2 (\cos^2\theta + \sin^2\theta + 2\sin\theta\cos\theta) \\ &= \frac{A_\alpha^2}{8}(1 - \sin 2\theta), \\ \langle x^2 \rangle_\beta &= \frac{A_\beta^2}{8}(1 + \sin 2\theta). \end{aligned} \tag{3.10}$$

For the beams undergoing thermal motion, the variance is given by the equipartition theorem:

$$\langle x^2 \rangle_\alpha = \frac{k_\mathrm{B} T}{m_\alpha \Omega_\alpha^2}, \quad \langle x^2 \rangle_\beta = \frac{k_\mathrm{B} T}{m_\beta \Omega_\beta^2}, \tag{3.11}$$

where $m_\alpha$ and $m_\beta$ are the effective mass of these modes. As shown in section 3.2.1, the effective mass of the fundamental mode of a doubly-clamped beam with respect to its maximum displacement is $m_\mathrm{eff} \approx 0.396 m_\mathrm{tot}$. With our choice of the displacement coordinate $x$, we find that the effective mass for the differential mode of two coupled half-beams is also given by $m_\mathrm{diff} \approx 0.396 m_\mathrm{tot}$, where the total mass $m_\mathrm{tot}$ is the mass of both half-beams. Evaluating eqs. (3.10) and (3.11) for a differential mode ($\theta = \pi/4$) yields $A_\alpha^2 = 4 k_\mathrm{B} T / m_\mathrm{diff} \Omega_\alpha^2$ and similarly for $A_\beta^2$. Substituting this back into eq. (3.10), we arrive at

$$\langle x^2 \rangle_\alpha = \frac{k_\mathrm{B} T (1 + \sin 2\theta)}{m_\mathrm{diff} \Omega_\alpha^2}, \quad \langle x^2 \rangle_\beta = \frac{k_\mathrm{B} T (1 - \sin 2\theta)}{m_\mathrm{diff} \Omega_\beta^2}. \tag{3.12}$$

Thermal variance is related to the zero-point fluctuations $x_\mathrm{zpf}$ as

$$\langle x^2 \rangle_i = 2 \frac{k_\mathrm{B} T}{\hbar \Omega_i} (x_{\mathrm{zpf},i})^2, \text{ so } x_{\mathrm{zpf},i} = \sqrt{\frac{\hbar(1 \pm \sin 2\theta)}{4 m_\mathrm{diff} \Omega_i}}, \tag{3.13}$$

where $i \in \{\alpha, \beta\}$, and the sign for the term $\sin 2\theta$ is chosen to be $+$ and $-$, respectively. It follows that the ratio between the zero-point fluctuations for the coupled modes $\alpha$ and $\beta$ is given by

$$\frac{x_{\mathrm{zpf},\alpha}}{x_{\mathrm{zpf},\beta}} = \sqrt{\frac{\Omega_\beta (1 + \sin 2\theta)}{\Omega_\alpha (1 - \sin 2\theta)}}. \tag{3.14}$$

Finally, we note that the ratio between the variances of the optical power at the two resonance frequencies is equal to the ratio between the variances of $x$, given

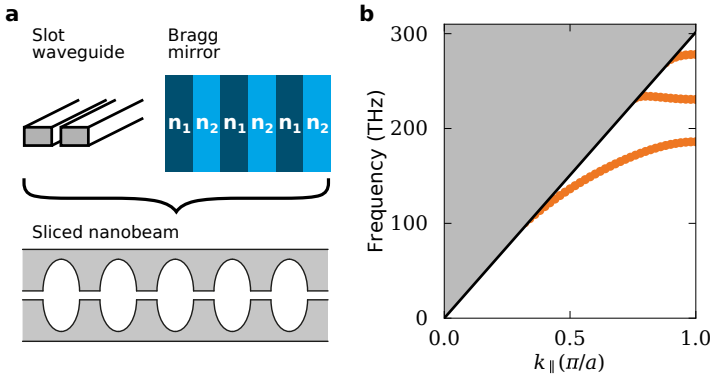


Figure 3.3: (a) Illustration of the concept of the sliced photonic crystal nanobeam. It combines a slot waveguide with periodic modulation of the refractive index by including holes in the structure. The slot waveguide geometry provides confinement of light by total internal reflection, while the periodic modulation, like in a Bragg mirror, can efficiently reflect light for a range of frequencies, where the scattering from the individual holes constructively interferes in the backward direction. (b) Simulated band diagram for TE-like guided modes of a periodic sliced nanobeam like the one shown in (a); the dimensions are listed in table 3.1 under "mirror D". The black solid line indicates the light-line $\omega = ck_{\parallel}$, above which light can escape to free space, since there it is not confined by total internal reflection.



in eq. (3.12), and to the square of the ratio between the zero-point fluctuations in eq. (3.14). Therefore, we can determine the ratio of the optomechanical coupling rates $g_0$ directly from a measurement of the ratio between the measured band powers.

## 3.3. Optical resonances of sliced nanobeams

The mechanisms for the confinement of light in sliced photonic crystal nanobeams are illustrated in fig. 3.3a: total internal reflection prevents light from escaping the free-standing silicon nanobeam, like in a slot waveguide, while the periodic patterning of holes works like a Bragg mirror which can efficiently reflect light in a range of frequencies. In an infinitely periodic structure, we can represent this with a photonic band diagram [88] such as the one shown in fig. 3.3b, where the orange data points show allowed frequencies as a function of $k_{\parallel}$, the component of the wavevector of the light parallel to the nanobeam. The black line represents the light line $\omega = ck_{\parallel}$, above which there is a continuum of modes available in free space. The wavevector at the light line for a specific frequency corresponds to the critical angle for total internal reflection at that frequency. In this diagram, we only show solutions where the electric field is oriented horizontally—across the gap in the sliced nanobeam—which we refer to as "TE-like" in analogy to the transverse electric (TE) modes of an infinite slab waveguide. As fig. 3.3b shows, in a range of frequencies near $200\,\mathrm{THz}$ there are no TE-like guided modes, thus opening a photonic bandgap. This is not a full bandgap, since transverse magnetic (TM)-like waveguide modes (with electric field oriented vertically) exist in

the gap region. If the symmetry of the structure is broken, light in the bandgap region for TE-like modes can scatter to the TM-like modes and propagate along the nanobeam.

In order to create a localized cavity mode, we introduce a defect in the periodicity of the photonic crystal [88]. The resulting mode is closely related to the waveguide modes at the edge of the bandgap, but shows evanescent decay in the periodic "mirror" regions that surround it. If the defect constitutes a local decrease of the effective refractive index, the defect cavity mode will resemble the lower guided mode at the edge of the bandgap, and vice versa. We note that it was recently shown that with a similar approach, photonic crystal nanobeam cavities that include subwavelength slots can be created that simultaneously have a high quality factor and an ultrasmall mode volume [20, 92–94].

The optical losses of a photonic crystal cavity mode have two main components, aside from material absorption, namely losses through propagation along the nanobeam and radiation losses to free space. The losses from propagation along the nanobeam can be decreased by increasing the length of the photonic crystal region, or by ensuring the mirror strength of the photonic crystal is large. The mirror strength is related to the decay length of the evanescent waves extending from the defect region, and is dependent on the frequency range of the bandgap as well as the frequency difference of the cavity mode with the guided modes at the edges of the bandgap. The radiation losses, on the other hand, depend on the overall mode profile of the optical cavity [95]. A mode that is localized in space necessarily includes a range of wavevectors, since its spatial profile and the distribution of wavevectors in the mode are related by a Fourier transform. The wavevector components smaller than the wavevector at the light line for the cavity resonance frequency $\omega_c$, given by $k_0 = \omega_c/c$, correspond to overlap between the localized cavity mode and the continuum of free-space modes that exist above the light line. The relative amount of such wavevector components above the light line thus determines the loss rate of the cavity due to radiation, which implies low radiation losses can be obtained by using guided modes far below the light line and an optimized field profile.

The design of a photonic crystal cavity starts from the unit cells of the periodic structure, since the frequency range of the bandgap ultimately determines the achievable resonance frequency and optical loss rates of a defect cavity in the photonic crystal. The optomechanical coupling depends strongly on the characteristics of the guided modes in the periodic structure as well, since the cavity mode is derived from them. The strategy we follow to subsequently optimize the shape of the defect region is similar to the one laid out by Quan & Lončar [87], who use a Gaussian field profile for the cavity mode to obtain low losses since Gaussian distribution functions minimize the product of the widths of a distribution and its Fourier transform. Given sufficient CPU time and sufficiently fast methods to evaluate the characteristics of a given cavity design, one can also implement a computational optimization that explores a predefined parameter space [44, 96].

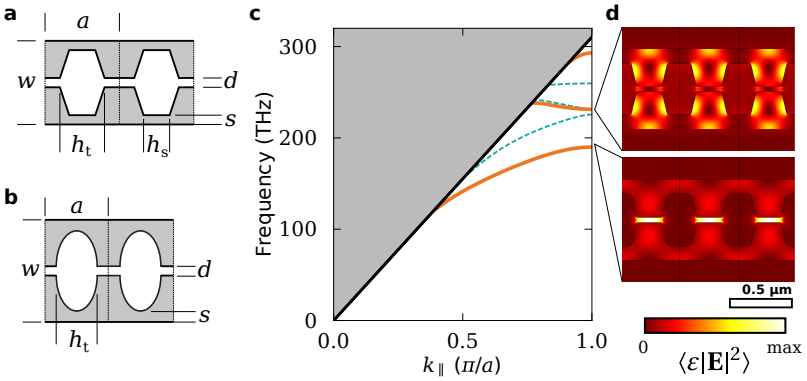


Figure 3.4: (a),(b) Unit cells with indicated geometrical parameter labels for periodic sliced nanobeams with (a) trapezoidal and (b) elliptical holes. Two unit cells are shown (separated by dotted lines) for ease of labeling. (c) Simulated band diagram of a periodic sliced nanobeam with trapezoidal holes (see panel (a)), with the dimensions listed in table 3.1 as "Cavity N". Orange solid lines show TE-like guided modes, while teal blue dashed lines show TM-like modes. (d) Simulated energy density of TE-like guided modes at the Brillouin zone edge ($k_\parallel = \pi/a$). Three unit cells are shown, separated by vertical solid lines. The lower frequency band has a higher fraction of energy concentrated in the gap between the teeth compared to the upper band.



### 3.3.1. Photonic band structure of sliced nanobeams

We first study the waveguide modes of periodically patterned nanobeams. The properties we are mainly interested in are the frequencies of the waveguide modes, the size of the bandgap, and the sensitivity of the waveguide mode frequencies to displacement of the beam halves. To obtain these properties, we use numerical finite-element simulation (COMSOL Multiphysics) of the eigenmodes with periodic boundary conditions to find the Bloch-Floquet periodic eigenmodes of the structure at a specific value of the parallel component of the wavevector $k_\parallel$. In the other directions, we use perfect electric conducting boundary conditions at several micrometers distance from the structure. We consider unit cells with either trapezoidal or elliptical holes, depicted in figs. 3.4a and 3.4b. The parameters that define the geometry are the overall thickness $t$ and width $w$ of the nanobeam, the gap size $d$, the width $s$ of the narrow "support" at the positions of the holes, the period of the photonic crystal structure $a$, and the hole size $h_t$, which is also the distance between the "teeth" of the structure. In the case of trapezoidal holes, the size of the holes $h_s$ at the supporting rails on the outside of the beam is an additional free parameter.

Figure 3.4c shows the simulated photonic band diagram for both TE-like (orange solid lines) and TM-like modes (teal blue dashed lines), obtained with the parameters labeled "Cavity N" in table 3.1. Like the band diagram in fig. 3.3b, which corresponds to a structure with elliptical holes with parameters "Mirror D" in table 3.1, a quasi-bandgap is opened for the TE-like modes. The energy density profiles of the guided modes at the Brillouin zone edge are shown in fig. 3.4d. The lower-frequency mode, which in general would have a larger fraction of the

Table 3.1: Design parameters used to create cavity designs (see fig. 3.4), with the absolute value of $G = -\partial\omega/\partial x$ and bandgap from periodic waveguide simulations indicated. The asterisks for "Mirror D", "Cavity L" and "Mirror L" indicates the fact that these structures used elliptical holes, which are defined by their short and long axes given by $h_t$ and $w - 2s$, respectively.

| | $t$ (nm) | $a$ (nm) | $w$ (nm) | $h_t/a$ | $h_s/a$ | $d$ (nm) | $s$ (nm) | $\lvert G\rvert/2\pi$ (THz/nm) | Bandgap (THz) |
|---|---|---|---|---|---|---|---|---|---|
| Mirror D | 200 | 495 | 1040 | 0.63* | N/A* | 60 | 85* | 0.4 | 45 |
| Cavity L | 200 | 417.6 | 940.5 | 0.64* | N/A* | 63 | 108 | 0.42 | 41.4 |
| Mirror L | 200 | 486.9 | 940.5 | 0.60* | N/A* | 63 | 108 | 0.42 | 37.5 |
| Cavity N | 250 | 483 | 650 | 0.58 | 0.40 | 40 | 120 | 0.88 | 41.3 |
| Mirror N | 250 | 583 | 650 | 0.52 | 0.46 | 40 | 120 | 0.71 | 38.4 |
| Cavity W | 250 | 450 | 900 | 0.58 | 0.70 | 40 | 120 | 0.60 | 90.3 |
| Mirror W | 250 | 563 | 900 | 0.52 | 0.64 | 40 | 120 | 0.48 | 62.8 |



mode's energy in the high-index material between the holes, has a large energy density in the gap between the "teeth". Therefore we expect this mode to be the most sensitive to displacements that change the gap size.

To obtain more insight in the influence of various parameters on the properties of the waveguide modes, we calculate the mode frequencies at the Brillouin zone edge in a large, multi-dimensional parameter space. For each set of parameters, we perform the simulation both with and without an outward displacement of both half-beams by $1\,\mathrm{nm}$. Since we defined $x \equiv (d - d_0)/2$, the difference in simulated frequency directly yields $G = -\partial\omega/\partial x$ per nanometer displacement. In fig. 3.5 we show one-dimensional cross sections of the simulated parameter space. Each of the panels shows the first three mode frequencies and the light line at the Brillouin zone edge, as well as the absolute value of $G$ for the first two modes. The parameters that are not varied in each plot are chosen as close as possible to the parameters "Cavity N" in table 3.1, indicated with a dashed vertical line in each panel. As expected from the mode profiles shown in fig. 3.4d, the highest value of $G$ is always found for the lowest guided mode.

In general, we see that all parameter changes that increase the amount of silicon per period of the photonic crystal (larger width $w$, smaller hole sizes $h_t$, $h_s$, smaller gap size $d$, larger "support" size $s$) pull down the frequencies of the guided modes with respect to the light line. The size of the bandgap is increased by all parameter changes that increase the photonic strength, or "contrast" of the periodic modulation, either directly (larger $h_t$ and $h_s$, smaller $d$, smaller $s$) or indirectly (lateral hole size is $w - 2s$, so larger $w$ increases the relative size of the holes). To create short nanobeams, with a relatively small number of periods of the photonic crystal to prevent propagation losses along the nanobeam, the strong increase of bandgap size with $h_s$ is especially interesting. However, there is an inherent trade-off between large concentration of the field of the mode inside the low-index gap, and using the high-index silicon to decrease the mode frequency

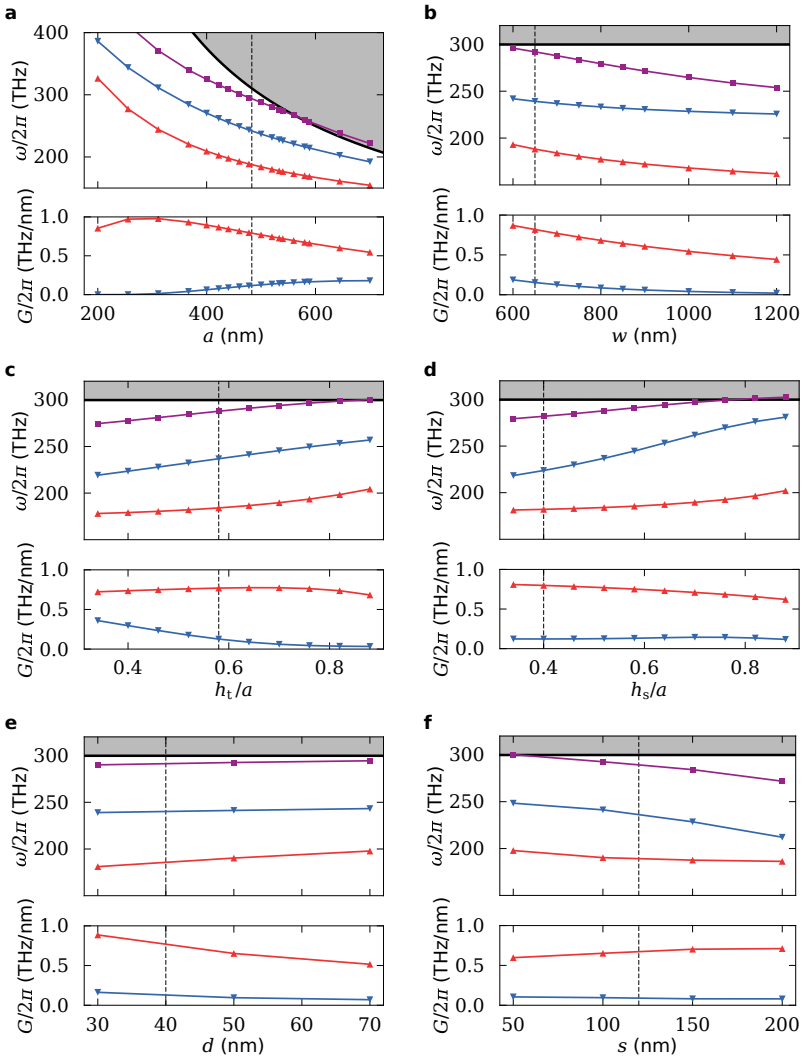


Figure 3.5: Simulated mode frequencies $\omega$ of TE-like waveguide modes at the Brillouin zone edge, and the absolute value of the optomechanical coupling rates $G = -\partial\omega/\partial x$ for the two lowest-frequency modes, as a function of structure parameters (see fig. 3.4). The dashed black line indicates the nominal value taken for the eventual design "cavity N" (see table 3.1). The data was plotted as much as possible around these design parameters. For (a)–(d): $a = 500\,\mathrm{nm}$, $w = 700\,\mathrm{nm}$, $h_t/a = 0.58$, $h_s/a = 0.52$, $d = 40\,\mathrm{nm}$ and $s = 120\,\mathrm{nm}$. (e),(f) were simulated with a different set of parameters and are plotted with $a = 500\,\mathrm{nm}$, $w = 700\,\mathrm{nm}$, $h_t/a = 0.60$, $h_s/a = 0.50$, $d = 50\,\mathrm{nm}$ and $s = 100\,\mathrm{nm}$.

and increase the bandgap. This is directly related to one of the guidelines we found at the end of section 2.2.2: maximize the amount of high-index material close to the gap to increase $G$. We see the result of this in fig. 3.5, where $G$ decreases strongly for larger $w$. This means we can't use the design strategy laid out by Quan & Lončar [87] directly, as they recommend using large width $w$ to pull down the guided modes in frequency, away from the light line. At the same time, if we use a small width $w$, we need to increase $a$ to decrease the mode frequency to our target frequency of $190\,\mathrm{THz}$, which also correlates with decreased $G$ (fig. 3.5a). From just these one-dimensional cross sections of possible combinations of parameters we cannot unequivocally judge the best combination of these two parameters. Similarly, the shape of the hole, parametrized by $h_\mathrm{s}$ and $h_\mathrm{t}$, might lead to complex reshaping of mode profiles such that the resulting behavior of the bandgap, mode frequency and $G$ cannot be predicted from just a one-dimensional cross section.

From fig. 3.5e we see that our first guideline from section 2.2.2 (minimize the gap size to maximize $G$) leads to only beneficial results here: apart from increasing $G$, it decreases the mode frequency and increases the bandgap. We therefore choose a value slightly below the limits of our current fabrication process, namely $40\,\mathrm{nm}$ (see section 3.4), as the design value. The parameter $s$ strongly influences the mechanical resonance frequency since it effectively determines the stiffness of the nanobeam, in addition to the influence on the optical mode seen in fig. 3.5f. Extremely small values of $s$ lead to problems in fabricating the structures due to the small feature size, but especially due to the low stiffness of the resulting structure (see section 3.4.2). Therefore we choose a value of $120\,\mathrm{nm}$, which leads to structures that can be fabricated with relatively high yield.

To visualize the interaction between two parameters in their effect on the properties of the structure, we create two-dimensional color maps. One set of such color maps is shown in fig. 3.6, with on the axes the period $a$ and width $w$. These parameters can strongly influence the mode frequency, especially since they can be varied over a wide range of values. The four panels show, in the same range of parameters, the frequency of the lowest guided mode at the Brillouin zone edge (fig. 3.6a), the simulated absolute value of $G$ for this mode (fig. 3.6b), the bandgap (fig. 3.6c) and the distance to the light line (fig. 3.6d). The color scale for the frequency plot in fig. 3.6a is centered around the target frequency of $190\,\mathrm{THz}$, making it easy to judge which combinations of $a$ and $w$ can lead to a structure with the desired frequency. Looking at the other three panels around those values, indicated with the white dashed lines, we see that the highest values of $G$ can be obtained for small values of $w$. However, as we already saw in the one-dimensional cross sections, this leads to smaller bandgaps and modes that are closer to the light line. For this reason, we choose to create two sets of cavity parameters as starting points of our designs, a narrow design which is more strongly optimized to have large $G$ ("Cavity N" in table 3.1), and a wider design which has a larger bandgap and distance to the light line at the expense of a smaller achievable optomechanical coupling rate $G$ ("Cavity W" in table 3.1).

Figure 3.7 shows the same properties of the waveguide mode(s) as a function

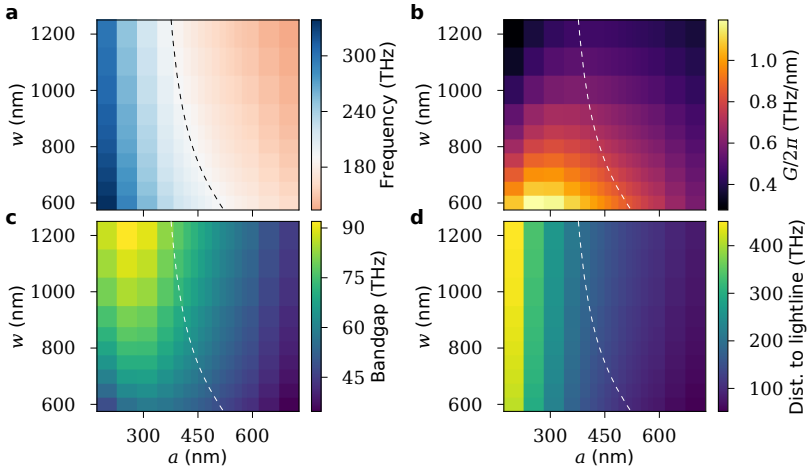


Figure 3.6: Visualization of the tuning behavior of several properties as a function of the width $w$ and period length $a$ of a unit cell (see fig. 3.4). The other parameters were taken as close as possible to the parameters of the eventual design "cavity N" (see table 3.1): here $h_t/a = 0.58$, $h_s/a = 0.52$, $d = 40\,\mathrm{nm}$ and $s = 120\,\mathrm{nm}$. The depicted properties are: (a) frequency of the lowest guided mode at the band edge, with the color scale centered around the target frequency of $190\,\mathrm{THz}$; (b) absolute value of the optomechanical coupling rate of the guided mode $G$; (c) bandgap between the lowest two bands; (d) distance to the light line for the lowest guided mode at the band edge. The black and white dashed lines are a guide to the eye along the parameter combinations that result in a mode at the target frequency.



of the shape of the holes. The same trade-offs seem to occur here: to obtain large $G$ at the desired target frequency, a hole that is larger in the middle of the beam than on the outside is preferred ($h_t$ large, $h_s$ small, see fig. 3.7b). For those parameter values, the bandgap is decreased. Again we choose to optimize "Cavity N" more for high $G$, at a small value of $h_s$, while "Cavity W" uses holes that are wider at the outside than in the middle of the beam.

Table 3.1 lists the parameters chosen as a starting point for our design, as well as the simulated values for $G$ and for the bandgap. We used values equal to points in the simulated parameter space (positions of data points in figs. 3.5 to 3.7) except for the period $a$, where we used an interpolation of the simulated mode frequencies to find the value of $a$ corresponding to a target frequency of $190\,\mathrm{THz}$. The values for "Mirror N" and "Mirror W" were chosen to yield a bandgap centered around this target frequency, again using an interpolation to choose the value of $a$. Since this required decreasing the mode frequencies, to avoid strong reduction of $G$, the guided modes with the "Mirror" parameters have a smaller bandgap than with the "Cavity" parameters. We note that in the absence of a strong reason to use the lower band edge to create a cavity mode (such as the larger $G$ this mode has in our case), one would prefer to use the higher-frequency mode, since then this trade-off where lowering the mode frequency decreases the bandgap occurs in the cavity region instead of in the mirror region. The values for "Mirror D" shown in this table were created using only one-dimensional

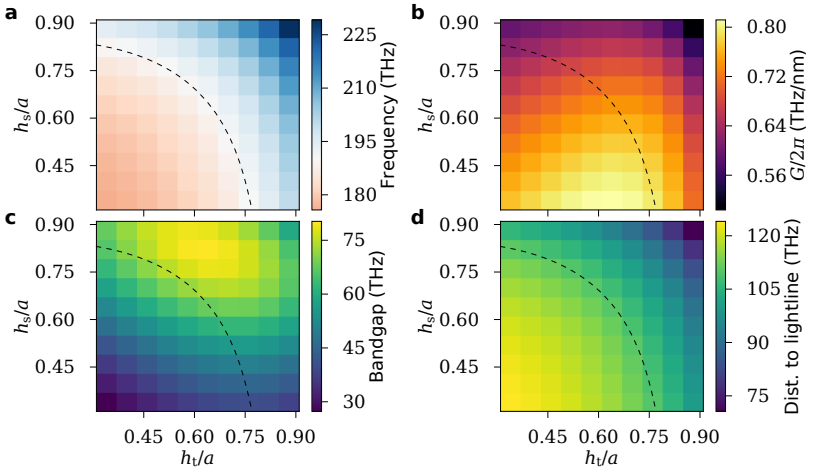


Figure 3.7: Visualization of the tuning behavior of several properties (see caption of fig. 3.6) as a function of the hole sizes $h_t/a$ and $h_s/a$ in a periodic structure (see fig. 3.4). The other parameters were taken as close as possible to the parameters of the eventual design "cavity N" (see table 3.1): here $a = 500\,\mathrm{nm}$, $w = 700\,\mathrm{nm}$, $d = 40\,\mathrm{nm}$ and $s = 120\,\mathrm{nm}$. The black dashed lines are a guide to the eye along the parameter combinations that result in a mode at the target frequency.



explorations of the parameter space, for a structure with elliptical holes. These parameters were used to create the simple defect cavity that is described in the next section, and characterized in chapter 4. The values for "Cavity L"/"Mirror L" were found by a parameter space exploration documented by Freisem [97]. A structure based on these parameters is used as "device 2" in chapter 5.

### 3.3.2. Simple defect cavity

To create a localized optical cavity mode that is derived from the lower band edge, we first consider introducing a simple defect in the photonic crystal nanobeam. We use the "Mirror D" parameters in table 3.1 for the periodic structure, and the defect is formed by a local decrease in the distance between the centers of two elliptical holes by $10\,\%$. This decreases the local effective refractive index and creates defect states in the bandgap region. Figure 3.8a shows the first two cavity modes created in this way in the sliced nanobeam. To simulate these cavity modes, a full nanobeam including support pad is modeled with perfectly matched layers on all sides, at several micrometers distance from the beam. Note that the higher-order cavity modes have a lower frequency, since they are less confined near the defect, such that the frequency is closer to that of the waveguide mode in the periodic structure. For the same reason, the higher-order optical modes are also less sensitive to the motion of the fundamental mechanical resonance, since that has the largest displacement in the center of the beam. The simulated optical quality factor of the fundamental mode is $Q \approx 1.2 \times 10^3$ and for the second-order mode $Q \approx 1.4 \times 10^2$, which is lower due to the wider extent of the mode and the relatively short length of the nanobeam.

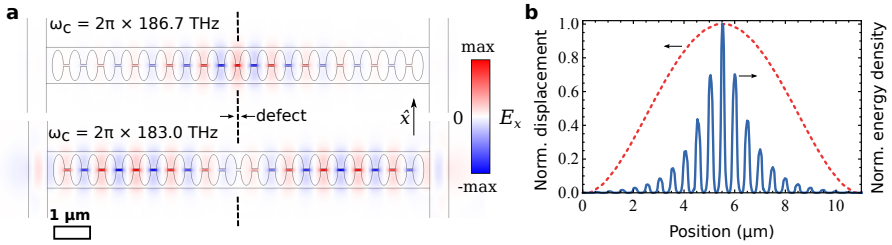


Figure 3.8: (a) Simulated transverse electric field profiles of the first two cavity modes of a sliced nanobeam with dimensions listed in table 3.1 as "mirror D". The defect that is responsible for the creation of these modes is a slightly smaller distance between the two holes in the center of the beam. (b) Normalized resonant mode profiles of the fundamental optical and mechanical resonance of the sliced nanobeam shown in (a). The red dotted line shows the displacement along the length of the beam, while the blue solid line represents the local energy density.

The frequency shift of the optical resonance of the sliced nanobeam due to mechanical motion depends on the overlap between the optical and mechanical mode profiles. To estimate the influence of the finite extent of the mode profiles on the response, we extract these profiles from the numerical simulation. Figure 3.8b shows the normalized displacement profile of the mechanical resonance and the normalized electromagnetic energy density profile of the optical cavity mode, as a function of the position along the nanobeam.

As previously shown in fig. 3.1, the mechanical mode profile closely resembles the mode profile of the fundamental mode of a doubly-clamped beam [91]. From the simulated displacement profile we calculate the effective mass for this purely anti-symmetric motion to be $m_{\mathrm{eff}} \approx 0.39 m_{\mathrm{tot}}$ (see eq. (3.6)), with $m_{\mathrm{tot}}$ the total mass of the sliced nanobeam. This value is very close to the value obtained from the analytical displacement profile of a uniform doubly-clamped beam. In the optical mode profile, the localization of the energy density in the small gaps between the silicon "teeth" of the structure can be clearly recognized. Overall, the profile shows exponential decay away from the defect, where the optical frequency lies inside the photonic quasi-bandgap.

We compute the correction on the optomechanical coupling rate due to the finite extent of the modes from the overlap integral between these two mode profiles. We find a factor of $0.90$ with respect to the frequency shift of the optical cavity mode for a uniform displacement of the beam. As we show in more detail in chapter 4, this results in an overall prediction for the photon-phonon coupling rate of $g_0/2\pi = 26\,\mathrm{MHz}$.

### 3.3.3. Tapered defect cavity

To create a photonic crystal nanobeam cavity with low optical losses, an optical cavity field profile with a low relative amount of wavevector components above the light line is required. A Gaussian field profile will lead to low losses for a mode that is still localized in a small volume, since the product of the width of the distri-

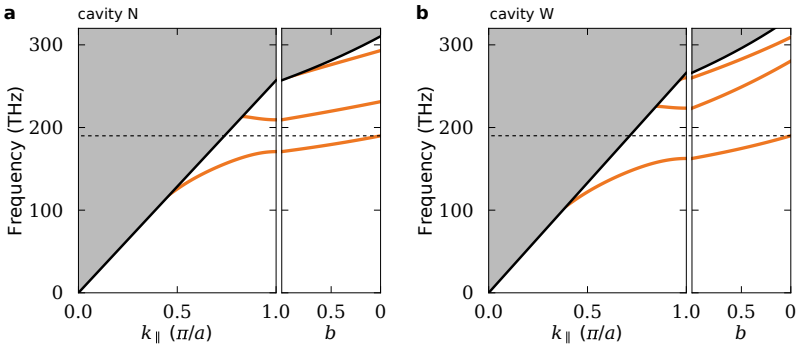


Figure 3.9: Band diagrams and transitions between "cavity" and "mirror" parts of sliced nanobeams with tapered cavity designs. On the left in each panel, the simulated band diagram is shown for a periodic structure with dimensions listed in table 3.1 as (a) Mirror N and (b) Mirror W. Only TE-like modes are shown. The right part shows the simulated mode frequencies at the Brillouin zone edge as a function of the geometrical parameter $b$, which transforms the structure from the mirror parameters (at $b = 1$) to the cavity parameters (at $b = 0$) listed in table 3.1 as (a) Cavity N and (b) Cavity W. The horizontal dashed lines indicate the target frequency, which is in the middle of the bandgap in the mirror region and equal to the lower band edge for the cavity parameters.



bution and that of its Fourier transform is minimized for a Gaussian distribution. If we use a periodic structure, like in the simple defect cavity of the previous section, the field decays exponentially away from the defect region as $\exp(-\gamma y)$. To obtain a Gaussian mode profile, we would ideally create a linear change in mirror strength $\gamma = Ay$. In that case, the decay of the field profile should follow $\exp(-Ay^2)$, thus creating a Gaussian profile. We can approximate a linear change of the mirror strength by changing the parameters of the building blocks of the photonic crystal nanobeam around the defect gradually between the cavity region to a mirror region, where we again use a periodic structure. To do this, we first find both start and end points for such a transition as described in section 3.3.1. Figure 3.9 shows the band structure for the mirror region parameters "Mirror N" (fig. 3.9a) and "Mirror W" (fig. 3.9b), as well as the transition between those and the parameters at the cavity positions, respectively "Cavity N" and "Cavity W". Here we define a geometry parameter $b$, such that for all the structure parameters $\{a, w, h_t, h_s\}$, their value is found from, for example, $w_b = w_{cav} + (w_{mir} - w_{cav})b$, where $w_{cav}$ is the value of $w$ at the cavity position, and $w_{mir}$ is the value of $w$ in the mirror region.

To find the profile of structure parameters $b$ that will lead to a linear change in mirror strength and thus a Gaussian profile, we use the approximation $\gamma^2 + \delta^2 = \delta_{max}^2$, where $\delta$ is the frequency detuning of the mode from the bandgap center, and $\delta_{max}$ is equal to half of the bandgap size [87]. Figure 3.10a shows this relation. We additionally approximate the shift of the bands as a function of $b$ to be linear, which means that we expect a quadratic change of the geometry parameters $b$ to yield a linear change in mirror strength $\gamma$. The detuning from the bandgap center

and the maximum detuning $\delta_{\text{max}}$ can then be written as

$$\delta = \delta_{\text{max}}^{\text{cav}}(1-b), \tag{3.15}$$

$$\delta_{\text{max}} = \delta_{\text{max}}^{\text{cav}}(1-b) + \delta_{\text{max}}^{\text{mir}} b, \tag{3.16}$$

where the superscripts "cav" and "mir" indicate the values at $b = 0$ and $b = 1$, respectively. We define the ratio between the bandgap for the cavity parameters and for the mirror parameters as $r \equiv \delta_{\text{max}}^{\text{cav}}/\delta_{\text{max}}^{\text{mir}}$, such that we obtain

$$\left(\frac{\gamma}{\delta_{\text{max}}^{\text{mir}}}\right)^2 = (1-2r)b^2 + 2rb. \tag{3.17}$$

This is a quadratic equation for $b$ with positive solution

$$b = \frac{-r + \sqrt{r^2 + (1-2r)(\gamma/\delta_{\text{max}}^{\text{mir}})^2}}{1-2r}. \tag{3.18}$$

The maximum mirror strength, according to this model, is given by

$$\frac{\gamma_{\text{max}}}{\delta_{\text{max}}^{\text{mir}}} = \sqrt{\frac{r^2}{2r-1}}, \text{ for } b_{\text{max}} = \frac{r}{2r-1}. \tag{3.19}$$

Therefore, if the bandgap changes as a function of the geometry parameter $b$ (i.e., $r \neq 1$), the maximum mirror strength is not obtained for $b = 1$ where $\delta = 0$, but slightly before or after this point. Equation (3.18) is shown in fig. 3.10b with $r = 1$ and for the case of the parameters "Cavity N"/"Mirror N", where $r = 1.08$.

If the parameters in the cavity and mirror region have the same period, we can simply implement a linear change of $\gamma$ as a function of hole number, but if the period changes, such an approach does not lead to a linear change of $\gamma$ as a function of position [97]. The positions $y_i$ of the holes, given assigned values of $b_i$ for the holes, can be calculated from the periods $a_i = a_{\text{cav}} + (a_{\text{mir}} - a_{\text{cav}})b_i$ as

$$y_i = 0.5a_i + \sum_{k=1}^{i-1} a_k. \tag{3.20}$$

Conversely, we can calculate the desired profile of $b(y)$ as a function of position along the nanobeam by first defining $\gamma(y) = \gamma_{\text{max}} y/y_{\text{max}}$, where $y_{\text{max}}$ is the position at which $\gamma$ reaches its maximum value $\gamma_{\text{max}}$. We can substitute this in eq. (3.18) together with the definitions in eq. (3.19) which yields

$$b(y) = b_{\text{max}}\left(1 - \sqrt{1-(y/y_{\text{max}})^2}\right). \tag{3.21}$$

To obtain a tapering profile for $N$ holes, we first set $b_i = 0$. The profile is improved by calculating the hole positions $y_i$ up to $i = N+1$ using eq. (3.20), then adjusting $b_i$ using eq. (3.21) with $y_{\text{max}} = y_{N+1}$. We repeat this procedure using the new $b_i$ as input, until the changes in $b_i$ are negligible, which happens within a few iterations. The blue data points in fig. 3.10b show the result of this procedure for the "Cavity

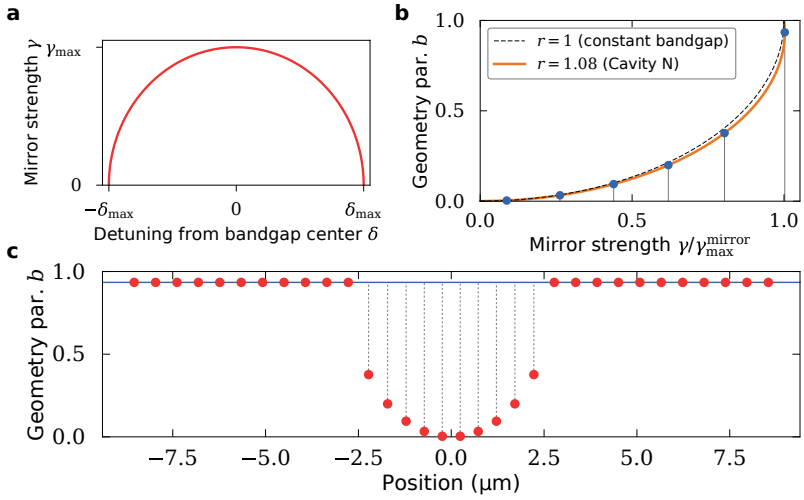


Figure 3.10: Tapering strategy based on linear increase in mirror strength $\gamma$. (a) Mirror strength as a function of detuning from the center of the bandgap. At a detuning $\delta = \delta_{\text{max}}$, the frequency of the cavity coincides with one of the waveguide modes at the edge of the bandgap. (b) Geometrical parameter $b$ as a function of the mirror strength, assuming a linear shift of the mode frequencies as a function of $b$. The parameter $r$ parametrizes the change in bandgap across the transition, which distorts the relation between $b$ and $\gamma$ away from the dashed line. The blue points indicate the steps for a tapering with five holes, using $r = 1.08$ corresponding to the dimensions of "Mirror N"/"Cavity N" in table 3.1. (c) Overall tapered cavity profile using a five-hole tapering as indicated in panel (b).

N"/"Mirror N" parameters, which we use to create the five-hole tapering shown as a function of position in fig. 3.10c. We note that according to Chan [98], the large changes in parameters at the outside of the taper region, near the mirror region, can lead to optical losses themselves, therefore he implemented a taper profile which was "smoothed" between the taper and mirror regions.

In fig. 3.11, we compare the simulated field profiles of a cavity with a five-hole tapering according to this design strategy with the simple defect cavity of section 3.3.2. Figure 3.11c shows the magnitude of the electric field in the middle of the gap, along the sliced nanobeam, for both cavities shown in figs. 3.11a and 3.11b. On the logarithmic scale, we can recognize the exponential decay in the case of the simple defect cavity and the Gaussian profile in our tapered cavity. We simulated nanobeam cavities with taper regions with $3$, $5$, $7$, $9$ and $11$ holes and show the resulting cavity parameters in figs. 3.12a to 3.12c. Our estimate of $G$ is based on a simulation with a uniform displacement of the whole nanobeam of $1\,\text{nm}$. We find simulated optical quality factors of close to $10^6$ for cavities with a five-hole taper. Despite the higher bandgap size of the cavities based on the "Cavity W"/"Mirror W" parameters, the optical quality factors we find are comparable to those for the "Cavity N"/"Mirror N" parameters, which as expected have a much higher value of $G$.

We also varied the total nanobeam length, which varies the number of periods

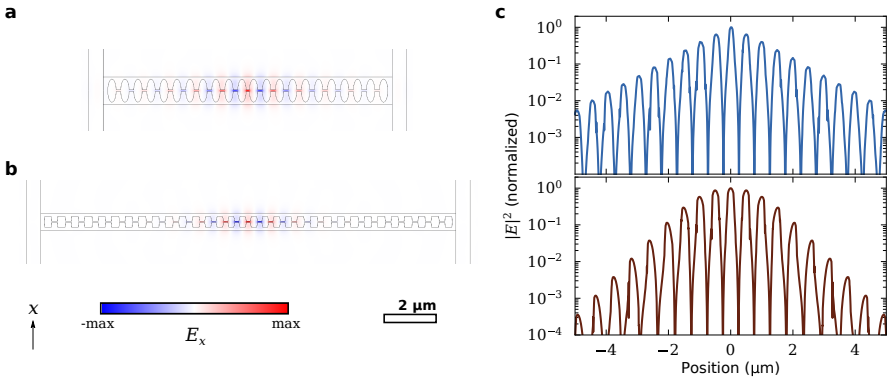


Figure 3.11: Comparison of the optical electric field profiles for (a) the simple defect cavity with dimensions "Mirror D" (see fig. 3.8) and (b) the cavity design with five-hole tapering using dimensions "Mirror N"/"Cavity N" (see fig. 3.10). (c) Normalized energy density along the center of the cavity (in the gap) for the cavity designs shown in (a) and (b) (upper and lower panel, respectively). The simple defect cavity shows an exponential decay, while the tapered defect leads to an overall Gaussian profile.

3

of the photonic crystal in the mirror region. Figures 3.12d to 3.12f show the resulting cavity parameters. While the cavity frequency and $G$ are hardly affected, shorter beams lead to a decrease in quality factor due to an increase in waveguide losses. For the cavities based on the "Cavity N"/"Mirror N" parameters, the waveguide losses start to dominate for lengths below approximately $18\,\mu\mathrm{m}$. Here, the higher bandgap size of the cavities based on the "Cavity W"/"Mirror W" parameters does result in a higher quality factor. In other words, the same quality factor can be obtained with nanobeams that are several micrometers shorter when using the parameters which show a higher bandgap in the periodic simulation.

### 3.3.4. Double-period modulation to improve outcoupling

The tapered defect cavities, engineered to have low radiation losses, necessarily have low coupling to the focused laser beam at normal incidence that we use in our free-space detection scheme. The better we succeed in our goal of creating a Gaussian mode profile, the lower the amount of wavevector components around $k_\parallel = 0$, which corresponds to normal incidence [87, 99]. It is possible to preferentially increase the wavevector components around $k_\parallel = 0$ by introducing a modulation of the photonic crystal structure with a period that is twice as large as the photonic crystal period $a$ [100, 101]. This technique, also called "band folding" because it folds part of the photonic band structure back toward $k_\parallel = 0$, works by effectively introducing an outcoupling grating inside the structure itself. To obtain large in- and outcoupling efficiencies $\eta_{\mathrm{in}}$ and $\eta_{\mathrm{out}}$ in a cavity with low total optical losses $\kappa$, it is best if the optical losses are as low as possible before the introduction of the double-period modulation, such that the extra losses due to the band folding can easily become a large fraction of the total optical losses. We im-

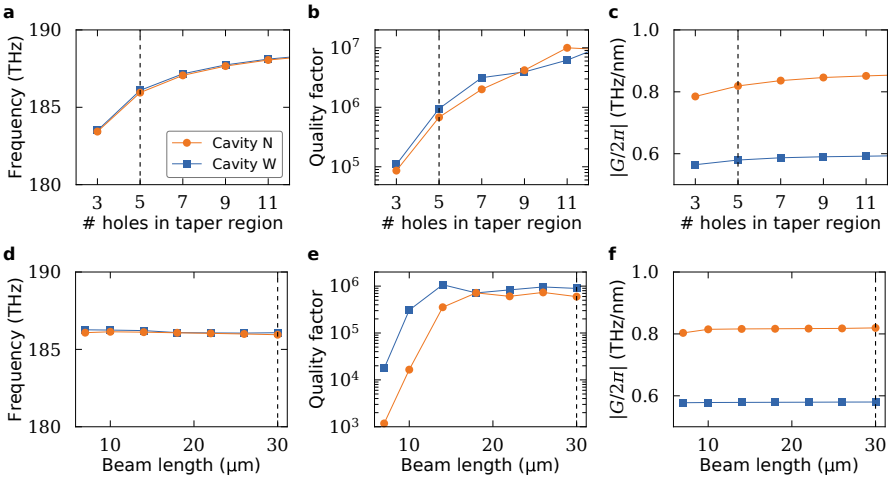


Figure 3.12: Simulated cavity parameters of tapered cavity designs. Panels (a)–(c) show parameters of nanobeam cavities with a total length of $30\,\mu\mathrm{m}$, with a varying number of holes in the taper region on each side of the cavity location. The total number of holes in the nanobeam on each side of the cavity location is 26 or more. For panels (d)–(f), the taper region was chosen to have five holes, and the total beam length was varied. The resonance frequency (a,d) and optical quality factor (b,e) were extracted from a single simulation, while $G = -\partial\omega_c/\partial x$ (c,f) was estimated by simulating the cavity twice, with and without a displacement of $1\,\mathrm{nm}$ along the full length of the beam. The largest difference in performance between the two sets of design parameters "Cavity N"/"Mirror N" (orange circles) and "Cavity W"/"Mirror W" (blue squares) is seen in the position dependence $G$ (panels (c) and (f)).

plement double-period modulation in our tapered defect cavities by alternatingly increasing and decreasing the hole widths $h_t$ and $h_s$. Figures 3.13a and 3.13b show simulated field profiles for structures using $5\,\%$ and $15\,\%$ of modulation, respectively. While these field profiles still strongly resemble the field profiles without double-period modulation, the effect can be seen from the Fourier transform of the field profiles along the beam, shown in fig. 3.13c. For successively higher double-period modulation, the wavevector components at $k_{\|} = 0$ significantly increase. For comparison, we also show the Fourier transform of the field profile for the simple defect cavity of section 3.3.2, which indeed has a larger relative fraction of its wavevector components above the light line ($k_{\|} < k_0$).

Like before, we perform several simulations to obtain the cavity parameters, here as a function of the double-period modulation. The results are shown in fig. 3.14. As expected, increased double-period modulation leads to higher optical losses and thus to a decrease in the optical quality factor. The optical frequency and sensitivity to motion are hardly affected. We also extracted far-field radiation profiles from the numerical simulations, which are visualized in fig. 3.15. These profiles confirm that the double-period modulation leads to a relative increase of radiation at normal incidence (corresponding to the center of the color maps). If we assume all the extra losses due to double-period modulation are ra-

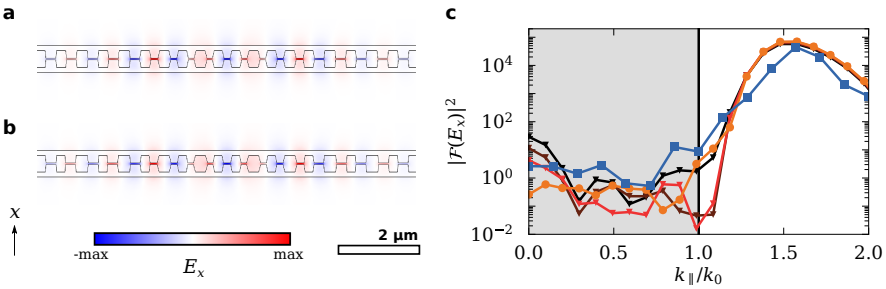


Figure 3.13: (a),(b) Simulated transverse electric field profiles of five-hole tapered cavities with dimensions "Cavity N"/"Mirror N" (see table 3.1), additionally modified with double-period modulation of (a) $5\,\%$ and (b) $15\,\%$. The double-period modulation alternatingly increases and decreases the hole width ($h_t$ and $h_s$) by the specified percentage. (c) Fourier transform of the normalized electric field profile along the middle of the beam (in the gap). $k_0$ is the wavevector at the light line for light with a frequency of $190\,\mathrm{THz}$. Blue squares: simple defect cavity with dimensions "Mirror D" (see fig. 3.11a); orange circles: five-hole tapered cavity with dimensions "Cavity N"/"Mirror N" (see fig. 3.11b); red, brown and black triangles: the same design, modified with respectively $5\,\%$, $10\,\%$ and $15\,\%$ double-period modulation. The double-period modulation clearly adds extra field components at $k_\parallel = 0$.

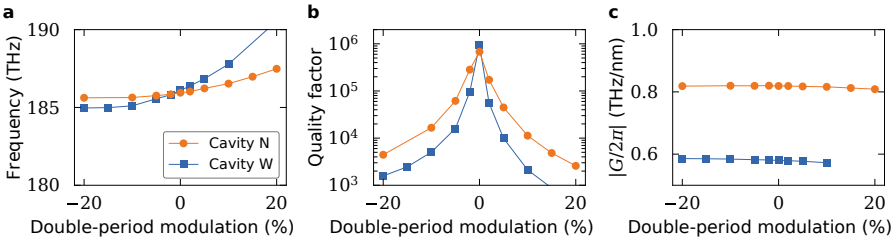


Figure 3.14: Simulated cavity parameters of five-hole tapered cavity designs with a varying amount of double-period modulation—negative numbers correspond to starting with decreasing the hole size of the first hole instead of increasing it. The nanobeams were $30\,\mu\mathrm{m}$ long. The resonance frequency (a) and optical quality factor (b) were extracted from a single simulation, while $G = -\partial\omega_c/\partial x$ (c) was estimated by simulating the cavity twice, with and without a displacement of $1\,\mathrm{nm}$ along the full length of the beam. The double-period modulation clearly has a large effect on the optical quality factor (b), while hardly affecting the frequency and position dependence of the cavity mode.

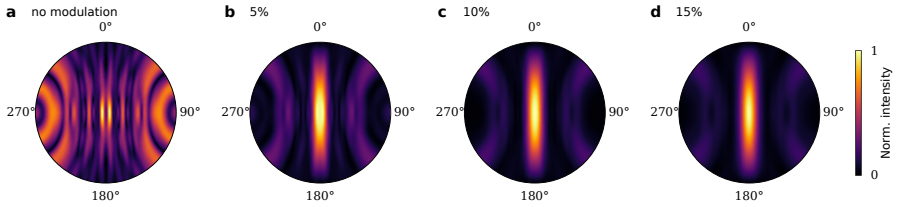


Figure 3.15: Simulated far-field radiation patterns of a five-hole taper cavity with dimensions "Cavity N"/"Mirror N", unmodified (a) and modified by a double-period modulation of (b) $5\,\%$, (c) $10\,\%$ and (d) $15\,\%$. In these images, the points furthest "East" and "West" in each circle (respectively labeled $90°$ and $270°$) represent (near-)horizontal emission along the axis of the nanobeam, while the "North" and "South" points ($0°$ and $180°$) represent (near-)horizontal emission perpendicular to the nanobeam. The point in the center represents emission straight up, normal to the substrate surface, which is the direction that can be most efficiently collected in the setup geometry we use.



diated within the numerical aperture of our detection system, the structure with $5\,\%$ double-period modulation, which has a quality factor almost ten times lower than the structure without double-period modulation, should have a coupling efficiency of approximately $\eta = 45\,\%$. In the implementation by Tran *et al.* [100], the simulated coupling efficiency of a (non-sliced) photonic crystal nanobeam was improved to at least $\eta = 20\,\%$. In a recent publication by Rousseau *et al.* [101], a more than tenfold improvement of the experimentally detected intensity was realized by implementing double-period modulation of the sidewalls, while the total quality factors of the modes were still dominated by scattering due to fabrication imperfections. Therefore we expect a similar improvement of the outcoupling efficiency, even if the experimentally measured optical linewidths are not affected by the double-period modulation.

## 3.4. Fabrication of sliced nanobeams

To create the designed sliced nanobeam structures, we use well-established nanofabrication processes. Nevertheless, creating free-standing structures with extremely small gaps is challenging, requiring careful optimization. We first describe the fabrication steps and then discuss the challenges that remain in the fabrication process.

### 3.4.1. Overview

The fabrication process is shown schematically in fig. 3.16. Here we describe the steps individually.

**Substrate preparation**

The sample is a piece of a silicon-on-insulator wafer (SOITEC), which consists of a thin layer of silicon ($\sim 200\,\mathrm{nm}$) on top of a thicker layer of oxidized silicon ($\sim 1\,\mu\mathrm{m}$), on top of a thick silicon substrate ($\sim 500\,\mu\mathrm{m}$). In this thesis, we used two types of SOI substrate, one with thicknesses $200\,\mathrm{nm}$ and $1\,\mu\mathrm{m}$, and one with

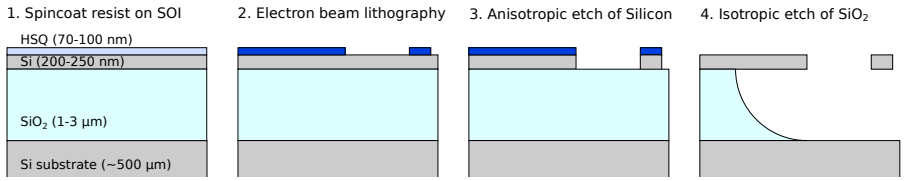


Figure 3.16: Schematic representation of the fabrication process used to create sliced nanobeams. The diagrams show a cross section of the sample, with materials and thicknesses indicated in the leftmost panel (SOI: silicon-on-insulator; HSQ: hydrogen silsesquioxane). (1,2) The desired pattern is created in the HSQ resist mask by electron beam exposure and subsequent removal of the unexposed resist. (3) This pattern is then transferred to the top silicon layer of the silicon-on-insulator using reactive ion etching. (4) Finally, the sacrificial oxide layer as well as the remaining resist is etched away by wet etching with hydrogen fluoride (HF), followed by critical point drying to prevent the sliced nanobeam from sticking together due to capillary forces in the drying process.

thicknesses $250\,\mathrm{nm}$ and $3\,\mu\mathrm{m}$, respectively for the device layer and buried oxide layer. The thicker buried oxide layer in principle allows creating optical cavities with lower losses, since the evanescent field of the cavity mode that overlaps with the high-index substrate has decayed more if it is further away from the cavity.

A thin layer ($70\,\mathrm{nm}$ to $100\,\mathrm{nm}$) of hydrogen silsesquioxane (HSQ) (FOX-15, Dow Corning) is spincoated to be used as an electron beam resist [102]. Since the sensitivity of HSQ goes up, while the achievable resolution goes down, if the HSQ is left to "age" on the sample before the electron beam exposure [103], we made sure to spincoat a fresh layer of HSQ within a few hours of loading the sample into the electron beam lithography system.

**Electron-beam lithography**
The HSQ works as a negative resist, as the electron exposure crosslinks the material which reduces its solubility [102]. After exposure with an electron beam lithography system (Raith e-Line) at an acceleration voltage of $30\,\mathrm{kV}$, the unexposed resist is dissolved using a solution of $25\,\%$ tetramethylammonium hydroxide (TMAH) at $50\,^{\circ}\mathrm{C}$. The exposed HSQ resist forms a type of silicon oxide, which can act as an etch mask for etching of the silicon layer.

**Anisotropic etching of silicon**
To transfer the pattern in the resist mask to the silicon layer, reactive ion etching assisted by an inductively coupled plasma is employed. In this thesis, we used two different processes. The first devices were fabricated using an etch process with $SF_6/O_2$ gases (Oxford Plasmalab 80), where we optimized the process parameters for anisotropy and selectivity [104, 105]. Later devices were created using a main etch step with $HBr/O_2$ gases preceded by a short breakthrough etch with $Cl_2$ gas (Oxford PlasmaPro 100) [106–108]. This process has a very high selectivity for etching silicon over silicon oxide, which allows using a thinner layer of resist.

**Isotropic etching of oxide and critical point drying**
The sacrificial oxide layer as well as the leftover resist are removed by a wet etch using a solution of $20\,\%$ hydrogen fluoride (HF). Passivation layers deposited

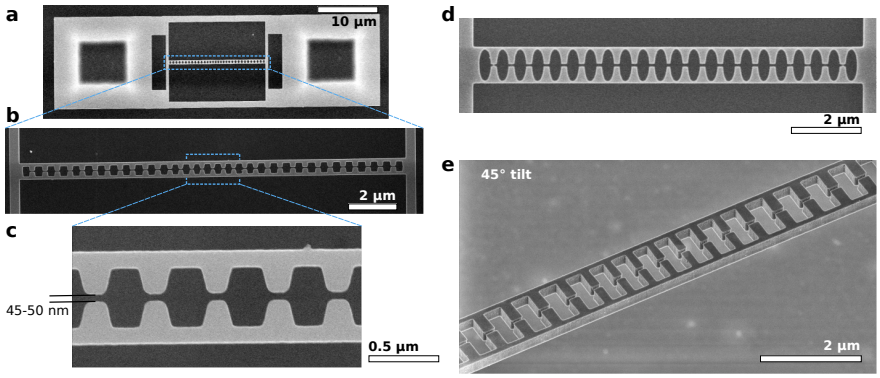


Figure 3.17: Electron microscope images of successfully fabricated sliced nanobeam devices. Panels (a)–(c) show the same structure (parameters based on "cavity N") at different levels of magnification. In (a), the dark squares show the outline of the supporting pillars connecting the mostly freestanding structure to the substrate. (d) Structure according to parameters "mirror D". (e) Image taken with the sample tilted by $45°$. Acceleration voltages: (a) $10\,\mathrm{kV}$; (b) $20\,\mathrm{kV}$; (c) $10\,\mathrm{kV}$; (d) $5\,\mathrm{kV}$; (e) $1\,\mathrm{kV}$. Device thickness: (a)–(c),(e): $250\,\mathrm{nm}$; (d) $200\,\mathrm{nm}$. Silicon etch process: (a)–(c),(e) $Cl_2$,HBr/$O_2$; (d) $SF_6/O_2$.



during the etching process are also removed by the HF. The sample is dried using a $CO_2$ supercritical point drying process (Tousimis Autosamdri-815), to avoid capillary forces associated with normal drying, which can result in the two half-beams sticking together or even collapsing to the substrate.

### Results

Figure 3.17 shows scanning electron microscope images of successfully fabricated sliced nanobeams. In fig. 3.17a, the supporting structure for the sliced nanobeam can be seen. The connector beams parallel to the sliced nanobeam decrease the compressive stress on the nanobeam, further reduced by the transverse connections of the nanobeam to its support pad. The acceleration voltage of $10\,\mathrm{kV}$ penetrates the device layer enough that the interface of the support pad with the oxide pillar supporting it can be seen as a dark square outline. As the higher magnification images in figs. 3.17b and 3.17c show, we achieve faithful reproduction of the design geometry, with gap distances between the teeth of $45\,\mathrm{nm}$ to $50\,\mathrm{nm}$. Figure 3.17d shows a sliced nanobeam fabricated using the earlier version of the fabrication process. For this structure, the connectors parallel to the nanobeam were not present, leading to a higher amount of compressive stress. The gap size achieved here was approximately $60\,\mathrm{nm}$. The development of the newer version of the fabrication process was largely documented in the Master's thesis by Freisem [97], who also implemented the first sliced nanobeam cavities with a tapered design, one of which is shown in fig. 3.17e.

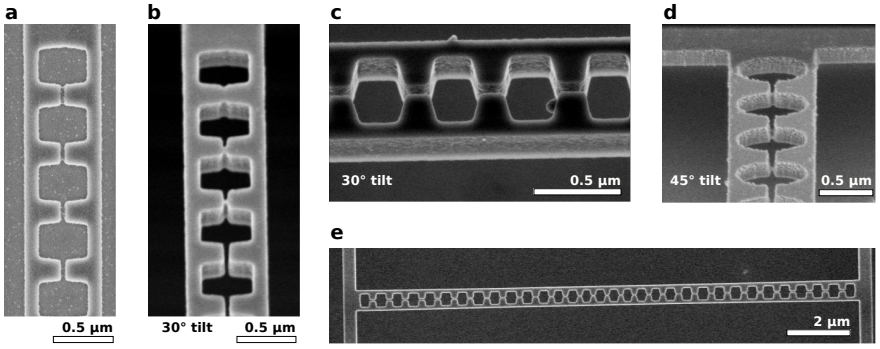


Figure 3.18: Electron microscope images illustrating challenges in fabrication. Panels (a) and (b) show the same structure at different stages in the fabrication process. (a) HSQ resist after exposure and development. Careful inspection of the image shows small "bridges" connecting across the upper three gaps between the teeth. In (b), the structure is shown at the end of the fabrication process. The "bridges" in the resist have been transferred to the silicon, where the gap between the teeth has not been fully opened in the upper three gaps. This image was taken with the sample tilted by $30°$. (c) Two nanoscale particles are present on the finished structure. Such particles were found on multiple structures and samples, but their origin remains unknown. (d) Tilted image of a finished nanobeam using the first version of the fabrication process, which shows high sidewall roughness. (e) Overview image of a sliced nanobeam which is stuck together in the middle, despite critical point drying (note the open gaps at the ends of the beam). Acceleration voltages: (a)–(c),(e) $2\,\mathrm{kV}$; (d) $1\,\mathrm{kV}$. Device thickness: (a)–(c),(e) $250\,\mathrm{nm}$; (d) $200\,\mathrm{nm}$. Silicon etch process: (a)–(c),(e) $Cl_2$,HBr/$O_2$; (d) $SF_6/O_2$.



## 3.4.2. Challenges

The fabrication process poses limitations on the geometries we can achieve. We list the main challenges, related to the specifics of the sliced nanobeam structures.

**Small gap size in electron beam lithography**

The gap sizes we achieve between the teeth of the nanobeam are mainly limited by proximity effects in the electron beam lithography step. We can conclude this on the basis of direct inspection of the etch mask using a scanning electron microscope, comparing it with the final results on the same structure after the full fabrication process. Such a set of "before" and "after" images is shown in figs. 3.18a and 3.18b. Near the support pads, at the end of the nanobeam, the background exposure of the resist is higher due to the proximity of these large exposed areas. This triggers small connections of exposed resist to form in the gap between the teeth of the nanobeam, which can (barely) be seen in fig. 3.18a. Despite the fact that these resist "bridges" are not the same thickness as the rest of the exposed resist, the selective etch process can transfer these to the silicon, where similar connections remain across the gap, or even merging teeth together entirely, as shown in fig. 3.18b. With smaller gap widths in the design, this issue becomes rapidly worse, such that soon all teeth are connected and no gap remains.

To mitigate this issue, it could be useful to decrease the thickness of the resist layer, thus requiring lower exposure doses which reduces the proximity effect.

Using profilometer measurements, we estimate that up to $50\,\mathrm{nm}$ of the resist layer remains after the silicon etch step with $Cl_2$ and $HBr/O_2$. This would suggest the resist layer can be made up to two times thinner without being eroded away by the silicon etch process. Another possibility would be to use an electron beam lithography tool with a higher acceleration voltage than $30\,\mathrm{kV}$, which creates a more evenly distributed background exposure due to the larger penetration depth and scattering length of the higher-energy electrons. Finally, locally changing the exposure of features likely to suffer from proximity effect can be implemented using proximity correction algorithms.

Ultimately, the feature size is limited by the molecular structure of the resist. For the fabrication of lines, in HSQ resist feature sizes down to sub-$10\,\mathrm{nm}$ have been demonstrated [109]. Small gap sizes in the more complicated sliced nanobeam structure is more complicated to achieve, but careful optimization and using the techniques mentioned above should allow reaching gap sizes even smaller than the current values of $45\,\mathrm{nm}$ to $50\,\mathrm{nm}$.



**Smooth, selective and anisotropic etching of silicon**

In fig. 3.18c, the surface quality of the silicon structure after etching can be judged from the high-magnification, low-acceleration-voltage electron microscope image, taken with the sample tilted by $30°$. Surface roughness is associated with optical losses through scattering, and the losses of optical ring resonators have even been used to demonstrate the smoothness of the $HBr/O_2$ etching recipe in the literature [106]. At the same time, this process achieves a high selectivity, leaving up to $50\,\mathrm{nm}$ of an initial resist layer of $80\,\mathrm{nm}$ thickness behind while etching $250\,\mathrm{nm}$ of silicon. The angle of the etched sidewalls can be tuned for example by changing the gas composition [108] or the temperature at which the process is performed [97], without much effect on the selectivity or roughness.

The high selectivity of the $HBr/O_2$ process leads to the fact that any small irregularities at the resist edge, even with very low thickness, are transferred to the silicon as well, leading to vertical irregularities in the sidewalls. To prevent this, we lengthened the "breakthrough" $Cl_2$ etch step, which is less selective and is responsible for the bulk of the erosion of the HSQ etch mask. The longer breakthrough step also etches a substantial amount of silicon, possibly accounting for the slightly larger roughness in the upper part of the sidewalls seen in fig. 3.18c. Alternatively, one could try to address the resist roughness by changing the pre- and post-exposure resist processing [110].

Another feature that can be observed in fig. 3.18c is the presence of two particles with a diameter of several tens of nanometer. These were sometimes found after the HF etch step, but we were not able to determine their origin. Possible sources are partially etched pieces of silicon from parts of the sample where our resist mask was underexposed and eroded away during the etch process, or inclusions in the oxide layer of the SOI substrate which the HF etch step did not dissolve.

Figure 3.18d shows a structure created with the earlier version of the fabrication recipe with $SF_6/O_2$ gases, which was optimized for selectivity and anisotropy

[105]. Using this fluoride-based chemistry, smooth and anisotropic etching of silicon has been reported, usually by cooling the substrate significantly. This option was not available on the machine we used, resulting in a compromise. As can be seen in this electron microscope image, the sidewall roughness using this process was very large.

**Free-standing structures with low stiffness**
The sliced nanobeam structures we create are strongly affected by compressive stress, present in the device layer of SOI wafers [66, 111]. To alleviate this, we designed the support structure shown in fig. 3.17a, with transverse connections at the ends of the nanobeam [112], used for all structures shown in chapters 4 to 6, and separate supporting beams parallel to the nanobeam, used for the structures shown in chapters 5 and 6. Nevertheless, despite the supercritical point drying, some of the beams would be stuck together as shown in fig. 3.18e. We note that when inspecting the finished nanobeams with a scanning electron microscope, charge accumulating in the device layer causes the two half-beams to repel each other, possibly damaging the nanobeam. This could mostly be avoided by using low currents and ensuring the field of view excluded most of the support structure.



## 3.5. Conclusion

The sliced nanobeam design allows simultaneously reaching high optomechanical coupling rates and low optical losses, with simulated values up to $|G|/2\pi = 0.8\,\mathrm{THz\,nm^{-1}}$ and $Q > 10^5$ in current designs, while double-period modulation provides a method to improve the coupling efficiency to values of potentially larger than $20\,\%$. We have presented design guidelines and optimization strategies to achieve this, as well as the fabrication method used to realize the designs, along with its current limitations. Further improvement of the designs is expected using similar methods by identifying the factors limiting the optical losses, which allows a more informed choice for the starting point in parameter space. Alternatively, a computational optimization [44, 96] could be performed to explore different cavity designs without the heuristic design method employed here. The optimized designs presented in this chapter could in that case be used as starting points, and the insights from the heuristic method could be used to constrain the search space for the optimization.

Two recent publications by Hu & Weiss [113] and by Choi, Heuck & Englund [114] took the principle of using a small gap to create field confinement a step further and showed that by using “bow-tie” shapes in a photonic crystal nanobeam, extremely small mode volumes can be created. Combining such structures with the strategy of extreme field confinement at the positions where mechanical motion has the strongest influence might lead to improved optomechanical coupling rates for high-frequency mechanical resonances (in the gigahertz range).

# 4

# Large optomechanical interactions in a sliced photonic crystal nanobeam

*Coupling between mechanical and optical degrees of freedom is strongly enhanced by using subwavelength optical mode profiles. We realize an optomechanical system based on a sliced photonic crystal nanobeam, which combines such highly confined optical fields with a low-mass mechanical mode. Analyzing the transduction of motion and effects of radiation pressure we find that the system exhibits a photon-phonon coupling rate* $g_0/2\pi \approx 11.5\,\mathrm{MHz}$*, exceeding previously reported values by an order of magnitude. We show that the large optomechanical interaction enables detecting thermal motion with detection noise below that at the standard quantum limit, even in broad bandwidth devices, important for both sensor applications as well as measurement-based quantum control.*

This chapter is based on Leijssen, R. & Verhagen, E. Strong optomechanical interactions in a sliced photonic crystal nanobeam. *Scientific Reports* **5,** 15974 (2015) [70].

## 4.1. Introduction

The motion of a mechanical resonator can be read out with extreme sensitivity in a suitably engineered system whose optical response is affected by the displacement of the resonator. The resultant coupling between optical and mechanical degrees of freedom also gives rise to a radiation pressure force that enables actuation, tuning, damping, and amplification of the resonator, with applications ranging from classical information processing to quantum control of macroscopic objects [7, 115]. Such control can be established either passively, by employing the intrinsic dynamics of the system [13, 15, 26], or actively, by using the outcome of displacement measurements [8]. Fast, sensitive measurement of nanomechanical displacement can as such be used for optical cooling [8, 27], squeezed light generation [17], quantum non-demolition measurements [25, 116] and enhancing sensor bandwidth [117, 118].

In a cavity optomechanical system, which has an optical resonance frequency $\omega_c$ that depends on the position of a resonator, both the sensitivity of a displacement measurement and the magnitude of effects caused by radiation pressure forces are governed by two parameters: on the one hand the strength with which acoustic and optical degrees of freedom interact, expressed as the magnitude of the resonator's influence on the frequency $\omega_c$, and on the other hand the cavity linewidth $\kappa$. The interaction strength is characterized at the most fundamental level by the vacuum optomechanical coupling rate $g_0$ introduced in section 1.2.1, as it appears in the optomechanical interaction Hamiltonian eq. (1.4).

Per photon in the cavity, the effective optomechanical measurement rate [17, 27], as well as the radiation-pressure induced alteration of a resonator's frequency and damping through dynamical backaction, scale with $g_0^2/\kappa$. Improving this ratio is thus desirable for more sensitive measurements and for better optical control of the mechanical resonator. Decreasing the optical damping $\kappa$ to a low value has been very fruitful, but can present several drawbacks as well: narrow linewidths place stringent demands on excitation sources and fabrication tolerances, and make integration of many devices, for example in practical sensor arrays, difficult. Moreover, dynamical instabilities and nonlinear linewidth broadening limit the number of photons with which a high-$Q$ cavity can be populated. Finally, several schemes for measurement and control in fact rely on fast, broadband optical response [41, 115, 119].

In this chapter, we show that optomechanical coupling rates can be significantly enhanced by using photonic modes with subwavelength confinement. We realize a sliced photonic crystal nanobeam in which light is highly confined in a nanoscale volume near the moving dielectric interfaces of a low-mass resonator, leading to unprecedented interaction strengths. We use a simple free-space optical setup to address the structure and demonstrate optical tuning of the mechanical resonance frequency, as well as sensitive readout of mechanical motion. The observed optical forces and measurement sensitivity provide us with two independent ways to determine the vacuum coupling rate to be $g_0/2\pi \approx 11.5\,\mathrm{MHz}$. We demonstrate displacement readout with a detection imprecision below that at the standard quantum limit, that is, with a noise level that is comparable to the quan-

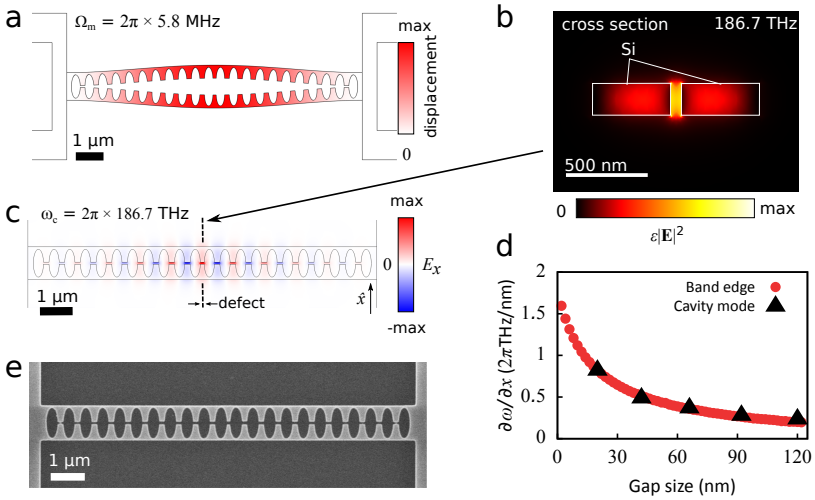


Figure 4.1: Resonances and geometry of the sliced nanobeam. (a) Simulated displacement profile of the fundamental (in-plane) mechanical resonance of the structure. (b) Cross section in the center of the sliced nanobeam (indicated by the dashed line in c), showing the simulated energy density distribution of the fundamental optical cavity mode of the structure. (c) Simulated transverse electric field profile of the fundamental optical cavity mode of the structure. (d) Simulated frequency shift as a result of an outward displacement of 1 nm. The cavity mode shift was determined by simulating the full nanobeam and introducing a uniform displacement along the beam. (e) Electron micrograph of a fabricated device. The thickness of the structure is 200 nm, both in the simulations and in the fabricated device.

tum fluctuations of the resonator. We achieve this using only 22 µW of detected power even in a system with modest optical and mechanical quality factors. The operation with a relatively large cavity bandwidth is especially attractive for system integration and miniature sensor technologies as well as measurement-based control in nano-optomechanical systems.

## 4.2. Results

### 4.2.1. Working principle

A displacement-induced frequency shift of an optical mode depends on the fraction of the energy density that is located near the moving dielectric boundaries [56]. Therefore, to realize a large photon-phonon coupling rate $g_0 = Gx_{\mathrm{zpf}}$, the optical cavity mode should be localized at the positions where it is most influenced by the motion of the mechanical resonator. Crucially, it is most important to optimize the optical confinement along the directions in which the mechanical mode is also strongly localized.

We study sliced photonic crystal nanobeams as introduced in chapter 3. The fundamental in-plane mechanical resonance of the sliced nanobeam is shown in fig. 4.1a. The small width (80 nm) of the narrowest parts of the half-beams ensures both the mass ($\approx$ 2.4 pg) and the spring constant of the nanobeam are small,

leading to large zero-point fluctuations $x_{\mathrm{zpf}}$.

To enable confinement along the length of the beam, we introduce a periodic patterning. This creates a photonic crystal, with a quasi-bandgap for transverse electric (TE) polarized modes guided by the beam (see section 3.3). The waveguide mode at the lower edge of the bandgap is strongly confined in the nanoscale gap separating the two half-beams (fig. 4.1b). We introduce a simple defect in the photonic crystal by only reducing the width of the central pair of 'teeth'. This creates confined cavity modes with a frequency in the bandgap that are derived from the desired waveguide mode (fig. 4.1c).

Like the mechanical mode, the field profile of the lowest-order optical cavity mode extends along the beam, but importantly is highly confined perpendicular to the motion (figs. 4.1b and 4.1c). The truly subwavelength character of the transverse confinement is revealed by calculating the effective *mode area* of the waveguide mode it is derived from. We define the mode area as $A = \int \mathrm{d}V\, W(\mathbf{r})/(aW_{\mathrm{max}})$, where the energy density $W(\mathbf{r}) = \varepsilon(\mathbf{r})|\mathbf{E}(\mathbf{r})|^2$ has its maximum $W_{\mathrm{max}}$ just at the vacuum side of the gap boundary, and we integrate over a full unit cell with period $a$. The mode area is only $2.38 \times 10^{-14}\,\mathrm{m}^2$ for a gap width of $60\,\mathrm{nm}$, or in other words $A = 0.011\lambda^2$, with $\lambda$ the wavelength in vacuum. In fact, it is even eight times smaller than the squared wavelength *in silicon*, even though the maximum energy density is actually localized in the vacuum gap (fig. 4.1b). This subwavelength mode area is essential to the sliced nanobeam and makes it stand out with respect to other designs, including the related double-beam 'zipper' cavity [16, 17, 42, 120], where the optical cavity modes of two photonic-crystal nanobeams are coupled by placing the beams close together.

Numerical simulations confirm that the frequency of both the band edge and the defect cavity mode derived from it respond strongly to a displacement of the two half-beams, reaching $G = -\partial\omega_{\mathrm{c}}/\partial x \approx -2\pi \times 0.4\,\mathrm{THz\,nm^{-1}}$ for a gap width of $60\,\mathrm{nm}$ (fig. 4.1d). As expected, this value increases for smaller gap sizes $d$, due to an increase of the fraction of the energy in the gap [56, 82, 83]. We define the displacement coordinate as $x = (d - d_0)/2$, where $d_0$ is the equilibrium gap size, such that $x$ can be directly related to the maximum lab-frame displacement of the antisymmetric mechanical mode depicted in fig. 4.1a. Note that the choice of the definition of $x$ is in principle arbitrary (with a properly matched definition of $m_{\mathrm{eff}}$), whereas the coupling rate $g_0$ is independent of this definition. To determine the optical frequency shift, the entire half-beams are displaced in the simulation. The displacement of the actual mechanical mode is not uniform along the beam (fig. 4.1a), meaning that due to the finite extent of the optical mode the value of $G$ will be slightly reduced. Taking into account the optical and mechanical mode profiles (figs. 4.1a and 4.1c), we estimate it to be $0.90$ times the value shown in fig. 4.1d (see section 3.3.2).

Using standard lithography techniques (see section 3.4 and section 4.5.1), we realize free-standing sliced nanobeams in silicon with a thickness of $200\,\mathrm{nm}$ and a length of $11\,\mu\mathrm{m}$, separated by an average gap size of $60\,\mathrm{nm}$. The full set of design parameters for the periodic part of the structure is listed in table 3.1 under "Mirror D". An electron micrograph of a fabricated device is shown in fig. 4.1e.

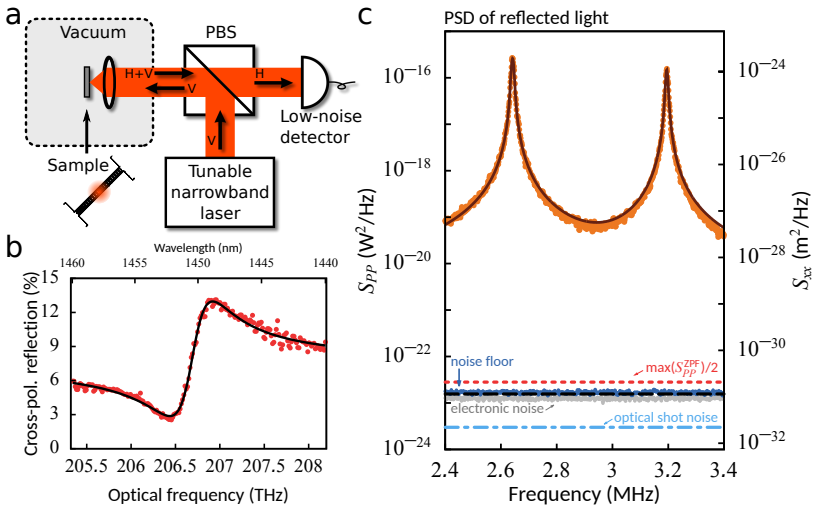


Figure 4.2: (a) Schematic diagram of the free-space readout method (PBS: polarizing beamsplitter; H,V: horizontally and vertically polarized light). See section 4.5.2 for more details. (b) Reflection spectrum (red data points) and fit with a Fano lineshape (black line). (c) Power spectral density of the reflected light obtained with the laser frequency on-resonance with the cavity (orange data points), and a fit of the two mechanical resonances (brown line). The noise floor (blue data points) was obtained by reflecting the laser light from the unpatterned substrate and matching the intensity on the detector. The black dashed line is the sum of the measured electronic noise (gray data points) and the optical shot noise calculated from the intensity on the detector (light blue dash-dotted line). The red dotted line shows the peak value of $S_{PP}^{\mathrm{zpf}}/2$ for the lowest-frequency resonance, which we obtained from the fit of the measured thermal spectrum via the relation $S_{PP}^{\mathrm{zpf}}(\Omega_{\mathrm{m}})/2 = S_{PP}^{\mathrm{th}}(\Omega_{\mathrm{m}})\hbar\Omega_{\mathrm{m}}/4k_{\mathrm{B}}T$.



### 4.2.2. Free-space readout

We address our structure using a simple reflection measurement, schematically shown in fig. 4.2a. The employed resonant scattering technique [121] places the sample between crossed polarizers to allow the detection of light scattered by the cavity mode (whose dominant polarization is oriented at $45°$ to the polarizers) while suppressing light reflected by the substrate to significantly below $1\,\%$. By scanning the frequency of a narrow-band laser we record the reflection spectrum, depicted for one of the samples in fig. 4.2b. The dispersive lineshape is caused by interference of the resonant scattering of the cavity with nonresonant scattering by the nanobeam. The cross-polarized reflectance $R$ is described by eq. (1.15). Fitting it to the reflection spectrum yields the center frequency $\omega_{\mathrm{c}}$ and linewidth $\kappa$ of the cavity, as well as a value for $\eta \equiv \sqrt{\eta_{\mathrm{in}}\eta_{\mathrm{out}}}$, where $\eta_{\mathrm{in}}$ and $\eta_{\mathrm{out}}$ denote the optical in- and outcoupling efficiencies. We determine $\eta \approx 0.29$ and the optical quality factor $Q_{\mathrm{opt}} = \omega_{\mathrm{c}}/\kappa \approx 400$. Based on the large measured coupling efficiency, for these structures a non-cross-polarized measurement would likely have yielded good results as well (see section 4.5.2). The measured $Q_{\mathrm{opt}}$ is two to three times lower than the simulated one, a discrepancy that we attribute to fabrication imperfections.

Thermal motion of the nanobeam $\delta x$ modulates the cavity frequency by

$\delta\omega_c = (\partial\omega_c/\partial x)\delta x$. This produces a change in detected power proportional to the derivative of the reflection spectrum: $\delta P = P_{in}(\partial R/\partial\omega_c)\delta\omega_c$. Here we assumed the intracavity amplitude is instantaneously affected by the mechanical motion, which is justified since $\Omega_m \ll \kappa$ (see section 1.5.4 for the more general case). Thus, the power spectral densities of $x$ and $P$ are related as

$$\begin{aligned} S_{PP}(\Omega) &= P_{in}^2 \left(\frac{\partial R}{\partial \omega_c}\right)^2 \left(\frac{\partial \omega_c}{\partial x}\right)^2 S_{xx}(\Omega) \\ &= 4P_{in}^2 \left(\frac{\partial R}{\partial u}\right)^2 \frac{g_0^2}{\kappa^2 x_{zpf}^2} S_{xx}(\Omega), \end{aligned} \tag{4.1}$$

where $u \equiv 2\Delta/\kappa = 2(\omega_L - \omega_c)/\kappa$ is the relative detuning between the laser frequency and the cavity resonance.

Figure 4.2c shows the detected spectral density $S_{PP}$ for the laser tuned to the optical resonance frequency, with a relatively high optical power incident on the sample ($P_{in} = 367\,\mu W$), corresponding to a detected power of $22\,\mu W$. Because of the linear relation between $S_{PP}$ and $S_{xx}$ shown in eq. (4.1), this is a direct measurement of the spectrum of thermal motion in the nanobeam.

The two peaks at $2.6\,MHz$ and $3.2\,MHz$ correspond to the two fundamental in-plane modes of the coupled halves of the nanobeam. For a perfectly symmetric structure, the (weak) coupling leads to two eigenmodes: a common mode, for which the half-beams move in phase and their separation $d$ is not affected, and a differential mode, for which antiphase movement of the half-beams results in maximal variation of $d$. Fabrication-related imperfections can break the symmetry of the system, such that the actual normal modes have displacement profiles $\mathbf{U}_{\alpha,\beta}$ that are linear combinations of those of the half-beam eigenmodes $\mathbf{U}_{1,2}$ [74]: $\mathbf{U}_\alpha = A_\alpha(\mathbf{U}_1 \sin\theta - \mathbf{U}_2 \cos\theta)$ and $\mathbf{U}_\beta = A_\beta(\mathbf{U}_1 \cos\theta + \mathbf{U}_2 \sin\theta)$, where $\theta$ can in principle take any value. As we show in section 4.5.1, the frequencies of these mixed modes $\Omega_m^{\alpha,\beta}$ are reduced with respect to the simulated value of $6\,MHz$ due to the presence of compressive stress in the studied sample, which also enhances the splitting between the two mode frequencies. Since the two modes generally affect the separation $d$ differently, they have different photon-phonon coupling rates $g_0$, which are maximal for a purely differential mode ($\theta = \pi/4$). With our definition $x = (d - d_0)/2$, this is reflected in the fact that the ratio between the zero-point fluctuation amplitudes of the normal modes is $x_{zpf}^\alpha / x_{zpf}^\beta = [\Omega_\beta(1 + \sin 2\theta)/\Omega_\alpha(1 - \sin 2\theta)]^{1/2}$ (see section 3.2.3). The variance in $x$ due to thermal motion in the two modes is set by the equipartition theorem, taking into account this difference in $x_{zpf}$. The ratio between the areas of the two resonance peaks in the experimental spectrum of $S_{PP}$ therefore directly yields the mixing angle $\theta$.

In fact, fitting two resonant modes to the displacement spectrum also allows determining the transduction factor that relates the measured optical power spectral density $S_{PP}$ to the displacement spectrum $S_{xx}$. To do so, we calculate the thermal variance $\langle x^2 \rangle_{th} = 2x_{zpf}^2 \bar{n}_{th}$. We determine $x_{zpf}$ from the measured $\theta$ and from the effective mass of purely antisymmetric motion, which we computed

from the simulated displacement profile to be $m_{\text{eff}} \approx 0.39m$, with $m$ the total mass of the beam. We further assume that the temperature $T$ of the mechanical bath is equal to the lab temperature. The validity of this assumption is tested by performing power- and detuning-dependent measurements presented in section 4.5.4. The resulting scale for the displacement spectral density $S_{xx}$ is shown on the right side of fig. 4.2c. Note that the chosen convention of $x$ allows directly comparing the readout of the two mechanical resonances on this scale.

To determine the sensitivity with which the displacement spectrum of the beam can be read out, we consider the detection noise floor for the measurement shown in fig. 4.2c, which is composed of electronic noise of the photodetector and the optical shot noise of the detected light. Their measured combined imprecision (blue data points in fig. 4.2c) is over seven orders of magnitude smaller than the measured signal.

A general assessment of the sensitivity capabilities of the measurement is made by comparing the detection noise imprecision to the (shot noise) imprecision $S_{xx}^{\text{imp}}(\Omega_{\text{m}})$ of a resonator read out at the standard quantum limit (SQL) [14, 122]. The imprecision at the SQL is equal to half of the spectral density of the zero-point fluctuations $S_{xx}^{\text{zpf}}(\Omega_{\text{m}})/2$, as derived in section 1.5.3. We determine this value from the measured thermal noise spectrum of the lowest-frequency mode via the average phonon occupancy of the mechanical mode $\bar{n}_{\text{th}} = k_B T/\hbar\Omega_{\text{m}}$, and indicate it in fig. 4.2c with the red dotted line. The optical shot noise of the light impinging on the detector, and even the total measurement noise floor, are lower than the imprecision noise at the SQL.

Readout of a nanomechanical resonator with an imprecision below that at the SQL was first achieved in 2009 [14, 122] making use of high-quality optical and mechanical modes. These high quality factors were instrumental because the ability to perform a measurement with SQL-level sensitivity scales, per intracavity photon, with the single-photon cooperativity $C_0 = 4g_0^2/\kappa\Gamma$. This shows it depends on the photon-phonon coupling strength as well as the optical linewidth $\kappa = \omega_{\text{c}}/Q_{\text{opt}}$ and the mechanical linewidth $\Gamma = \Omega_{\text{m}}/Q_{\text{m}}$. The fact that here we achieve a detection noise imprecision below that at the SQL with optical and mechanical quality factors of both less than $500$ attests to the large optomechanical coupling strength, and could have important application in broadband, sensitive nanoscale sensors.



### 4.2.3. Determining the photon-phonon coupling rate

To quantify the optomechanical interaction strength in the fabricated devices, we model the transduction of thermal displacement fluctuations using eq. (4.1) and use it to fit a low-power measurement on a structure for various laser detunings. We do this by calculating the variance of the optical power fluctuations $\delta P$ at the detector resulting from displacement fluctuations $\delta x$ of a mechanical mode with known (thermal) variance. Integrating eq. (4.1) over a single mechanical mode and using our expression for the reflection spectrum $R(u)$ eq. (1.15) (see also

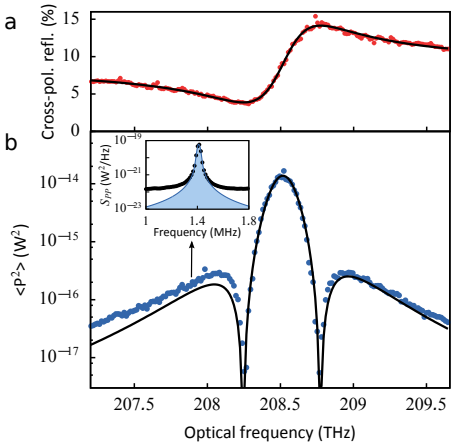


Figure 4.3: Sensitivity of the displacement measurement. (a) Reflection spectrum (red data points) and fit with Fano lineshape (black line) for this particular nanobeam. (b) Detected optical variance in the fundamental mechanical resonance (blue data points) with power incident on the sample $P_{\mathrm{in}} = 8.5\,\mu\mathrm{W}$. The data points were obtained by fitting the fundamental mechanical resonance peak in the measured modulation spectra (inset). The signal originates from thermal motion so it varies only with the sensitivity of the measurement. The black line shows our model, which uses the parameters obtained from the reflection spectrum in (a) and is fitted to the data to determine $g_0/2\pi = 11.5\,\mathrm{MHz}$.

eqs. (1.63) and (1.65)), yields

$$\langle P^2 \rangle = \frac{128 P_{\mathrm{in}}^2 g_0^2 \bar{n}_{\mathrm{th}} \eta^2}{\kappa^2} \frac{\left[2u\eta - 2uc\cos\varphi + (1-u^2)c\sin\varphi\right]^2}{(1+u^2)^4}, \tag{4.2}$$

which is independent of the choice of the displacement coordinate $x$, but does depend on the phase $\varphi$ and amplitude $c$ of the nonresonant reflection.

The measured variance of the optically modulated signal due to the lowest-frequency mechanical mode is shown in fig. 4.3b. The variance is minimal when the derivative of the reflection signal (fig. 4.3a) vanishes. Interestingly, due to the dispersive lineshape the transduction is largest for the laser tuned to resonance. The line shown in fig. 4.3b is a fit of eq. (4.2) to the data, using only $g_0$ as a free fitting parameter (all other parameters having been determined in independent measurements). The corresponding value for $g_0/2\pi$ is $11.5\,\mathrm{MHz}$, which is an order of magnitude larger than previously reported values [11, 12, 15, 17, 19, 42, 44].

To compare this photon-phonon coupling rate to the prediction from our simulation we estimate the zero-point fluctuations of the structure. Using the measured mechanical resonance frequency and the simulated effective mass, we obtain $x_{\mathrm{zpf}} = \sqrt{\hbar/2m_{\mathrm{eff}}\Omega_{\mathrm{m}}} \approx 0.08\,\mathrm{pm}$ for a purely antisymmetric mode. With the simulated frequency response $G$, this yields a prediction of $g_0/2\pi \approx 26\,\mathrm{MHz}$. To take into account the observed asymmetry of the mechanical mode, we should apply a correction factor of $0.76$, based on our knowledge of $\theta$ (see section 3.2.3). This results in an expected value of $g_0/2\pi \approx 20\,\mathrm{MHz}$. We attribute the remaining discrepancy to fabrication imperfections, which could result in a different overlap

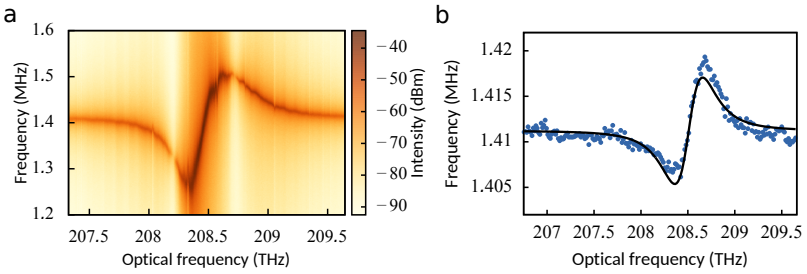


Figure 4.4: (a) Spectrogram showing optical tuning of mechanical resonance frequency with power incident on the sample $P_{\text{in}} = 140\,\mu\text{W}$. (b) Fitted frequency of the fundamental mechanical resonance (blue data points) with $P_{\text{in}} = 8.5\,\mu\text{W}$. The black line shows a fit using the model for optical spring tuning (eq. (1.35)).

of the optical and mechanical modes than simulated. This implies that a further increase of $g_0$ even beyond the measured value is possible. In fact, we expect to be able to improve the fabrication process to produce smaller gaps, which increases the coupling rate significantly (fig. 4.1d). If we for example assume a gap width of $25\,\text{nm}$ and an antisymmetric mode, the simulations predict $g_0/2\pi$ would reach a value as large as $53\,\text{MHz}$.

### 4.2.4. Optical spring tuning

While we tune the laser frequency across the optical resonance a pronounced shift of the mechanical resonance frequency is observed. In fig. 4.4a this is shown for the same structure we studied in fig. 4.3. This well-known optical spring effect was described in section 1.4.2. The equation that describes this behavior in the limit of a large cavity linewidth ($\kappa \gg \Omega_{\text{m}}$), with constant optical input power $P_{\text{in}}$, is given by eq. (1.35). From that equation, we recognize that the optical spring tuning shown in fig. 4.4 provides a second, independent way to characterize the photon-phonon coupling rate. Figure 4.4b shows the center frequency of the mechanical resonance extracted from the same measurement as the variances in fig. 4.3b, as well as a fit using eq. (1.35).

To estimate $g_0$ from this fit we need to know $\eta_{\text{in}}$, which we cannot easily determine as it generally depends on the overlap between the focused Gaussian beam and the cavity mode profile. However, we can find bounds for $\eta_{\text{in}}$ by considering $\eta = \sqrt{\eta_{\text{in}}\eta_{\text{out}}}$, which was determined from the fit to the reflection spectrum. On the one hand we know $\eta_{\text{in}} \leq \eta$, in other words, the collection efficiency is at least as efficient as the overlap with a Gaussian beam, and on the other hand $\eta_{\text{in}} \geq 2\eta^2$, that is, at most half of the light escaping from the cavity can be collected because of the vertical symmetry of the structure. Combining these bounds with the fit of the optical spring effect yields a range for $g_0$ between $10\,\text{MHz}$ and $13\,\text{MHz}$. This range is in good agreement with the value obtained from the analysis of measurement transduction, and moreover both are consistent with the theoretical predictions. Therefore no alternate transduction mechanisms need to be invoked to explain the results. Additionally, the fact that the spring shift can be fully ex-

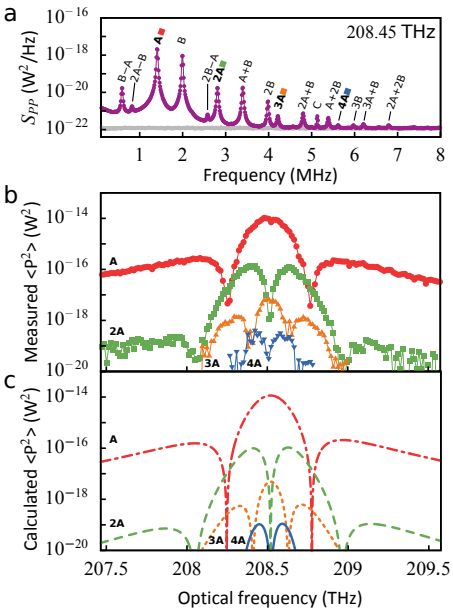


Figure 4.5: Nonlinear transduction. (a) Measured mechanical spectrum of the sliced nanobeam (purple data points), using near-resonant light with power incident on the sample $P_{\mathrm{in}} = 8.5\,\mu\mathrm{W}$. Three peaks A, B and C are mechanical resonances of the nanobeam, all other visible peaks correspond to integer multiples and combinations of frequencies A and B. The electronic noise floor is shown with gray data points. (b) Areas under the peaks corresponding to integer multiples of frequency A, obtained by fitting the peaks in the spectrum. (c) Calculated variance of the reflected signal, using the experimentally obtained parameters.

4

plained by the radiation pressure force as predicted by eq. (1.35) shows that forces due to photo-thermo-elastic effects (see appendix A.3 and ref. [123]) are likely insignificant compared to radiation pressure. We note that further quantification of the individual magnitudes of $\eta_{\mathrm{in}}$ and $\eta_{\mathrm{out}}$ is in principle possible, for example through systematic variation of incident and detected mode profiles. This could prove valuable for cavities engineered to have lower radiation losses, such that $\eta$ is smaller and the bounds used here yield a wider range of possible values of $\eta_{\mathrm{in}}$.

### 4.2.5. Nonlinear transduction

As a consequence of the large photon-phonon coupling rate, the thermal motion of the nanobeam ($\delta x_{\mathrm{rms}} \approx 230\,\mathrm{pm}$) induces frequency changes $\delta\omega_{\mathrm{rms}} = \sqrt{2g_0^2\overline{n}_{\mathrm{th}}} = 2\pi \times 34\,\mathrm{GHz}$, which is appreciable with respect to the linewidth of the cavity. The resulting nonlinear transduction generates spurious signals at integer multiples of, and combinations of, the strongest modulation frequencies. Detection of such signals at multiples of the mechanical resonance frequency resulting from thermal motion was reported previously [16, 124, 125], compared to quadratic optomechanical coupling [126], and proposed as part of a method to prepare nonclassical states of motion in a mechanical resonator [127].

Figure 4.5a shows a transduced spectrum where we identify $15$ peaks as integer multiples and combinations of the two fundamental mechanical resonances at $1.4\,\mathrm{MHz}$ ("A") and $2.0\,\mathrm{MHz}$ ("B"): $\Omega_{j,k} = |j\mathrm{A} \pm k\mathrm{B}|$, with $j, k \in \{0, 1, 2, ...\}$. Peaks corresponding to different order $(j + k)$ have a different detuning dependence, but all peaks with the same order differ only by a constant factor. This further confirms our identifying them as nonlinear transduction peaks instead of separate mechanical resonances. To illustrate the detuning dependence of the higher-order peaks, we plot the variance of the peaks $j$A for $j = \{1, 2, 3, 4\}$ in fig. 4.5b.

### 4.2.6. Order-by-order approximation

The detected height of the higher-order peaks can be predicted by a Taylor expansion of the amount of light in the cavity around the average detuning. For the second-order transduction, this was shown by Doolin *et al.* [126], where also a quadratic optomechanical coupling was taken into account. Higher-order displacement spectra were discussed by Hauer, Maciejko & Davis [128], again with a special emphasis on the second-order case. The more general case of higher-order terms of nonlinear transduction, for homodyne detection with a Lorentzian optical reflection spectrum, was analyzed by Brawley *et al.* [127]. Here we derive the result for higher-order terms of nonlinear transduction, with an optical reflection spectrum that follows a Fano lineshape (eq. (1.15)).

In the non-resolved sideband regime ($\kappa \gg \Omega_\mathrm{m}$), the optical fields in the cavity reach a steady state much faster than the timescale of mechanical motion. The intracavity amplitude can then be written as

$$a(t) = \frac{\sqrt{\eta_\mathrm{in}\kappa}s_\mathrm{in}}{-i[\Delta_0 - \delta\omega_\mathrm{c}(t)] + \kappa/2}, \tag{4.3}$$

where $\Delta_0$ indicates the average detuning between the laser and the cavity resonance. Combined with the input-output relation with nonresonant scattering, $s_\mathrm{out} = ce^{i\varphi} - \sqrt{\eta_\mathrm{out}\kappa}a$ (eq. (1.14)), eq. (4.3) yields eq. (1.15), with $u = 2(\Delta_0 - \delta\omega_\mathrm{c}(t))/\kappa$. We now find the Taylor expansion of $R(u)$ for small $\delta\omega_\mathrm{c}$ around the average relative detuning $u_0 \equiv 2\Delta_0/\kappa$:

$$R(u) = R(u_0) - \frac{2\delta\omega_\mathrm{c}}{\kappa}\frac{\partial R(u_0)}{\partial u} + ... + \frac{(-2\delta\omega_\mathrm{c}/\kappa)^k}{k!}\frac{\partial^k R(u_0)}{\partial u^k}, \tag{4.4}$$

where the last term depicts the $k$th order in the Taylor expansion. The measurement output $P = P_\mathrm{in}R$ can similarly be expanded for small fluctuations $\delta\omega_\mathrm{c}$ around $\Delta$ to

$$P(\Delta + \delta\omega_\mathrm{c}) = P(\Delta) + \sum_{k=1}^{\infty}\frac{\delta\omega_\mathrm{c}^k}{k!}\frac{\partial^k P(\Delta)}{\partial\omega_\mathrm{c}^k}. \tag{4.5}$$

For completeness, we note that

$$\frac{\partial^k P(\Delta)}{\partial\omega_\mathrm{c}^k} = P_\mathrm{in}\frac{\partial^k R(\Delta)}{\partial\omega_\mathrm{c}^k} = P_\mathrm{in}\left(\frac{2}{\kappa}\right)^k\frac{\partial^k R(u_0)}{\partial u^k}. \tag{4.6}$$

For small harmonic fluctuations $\delta\omega_\mathrm{c} = \delta\omega_0 \cos\Omega t$, the individual terms of the expansion (eq. (4.5)) contribute at different frequencies. To leading order, $\cos^k \Omega t = \cos(k\Omega t)/2^{k-1}$, which means the higher-orders are completely spectrally separated, and we can consider this expansion *order by order*. If multiple mechanical modes are coupled to the optical cavity, the expansion will also include cross terms $\propto \cos(\Omega_1 t)^{j-k} \cos(\Omega_2 t)^k$, which are spectrally separated from higher-order terms in the same regime where the approximation holds for a single mechanical mode. This means we can account for multiple modes by simply summing the variances they contribute in a specific order $k$, and in the following we consider a single mode for simplicity.

In the experiment, we measure the power spectral density $S_{PP}(\Omega)$, whose integral over frequency gives the variance $\langle P^2 \rangle$. We now calculate the band power at a frequency $k\Omega_\mathrm{m}$, where only the $k$th term of the Taylor expansion contributes, as

$$\langle P^2 \rangle_{k\Omega_\mathrm{m}} \equiv \int_{k\Omega_\mathrm{m}} S_{PP} \mathrm{d}\Omega = \frac{1}{k!^2} \left( \frac{\partial^k P}{\partial \omega_\mathrm{c}^k} \right)^2 \left\langle \left(\delta\omega_\mathrm{c}^k\right)^2 \right\rangle_{k\Omega_\mathrm{m}}. \tag{4.7}$$

For thermal motion, and again using the order-by-order approximation [127, 128], we use

$$\left\langle \left(x^k\right)^2 \right\rangle_{k\Omega_\mathrm{m}} = \frac{k!}{2^{k-1}} \langle x^2 \rangle^k, \tag{4.8}$$

which we can substitute into eq. (4.7) with $\delta\omega_\mathrm{c} = G\delta x$, to obtain

$$\langle P^2 \rangle_{k\Omega_\mathrm{m}} = \frac{G^{2k}}{k!2^{k-1}} \left( \frac{\partial^k P}{\partial \omega_\mathrm{c}^k} \right)^2 \langle x^2 \rangle^k. \tag{4.9}$$

Finally, we substitute the thermal variance $G^2 \langle x^2 \rangle_\mathrm{th} = 2g_0^2 \bar{n}_\mathrm{th}$ and the derivative $\partial^k P / \partial \omega_\mathrm{c}^k$, such that we obtain

$$\left. \frac{\langle P^2 \rangle}{P_\mathrm{in}^2} \right|_{k\Omega_\mathrm{m}} = \left. \langle R^2 \rangle \right|_{k\Omega_\mathrm{m}} = \frac{2}{k!} \left( \frac{4g_0^2 \bar{n}_\mathrm{th}}{\kappa^2} \right)^k \left( \frac{\partial^k R(u_0)}{\partial u^k} \right)^2. \tag{4.10}$$

For $k = 1$, the result of eq. (4.2) is reproduced. The result of a calculation of the variances of $k = 1$–$4$, for the parameters used in the experiment, is shown in fig. 4.5c.

Note that the higher-order peaks in this calculation were not fitted to the data, but follow from the value of $g_0$ we obtained by fitting the first-order peak, as shown in fig. 4.3. The measured nonlinear sidebands are larger than expected (corresponding to a suggested increase of $g_0$ of about $15\,\%$). Possible explanations for this discrepancy include higher-order optomechanical coupling [126], mechanical nonlinearities [86], or the breakdown of the order-by-order approximation we used in this derivation (see chapter 5). However, the symmetry and shape of the curves match the experimental data, which confirms that the detuning dependence corresponds to the successive derivatives of the reflection spectrum (fig. 4.3a). We return in more detail to nonlinear transduction in the next chapter.

## 4.3. Discussion

The free-space readout method we employ provides an easy and robust way of coupling light to the cavity. We have intentionally engineered the cavity defect such that it has a significant dipole moment [129], allowing coupling to free space at an appreciable rate. This makes it unnecessary to create an explicit loss channel for coupling, for example in the form of a grating or feeding waveguide. The currently achieved coupling rate of $\eta = 0.29$ is comparable to that achieved with standard tapered fiber coupling (for example, $\eta = 0.13$ by Chan *et al.* [15]). In both cases, it is possible to engineer the system such that it couples more efficiently, as has recently been shown for fiber coupling [125]. The Fano-shape of the reflection spectrum allows direct transduction of motion to optical amplitude modulation for a laser tuned to the cavity resonance (where dynamical radiation pressure backaction is zero), without more complicated interferometric schemes. As a result of the efficient coupling to free space, the bandwidth of the cavity is large ($0.5\,\mathrm{THz}$), which is appealing in the context of applications that require frequency matching of multiple systems: together with the small system footprint, it could assist the integration of such optomechanical transducers in sensor arrays [130] or effective optomechanical metamaterials [131].

We expect that the mechanical quality factor for the nanobeams we employ can be improved with suitable design principles and optimization of the fabrication process. Indeed, measurements on similar-sized silicon nanobeams and cantilevers suggest that quality factors in the range of $10^4$ to $10^5$ should be possible at room and cryogenic temperature, respectively [17, 90]. Nonetheless, we point out that because of the large coupling rate, even with the current modest values of both optical and mechanical quality factors the single-photon cooperativity in this structure reaches $C_0 = 0.16$. The value of this quantity, which compares optomechanical coupling strength and dissipation, and is for example a measure for the capability of the system to perform measurements at the SQL, is on par with many recently reported systems with much higher quality factors [7].



## 4.4. Conclusions

In conclusion, we demonstrated an optomechanical device with a large photon-phonon coupling rate $g_0/2\pi = 11.5\,\mathrm{MHz}$, and used it to demonstrate sensitive measurement of nanomechanical motion and pronounced optical tuning of the mechanical resonance frequency. It is interesting to note that the regime of large coupling rate and modest optical linewidth is beneficial in the context of achieving strong mechanical tuning, as parametric instability is suppressed. We revealed that the working mechanism relies on an optical mode with a subwavelength mode area. We predict this approach can be extended to yield even larger coupling rates, or to be applied to modes with higher mechanical frequencies. In the current device the photon-phonon coupling rate $g_0$ exceeds the mechanical resonance frequency $\Omega_\mathrm{m}$, which is one of the requirements for ultrastrong coupling [7, 132–134]. With further improvements in both the coupling rate and the optical quality factor, the present approach might provide a route to simultaneously

reach $g_0 > \Omega_m$ and $g_0 \approx \kappa$. Indeed, the prediction that $g_0/2\pi$ can reach values of over $50\,\mathrm{MHz}$ with realistic fabrication requirements would approach state-of-the-art optical linewidths in photonic crystal cavities. This approach thus makes a significant step towards reaching the elusive regime of ultrastrong coupling ($g_0 > \kappa, \Omega_m$), where nonclassical effects, such as the observation of quantum jumps of phonon number or the occurrence of photon blockade, arise directly from the optomechanical interaction even in the absence of strong driving [7, 132, 134]. It will be interesting to explore to what extent this regime can be used to exploit nonlinear optomechanical interactions at the single-photon level.

## 4.5. Methods

### 4.5.1. Fabrication, experimental disorder and compressive stress

The fabrication process is described in detail in section 3.4. The structures presented in this chapter are fabricated from a silicon-on-insulator wafer with a device layer thickness of $200\,\mathrm{nm}$, and a buried oxide layer of $1\,\mu\mathrm{m}$ thick. We use an HSQ resist layer with a thickness of $80\,\mathrm{nm}$ and transfer the pattern to the silicon layer using the reactive-ion etch process with $SF_6/O_2$ gases.

The simulation of the ideal structure shown in fig. 4.1 predicts the resonance frequency of the fundamental in-plane resonance to be $6\,\mathrm{MHz}$, and additionally the frequency difference between the antisymmetric and symmetric mode is negligible. We expect the frequencies of the out-of-plane resonances to be larger than those of the fundamental in-plane modes, as the narrowest part of the half-beams ($80\,\mathrm{nm}$) is smaller than the silicon slab thickness ($200\,\mathrm{nm}$). In our experiment we find significantly smaller values of $2.6\,\mathrm{MHz}$ and $3.2\,\mathrm{MHz}$ for one structure, and $1.4\,\mathrm{MHz}$ and $2.0\,\mathrm{MHz}$ for a second structure. The differences between the frequencies of the two in-plane resonances are also larger than expected.

To find the origin of this effect we measure the experimentally observed disorder produced by the fabrication process of the second structure using a scanning electron microscope. We then introduce these dimensions into the simulation, which results in slightly different eigenfrequencies. However, the resulting values are still near $6\,\mathrm{MHz}$ and additionally the two fundamental modes still have only a small frequency difference. Finally, we add an extra step to the simulation to include a static compressive stress, which can result from the stress in the buried oxide layer of the silicon-on-insulator layer structure we use [111]. We define an initial displacement for one of the support pads along the length of the beam, which creates the stress. Increasing the amount of displacement, and therefore the stress, decreases the eigenfrequencies predicted by the simulation. This is in accordance with the theoretical expectation [135]. At the same time the difference between the eigenfrequencies of the two fundamental modes increases.

Figure 3.2 shows the displacement profiles that result from such a simulation. At a displacement value of $10\,\mathrm{nm}$ ($0.09\,\%$ of the length of the beam), the resonances occur at frequencies very close to the experimentally measured values, at $1.5\,\mathrm{MHz}$ and $1.9\,\mathrm{MHz}$, and the mode profiles are significantly more asymmetric.

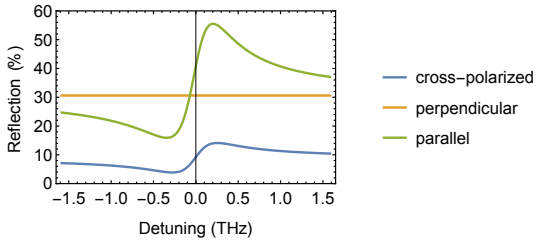


Figure 4.6: Calculated reflection curves for various polarization settings: cross-polarized (bottom, blue curve), with the cavity at $45°$ to both, and with input and output polarizers both oriented perpendicular and parallel to the cavity polarizability (middle (flat) orange curve and top green curve, respectively).

### 4.5.2. Free-space setup

The laser beam (New Focus Velocity 6725) was focused on the sample by an aspheric lens with a numerical aperture of $0.6$. We estimate the resulting spot size to be near the diffraction-limited value of $2.8\,\mu\mathrm{m}$. A polarizing beamsplitter provided a cross-polarized detection scheme, where any light that was directly reflected was rejected and only light that coupled to the sample, placed at $45°$, was transmitted to the detector. Both the lens and the sample were in a vacuum chamber to reduce mechanical damping by air molecules. The spectra in fig. 4.2 were taken while intermittently running the vacuum pump to obtain a pressure lower than $10^{-3}\,\mathrm{mbar}$. All other experimental results shown were obtained with the vacuum pump turned off, at a higher pressure of about $4\,\mathrm{mbar}$. While the higher pressure lowered the mechanical quality factor to approximately $200$, the subsequent analysis was independent of the mechanical linewidth.

In this chapter, we show only cross-polarized reflection spectra, with the cavity oriented at $45°$ with respect to both the input and output polarization. Our reflection setup does not allow measuring non-cross-polarized reflection directly due to our use of a polarizing beamsplitter. However, we can simulate what we expect for the reflection based on a simplified model of the experiment. For this we assume the coupling to the cavity, specifically its polarization response, can be described as coupling to a dipole polarizability. This means it will not couple at all when light is polarized perpendicular to the polarizability and the coupling will be exactly $1/2$ when oriented at $45°$. Additionally, we need to estimate the direct reflection when not using a cross-polarization scheme. The main contribution to this is the reflection of the flat silicon substrate interface, which we calculate using the Fresnel equations. This yields a reflectivity of $31\,\%$. The additional contribution of nonresonant scattering from the nanobeams as well as a possible contribution from the (unpolished) back surface of the silicon substrate have been neglected. Figure 4.6 shows the result of this calculation, using the fitted parameters from the reflection spectrum shown in fig. 4.3a.

In our experiment, we also inserted a quarter-wave plate between the polarizing beamsplitter and the sample. By turning the quarter-wave plate, we could

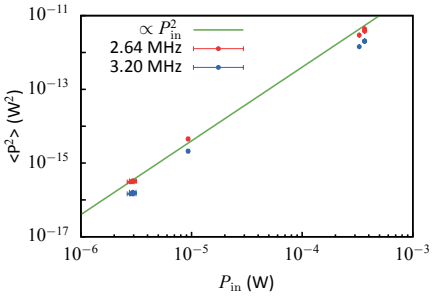


Figure 4.7: Power dependence. The red and blue data points show the measured signal from the two fundamental mechanical resonances, obtained by fitting both mechanical resonances in the spectra (see fig. 4.2 for such a spectrum). The data was taken at various input powers with resonant laser light (zero detuning). The green line is a guide to the eye, with a slope corresponding to quadratic dependence on input power. The error bars indicate readout error of the input power but don't take into account possible variations in incoupling efficiency due to slight changes in alignment.

tune the incident and outgoing polarization between linear and circular, simultaneously varying the degree of suppression of the direct reflection. We verified that this yielded the expected results: first a large effect on the shape of the resulting Fano lineshape, due to the amplitude change of the direct reflection as well as the phase delay introduced by the slow axis of the waveplate; second a relatively small effect on the rate of coupling to the cavity, since the rate of coupling to a dipolar resonator hardly changes when going from linear at $45°$ to circular polarization. We note that for some settings of the waveplate, it was possible to reach an almost perfect Lorentzian peak or dip in the reflection spectrum, which suggests the contribution of nonresonant scattering of the nanobeam can interfere destructively or constructively with direct reflection from the silicon substrate at these settings.



### 4.5.3. Analysis of modulated reflection signals

We detected the reflection signal using a low-noise InGaAs-based photoreceiver (Femto HCA-S) and analyzed it using an electronic spectrum analyzer (Agilent MXA). We fitted the peaks in the modulation spectra using a Lorentzian convolved with a Gaussian distribution, also called a Voigt lineshape. The Gaussian contribution accounted for the resolution bandwidth of the spectrum analyzer, as well as for frequency-noise broadening at relatively large optical input power $P_{\mathrm{in}}$. With high $P_{\mathrm{in}}$, small fluctuations in incoupling efficiency or laser intensity thermally shifted the cavity resonance, which resulted in frequency noise via optical spring tuning of the mechanical resonance.

### 4.5.4. Influence of optical input power

In the measurements shown in this chapter, we use up to $370\,\mu\mathrm{W}$ of optical power incident on the nanobeam. Using the parameters of our fit to the reflection spec-

trum, we estimate that this results in an intracavity intensity that corresponds to a maximum of $\approx 1000$ photons. For this intensity in the cavity, we do not expect an increase in the cavity temperature of more than a few Kelvin. As a first confirmation of this, we see thermal shifts of the cavity resonance wavelength of less than $1\,\mathrm{nm}$, which corresponds to a temperature increase of less than $10\,\%$.

To check the assumption more thoroughly we measured the signal strength of the two fundamental mechanical frequencies as a function of power incident on the structure. Figure 4.7 shows the result for resonant light, both from the zero-detuning point in swept measurements and from individual measurements where the detuning was set to zero by minimizing the optically induced shift of the mechanical frequency. Comparison with the line shows that the data points closely follow the expected quadratic dependence on input power for both peaks in the spectrum. The largest source of uncertainty in this measurement are differences in coupling efficiency between the incoming laser beam and the cavity due to small changes in alignments, which can influence the signal strength between measurements.

# 5

# Nonlinear cavity optomechanics with nanomechanical thermal fluctuations

*Although the interaction between light and motion in cavity optomechanical systems is inherently nonlinear, experimental demonstrations to date have allowed a linearized description in all except highly driven cases. Here we demonstrate a nanoscale optomechanical system, in which the interaction between light and motion is so large (single-photon cooperativity $C_0 \approx 10^3$) that thermal motion induces optical frequency fluctuations larger than the intrinsic optical linewidth. The system thereby operates in a fully nonlinear regime, which pronouncedly impacts the optical response, displacement measurement, and radiation pressure backaction. Specifically, we measure an apparent optical linewidth that is dominated by thermo-mechanically-induced frequency fluctuations over a wide temperature range, and show that in this regime thermal displacement measurements cannot be described by conventional analytical models. We perform a proof-of-concept demonstration of exploiting the nonlinearity to conduct sensitive quadratic readout of nanomechanical displacement. Finally, we explore how backaction in this regime affects the mechanical fluctuation spectra.*

This chapter is based on Leijssen, R. *et al.* Nonlinear cavity optomechanics with nanomechanical thermal fluctuations. *Nature Communications* **8,** 16024 (2017) [136].

## 5.1. Introduction

In cavity optomechanics, the interaction between light in an optical cavity and the motion of a mechanical resonator enables sensitive optical readout of displacement, as well as manipulation of the motion of the resonator through optical forces [7]. This has allowed demonstrations of sideband and feedback cooling of the mechanical resonator near its quantum ground state [13, 15, 26, 27], squeezing of light [17, 28, 29] and of the mechanical zero-point fluctuations [30–32], entanglement [33] and state transfer [34] between the optical and mechanical degrees of freedom, as well as detection of radiation pressure shot noise [24, 25] and nonclassical correlations [36–39]. In all of these examples, the coupling between fluctuations of the optical field and the mechanical displacement can be regarded as linear for all intents and purposes.

However, the optomechanical interaction is inherently nonlinear. Indeed, the cavity optomechanical interaction Hamiltonian reads $\hat{H}_{\text{int}} = -\hbar g_0 \hat{a}^\dagger \hat{a} \hat{x}/x_{\text{zpf}}$, where $\hat{a}$ ($\hat{a}^\dagger$) is the annihilation (creation) operator for the optical cavity field, $\hat{x}$ is the displacement operator for the mechanical resonator, and $\hbar$ is the reduced Planck constant. The photon-phonon coupling rate $g_0 = -(\partial\omega_{\text{c}}/\partial x)x_{\text{zpf}}$ quantifies the change of the cavity frequency $\omega_{\text{c}}$ due to a displacement the size of the zero-point fluctuations of the resonator $x_{\text{zpf}}$. This interaction Hamiltonian leads to nonlinear behavior, as the equations of motion it generates contain products of two operators (see section 1.2.1). The linearized form of the interaction $\hat{H}_{\text{int}} = -\hbar g_0 \bar{\alpha}(\delta\hat{a}^\dagger + \delta\hat{a})\hat{x}/x_{\text{zpf}}$ (see section 1.2.2) does not contain the nonlinear terms, but usually suffices to describe the dynamics of fluctuations [7]. This form emerges when the cavity field is written as the sum $\hat{a} = \bar{\alpha} + \delta\hat{a}$ of an average coherent field $\bar{\alpha}$ and fluctuations $\delta\hat{a}$, and the term containing $\delta\hat{a}^\dagger\delta\hat{a}\hat{x}$ is neglected by assuming $\delta\hat{a} \ll \bar{\alpha}$. The linearization is generally valid if the fluctuations $\delta\hat{a}$, insofar as they are induced by mechanical motion, do not approach or exceed the coherent field $\bar{\alpha}$. However, the assumption that $\delta\hat{a} \ll \bar{\alpha}$ is not valid if mechanical fluctuations shift the cavity completely in and out of resonance with the optical drive, that is, when they produce a cavity frequency shift comparable to the optical linewidth $\kappa$. Then, nonlinear processes become crucially important, and qualitatively different effects can occur.

In the quantum domain, intriguing implications of this nonlinearity are expected in the single-photon strong-coupling regime, when the coupling rate $g_0$ exceeds the optical and mechanical loss rates $\kappa$ and $\Gamma$, respectively. There, quantum-level mechanical fluctuations induce a nonlinear response, creating nonclassical states of both light and motion when the mechanical frequency $\Omega_{\text{m}}$ approaches the optical linewidth as well [132, 133, 137]. In the so-called bad-cavity limit ($\kappa > \Omega_{\text{m}}$), the nonlinearity of the interaction provides a useful path towards creating motional quantum states, for example through performing quadratic measurements of displacement (proportional to $\hat{x}^2$)[116, 126, 127, 138, 139].

In macroscopic or chip-based optomechanical implementations, the breakdown of linearity when $\delta\hat{a} \gtrsim \bar{\alpha}$ has so far only been experimentally relevant for mechanical resonators driven to large amplitude, for example through optomechanical parametric amplification. In that case, nonlinear effects determine the

maximum amplitude of optomechanical self-oscillation [7, 66, 140–143] and can lead to complex nonlinear dynamical phenomena such as chaos [144–146].

In this chapter, we establish and explore the regime where even intrinsic Brownian motion induces cavity frequency fluctuations larger than the optical linewidth. In this regime, the nonlinear nature of the cavity optomechanical interaction becomes important in all essential phenomena, including optomechanical displacement measurement and radiation pressure backaction. The regime is defined by $g_0\sqrt{2\bar{n}_{\mathrm{th}}} \gtrsim \kappa$, where $\bar{n}_{\mathrm{th}} = k_{\mathrm{B}}T/\hbar\Omega_{\mathrm{m}}$ is the average phonon occupancy of the mechanical mode with frequency $\Omega_{\mathrm{m}}$, in thermal equilibrium at a temperature $T$ and $k_{\mathrm{B}}$ is the Boltzmann constant. It is clear from this condition that any optomechanical system in which the ratio $g_0/\kappa$ is increased will enter this regime before reaching the single-photon strong-coupling regime, unless the mechanical resonator is pre-cooled to its ground state. The condition can equivalently be expressed as $C_0 \gtrsim \kappa/\gamma$, that is, the single-photon cooperativity $C_0 \equiv 4g_0^2/\kappa\Gamma$ being larger than the ratio of optical decay rate and mechanical thermal decoherence rate $\gamma \equiv \Gamma\bar{n}_{\mathrm{th}}$. In our experiments, we follow the strategy of exploiting subwavelength optical confinement, outlined in chapter 4 to reach single-photon cooperativity around $10^3$; two to three orders of magnitude larger than typical values in nanoscale optomechanical systems to date [7, 147, 148], and only comparable with cold-atom implementations [24, 149]. In the systems demonstrated here, the apparent optical linewidth is dominated by the transduced thermal motion over a wide range of temperatures, and the transduction becomes extremely nonlinear. We numerically implement a model that describes transduction in this regime, in contrast to the conventional analytical description, which fails for fluctuations that approach the linewidth. Moreover, we analyze how the nonlinear response of the radiation pressure force to stochastic fluctuations alters the shape of mechanical fluctuation spectra. Finally, we provide a proof-of-concept demonstration of exploiting the nonlinearity to conduct sensitive quadratic readout of nanomechanical displacement.

## 5.2. Results

### 5.2.1. Sliced photonic crystal nanobeam

Figure 5.1a shows the optomechanical system we employ. As described in chapters 3 and 4, it combines low-mass, megahertz-frequency, nanomechanical modes with subwavelength optical field confinement in a sliced photonic crystal nanobeam, to establish strong optomechanical interactions with photon-phonon coupling rates $g_0$ in the range of tens of MHz. The fundamental mechanical resonance of the sliced nanobeam, shown in fig. 5.1b, strongly influences the gap distance $d$ in the middle of the beam. The motion of the resonator in this mechanical mode is associated with a simulated effective mass of $1.5\,\mathrm{pg}$, leading to relatively large zero-point fluctuations $x_{\mathrm{zpf}} = \sqrt{\hbar/2m\Omega_{\mathrm{m}}} = 43\,\mathrm{fm}$. As shown in the optical field profile of the fundamental cavity resonance of the structure in fig. 5.1c, the nanoscale gap in the middle of the beam confines the light to a small area, which makes the optical cavity resonance frequency $\omega_{\mathrm{c}}$ strongly

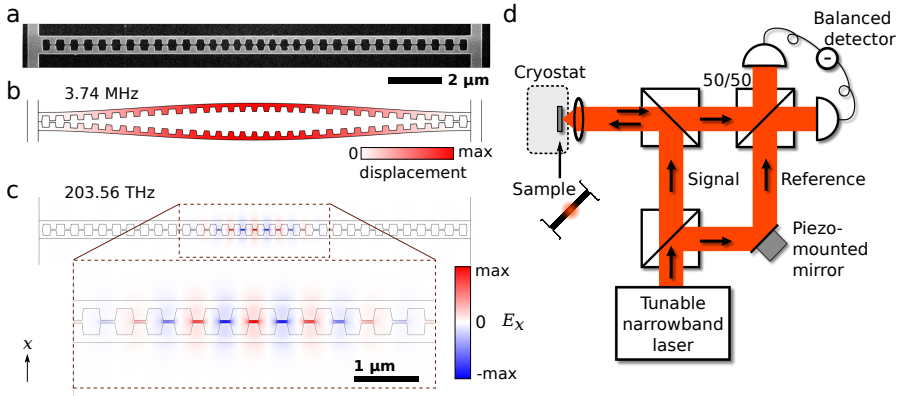


Figure 5.1: Structure and setup. (a) Electron microscope image of a silicon sliced nanobeam. The shown part is free-standing and has a thickness of $250\,\mathrm{nm}$. The scale bar is valid for panels (a–c). (b) Simulated displacement profile of the fundamental mechanical resonance, which strongly modifies the gap size. (c) Simulated transverse electric field of the fundamental optical cavity resonance. The inset shows an enlarged view of the cavity region, formed by a tapered variation of the distances between, and sizes of, the holes. (d) Schematic diagram of the employed balanced homodyne interferometer measurement setup. The reflection from the sliced nanobeam is interfered with the light from the reference arm, enabling near-quantum-limited measurement of fluctuation spectra even with low power incident on the sample (see section 5.4.2 for details).

dependent on the gap size $d$ between the two halves of the nanobeam. With the fabricated gap size of $45\,\mathrm{nm}$ to $50\,\mathrm{nm}$, we simulated the optical frequency change due to a displacement of the beams to be $\partial\omega/\partial x/2\pi = 0.8\,\mathrm{THz\,nm^{-1}}$, where $x \equiv (d - d_0)/2$, with $d_0$ the equilibrium gap distance. This leads to an expected optomechanical coupling rate of $g_0/2\pi = 35\,\mathrm{MHz}$. We decrease the optical cavity decay rate and increase the outcoupling at normal incidence by engineering the angular radiation spectrum of the sliced nanobeam structure [87, 100] (see section 5.4.1). The resultant simulated optical decay rate is $8.8\,\mathrm{GHz}$, showing that the sliced nanobeam design is capable of combining large optomechanical interactions with relatively low optical losses ($Q > 10^4$). We believe that further optimization along these lines could, in principle, lead to still larger optical quality factors.

We employ a balanced homodyne detection scheme, schematically shown in fig. 5.1d, to study the fluctuations imparted on the light in the nanobeam cavity through the optomechanical interaction (see section 5.4.2). Figure 5.2a depicts fluctuation spectra recorded with an electronic spectrum analyzer, showing the two fundamental mechanical resonances of one device, measured at $3\,\mathrm{K}$ with the laser on-resonance with the cavity. We ascribe the two resonances to the two half-beams moving at slightly different natural frequencies, instead of the ideal antisymmetric eigenmode depicted in fig. 5.1b. The fact that in this device the two resonances are nearly of equal strength indicates that the two half-beams are mechanically coupled at a rate smaller than their intrinsic frequency difference

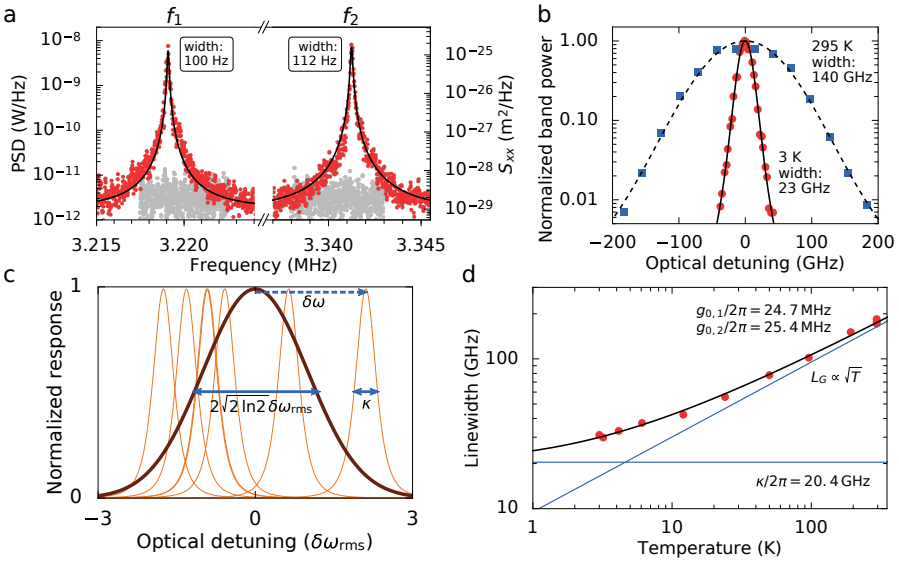


Figure 5.2: Optical linewidth broadening. (a) Recorded optically measured spectra of the two fundamental mechanical resonances with frequencies $f_1$ and $f_2$ (PSD: power spectral density, optical power incident on sample: $11.3\,\mathrm{nW}$). Grey noise spectra were recorded with the signal arm of the interferometer blocked. Black lines show the Lorentzian fit, used to determine the linewidths (full width at half maximum) shown in the figure. The displacement spectral density scale on the right-hand side assumes linear transduction of the known thermal motion of the structure at the cryostat temperature. (b) Detuning dependence of the measured transduced thermal motion, measured as the band power at $f_1$, the lowest mechanical frequency, at room temperature and at $3\,\mathrm{K}$. The black solid and dashed lines show fits with a Voigt lineshape squared (see section 5.4.4), with the widths (full width at half maximum) shown. (c) Schematic representation of thermal-motion-induced linewidth broadening: the thin orange lines represent the intrinsic cavity response at a few example detunings, while the thick brown line shows the overall response resulting from averaging over the fluctuating detuning. (d) Optical linewidth versus temperature. The solid line is a fit with a model that assumes a constant Lorentzian intrinsic linewidth $\kappa$ convolved with a Gaussian with a width $L_{\mathrm{G}}$ that depends on $\sqrt{T}$. The asymptotes (blue) of the fit function allow us to extract $\kappa$ and the optomechanical coupling rates $g_{0,i}$ for the two mechanical modes ($i = 1, 2$). Extracted values are shown in the figure.

(see section 3.2.3), and thus moving approximately independent of each other; stronger mechanical coupling would result in hybridization into symmetric and antisymmetric eigenmodes with different optical transduction strengths.

### 5.2.2. Modification of optical response

The signal strength of the transduced motion around the cavity resonance wavelength of $1457.5\,\mathrm{nm}$, measured at $3\,\mathrm{K}$ and at room temperature, is shown in fig. 5.2b as a function of laser detuning. The fluctuations are recorded while continuously sweeping the piezo-mounted mirror over multiple interferometer fringes, thus averaging the measured signal quadratures. As we derived in section 1.5.5, the resulting signal strength acquires a simple single-peaked detuning dependence with a maximum when the laser is tuned to the cavity resonance. As fig. 5.2b shows, the apparent linewidth of the optical resonance is strongly influenced by temperature. We infer from this that the frequency fluctuations of the cavity due to the thermal motion of the mechanical resonator dominate the response. This occurs when the frequency fluctuations are larger than the intrinsic optical linewidth, which is illustrated in fig. 5.2c: while the intrinsic optical response of the cavity is Lorentzian with linewidth $\kappa$ (orange thin lines), the distribution of cavity frequency fluctuations due to thermal motion has a Gaussian spectrum (brown thick line), whose linewidth $L_\mathrm{G}$ is related to the root-mean-square value of the frequency fluctuations $\delta\omega_\mathrm{rms}$ as $L_\mathrm{G} = 2\sqrt{2\ln 2}\delta\omega_\mathrm{rms}$. In the bad-cavity limit we consider here, we model the observed cavity response as a Voigt lineshape, which is a convolution between the Lorentzian cavity response and the Gaussian distribution of cavity resonance frequencies due to the Brownian motion. We note that the measured electronic power spectral density is proportional to the square of the optical response, which leads to a smaller apparent linewidth in the detuning dependence shown in fig. 5.2b. In the following, we only report the extracted linewidth (see section 5.4.4), which directly corresponds to the optical loss rate $\kappa$ in the low-temperature limit, and the full width at half maximum of the frequency fluctuation distribution in the high-temperature limit.

As the thermo-mechanical displacement variance is given by $\langle x_\mathrm{th}^2\rangle = 2\bar{n}_\mathrm{th}x_\mathrm{zpf}^2$ (assuming dynamical backaction is negligible), the induced frequency fluctuations due to a single mechanical mode at frequency $\Omega_\mathrm{m}$ are characterized by a root-mean-square amplitude

$$\delta\omega_\mathrm{rms} \equiv \sqrt{\langle\delta\omega^2\rangle} = g_0\sqrt{2\bar{n}_\mathrm{th}} = g_0\sqrt{2k_\mathrm{B}T/\hbar\Omega_\mathrm{m}}, \tag{5.1}$$

which reveals a square-root dependence on temperature. In case multiple independent mechanical modes are coupled to the optical cavity, the variances of the cavity frequency fluctuations are added, that is, $\delta\omega_\mathrm{rms}^2 = \sum_j\langle\delta\omega_j^2\rangle$, which preserves the overall temperature dependence. Figure 5.2d shows the full measured temperature dependence of the apparent linewidth, which exhibits the expected square-root dependence on temperature at higher temperatures. We fit the data points using an equation that approximates the linewidth of the Voigt lineshape (see section 5.4.4), with a fixed Lorentzian contribution due to the intrinsic optical loss and a Gaussian contribution that follows eq. (5.1). The resulting fit curve is shown

in fig. 5.2d, together with its asymptotes (thin blue lines). These asymptotes allow us to directly extract the intrinsic optical linewidth $\kappa$ and the variance of thermal-motion-induced frequency fluctuations of the cavity, without further calibration. There are two mechanical resonances that show significant coupling to the optical cavity resonance as shown in fig. 5.2a, and we derive the ratio between their coupling strengths from the ratio between the signal strengths at the two mechanical resonance frequencies (see section 3.2.3 and section 4.2.2). Using this ratio and the measured resonance frequencies, we obtain $g_0/2\pi = 24.7\,\mathrm{MHz}$ and $25.4\,\mathrm{MHz}$ for the two mechanical modes, which corresponds closely to the predicted value for an ideal antisymmetric mode of $35\,\mathrm{MHz}$, since $\sqrt{24.7^2 + 25.4^2} = 35.4$.

This large optomechanical coupling rate, combined with the extracted optical decay rate of $\kappa/2\pi = 20.4\,\mathrm{GHz}$ and the mechanical decay rate of $\Gamma/2\pi = 100\,\mathrm{Hz}$ (measured at $3\,\mathrm{K}$), means that this device has a single-photon cooperativity $C_0 = 4g_0^2/\kappa\Gamma = 1.1 \times 10^3$. The single-photon cooperativity is a metric that combines optomechanical coupling and losses [7, 148]. It signals the inverse of the number of intracavity photons needed to perform a measurement at the standard quantum limit, if all photons escaping the cavity could be employed towards that measurement. Interestingly, the combination of quadrature-averaged detection with temperature-dependent linewidth measurement allows direct extraction of $C_0$, with no other calibration than that of the mechanical bath temperature. The extremely high value we report here, which exceeds previously reported nano-optomechanical architectures by two to three orders of magnitude [7, 147, 148], highlights the prospects of such systems for measurement-based quantum control of motion.

### 5.2.3. Nonlinear transduction

When the relative cavity fluctuations $\delta\omega_{\mathrm{rms}}/\kappa$ are large, a typical mechanical oscillation samples the full width of its Lorentzian lineshape. Since this lineshape is nonlinear, higher-order harmonics are expected to appear in the transduced optical fluctuation spectrum. At room temperature, the cavity frequency fluctuations due to both mechanical modes have an amplitude $\delta\omega_{\mathrm{rms}} = \left(2\sum_j \bar{n}_{\mathrm{th},j} g_{0,j}^2\right)^{1/2} = 2\pi \times 69\,\mathrm{GHz} \approx 3.4\kappa$. As shown in fig. 5.3a, at room temperature the measurement signal indeed contains fluctuations at (mixed) integer multiples of the two fundamental mechanical resonances, that is $f_{j,k} = |jf_1 \pm kf_2|$, where $j, k \in \{0, 1, 2, ...\}$. Around the fundamental frequencies near $3.3\,\mathrm{MHz}$, we observe odd mixing terms up to ninth order (for example a peak is visible at $f_{5,-4} = 5f_1 - 4f_2$), and around the sum frequency at $6.6\,\mathrm{MHz}$, even mixing terms up to tenth order can be identified.

At a temperature of $3\,\mathrm{K}$, the ratio between the cavity frequency fluctuations, caused by both mechanical modes, and the intrinsic optical linewidth is $\delta\omega_{\mathrm{rms}}/\kappa = 0.34$, which still leads to significant higher-order transduction. Figure 5.3b shows a direct comparison of the spectra obtained at room temperature and at $3\,\mathrm{K}$. As a measure for the higher-order transduction, we take the ratio between the second- and first-order transduction. The ratio between the orders is independent of other parameters, such that it gives direct insight in the strength of the nonlinearity.

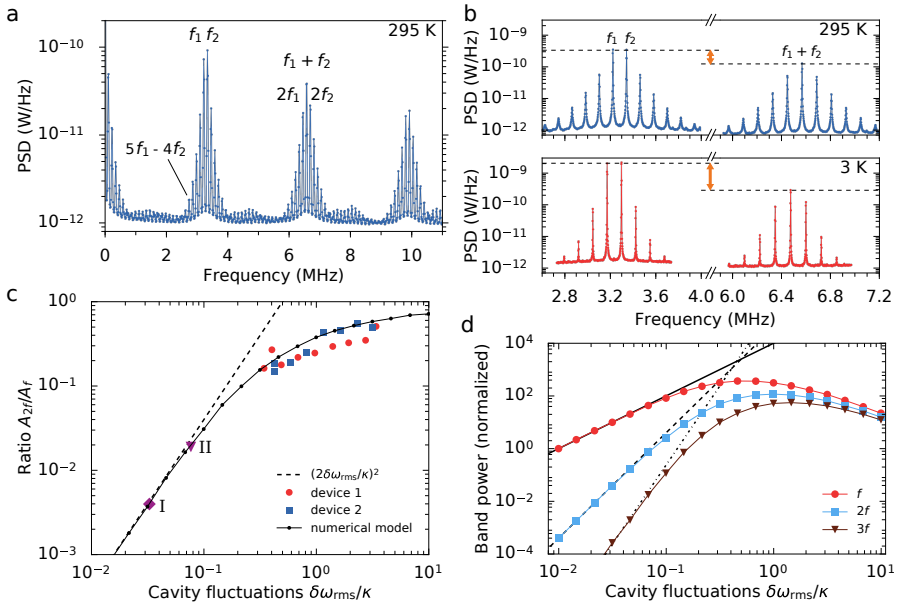


Figure 5.3: Nonlinear transduction. (a) Power spectral density of transduced thermal motion, measured at room temperature ($295\,\mathrm{K}$). (b) Power spectral density of the group of peaks around the fundamental mechanical frequencies $f_1, f_2$ and around $f_1 + f_2$, at room temperature (blue) and at $3\,\mathrm{K}$ (red). The orange arrows indicate the ratio between the maximum first and second-order transduction (dashed lines). (c) Ratio between the three second-order peaks around $f_1 + f_2$ and the peaks at the fundamental frequencies $f_1, f_2$ as a function of the relative cavity fluctuations $\delta\omega_{\mathrm{rms}}/\kappa$. Device 1 is the same device presented in the other figures in this chapter; device 2 is a similar device with different parameters from which more measurements are shown in section 5.5.2; room-temperature measurements from two recent publications are indicated with data points I (ref. [127]) and II (ref. [70], chapter 4 of this thesis). The dashed line indicates the prediction from an analytical model with an order-by-order approximation, while the black data points connected with solid lines represent a calculation based on a numerically generated time trace to simulate thermal motion. (d) Expected band power at the fundamental frequency $f$ as well as at $2f$ and $3f$, as a function of the relative cavity fluctuations, normalized to the band power for $f$ at $\delta\omega_{\mathrm{rms}}/\kappa = 10^{-2}$. Solid, dashed, and dash-dotted lines follow the order-by-order approximation, while the colored points are the outcome of our numerical model.

This ratio is clearly larger at higher temperature (its inverse is indicated with arrows in fig. 5.3b). The difference in the signal-to-noise ratio between low and high temperatures is due to the mechanical linewidth being smaller at low temperatures (by a factor of two) as well as a redistribution of modulation power among higher harmonics, as explained in the following.

Higher-order transduction (for a single mechanical mode) has previously been described with an analytical model that is based on a Taylor expansion of the measurement output around the average detuning [126, 127], an approach we also used in the previous chapter (see section 4.2.6). For low-amplitude modulation, the higher-order terms in this expansion can be approximated as independent. Mathematically, this is based on an order-by-order approximation $(\cos\Omega_{\mathrm{m}}t)^k \approx 2^{-(k+1)}\cos k\Omega_{\mathrm{m}}t$. The resulting expression for the maximum signal power measured at the (multiple of the) resonance frequency $k\Omega$ is

$$\langle P^2\rangle_{k\Omega} = 2A^2k!\left(\frac{2\langle\delta\omega^2\rangle}{\kappa^2}\right)^k, \tag{5.2}$$

where $A$ is a constant that depends on the optical power as well as the coupling efficiency to the cavity (for details, see section 5.4.3 and section 1.5.5).

In fig. 5.3c, the dashed line shows the ratio between the second- and first-order transduction that follows from this order-by-order approximation, $(2\delta\omega_{\mathrm{rms}}/\kappa)^2$. The data points labeled I and II, which represent room-temperature measurements reported in ref. [127] and chapter 4 of this thesis, respectively, are still well-explained by the order-by-order approximation. For the devices under study, $\delta\omega_{\mathrm{rms}}/\kappa$ is so large that this approach breaks down. This is shown by our temperature sweep data, where we take the fitted area $A_{f_j}$ under the peaks at the fundamental frequencies and at twice the frequency (labeled in fig. 5.3a), and plot their ratio: $(A_{2f_1} + A_{f_1+f_2} + A_{2f_2})/(A_{f_1} + A_{f_2})$. This ratio reduces to $A_{2f}/A_f$ if the two frequencies $f_1, f_2$ coincide, which supports directly comparing it to the single-mode prediction of the order-by-order approximation. The red circles indicate the results for the same device presented in the other figures in this chapter, while the blue squares represent a different device with $g_0/2\pi = 10.8\,\mathrm{MHz}$ and $\kappa/2\pi = 9.0\,\mathrm{GHz}$ (see section 5.5.2).

Where the order-by-order approximation breaks down, the nonlinear transduction still follows the prediction of our full model, in which we calculate the expected homodyne output from a numerical time-domain simulation of the thermal motion (see section 5.4.5). We then Fourier transform the simulated signal and plot the ratio of the band powers, noting that the numerical result does not depend on whether we include one or two mechanical resonances when plotted against total relative cavity fluctuations $\delta\omega_{\mathrm{rms}}/\kappa$. This full model prediction is shown by the black dots connected by solid lines in fig. 5.3c. The numerical simulation follows the experimentally observed trend, and shows that the ratio between second- and first-order transduction saturates close to unity at higher fluctuation amplitudes. We note that only such a numerical approach correctly takes into account the statistics of the transduced motion: the strongly nonlinear conversion of displacement to optical field precludes an analysis based solely on

one or several moments of the displacement distribution. In other words, a single peak in the fluctuation spectrum at $k\Omega_\mathrm{m}$ can no longer be dominantly associated with a specific scattering process involving $k$ phonons, but also contains contributions due to $k+2, k+4, \ldots$ phonons. Although some of the data lie below the expected curve we note that this cannot be explained by poor thermalization of the sample. If the sample would not be thermalized at low temperatures, our estimate of $\kappa$ would be too high and our estimate of $\delta\omega_\mathrm{rms}$ too low. Both such misestimations would lead to data points that lie above the predicted trend (black line) in fig. 5.3c, which is not what we observe. Independent measurements that vary optical power and radiation heat load also indicate good thermalization of the sample (see sections 5.5.1 and 5.5.2).

Using the numerical model, we calculate the absolute signal power due to thermal motion at the fundamental frequency $f$ and its multiples $2f$ and $3f$, shown as data points in fig. 5.3d. For cavity frequency fluctuations $\delta\omega_\mathrm{rms}/\kappa$ larger than about $10\,\%$, both linear and higher-order transduction no longer follow the order-by-order approximation given in eq. (5.2) (black lines), which predicts monotonic increases in signal strength. Instead, we recognize an optimum single-harmonic signal strength due to cavity frequency fluctuations, beyond which larger fluctuations cause the cavity to be off-resonance most of the time. This reduces the transduction at a single harmonic in the optical signal, instead distributing energy equally among an increasing number of harmonics as the system operates deeper in the nonlinear regime.

### 5.2.4. Quadratic measurement of motion

A measurement that is directly sensitive to the square of displacement, $x^2$, can be used to estimate the energy of the mechanical resonator. In the resolved sideband regime, displacement-squared optomechanical coupling hence provides a means to perform quantum non-demolition measurements of the phonon number [50, 150–153]. But also in the bad-cavity limit, measurements of $x^2$ have been proposed as a possible route to preparing nonclassical (superposition) states of motion of the mechanical resonator [126, 127, 154, 155]. It is important then to suppress both linear measurement and backaction, either through structural design or through active feedback schemes [127]. Measurements of $x^2$ can be performed using the nonlinear transduction we study here, by detecting the transduced motion at twice the fundamental frequency, $2f$, provided that the sample temperature is low enough such that the order-by-order approximation is valid. This gives rise to an effective quadratic coupling rate given by $g_0^2/\kappa$ (ref. [155]), which amounts to $2\pi \times 32\,\mathrm{kHz}$ in the device presented here. To put that number in perspective, one can compare it to the quadratic coupling rate $\mu_0 = (\partial^2\omega_\mathrm{c}/\partial x^2)x_\mathrm{zpf}^2$ in devices that are designed such that the frequency is directly proportional to the square of the displacement. A state-of-the-art double-slotted photonic crystal system recently demonstrated [152] a quadratic coupling rate of $\mu_0/2\pi = 245\,\mathrm{Hz}$.

In fig. 5.4 we show selective linear and quadratic measurements of mechanical displacement at $3\,\mathrm{K}$. Figure 5.4a shows the strength of the first- and second-order transduction (proportional to $x$ and $x^2$, respectively, in the order-by-order approx-

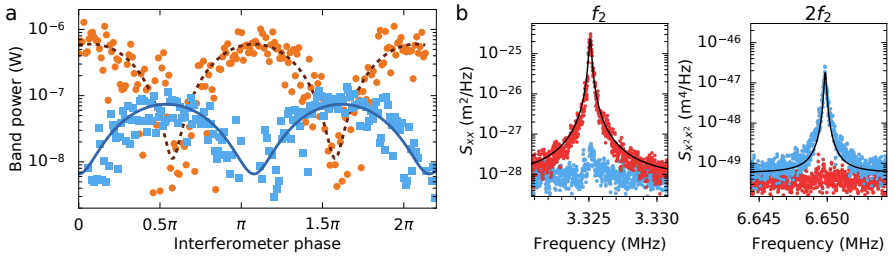


Figure 5.4: Quadratic measurement. (a) Transduction of first ($f_2$) and second ($f_1+f_2$) order peaks (orange and light blue data points, respectively) while sweeping the piezo mirror position, with $10.5\,\mathrm{nW}$ optical power incident on the sample. The solid lines show sinusoidal fits to the data. The horizontal scale was derived from the fit to the band power of $f_2$, and the data at $f_1 + f_2$ was shifted horizontally by about $3\,\%$ to compensate for measurement drift. (b) Spectra at $f_2$ and $2f_2$ at optimal mirror positions for linear and quadratic transduction (red and light blue data points, respectively), taken with $12.8\,\mathrm{nW}$ of incident optical power. The black solid lines are Lorentzian fits, whose area was used to calibrate the vertical scale.

imation) as a function of the piezo mirror position that controls the homodyne phase, which is now no longer continuously swept. The data follow the expected sinusoidal dependence.

We obtained the spectra in fig. 5.4b by positioning the piezo mirror at the optimum points for first- and second-order transduction, depicted by the red and blue data points respectively. The vertical scale was calibrated by using the order-by-order approximation, where the area under the peaks in the spectrum is proportional to the variance of the thermal motion of the structure, which here provides a lower limit for the sensitivity. This analysis yields an imprecision for the displacement-squared measurement of $2.0 \times 10^{-25}\,\mathrm{m^2\,Hz^{-1/2}}$. To provide some context for this value, with the current mechanical linewidth this level of imprecision corresponds to the ability to measure a phonon occupancy of $752$ with a signal-to-noise ratio of $1$, which is an improvement over the measurement sensitivity in the proof-of-concept experiment reported in ref. [127] by approximately a factor $50$. In the data shown here, the suppression of linear transduction is $28\,\mathrm{dB}$, which could be further improved by implementing a feedback loop to lock the homodyne interferometer phase to a desired value.

It is important to note that our numerical model, as shown in fig. 5.3d, predicts second-order transduction at only $10\,\%$ of the strength of the order-by-order approximation for $\delta\omega_{\mathrm{rms}}/\kappa \approx 0.34$, which is the size of the relative cavity fluctuations in our device at $3\,\mathrm{K}$. Therefore, we expect that if this device is cooled further, to the point where the order-by-order approximation accurately predicts the transduction, an even lower imprecision noise of $6.3 \times 10^{-26}\,\mathrm{m^2\,Hz^{-1/2}}$ would be recovered without any further optimization. This would be comparable to a phonon occupancy of $238$. In the regime where the order-by-order approximation holds,

this imprecision, expressed as a phonon number $n_{\mathrm{imp}}$ scales as

$$\frac{1}{n_{\mathrm{imp}}} = 16\left(\frac{g_0}{\kappa}\right)^2 \eta\sqrt{\frac{P_{\mathrm{in}}\xi}{\hbar\omega_{\mathrm{c}}\Gamma}}, \tag{5.3}$$

with $\eta$ the coupling efficiency to our cavity, $P_{\mathrm{in}}$ the incident optical power, and $\xi$ a constant incorporating the technical homodyne detector measurement efficiency for both signal and local oscillator (see section 5.5.3). With relatively modest improvements an imprecision at the single-phonon level could be within reach, such as by improving $g_0$ and $\kappa$ by factors of $\sqrt{2}$ and 2, respectively, as well as increasing $\eta$ to $40\,\%$ from the $1.3\,\%$ estimated in the current device (see section 5.5.4), for example by employing waveguide-based coupling strategies [156]. The powers used for acquiring the data above are also low, corresponding to an average cavity occupancy of $\sim 0.2$ photons. At higher powers, the mechanical spectrum was affected by low-frequency noise of the laser through the effects explored in the next section, an effect that could be ameliorated by for example shorter measurement times.

It is important to note that to use such measurements to create quantum superposition states, significant further advances are needed: first, the nonlinear measurement rate should exceed the thermal decoherence rate, requiring an imprecision $n_{\mathrm{imp}} < (2\bar{n}_{\mathrm{th}})^{-1/2}$. As such, lower bath temperature and larger intracavity photon number would be highly beneficial. Second, active feedback at the mechanical frequency would be needed to suppress quantum backaction associated with the existent linear coupling. As noted by Brawley *et al.* [127], suppressing this to the single-phonon level requires a measurement efficiency $\zeta$ that satisfies $g_0^2/\kappa^2 > (1-\zeta)/(8\zeta)$, where $\zeta = h\eta$, and $h$ is the quantum efficiency of our measurement setup (see sections 5.5.3 and 5.5.4). Fulfilling this thus requires a strong investment in reaching near-unity extraction efficiencies and larger optical quality factors in these devices.

### 5.2.5. Radiation pressure force with large cavity fluctuations

The nonlinear regime not only impacts optical transduction of motion, but also pronouncedly affects the mechanical fluctuations themselves through its influence on radiation pressure backaction. The strongest manifestation of backaction in the regime where the cavity reacts nearly instantaneously to the mechanical motion ($\kappa \gg \Omega_{\mathrm{m}}$) is the optical spring effect, which alters the mechanical resonance frequency depending on the detuning between a drive laser frequency and the cavity resonance [7]. Figures 5.5a and 5.5d show experimentally obtained spectrograms at low temperature ($3\,\mathrm{K}$, incident optical power $20.6\,\mathrm{nW}$) and at room temperature ($295\,\mathrm{K}$, incident optical power $124\,\mathrm{nW}$) around the fundamental harmonic of one of the mechanical modes, while figs. 5.5c and 5.5f show several cross sections at selected detunings. At low temperature, the observed effect is very similar to the normal (linearized) optical spring effect, where a blue detuned laser shifts the mechanical frequency upwards and vice versa for red detuning. However, we additionally observe a broadening of the obtained spectra both when the laser is red- and blue-detuned by $\Delta \approx 10\,\mathrm{GHz}$ ($\sim \kappa/2$). At

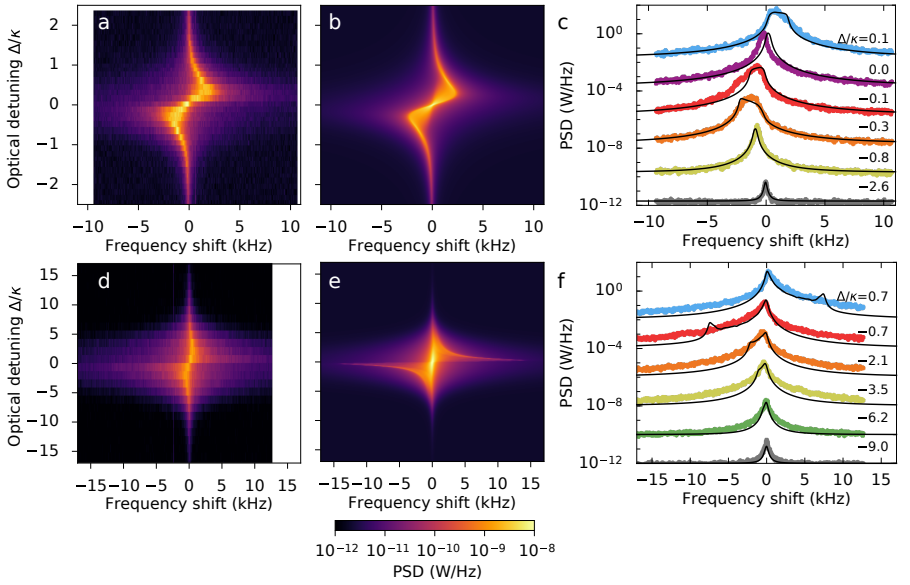


Figure 5.5: Optical spring effect modified by large cavity frequency fluctuations. (a,d) Experimental spectrograms, showing transduced mechanical spectra (horizontal axis) versus the optical laser frequency (vertical axis) at two different experimental conditions: (a) cooled at $3\,\mathrm{K}$, incident laser power $20.6\,\mathrm{nW}$; (d) room temperature, $295\,\mathrm{K}$, with incident laser power $124\,\mathrm{nW}$. (b,e) Simulated spectrograms corresponding to those shown in (a,d), obtained by calculating frequency shifts for a large number of motional amplitudes sampled from a thermal distribution, and averaging Lorentzian lineshapes with center frequencies given by the calculated shifts. The color bar below panel (e) is shared for all the spectrograms (PSD: power spectral density). (c,f) Individual spectra at various detunings (colored symbols), overlaid with the corresponding simulated spectrum (solid black lines). Spectra were offset by a factor of $10^2$ between them to avoid overlap.

room temperature, the spectra also become asymmetric: instead of a symmetric Lorentzian lineshape, the peak in spectra close to the optical resonance has a much steeper edge on one side than on the other side. In addition, the shift of the peak due to the optical spring effect usually scales linearly with the incident optical power, but the data set at room temperature shows a smaller, rather than a larger shift than the data set at $3\,\mathrm{K}$, even though the used optical power is five times higher.

To account for these observations, we again need to take the large fluctuations of the cavity frequency due to thermal motion into consideration. The typical optomechanical model for the optical spring effect is based on the linearized equations of motion [7] (see section 1.2.2), which do not apply in the nonlinear regime we reach here. To model a single mechanical mode, we instead calculate an effective spring constant from the first Fourier coefficient of the radiation pressure force, while the resonator oscillates harmonically, $x(t) = x_0 \cos \Omega t$. For this,

we express the radiation pressure force in the cavity as

$$F_{\text{rad}} = \frac{\hbar(\partial\omega_{\text{c}}/\partial x)n_{\text{c}}^{\text{max}}}{1+u^2}, \tag{5.4}$$

where $u \equiv \frac{2}{\kappa}(\Delta_0 - (\partial\omega_{\text{c}}/\partial x)x)$ with $\Delta_0$ the average detuning between the laser and cavity frequency, and $n_{\text{c}}^{\text{max}}$ is the maximum number of photons in the cavity when it is driven at resonance. The effective spring constant can be directly rescaled to obtain the frequency shift (see section 5.5.5). As before, we numerically sample a thermal distribution to model the behavior of the system, in this case by averaging over $10^4$ different amplitudes $x_0$, such that the displacement variance equals that from both mechanical modes in the experiment. Finally, we average the same number of Lorentzian lineshapes with the center frequencies given by the simulated frequency shifts and their widths set to the median linewidth measured in the experiment, to approximate the intrinsic linewidth at that temperature (see section 5.5.5). The resulting simulated spectra are shown in figs. 5.5b and 5.5e and plotted as black solid lines in figs. 5.5c and 5.5f. To allow overlaying the simulated spectra with the experimental cross sections, we rescaled all the simulated spectra such that the maximum value of the spectrum closest to resonance matched the experimental value. The model reproduces the broadening of the peaks as well as the asymmetry for the high-temperature data. At room temperature, a strong edge at larger frequency shifts is observed in the model, which is absent in the measurements. We attribute this to the presence of two mechanical modes, which will tend to soften this effect. An interesting feature in this model is that the spectra obtained with the laser on-resonance are not affected at all, and we indeed observed experimentally that at $\Delta_0/\kappa = 0$ the effect is much smaller if not entirely absent.

We also observe that at higher optical powers, beyond $\sim 100\,\text{nW}$ at $3\,\text{K}$, the influence of the nonlinear regime on the optical spring effect leads to imprinting of low-frequency noise on the mechanical motion as random drifting of the mechanical frequency. At higher powers still, self-oscillation regularly occurs. However, the fluctuations due to thermal motion can be larger than the amplitude at which a self-oscillating state would normally saturate, leading to highly complex dynamics. We believe this leads to observed irregular behavior, including random hopping of the oscillation frequency between the two mechanical modes, and occasional occurrence of instabilities for both blue and red detuning. Further study and modeling is needed to explore this regime.



## 5.3. Discussion

Our analysis of both nonlinear transduction and backaction relies on a numerical model instead of an analytical description, as the typical order-by-order approximation to describe transduction breaks down at large relative cavity fluctuation strengths. This breakdown is related to the fact that the Taylor expansion used to describe the intracavity field [127] as a function of the relative detuning $u \equiv \frac{2}{\kappa}(\Delta_0 - \delta\omega)$ does not converge for all $u$. For example, at average detuning

$\Delta_0 = 0$, the intracavity field can be written as

$$a = \frac{\sqrt{n_c^{max}}}{1+iu} \approx \sqrt{n_c^{max}}(1 - iu - u^2 + iu^3 + u^4 ...), \tag{5.5}$$

which does not converge for $|u| > 1$. At this detuning, $u = -2\delta\omega/\kappa$ represents the cavity frequency fluctuations due to the thermal motion, meaning the power series does not converge when the mechanical motion changes the cavity frequency by more than a linewidth. Therefore, this model cannot be used to extrapolate the expected sensitivity of optomechanical measurements in the nonlinear regime we describe here. Our numerical model relies on a direct calculation of the optical response to mechanical motion, which can be performed for any cavity frequency change $\delta\omega$. It is however crucial to correctly simulate the distribution of mechanical amplitudes within the thermal mechanical state.

We have demonstrated the effects of the optomechanical nonlinearity in a system that operates in the regime $\sqrt{2\bar{n}_{th}}g_0/\kappa \gtrsim 1$, and described how it modifies the optical response, transduction, and backaction over a wide range of temperatures. It is to be expected that a growing number of optomechanical systems will operate in this regime as parameters continue to improve, and the single-photon strong coupling regime ($g_0 > \kappa, \Gamma$) is approached. Indeed, various characteristics of the nonlinear regime we demonstrate are reminiscent of the expected effects due to quantum fluctuations in the single-photon strong coupling regime, including a modification of the optical response and the appearance of strong higher-order sidebands in optical fluctuation spectra. Whereas our sliced photonic crystal nanobeam devices demonstrate these effects for the bad-cavity limit, the regime has equally important impact for devices in the resolved-sideband regime ($\kappa \ll \Omega_m$), although precise manifestations are expected to vary. In particular, the optical excitation spectrum will be altered by displaying multiple discrete sidebands [132, 133]. Moreover, backaction forces acquire an additional delay factor due to the longer lifetime of cavity excitation, which will lead to fluctuating damping and driving forces affecting the motion. As the manipulation of mechanical thermal noise is a topic of interest, for example in sensing applications, it could be worthwhile to investigate the effects of the combination of dynamical backaction and the optomechanical nonlinearity. Notably, it would allow manipulating thermal fluctuations beyond a Gaussian distribution. Similar aims in the bad-cavity limit could be reached through nonlinear measurement, such as the displacement-squared measurements we demonstrated.

Interestingly, the alteration of the optical response due to thermal motion provides a new method to directly determine the intrinsic optical linewidth $\kappa$ and the optomechanical coupling rate $g_0$: the ratio of different harmonics of the transduced mechanical spectrum allows retrieving the relative frequency fluctuations $\delta\omega_{rms}/\kappa$. Together with a measurement of the optical excitation linewidth (see section 5.4.4, eq. (5.7)) this uniquely determines both $g_0$ and $\kappa$. This method only requires further knowledge of the bath temperature and the mechanical frequency. We note that there is no need for any other calibration, including characterization of optical powers.

The large single-photon cooperativity $C_0$ in the structures we present here offers prospects beyond the exploitation of the optomechanical nonlinearity, in particular for quantum measurement and control of mechanical motion. For example, the requirement for feedback cooling to the ground state (thermal occupancy below 1) is that the cooperativity $C_0 n_\mathrm{c} > \bar{n}_\mathrm{th}/(9\zeta - 1)$, where $n_\mathrm{c}$ is the number of photons in the cavity [27, 41, 89]. In our sliced nanobeam structure, the measurement sensitivity is currently limited by the coupling efficiency, which we estimate to be $\eta \approx 1.3\,\%$ (see section 5.5.4). The double-period modulation method we use to improve the coupling efficiency of a photonic crystal nanobeam cavity at normal incidence has previously been shown [100] to yield a simulated collection efficiency of more than $20\,\%$. Therefore we expect that by either improving the optical design, or by employing waveguide-based coupling schemes [89, 156], the coupling can be further increased in our current free-space set-up. For example, with a detection efficiency of $2/9$, ground state preparation would be in reach at a very modest minimum cavity occupancy of $n_\mathrm{c} > 17$ photons with the demonstrated parameters. Finally, the large optomechanical coupling strength in combination with low loss provides other opportunities for measurement-based control in the bad-cavity limit, such as conditional state preparation of the mechanical resonator by pulsed measurements [119], or quantum state swapping between the optical and mechanical degrees of freedom [139].

## 5.4. Methods

### 5.4.1. Sliced photonic crystal nanobeam design and fabrication

A comprehensive description of the cavity design can be found in chapter 3. The device presented in this chapter is based on the periodic parameters labeled "Mirror N"/"Cavity N" in table 3.1, with the periodicity scaled by $90\,\%$ to shift the cavity resonance frequency into the range of the laser. We use a taper region of five holes and create a low-efficiency outcoupling grating in the structure by making the hole sizes alternatingly $5\,\%$ wider and narrower. Our experimental results indicate that this double-period modulation strategy (see section 3.3.4) increases the coupling efficiency to the optical cavity from approximately $0.1\,\%$ to 1–2 % (see section 5.5.4).

The fabrication process is described in detail in section 3.4. The devices presented here are fabricated from a silicon-on-insulator substrate (SOITEC) with $3\,\mu\mathrm{m}$ silicon oxide below a $250\,\mathrm{nm}$ silicon device layer, on top of which we spin-coat an $80\,\mathrm{nm}$ thick layer of HSQ resist. The silicon layer is etched in an inductively coupled plasma etcher using a combination of $Cl_2$ and $HBr/O_2$ gases.

We note that the fabricated devices exhibit optical quality factors that are somewhat lower (by a factor $\sim 2$) compared to the designed value, likely due to remaining surface roughness, and structural deviation from the designed pattern.

### 5.4.2. Measurement setup

A closed-cycle cryostat (Montana Cryostation C2) was used to control the sample temperature between 3 and $300\,\mathrm{K}$. We used an aspheric lens positioned out-

side the cryostat window with an effective focal length of $8\,\mathrm{mm}$ and a numerical aperture of $0.55$ to focus the laser beam (New Focus Velocity 6725, linewidth $\leq 200\,\mathrm{kHz}$) on the sample and to collect the reflection in free space. A balanced detector with two nominally identical photodiodes (New Focus 1817-FS) detected the output of the homodyne interferometer, schematically shown in fig. 5.1c. The detector signal was then Fourier transformed and the spectrum recorded with an electronic real-time spectrum analyzer (Agilent MXA). The optical power in the reference arm was $135\,\mu\mathrm{W}$ or more, ensuring that the optical shot noise was at least as large as the electronic noise. The pressure in the cryostat was typically $0.3\,\mathrm{mbar}$ at room temperature, and well below $10^{-4}\,\mathrm{mbar}$ at cryogenic temperatures.

A measurement of the power dependence of the transduced signal (see section 5.5.1) was performed to verify that the measurement of the thermal motion of the nanobeam is not influenced by additional heating by the laser beam down to the lowest temperature. We then used the temperature sensor placed next to the sample in the cryostat to calibrate the scale for the displacement power spectral density $S_{xx}$ in fig. 5.2a and fig. 5.4b. Measurements with different thermal radiation heat loads show that the presence of a cold window ensures that the sample is thermalized at all temperatures (see section 5.5.2).

### 5.4.3. Nonlinear transduction with order-by-order approximation

In section 4.2.6 we derived an expression for higher-order transduction in the case of a direct reflection measurement. To derive that expression, we used an order-by-order approximation, valid for small fluctuations $\delta\omega_{\mathrm{rms}} \ll \kappa$, which essentially uses the fact that to leading order, $\cos^k \Omega t = \cos(k\Omega t)/2^{k-1}$, such that the $k$-th term in the Taylor expansion of the measurement output $P$ contributes only at its own frequency $k\Omega$. By considering the $k$-th order derivative of the measurement output to the cavity resonance frequency, $(\partial^k P/\partial\omega^k)$, we can find a similar expression for the higher-order transduction of thermal motion in the case of balanced homodyne detection. Averaging over the homodyne phase, the detuning dependence for $(\partial^k P/\partial\omega^k)^2$ has a simple Lorentzian lineshape, raised to the power $(k+1)$, as we showed in section 1.5.5. The maximum contribution is therefore at resonance ($\Delta_0 = 0$) and can be expressed as

$$\left(\frac{\partial^k P}{\partial\omega^k}\right)^2 = A^2 k!^2 \left(\frac{2}{\kappa}\right)^{2k}, \tag{5.6}$$

where $A^2 = 8P_{\mathrm{in}}P_{\mathrm{LO}}\eta^2$ is a constant prefactor that depends on the optical powers $P_{\mathrm{in}}, P_{\mathrm{LO}}$ in the signal and reference arm, respectively, and on the coupling efficiency to the cavity $\eta$. This result can directly be substituted into eq. (4.9) to obtain eq. (5.2).

Figure 5.6 shows a spectrogram demonstrating the detuning dependence of the nonlinear transduction.

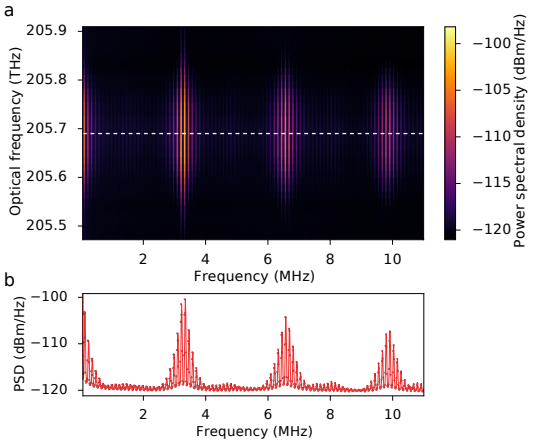


Figure 5.6: Nonlinear transduction as a function of detuning. (a) Electronic spectrum analyzer signal taken at room temperature, as a function of the optical frequency. (b) Cross section at cavity resonance frequency corresponding to fig. 5.3a. As can be seen in (a), due to the quadrature-averaged homodyne detection, all peaks show a single-peaked detuning dependence which is maximum at resonance.

### 5.4.4. Power spectral density and Voigt linewidth

We plot the power spectral density of the electronic output signal of our measurement setup, which has units of $\mathrm{W\,Hz^{-1}}$. This corresponds to a power spectral density of a (virtual) optical power $P$, $S_{PP}$, which has units of $\mathrm{W^2\,Hz^{-1}}$. As a consequence, the Lorentzian detuning dependence of the optomechanical transduction leads to a Lorentzian-squared dependence in the power spectral density. Similarly, we observe the square of the Gaussian distribution of cavity frequencies due to thermal motion. Therefore, we fit the square of a Voigt lineshape, which models the convolution of a Lorentzian and a Gaussian lineshape, to our data, and extract the linewidth of the non-squared Voigt lineshape. This value then directly corresponds to either the optical loss rate $\kappa$ or the amplitude of the frequency fluctuations $\delta\omega_{\mathrm{rms}}$, in the respective limits where $\kappa \ll \delta\omega_{\mathrm{rms}}$ or vice versa.

We use an empirical equation for the linewidth of a Voigt lineshape [157]

$$0.5346\kappa + \sqrt{0.2166\kappa^2 + 8\ln 2\,\delta\omega_{\mathrm{rms}}^2}, \tag{5.7}$$

where $\kappa$ is the linewidth of the Lorentzian lineshape and $2\sqrt{2\ln 2}\delta\omega_{\mathrm{rms}}$ is the linewidth of the Gaussian lineshape. To fit the linewidth as a function of temperature, we substitute $\delta\omega_{\mathrm{rms}} = \sqrt{2g_0^2 k_{\mathrm{B}} T/\hbar\Omega_{\mathrm{m}}}$. To account for multiple independent mechanical modes, we can calculate the individual optomechanical coupling rates from the asymptote of the fit curve if we know the ratio between the transduced peaks in the spectrum (see section 3.2.3). The variances due to the modes $j$ add up, $\delta\omega_{\mathrm{rms}}^2 = \sum_j \langle\delta\omega_j^2\rangle$, which means eq. (5.1) is modified to

$$\delta\omega_{\mathrm{rms}}^2 = 2k_{\mathrm{B}}T\sum_j \frac{g_{0,j}^2}{\hbar\Omega_{\mathrm{m},j}}. \tag{5.8}$$

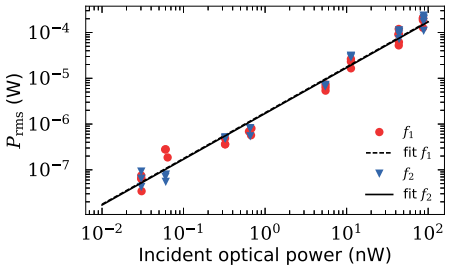


Figure 5.7: Power dependence. Measured band power of the two fundamental mechanical frequencies $f_1$ and $f_2$ (area under the fitted Lorentzian peak) as a function of the incident optical power $P_{\mathrm{in}}$, with the laser frequency on-resonance with the cavity. The power in the reference arm, $P_{\mathrm{LO}}$, was kept constant. The black dashed and solid lines show linear fits to the data for $f_1$ and $f_2$, respectively.

### 5.4.5. Numerical model for nonlinear transduction

Time traces for the mechanical displacement $x$ were generated for one or two resonance frequencies $\Omega_{\mathrm{m}}$. To simulate thermal motion, we randomly change the amplitude $A$ and phase $\varphi$ of harmonic motion $x = A\cos(\Omega_{\mathrm{m}}t + \varphi)$. The points at which $A$ and $\varphi$ are changed are taken from a Poissonian distribution with mean time between jumps taken to be the mechanical damping time $1/\Gamma$. The new amplitude is taken from an exponential distribution characterized by a mean proportional to the average thermal occupancy $\bar{n}_{\mathrm{th}}$, while the phase is taken from a uniform distribution. A time trace of the measurement output $P$ was generated from the position time trace using our full model for the transduction (eq. (1.66)) and phase-averaging the homodyne measurement. The discrete Fourier transform of this time trace allowed us to extract the signal strength at $\Omega_{\mathrm{m}}$ and at higher-order multiples or mixing terms.

## 5.5. Appendices

### 5.5.1. Power dependence of transduced mechanical motion

The transduction of mechanical motion depends on the optical power used, as shown in the dependence of $\langle P^2 \rangle$ on $A^2 \propto P_{\mathrm{in}}P_{\mathrm{LO}}$ in eq. (5.2). In particular, we expect the measured band power to be linear in both the power in the signal arm $P_{\mathrm{in}}$, incident on the cavity, and the power in the reference arm $P_{\mathrm{LO}}$. Deviations from a linear relation indicate heating or cooling of the mechanical motion due to the additional laser power [7]. Figure 5.7 shows transduced mechanical motion as a function of the incident optical power, with the laser on-resonance with the cavity and while the device was cooled to $3\,\mathrm{K}$. The data was corrected for the local oscillator power, which was mostly kept constant and did not vary by more than a factor ten. At higher powers (near $100\,\mathrm{nW}$), fluctuations in the center frequency and shape of the peak could be observed (similar to the effects shown off-resonance in fig. 5.5), however the peak area still follows the linear dependence as a function of the optical power incident at the structure. This shows that for all probe powers used here, there is no significant heating due to the incident

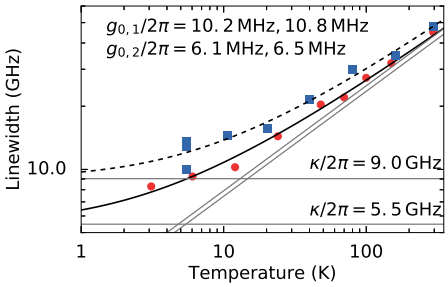


Figure 5.8: Characterization of a second device, using the temperature dependence of the optical linewidth. For the data set with blue squares a second cryostat window at $50\,\mathrm{K}$ was not in place, hence exposing the sample to thermal radiation from the outer window at room temperature. The solid and dashed black lines are fits with a model that assumes a constant Lorentzian intrinsic linewidth $\kappa$ convolved with a Gaussian with a width $L_\mathrm{G}$ that depends on $\sqrt{T}$. The asymptotes (straight gray lines) of the fit functions allow us to extract $\kappa$ and the optomechanical coupling rates $g_{0,i}$ for the two mechanical modes ($i = 1, 2$). Extracted values are shown in the figure. We assign the discrepancy in extracted values of $\kappa$ to bad thermalization of the sample in the case where the inner window was not in place.

laser light.

### 5.5.2. Characterization of a second device and thermalization estimate

The data labeled as “device 2” were taken on a sample with a slightly different design, which had a different shape of the holes, and did not include the double-period modulation to increase the outcoupling. The design parameters can be found in table 3.1 as “Cavity L”/“Mirror L”. The optical linewidth as a function of temperature for this device is shown in fig. 5.8, in two separate data sets. The data set shown by blue squares was taken with only one window in the cryostat, which was at room temperature, such that the sample was not shielded from thermal radiation. The other data set was taken with the second window (cooled to around $50\,\mathrm{K}$) in place. Therefore the sample temperature for the blue data set was most likely higher than the thermometer temperature, which we used to plot and fit these data. Although this leads to a relatively large difference in the fitted optical loss rate $\kappa$, both data sets yield very similar coupling rates $g_0$, since at high temperatures the sample is well thermalized. We note that the different estimate of $\kappa$ in the absence of the cold window is of course the direct result of the fact that the nanobeam temperature is larger than that of the nearby thermometer (which is plotted on the horizontal axis of fig. 5.8). Comparing the solid and dashed curves shows that the temperature is raised by ∼10 degrees from the base temperature. Since this temperature rise can be related to the presence of the nearby $300\,\mathrm{K}$ window, we can now estimate the rise that is expected due to the $\sim 50\,\mathrm{K}$ cold window that is in place during all other measurements presented in this chapter. Assuming a $\propto T^4$ dependence of heat transfer rates results in an expected temperature rise of $\sim 0.1\,\mathrm{K}$. This shows that the nanobeams are very

likely thermalized well down to the lowest cryostat temperatures. We finally remark that it is not straightforward in our case to verify thermalization using a phase modulation calibration, as described by Gorodetsky *et al.* [52]: the strong intrinsic cavity frequency modulation means that such a calibration tone will inevitably mix with the mechanically-induced modulations, such that its magnitude is strongly altered and in fact itself depends on temperature.

### 5.5.3. Quadratic displacement measurements

The signal-to-noise ratio (SNR) of a quadratic displacement measurement, in the regime where the order-by-order approximation is valid, can be found by considering eq. (5.2), and assuming the measurement is shot-noise limited. If the optical power in the reference arm is much larger than in the signal arm of the interferometer ($P_{\mathrm{LO}} \gg P_{\mathrm{in}}$), the power spectral density due to the optical shot noise is given by $S_{PP}^{\mathrm{SN}} = \hbar\omega_{\mathrm{c}} P_{\mathrm{LO}} h'$, with $h'$ quantifying the measurement efficiency for the local oscillator light (that is, losses between the homodyne beamsplitter and the detector, and the quantum efficiency of the detector). The band power at $2\Omega_{\mathrm{m}}$ due to thermal mechanical fluctuations is given by eq. (5.2), with $k = 2$ and $\langle \delta\omega^2 \rangle = 2\bar{n}_{\mathrm{th}} g_0^2$, leading to

$$\langle P^2 \rangle_{2\Omega_{\mathrm{m}}} = 512 P_{\mathrm{in}} P_{\mathrm{LO}} h \eta^2 \left(\frac{g_0}{\kappa}\right)^4 \bar{n}_{\mathrm{th}}^2, \tag{5.9}$$

where we also substituted $A^2 = 8 P_{\mathrm{in}} P_{\mathrm{LO}} h \eta^2$, where $h$ accounts for the finite measurement efficiency for the signal beam (see section 5.5.4). The power spectral density will show a Lorentzian peak with linewidth $2\Gamma$ at the frequency $2\Omega_{\mathrm{m}}$, which means its peak value is related to the band power (area under the peak) as $S_{PP}^{\mathrm{max}} = \langle P^2 \rangle_{2\Omega_{\mathrm{m}}} / 2\Gamma$. Finally, we take the signal-to-noise ratio

$$\mathrm{SNR} \equiv \frac{S_{PP}^{\mathrm{max}}}{S_{PP}^{\mathrm{SN}}} = 256 \frac{P_{\mathrm{in}} \xi \eta^2}{\hbar\omega_{\mathrm{c}}\Gamma} \left(\frac{g_0}{\kappa}\right)^4 \bar{n}_{\mathrm{th}}^2, \tag{5.10}$$

where we have defined $\xi \equiv h/h'$. We set SNR to $1$ to find the imprecision in terms of a phonon number $n_{\mathrm{imp}}$, leading to

$$\frac{1}{n_{\mathrm{imp}}} = 16 \left(\frac{g_0}{\kappa}\right)^2 \eta \sqrt{\frac{P_{\mathrm{in}} \xi}{\hbar\omega_{\mathrm{c}}\Gamma}}. \tag{5.11}$$

Figure 5.9 shows additional data for the quadratic measurement presented in fig. 5.4. The top panel shows the peak around the fundamental frequency decrease at the same piezo mirror position where the peaks at twice the frequency are strongest, further confirming the ability to suppress the linear measurement while performing the quadratic measurement. The bottom panel shows the linear and quadratic measurements at optimum positions of the piezo mirror for both fundamental frequencies and all four second-order combinations.

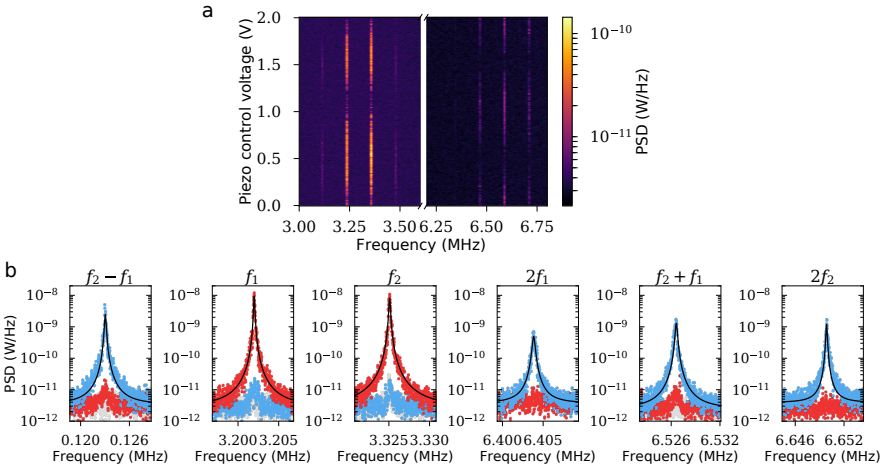


Figure 5.9: Selective linear and quadratic measurement. (a) Spectra showing the first and second order transduction obtained simultaneously, as a function of the piezo mirror position. (b) Maximum and minimum linear and quadratic transduction at different settings of the homodyne phase, for the fundamental frequencies $f_1$ and $f_2$ as well as all second-order peaks. Red (blue) data points: homodyne phase set to maximize linear (quadratic) transduction; black solid lines show Lorentzian fits to the peaks. Grey data points were taken with no incident optical power in the signal arm. For these measurements, the sample was at $3\,\mathrm{K}$, and incident optical power was $12.8\,\mathrm{nW}$.

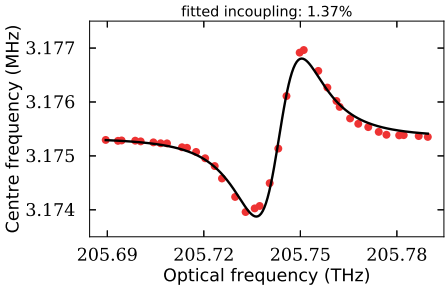


Figure 5.10: Optical spring effect at low temperature. The data points show the fitted center frequency of the mechanical resonance $f_1$ with the structure at $3\,\mathrm{K}$ and $P_{\mathrm{in}} = 20.6\,\mathrm{nW}$, as a function of the laser frequency (corresponding to the data set shown in fig. 5.5a). The solid line shows a fit of the data according to the linearized model for the optical spring effect, where the magnitude of the effect depends on the incoupling efficiency $\eta$. The extracted value is shown in the figure.

### 5.5.4. Coupling and measurement efficiency

Figure 5.10 shows the fitted center frequency of the mechanical resonance $f_1$ at $3\,\mathrm{K}$ with $P_{\mathrm{in}} = 20.6\,\mathrm{nW}$, corresponding to the spectrogram shown in fig. 5.5a. Fitting the change in frequency as a function of the optical detuning with the function describing the optical spring effect in the bad-cavity limit [7] (see section 4.2.4) provides us with an estimate of the incoupling efficiency $\eta$. We measure the optical power $P_{\mathrm{in}}$ before the objective lens, so aside from polarization mismatch and mode overlap with a Gaussian beam, $\eta$ also includes transmission losses from the (antireflection-coated) objective lens and two (uncoated) cryostat windows. The average over five measurements at different input power yielded a coupling efficiency $\eta = 1.3\,\%$, with a standard deviation of $0.3\,\%$.

This analysis ignores the effects of the large thermal fluctuations, which as we show in section 5.2.5 broadens and reduces the strength of the optical spring effect. This means the obtained coupling efficiency provides a lower limit for the actual coupling efficiency. However, the numerical model we used to generate the simulated spectra in fig. 5.5 shows that the fluctuations at $3\,\mathrm{K}$ mainly broaden the mechanical spectra but do not yet lead to strong reduction in the strength of the optical spring effect.

In order to characterize the full measurement efficiency $\zeta = h\eta$, we also need to consider the quantum efficiency of our homodyne detection ($h$). This includes mainly the overlap of the signal and local oscillator beams ($\sim 40\,\%$ in the measurements presented), and the quantum efficiency of our photodiode ($\sim 80\,\%$). We also lose some photons via losses in the optical path and by using a variable aperture to balance the powers reaching the two photodiodes of our balanced photodetector. Overall, we estimate $h \approx 25\,\%$ in experiments in this chapter. We note that we did not try extensively to optimize $h$, and we expect it could be improved significantly with modest effort. This would be essential for the feedback schemes mentioned in section 5.2.4.

### 5.5.5. Radiation pressure force model

We express the radiation pressure force in the cavity as

$$F_{\mathrm{rad}} = \frac{\hbar(\partial\omega_{\mathrm{c}}/\partial x) n_{\mathrm{c}}^{\mathrm{max}}}{1+u^2}, \tag{5.12}$$

where $u \equiv \frac{2}{\kappa}(\Delta_0 - (\partial\omega_{\mathrm{c}}/\partial x)x)$ and $n_{\mathrm{c}}^{\mathrm{max}}$ is the maximum number of photons in the cavity when it is driven at resonance. We assume the resonator moves harmonically: $x(t) = x_0 \sin\Omega t$. This results in a time-dependent normalized detuning $u(t) = u_0 - u_x \sin\Omega t$, where $u_x = 2(\partial\omega_{\mathrm{c}}/\partial x)x_0/\kappa$.

Given an amplitude $x_0$, we extract the first Fourier coefficient of the force (at the resulting harmonic frequency $\Omega$):

$$a_1^{\mathrm{rad}} = \frac{\Omega}{\pi}\int_0^{2\pi/\Omega} F_{\mathrm{rad}}(t')\sin\Omega t' dt'. \tag{5.13}$$

In analogy with the mechanical restoring force, we can calculate an effective

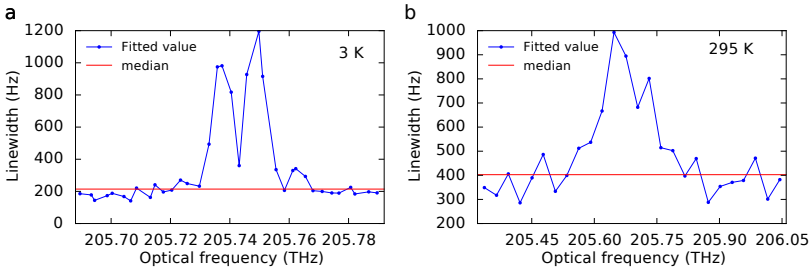


Figure 5.11: Fitted mechanical linewidth as a function of laser frequency at (a) $3\,\mathrm{K}$ and (b) $295\,\mathrm{K}$, corresponding to the detuning sweeps shown in figs. 5.5a and 5.5d. The solid horizontal lines show the median value of the fitted linewidth, which was used as the intrinsic linewidth for the simulated spectrograms shown in figs. 5.5b and 5.5e.

spring constant from the Fourier coefficient: with $F = -kx$ and $x(t) = x_0 \sin \Omega t$, $F = \sum_{n=1}^{\infty} a_n \sin n\Omega t$ implies that $a_1 = -kx_0$.

Finally, a correction on the spring constant results in a correction on the frequency $\Omega$:

$$\Omega = \sqrt{\frac{k + k_{\mathrm{rad}}}{m}} = \sqrt{\frac{k}{m}}\sqrt{1 + \frac{k_{\mathrm{rad}}}{k}}, \tag{5.14}$$

which we can approximate using $\sqrt{1+x} \approx 1 + x/2 + ...$:

$$\Omega \approx \sqrt{\frac{k}{m}}(1 + \frac{k_{\mathrm{rad}}}{2k}), \tag{5.15}$$

therefore

$$\delta\Omega \approx \sqrt{\frac{k}{m}}\frac{k_{\mathrm{rad}}}{2k} = \frac{k_{\mathrm{rad}}}{2m\Omega}. \tag{5.16}$$

To obtain the results presented in fig. 5.5, we perform this calculation for $10^4$ amplitudes $x_0$. These amplitudes are sampled from a Rayleigh distribution, which describes the thermal motion (equivalently, we take $\sqrt{x_1^2 + x_2^2}$ with $x_1, x_2$ independently sampled from a normal distribution). The mean amplitude is set such that the variance of $u$ corresponds to the total variance we expect from both mechanical modes, using the measured values of $\kappa, g_{0,i}, \Omega_{\mathrm{m},i}$ and the temperature. To generate spectra that can be compared to the experimental data, we then average together Lorentzian lineshapes with center frequencies given by the resulting set of frequency shifts. Since the mechanical linewidth changes with temperature, we choose the widths of these individual Lorentzian peaks based on the median value of the measured linewidth. As fig. 5.11 shows, this is a good approximation of the intrinsic mechanical linewidth, which we measure for large detuning.

# 6

# Pulsed optomechanical measurements

*The sensitivity of continuous measurements of the displacement of a mechanical resonator is limited by the standard quantum limit, which leads to a minimum displacement uncertainty equal to the ground-state uncertainty $x_{zpf}$. By probing a mechanical resonator with a short, pulsed measurement, one can in principle measure the displacement of a mechanical resonator to arbitrary precision, even below this limit. The state, conditional on the outcome of such a pulsed measurement, has a narrower probability distribution than the initial state, an effect that can be interpreted as "cooling by measurement." Since the pulsed measurements only interact with the system for a short time, achieving high sensitivity requires a strong interaction of the measurement probe with the resonator.*

*Here, we implement and analyze pulsed optical readout of our sliced photonic crystal nanobeam system. We find an upper limit for the imprecision of our measurements of $60\,x_{zpf}$ and discuss the improvements that could lead to a sensitivity below the standard quantum limit.*

## 6.1. Theory of pulsed optomechanical interaction

Measurements play a central role in quantum theory and experiments. The influence and definition of measurements in quantum physics has historically been the topic of heated debate. Experimental evidence gathered over a century has decisively shown that quantum systems behave differently when they are measured than they do when they are allowed to evolve freely. Although the philosophical interpretation of this is still up for debate, the mathematical framework of quantum measurements rests on a solid experimental ground [1, 2].

Two fundamental (and connected) properties that arise from this framework are the quantum state modification due to measurements, and the fundamental limits to the precision with which some observables can be simultaneously measured. The fuzzy state of a quantum system before a measurement ("wavefunction") can be localized to a state with a precisely known value of the measured observable ("eigenstate") by a measurement, at the cost of losing all predictive power for other, incompatible, observables. The canonical example is an infinitely accurate measurement of the position of a free particle, which will inevitably give the particle a totally unpredictable force kick, hence losing all information about its momentum. As the position measurement is made weaker, the disturbance of the momentum also becomes weaker, leading to a fundamental limit on the product of the uncertainty of these two observables: the Heisenberg uncertainty relation.

In this chapter we discuss pulsed optical measurements of the mechanical displacement of a resonator. In principle, such pulsed measurements could be made arbitrarily short and precise—at the cost of disturbing the momentum of the resonator. We first introduce this concept in more detail.

### 6.1.1. Concept

In previous chapters, we discussed continuous measurements of the displacement $x$ of a mechanical resonator. Such measurements are fundamentally limited in sensitivity by the standard quantum limit [1, 7], which is essentially a manifestation of Heisenberg's uncertainty principle, because a continuous measurement record of $x$ also provides information on the momentum $p$ of the resonator. The limit is enforced by the photon shot noise of the light used to probe the resonator, which imprints fluctuations on the displacement via the radiation pressure force. This stochastic force directly changes the momentum of the mechanical resonator, leading to a change in displacement a short time later. A mechanical resonator moves harmonically on timescales significantly shorter than its damping time [158], so a change of momentum at time $t = 0$ does not affect the displacement of a resonator with period $T_\mathrm{m}$ at times $t = kT_\mathrm{m}/2$, an integer number $k$ of half-periods later. To discuss this in a more quantitative way, we define the quadratures of motion of a mechanical resonator with mass $m$ and resonance frequency

$\Omega_\mathrm{m} = 2\pi/T_\mathrm{m}$ in terms of the displacement and momentum $x$ and $p$:

$$X = \sqrt{\frac{m\Omega_\mathrm{m}}{\hbar}}x = \frac{x}{\sqrt{2}x_\mathrm{zpf}}, \tag{6.1}$$

$$P = \sqrt{\frac{1}{\hbar m\Omega_\mathrm{m}}}p = \frac{p}{\sqrt{2}x_\mathrm{zpf}m\Omega_\mathrm{m}}. \tag{6.2}$$

Harmonic motion of the oscillator can be decomposed in terms of slowly-evolving co-rotating quadratures $X_\mathrm{r}, P_\mathrm{r}$ [51, 159]:

$$X(t) = X_\mathrm{r}(t)\cos\Omega_\mathrm{m}t + P_\mathrm{r}(t)\sin\Omega_\mathrm{m}t, \tag{6.3}$$

$$P(t) = P_\mathrm{r}(t)\cos\Omega_\mathrm{m}t - X_\mathrm{r}(t)\sin\Omega_\mathrm{m}t. \tag{6.4}$$

From this, it follows that a change in the momentum at $t = 0$ (that is, a change in $P_\mathrm{r}(t)$) will result in a change in displacement a quarter of a period later, when $\Omega_\mathrm{m}t = \pi/2$. The change in momentum has no influence on a measurement if one makes sure to probe only one of the quadratures, for example by modulating the measurement strength such that one only measures when $\sin\Omega_\mathrm{m}t \approx 0$. Such measurements are called backaction-evading (BAE) [159, 160]. These make it possible to measure one quadrature ($X_\mathrm{r}$) with in principle arbitrary precision, letting measurement backaction (i.e., radiation pressure shot noise) only affect the quadrature that is not measured ($P_\mathrm{r}$).

Two natural ways to implement BAE measurements in optomechanical systems are stroboscopic and pulsed measurements. Stroboscopic measurements [51] rely on periodically modulating the intensity in the optical cavity to modulate the measurement strength. This is achieved by sending in an intensity-modulated laser beam. Due to the two sidebands such a beam has in frequency space, this technique is also referred to as two-tone driving. In microwave circuit optomechanical systems, several experimental demonstrations of the stroboscopic measurement technique were reported [32, 161, 162]. For optomechanical systems that are not in the resolved-sideband regime, that is, $\kappa \gg \Omega_\mathrm{m}$, the stroboscopic technique also measures the conjugate quadrature via terms oscillating at $2\Omega_\mathrm{m}$. Therefore, in this regime, stroboscopic measurements are not backaction-evading. However, with a fast cavity response, it is possible to perform pulsed optical measurements which are shorter than a mechanical period [119]. In addition to characterizing the state of the mechanical resonator, such pulsed measurements can also be useful in state preparation or purification [119], as we explain below. A proof-of-principle experiment using this technique in the classical regime was performed by Vanner *et al.* [116] at room temperature using an interferometer measurement of the position of a mirror on a cantilever.

A quantum state represents our knowledge about the outcomes of our future measurements on a system [2]. By measuring the displacement of the resonator at a particular point in time, we reduce uncertainty: the resulting state, conditional on the outcome of the measurement, has a narrower probability distribution. In other words, we need the measurement outcome to predict future measurements

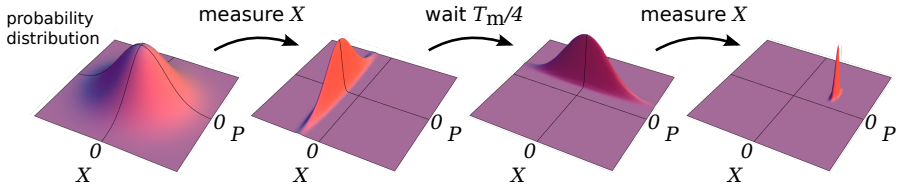


Figure 6.1: Visual representation of the probability distribution of the displacement and momentum quadratures (see eq. (6.2)) of a mechanical resonator during a measurement sequence with two fast measurements of displacement, separated by a delay of $T_\mathrm{m}/4$, a quarter of the resonant period. Without external input (including decoherence), the state evolves according to eq. (6.4). Initially, the resonator is in a thermal state, where $X$ and $P$ are normally distributed around $0$. Measuring the displacement yields a state with a known $X$, with uncertainty determined by the measurement accuracy, while slightly increasing the uncertainty in momentum $P$ due to the radiation pressure shot noise.

with less uncertainty that we had initially. We note that, for an independent observer, who does not have access to our measurement result, the uncertainty of the state has not changed (or more accurately, it has actually increased in the quadrature we did not measure, due to the measurement backaction). The conditional, lower-uncertainty state could be considered as having a lower entropy, or effective temperature than the initial, thermal state. In other words, this constitutes a form of *cooling by measurement*. In fig. 6.1, the scheme proposed by Vanner *et al.* [119] is schematically illustrated. Initially, the quadratures $X, P$, as well as the displacement and momentum $x$ and $p$, are normally distributed in a thermal state with variance $\langle x^2 \rangle = 2x_\mathrm{zpf}^2 k_\mathrm{B} T/\hbar\Omega_\mathrm{m}$, where $k_\mathrm{B}$ is the Boltzmann constant, $T$ is the temperature, and $\hbar$ is the reduced Planck constant. This initial thermal state is shown with the 2-D Gaussian distribution in the left-most panel in fig. 6.1. After a measurement of the displacement at $t = 0$ (second panel), $X_\mathrm{r}$ is known with an uncertainty determined by the measurement accuracy, which means the uncertainty is reduced with respect to the initial state. In principle, the same procedure can be applied to the second quadrature, $P_\mathrm{r}$, about which no knowledge has been gained with the first measurement. To do so, one first waits for a quarter of the mechanical resonance period $T_\mathrm{m}$ (third panel), after which the state has evolved such that the displacement $X$ (shown on the axis in fig. 6.1) is totally determined by the co-rotating quadrature $P_\mathrm{r}$, which still has the uncertainty due to thermal motion. The momentum is now determined by $X_\mathrm{r}$, which is known from the first measurement. If one now additionally performs a second displacement measurement, $P_\mathrm{r}$ is also determined with an uncertainty set by the measurement accuracy. This leads to a state with a much lower uncertainty than it initially had due to the thermal motion, for one or both quadratures of the motion.

After such a measurement of one or both quadratures, one can (partly) predict the trajectory of the resonator while $X_\mathrm{r}(t), P_\mathrm{r}(t)$ have not yet changed appreciably. Fundamentally, the only unavoidable factors influencing the resonator are the thermal bath and the measurement itself. We will discuss the thermal decoherence in section 6.1.3. To include the effect of measurement backaction into our analysis, we need to take into account that the measurements of displace-

ment will disturb the momentum of the resonator, in this case due to the radiation pressure shot noise. Therefore after the first measurement, the uncertainty in $P_\mathrm{r}$ is increased. However, for an optimal quantum-limited measurement, this effect contributes only an additional variance of $x_\mathrm{zpf}^2$ in units of the displacement $x$ (equivalent to the limit for continuous measurements). For measurements with finite measurement efficiency $\zeta$, a measurement with an imprecision equal to the ground state uncertainty will induce more backaction, with a variance of $x_\mathrm{zpf}^2/\zeta$. We note that this contribution will most likely be a small effect relative to the initial thermal distribution. The effect of a second measurement, if performed, is equivalent, increasing the uncertainty of $X_\mathrm{r}$ above the "initial" value, which in this case is given by the measurement accuracy.

The main challenge for performing pulsed measurements is that it requires a large measurement strength, such that the measurement uncertainty can be reduced below the quantum limit even for a pulse much shorter than one mechanical resonance period. To reach the standard quantum limit for continuous measurements, the measurement time in which this condition is reached is a full mechanical damping time, which is $Q_\mathrm{m}$ times longer than the mechanical period. The shorter measurement time can be compensated by using a higher optical intensity, but eventually nonlinear effects prevent the further increase of optical intensity (see section 1.3.2 and appendix A). The sliced nanobeam structure provides an opportunity to reach backaction-evading pulsed displacement measurements, due to the large optomechanical coupling rate. This could allow reaching the required large measurement strengths with a limited optical intensity.

### 6.1.2. State tomography

State tomography refers to the use of repeated measurements on a well-prepared ensemble to retrieve probability distributions of system variables [53]. One can retrieve the position distribution of a mechanical resonator by performing many pulsed position measurements. Information of momentum can be gained by first allowing the state to evolve for a quarter period. To fully reconstruct the quantum state of the resonator, measurements are needed for all different delays $0 < \tau \leq 2\pi/\Omega_\mathrm{m}$, corresponding to different projections $X_\theta = X_\mathrm{r}\cos\theta + P_\mathrm{r}\sin\theta$, with $\theta = \Omega_\mathrm{m}\tau$ [1, 115].

Conditional states can also be characterized using tomographic methods, if one analyzes the differences between the outcome of a tomographic measurement and the conditioning measurement that precedes it. In the following, we will focus on Gaussian states, where the quadratures $X_\mathrm{r}$, $P_\mathrm{r}$ are normally distributed. Prior to a measurement, the initial thermal state of the resonator is a Gaussian state with equal width in both quadratures. Moreover, after a measurement, the corresponding quadrature of the conditional state is also normally distributed around the measurement outcome, with a width determined by the measurement accuracy. We note that in this latter case the width of the distribution can be different for the two quadratures.

Figure 6.2 shows expected distributions of ideal measurement outcomes, when the mechanical resonator is in a state with a Gaussian probability distribution

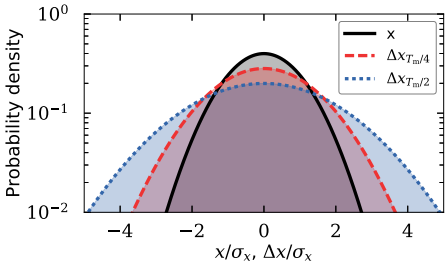


Figure 6.2: Expected distributions of displacement and differences in displacement for delays of a quarter and half mechanical period $T_\mathrm{m}$, if the resonator is in a Gaussian state with equal variances in both quadratures, such as a thermal state.

for $X_\mathrm{r}, P_\mathrm{r}$ with equal variances. Individual pulses measure the displacement $x$. In a thermal state, the two quadratures are normally distributed around 0. This means any measurements of displacement $x$ are also normally distributed around the equilibrium position of the resonator $x = 0$, with variance $\sigma_x^2 \equiv \langle x^2 \rangle = 2x_\mathrm{zpf}^2 k_\mathrm{B} T/\hbar\Omega_\mathrm{m}$. We also plot the expected difference $\Delta x_\tau$ between two measurements of displacement after letting the mechanical resonator evolve for a certain time $\tau$. As mentioned above, such difference measurements can be used to characterize conditional states.

There are a few special cases for the delay $\tau$, in terms of the mechanical resonance period $T_\mathrm{m}$, where we can easily write down the expected distribution of $\Delta x_\tau$. The general case is explored in section 6.1.3. With a quarter period delay ($\tau = T_\mathrm{m}/4$), the two measurements of displacement $x_1, x_2$ correspond to measurements of the two quadratures $X_\mathrm{r}, P_\mathrm{r}$, which means their outcomes are independent. The difference $\Delta X_{T_\mathrm{m}/4} = X_\mathrm{r} - P_\mathrm{r}$ of two independent, normally distributed values, is itself normally distributed, with the variance $\langle \Delta X_{T_\mathrm{m}/4}^2 \rangle = \langle X_\mathrm{r}^2 \rangle + \langle P_\mathrm{r}^2 \rangle$. For the thermal state, we therefore expect the displacement difference $\Delta x_{T_\mathrm{m}/4}$ to be normally distributed with variance $\langle \Delta x_{T_\mathrm{m}/4}^2 \rangle = 2\sigma_x^2$. After a half period delay ($T_\mathrm{m}/2$), we expect to measure the same quadrature in both measurements, but with the sign switched: $x_1 = \sqrt{2} x_\mathrm{zpf} X_\mathrm{r}; x_2 = -\sqrt{2} x_\mathrm{zpf} X_\mathrm{r}$. For any initial distribution of outcomes $x_1$, this means the expected distribution of differences $\Delta x_{T_\mathrm{m}/2} = 2x_1 = 2\sqrt{2} x_\mathrm{zpf} X_\mathrm{r}$ is twice the width of the original distribution. This leads to a variance of $\langle \Delta x_{T_\mathrm{m}/2}^2 \rangle = 4\sigma_x^2$ in the case of a thermal state.

The last special case is after a full period delay ($T_\mathrm{m}$), in which case the ideal measurement outcomes are always identical: $x_1 = x_2 = \sqrt{2} x_\mathrm{zpf} X_\mathrm{r}$. Since we have not included measurement noise and decoherence of the mechanical resonator in this discussion, these predictions are perfectly periodic with a period equal to $T_\mathrm{m}$. We will now consider various noise mechanisms that do lead to uncertainty in the prediction of the second measurement, that is, to a finite width of the probability distribution of $\Delta x_{T_\mathrm{m}}$.

### 6.1.3. Intrinsic mechanical noise

Even if we have measured both quadratures $X_\mathrm{r}$ and $P_\mathrm{r}$ with the minimum uncertainty, we can not predict the trajectory of the resonator with only the Heisenberg uncertainty limiting the precision. Most fundamentally, the resonator is coupled to a thermal bath which induces random changes in the motion of the resonator, an effect known as thermal decoherence. Additionally, if multiple mechanical modes are coupled to the optical cavity, we would need to characterize the quadratures of all these modes to be able to accurately predict the trajectory. If we don't characterize all of the mechanical modes, the ones we did not characterize can be interpreted as a source of decoherence for the other modes; their presence limits our ability to make predictions of future measurements.

**Thermal decoherence**

As long as we don't apply any measurement pulses, the state will change only due to the random influence of thermal motion, which is characterized by the thermal decoherence rate $\Gamma_\mathrm{decoh} = \bar{n}_\mathrm{th}\Gamma_\mathrm{m}$ [7, 40, 158]. This can be interpreted as the inverse of the average time it takes for one quantum of energy to enter from the environment, resulting in an increase of fluctuations of twice the uncertainty in the ground state, or $2x_\mathrm{zpf}^2$. Alternatively, it gives the rate at which the state diffuses in phase space by more than the zero-point fluctuations. By comparing it to the mechanical resonance frequency we can also find the number of coherent oscillations in the presence of thermal decoherence $\Omega_\mathrm{m}/(\bar{n}_\mathrm{th}\Gamma_\mathrm{m}) = Q_\mathrm{m} f_\mathrm{m} h/(k_\mathrm{B} T)$. In our nanobeam cavity with $\Omega_\mathrm{m}/2\pi = 3.2\,\mathrm{MHz}$, $\Gamma_\mathrm{m}/2\pi = 120\,\mathrm{Hz}$, at $T = 3\,\mathrm{K}$, this number is approximately $\Omega_\mathrm{m}/(\bar{n}_\mathrm{th}\Gamma_\mathrm{m}) = 1.4$. In principle, this allows sensitivity beyond the standard quantum limit for measurements within $1.4$ mechanical periods. Further improvement of this fundamental decoherence time, if desired, requires cooling of the environment to lower temperatures or samples with a higher $Qf$-product.

The added variance after a delay $\tau$ in the quadrature $X_\mathrm{r}$ that we measured in the first pulse is

$$\langle(\Delta X_\mathrm{r}(\tau))^2\rangle = \frac{\Gamma_\mathrm{decoh}}{2\pi}\tau = \frac{\Gamma_\mathrm{m}}{2\pi}\bar{n}_\mathrm{th}\tau. \tag{6.5}$$

If the delay is an integer multiple of the mechanical period, that is, $\tau = kT_\mathrm{m}$, then both pulses measure the same quadrature $X_\mathrm{r}$. In that case, we can directly use eq. (6.5) and $x = \sqrt{2}x_\mathrm{zpf}X$ to find the variance of $\Delta x_{kT_\mathrm{m}} = x(kT_\mathrm{m}) - x(0)$ as

$$\langle\Delta x_{kT_\mathrm{m}}^2\rangle = \frac{2k\Gamma_\mathrm{m}x_\mathrm{zpf}^2\bar{n}_\mathrm{th}}{\Omega_\mathrm{m}} = \frac{2kx_\mathrm{zpf}^2\bar{n}_\mathrm{th}}{Q_\mathrm{m}}. \tag{6.6}$$

**Multiple mechanical resonances**

In our sliced nanobeam devices, we typically find two mechanical modes coupled to the optical cavity mode, with comparable frequencies and coupling rates. Because the frequencies are not exactly equal, a delay time of exactly one mechanical period for one of the mechanical resonances will be slightly shorter or longer than a full period for the other resonance: $T_1 \neq T_2$. Therefore, one of the

resonances will always contribute some uncertainty for $\Delta x_\tau$ except when $\tau$ is a common multiple of $T_1$ and $T_2$. This can be interpreted as additional mechanical decoherence.

Here we discuss the expected influence of a second mechanical mode on measurements such as the ones proposed in section 6.1.2, by considering the expected variance of $\Delta x_\tau$ for two mechanical modes at any delay $\tau$. Using eqs. (6.2) and (6.4), with appropriate labels $i$ for the different modes (with $i \in \{1, 2\}$), we write down an expression for displacement $x$ in terms of the quadratures of the two modes:

$$\begin{aligned} x &= \sum_i \sqrt{2} x_{\text{zpf},i} X_i \\ &= \sum_i \sqrt{2} x_{\text{zpf},i} \left( X_{\text{r},i} \cos \Omega_i t + P_{\text{r},i} \sin \Omega_i t \right). \end{aligned} \tag{6.7}$$

For thermal motion, the variance of the individual quadratures is given by $\langle X_i^2 \rangle \approx k_B T / \hbar \Omega_i = \bar{n}_{\text{th},i}$, in the limit where $\bar{n}_{\text{th}} \gg 1$. Consequently, the variance in $x$, as the sum of two independent variables $X_i$, is the sum of their variances

$$\langle x^2 \rangle_{\text{th}} = \sum_i 2 x_{\text{zpf},i}^2 \bar{n}_{\text{th},i}. \tag{6.8}$$

To find the influence on the difference of two measurements separated by a delay of quarter, half or full periods of one of the resonators, we first write down the general equation for the difference $\Delta x(\tau) = x(\tau) - x(0)$:

$$\Delta x_\tau = x(\tau) - x(0) = \sum_i \sqrt{2} x_{\text{zpf},i} \left[ X_{\text{r},i} \left( \cos \Omega_i \tau - 1 \right) + P_{\text{r},i} \sin \Omega_i \tau \right]. \tag{6.9}$$

We can use the fact that $\{X_{\text{r},i}, P_{\text{r},i}\}$ are independent variables, which means their cross-correlations vanish, to calculate the variance of the differences

$$\begin{aligned} \langle \Delta x_\tau^2 \rangle &= \sum_i 2 x_{\text{zpf},i}^2 \left[ \langle X_{\text{r},i}^2 \rangle \left( \cos \Omega_i \tau - 1 \right)^2 + \langle P_{\text{r},i}^2 \rangle \left( \sin \Omega_i \tau \right)^2 \right] \\ &= \sum_{i=1,2} 4 x_{\text{zpf},i}^2 \bar{n}_{\text{th},i} \left( 1 - \cos \Omega_i \tau \right). \end{aligned} \tag{6.10}$$

The second line is valid for thermal states, where $\langle X_{\text{r},i}^2 \rangle = \langle P_{\text{r},i}^2 \rangle = \bar{n}_{\text{th},i}$ due to the equipartition theorem.

From eq. (6.10) we see that, if the mechanical modes have comparable frequency and optomechanical coupling, they have nearly identical contributions to the variance when $\tau = T_i/4$ or $\tau = T_i/2$, since for delays around those values, $(1 - \cos \Omega_i \tau) \approx 1$ or $(1 - \cos \Omega_i \tau) \approx 2$ respectively. Therefore the expectation shown in fig. 6.2 for these delays still holds, if we take the variance $\langle x^2 \rangle$ to be the sum of the variance of the modes, given in eq. (6.8). For $\tau = T_i$, where for a single mode the difference vanishes, the contribution from the other mode $j$ still contributes to the variance of the difference

$$\langle \Delta x_{T_i}^2 \rangle = 4 x_{\text{zpf},j}^2 \bar{n}_{\text{th},j} \left( 1 - \cos \frac{2\pi T_i}{T_j} \right). \tag{6.11}$$

If the difference between the two resonance frequencies is small, the ratio $T_i/T_j$ is close to 1 and we can expand the cosine around $2\pi$ by writing $\cos 2\pi T_i/T_j = \cos 2\pi((T_i/T_j)-1)$. For convenience, we define $\Delta\Omega = \Omega_j - \Omega_i$ such that $(T_i/T_j)-1 = \Delta\Omega/\Omega_i$. This yields the approximation

$$\langle \Delta x^2_{T_i} \rangle \approx 8\pi^2 x^2_{\text{zpf},j} \bar{n}_{\text{th},j} \left( \frac{\Delta\Omega}{\Omega_i} \right)^2 . \tag{6.12}$$

We will revisit this contribution in section 6.1.5.

### 6.1.4. Measurement-induced noise

Up to now we have discussed the measurements of displacement without considering noise added by the measurement process. In this section, we will consider various noise sources, and express their expected effect in terms of the measured homodyne interferometer output $v'$. Like in the case of continuous measurements discussed in previous chapters, fundamentally we will always encounter the shot noise in the light used for the measurement. Additionally, electronic noise is always present in the electrical equipment used (such as the detector). Other sources of noise that could be present include classical laser noise, fluctuations in the optical path lengths in the interferometer, and fluctuations in the alignment of the laser beam.

**Shot noise**

In the balanced homodyne interferometer, usually the optical power in the reference arm (or *local oscillator* power, $P_{\text{LO}}$) is much larger than the optical power in the signal arm ($P_{\text{sig}}$). In that case, the measured fluctuations in the effective homodyne power $P_{\text{H}} = P_+ - P_-$ due to shot noise is given just by the fluctuations due to $P_{\text{LO}}$. To calculate the effect of the shot noise, we consider $N$, the number of photons measured during the pulse duration $\Delta t$. In the balanced detector, on both detectors the optical power is approximately equal to $\frac{1}{2}P_{\text{LO}}$, leading to the two variables $N_1, N_2$ with

$$\langle N_i \rangle = \bar{\dot{N}}\Delta t = \frac{1}{2}\frac{P_{\text{LO}}}{\hbar\omega_L}\Delta t. \tag{6.13}$$

The arrival times of the photons is random, so the variables $N_i$ are Poisson distributed. This implies their variance is equal to the mean: $\langle \Delta N_i^2 \rangle = \langle N_i \rangle$. The balanced detector amplifies the differential photocurrent, proportional to $K = N_2 - N_1$, and the resulting variable $K$ has mean $\langle K \rangle = \langle N_2 \rangle - \langle N_1 \rangle = 0$ and variance $\langle \Delta K^2 \rangle = \langle \Delta N_1^2 \rangle + \langle \Delta N_2^2 \rangle = 2\langle N_i \rangle$. Therefore the power spectral density due to shot noise is

$$S_{\dot{K}\dot{K}} = \frac{\langle \Delta K^2 \rangle}{\Delta t} = \frac{P_{\text{LO}}}{\hbar\omega_L}. \tag{6.14}$$

The actual output of the balanced detector has a finite bandwidth, or in other words, it cannot react instantaneously to the fluctuations of $\dot{K}$. The same is true for any sampling device we use to record the output voltage. The variance in the

filtered output can be found by integrating the power spectral density over the bandwidth $f_{\mathrm{B}}$. Referred back to the effective homodyne power $P_{\mathrm{H}}(t) = \hbar\omega_L \dot{K}$, the variance is

$$\langle P_{\mathrm{H}}^2 \rangle = \int_{-f_{\mathrm{B}}}^{f_{\mathrm{B}}} \hbar^2 \omega_L^2 S_{\dot{K}\dot{K}} df = 2 f_{\mathrm{B}} \hbar \omega_L P_{\mathrm{LO}}. \tag{6.15}$$

Finally, we integrate over the pulse duration $\Delta t$ to obtain the variance of the pulse outcomes $v' = \int_{\Delta t} \mathrm{d}t P_{\mathrm{H}}$, in this case in units of integrated optical power, due to the optical shot noise:

$$\langle v'^2 \rangle = \langle P_{\mathrm{H}}^2 \rangle \Delta t = 2 f_{\mathrm{B}} \hbar \omega_L P_{\mathrm{LO}} \Delta t \tag{6.16}$$

**Electronic noise**

Since our detector includes a transimpedance amplifier, which amplifies the photocurrent $i$ with a gain of $\sim 1 \times 10^4\,\mathrm{V\,A^{-1}}$, any fluctuations in this photocurrent will be amplified such that their contribution overwhelms all other sources of electronic noise in the system. This photocurrent noise is typically given as the *noise equivalent power* (NEP) of the detector, interpreted as the strength of an optical signal that would yield a signal-to-noise ratio of 1. The NEP is usually given as the square root of a single-sided power spectral density, which is assumed constant over a given bandwidth. Therefore we can easily calculate the optical power spectral density corresponding to the electronic noise:

$$S_{PP}^{\text{el.noise}} = \mathrm{NEP}^2/2. \tag{6.17}$$

Analogous to the case of optical shot noise, we integrate over the bandwidth of the detector and/or the measurement device, and subsequently integrate over the pulse duration $\Delta t$ to obtain the variance of the pulse outcomes $v'$,

$$\langle v'^2 \rangle_{\text{el.noise}} = \mathrm{NEP}^2 f_{\mathrm{B}} \Delta t. \tag{6.18}$$

**Other noise sources**

Instead of deriving full expressions for all the possible noise sources in our experiment, we will only explore the scaling laws with the optical powers $P_{\mathrm{LO}}, P_{\mathrm{sig}}$ in the two arms of the interferometer.

**Classical laser noise and alignment fluctuations.** Since the balanced detector subtracts the light on the two diodes, in theory any fluctuations present in the input laser light will be perfectly canceled. Imperfect subtraction can occur due to unequal arm lengths in the interferometer, unequal alignment of the light beam to the two detector diodes, and non-ideal properties of the detector. Since the optical power at the detector is dominated by $P_{\mathrm{LO}}$, any fluctuations in $P_{\mathrm{LO}}$ or in the way the light from the local oscillator is distributed over the two diodes of the detector, will scale linearly with $P_{\mathrm{LO}}$, which means the variance scales as $P_{\mathrm{LO}}^2$.

**Interferometer phase fluctuations.** In the absence of coupling to an optomechanical cavity, the effective homodyne power $P_{\mathrm{H}}$ depends on the power in the two interferometer arms as well as the interferometer phase, which is set by the arm length difference. $P_{\mathrm{H}} \propto \sqrt{P_{\mathrm{LO}} P_{\mathrm{sig}}} \sin\theta$, so the variance of fluctuation due this effect scales as $P_{\mathrm{LO}} P_{\mathrm{sig}}$. Fluctuation of the interferometer phase will also influence the sensitivity of the optomechanical measurement, which we discuss below.

**Sensitivity fluctuations.** The sensitivity of the optomechanical measurement depends on the optical powers, the interferometer phase, the laser detuning, and the alignment of the laser beam to the sample. Fluctuations in any of these quantities will lead to fluctuations in sensitivity. The variance of the resulting pulse outcomes (in absence of other noise) will increase with the variance of the sensitivity, which is negligible as long as the root-mean-square fluctuations of the sensitivity are much smaller than the mean sensitivity. If the variance of the sensitivity does play a role, it scales as $\propto P_{\mathrm{LO}} P_{\mathrm{sig}} \eta^2 \cos^2\theta$. The scaling with optical power follows from $P_{\mathrm{H}} \propto \sqrt{P_{\mathrm{LO}} P_{\mathrm{sig}}}$. As shown in previous chapters, the sensitivity scales with $\eta$, the coupling efficiency between the laser beam and the optomechanical cavity, which can fluctuate due to alignment fluctuations between the laser beam and the sample. This leads to the factor of $\eta^2$ in the scaling of the variance. Finally, the interferometer phase $\theta$ scales the sensitivity as $\cos\theta$ (the derivative of $P_{\mathrm{H}} \propto \sin\theta$), so the scaling of the variance includes a factor $\cos^2\theta$.

**Backaction.** Our short pulse will exert a force in the optical resonator, which results in a changed probability density for the quadrature that is not measured by that particular pulse. Ignoring fluctuations, this will only result in a shift of the mean for that second quadrature, since every pulse exerts the same force in the same direction. In principle any intensity fluctuations, including the unavoidable shot noise in the pulse will produce a fluctuating force, which will broaden the probability density somewhat. In fact, in the case of shot noise, this is the mechanism of the quantum backaction that ensures that the uncertainty $\Delta x \Delta p$ of conditional states always satisfies the Heisenberg uncertainty relation. For an optimal measurement with a sensitivity of $\sim x_{\mathrm{zpf}}$, we therefore expect a broadening of the order of the zero-point fluctuations $x_{\mathrm{zpf}}$. A sufficiently sensitive measurement should then find a shifted, broadened probability density for the second quadrature, when a first pulse has interacted with the sample to measure the first quadrature. The shift scales directly with the optical power $P_{\mathrm{sig}}$, while the optical shot noise broadens the probability density proportional to $\sqrt{P_{\mathrm{sig}}}$ (variance $\propto P_{\mathrm{sig}}$). However, as discussed below, the nonlinear readout in our system provides a mechanism through which the constant shift of the probability density of the displacement can result in a drastically different distribution of pulse outcomes. We analyze this in more detail in section 6.3.3.

**Finite pulse length and timing errors.** Since our measurement is not instantaneous, the mechanical state will evolve during the measurement pulse. This

means that some measurement backaction can evolve from momentum fluctuations into displacement fluctuations. For continuous measurements, this leads to the standard quantum limit, so the contribution to the variance for pulses shorter than $T_\mathrm{m}/4$, for an optimal measurement, is less than $x_\mathrm{zpf}^2$. Moreover, the uncertainty due to the finite pulse length can be reduced by using shorter, more intense pulses, since the added variance scales with the ratio of the pulse length and the mechanical period squared [119], $(\Delta t/T_\mathrm{m})^2$.

Timing errors, as well as uncertainty on the measurement of the mechanical resonance frequency, will influence the measurement in a different way, since due to such errors, we measure a different quadrature than the one we are interested in. The effect of this can be appreciated from eq. (6.10) and from fig. 6.6, if we take a delay $\tau$ slightly different from the resonance period $T_\mathrm{m}$. However, we expect these errors to be small, since the time resolutions in the pulse generation ($1\,\mathrm{ns}$) and in the measurement ($2\,\mathrm{ns}$) are much smaller than the mechanical resonance period of approximately $300\,\mathrm{ns}$, and the jitter should be smaller still.

### 6.1.5. Influence of nonlinear readout

As explored in the previous chapter, the expected root-mean-square fluctuations of the displacement due to thermal motion are an appreciable fraction of the optical linewidth for our device. This results in nonlinear readout of the displacement, which affects our pulsed measurements as well. To analyze this, we first look at the transduction function and the resulting sensitivity to small changes in the displacement. Using the known thermal state of the mechanical resonator, we then model the probability densities of the pulse outcomes as well as the differences between subsequent pulses for various delays.

#### Transduction function and sensitivity

The ideal normalized homodyne output versus detuning is

$$v(u) = \frac{2u}{1+u^2}, \tag{6.19}$$

where $u \equiv 2\Delta/\kappa = (2/\kappa)(\Delta_0 + Gx)$ is the dimensionless detuning. Figure 6.3a shows the ideal homodyne output versus detuning within two linewidths around $0$. In order to reconstruct the displacement distribution, we need the inverse of this transduction function, which is given by

$$u_\pm(v) = \frac{1 \pm \sqrt{1-v^2}}{v}. \tag{6.20}$$

This function is multivalued, depending on the sign chosen before the square root. This is illustrated in fig. 6.3a, where the two branches are plotted in solid and dashed lines.

In our experiment, if two pulses are separated by a mechanical period $T_\mathrm{m}$, ideally we expect the two detunings $u_1, u_2$ during those measurements to be identical. The strength with which small deviations $\delta u$ from this expectation are transduced

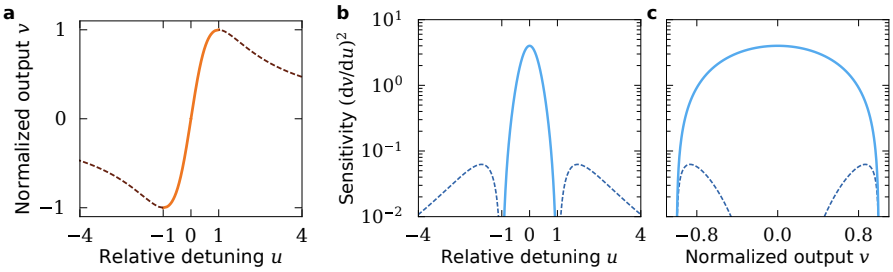


Figure 6.3: (a) Transduction function $v(u)$ of the balanced homodyne measurement at its optimal operating point. $u = 2\Delta/\kappa$ is the relative detuning. The inverse function $u(v)$ has two branches, indicated by the solid and dashed parts of the plot. (b),(c) The 'sensitivity', which here denotes the variance of the output $\langle \Delta v^2 \rangle$ due to small changes in the relative detuning with variance $\langle \Delta u^2 \rangle$, as a function of the initial detuning $u$ (b) and the corresponding initial output $v$ (v). The dashed lines again indicate the outer branch of the transduction function, where $|u| > 1$.

to a change in output $\delta v$ is given by the derivative $\mathrm{d}v/\mathrm{d}u(u)$, which depends on the initial detuning $u_1$, since

$$\frac{\mathrm{d}v}{\mathrm{d}u}(u) = \frac{2(1-u^2)}{(1+u^2)^2}. \tag{6.21}$$

The variance of many such measurements will scale as

$$\langle \delta v^2 \rangle = \left( \frac{\mathrm{d}v}{\mathrm{d}u}(u) \right)^2 \langle \delta u^2 \rangle. \tag{6.22}$$

In figs. 6.3b and 6.3c we show the dependence of this 'sensitivity' on the initial detuning (and displacement) $u$, and on the outcome $v$. The data for $|u| > 1$ is shown in dashed lines in both panels. We emphasize that for a linear readout, this sensitivity is assumed to be the same for any detuning $u$ or output $v$, typically because one can assume $|u| \ll 1$.

**Single pulse outcomes**

In a thermal state, we expect that the probability density of the displacement $\mathcal{P}(x)$ has a Gaussian distribution, which means that the relative detuning $u$ is also normally distributed:

$$\mathcal{P}(u) = \frac{1}{\sqrt{2\pi\langle u^2 \rangle}} \exp\left( \frac{-u^2}{2\langle u^2 \rangle} \right). \tag{6.23}$$

The normalized output $v$ then has the probability density

$$\mathcal{P}(v) = \mathcal{P}(u(v)) \left| \frac{\mathrm{d}u}{\mathrm{d}v} \right|, \tag{6.24}$$

which we can evaluate using $u(v)$ and its derivative. We explicitly deal with the fact that $u(v)$ is multivalued by summing the probability distribution due to the

two contributions. The derivative of the inverse transduction function $u(v)$, given in eq. (6.20), is

$$\frac{\mathrm{d}u_{\pm}}{\mathrm{d}v} = \frac{-1}{v^2}\left(1 \pm \frac{1}{\sqrt{1-v^2}}\right), \tag{6.25}$$

which leads to

$$\begin{aligned}\mathcal{P}(v) &= \mathcal{P}(u_+(v))\left|\frac{\mathrm{d}u_+}{\mathrm{d}v}\right| + \mathcal{P}(u_-(v))\left|\frac{\mathrm{d}u_-}{\mathrm{d}v}\right|, \\ &= \sum_{\pm} \frac{1}{\sqrt{2\pi\langle u^2\rangle}} \exp\left[\frac{-1}{2\langle u^2\rangle}\left(\frac{1 \pm \sqrt{1-v^2}}{v}\right)^2\right]\left|\frac{-1}{v^2}\left(1 \pm \frac{1}{\sqrt{1-v^2}}\right)\right|.\end{aligned} \tag{6.26}$$

To estimate how well we can reconstruct the displacement distribution from our measurement outcomes, we now calculate the chance that our measurement outcome is determined by the 'outer' branch of the transduction function. This coincides with the probability of finding $|u| > 1$. For a normally distributed variable $u$, the chance to find it more than $(1/\sigma_u)$ away from the mean is given by the *Q-function*:

$$\mathcal{P}(|u| > 1) = 2Q(1/\sigma_u) \equiv \frac{2}{\sqrt{2\pi}} \int_{1/\sigma_u}^{\infty} e^{-u'^2} du' = 1 - \mathrm{erf}\left(\frac{1}{\sqrt{2}\sigma_u}\right), \tag{6.27}$$

where $\mathrm{erf}$ denotes the *error function*. Figures 6.4a and 6.4b show $\mathcal{P}(|u| > 1)$ as a function of the root-mean-square fluctuations $\sigma_u$. We plot this on a logarithmic, as well as on a linear scale, to be able to evaluate the rapid change as a function of $\sigma_u$. The range within which the device used in the experiments operates between $3\,\mathrm{K}$ and room temperature is indicated, as well as the numerical values for $\mathcal{P}(|u| > 1)$. In particular, even at $3\,\mathrm{K}$, $16.5\,\%$ of the time, the displacement is such that $|u| > 1$ and therefore the measurement outcome is determined by the 'outer' branch of the transduction function.

In figs. 6.4c and 6.4d, we show the expected probability density for the normalized homodyne output $v$, with the root-mean-square fluctuations $\sigma_u$ for the device used in the experiments at $3\,\mathrm{K}$ ($\sigma_u = 0.72$) and at room temperature ($300\,\mathrm{K}$, $\sigma_u = 7.2$). We plot the contributions from the two branches of the transduction function separately, which shows that at $3\,\mathrm{K}$, practically all of the contributions of the 'outer' branch occur at the extreme output values, while at room temperature, the shape of the probability density is drastically changed by these contributions even close to middle of the distribution.

**Differences between pulse outcomes**

The experimental pulse outcomes $v'$ are not normalized and may have an arbitrary offset $\bar{v}'$. In our measurement, any slow drift in the mean pulse outcome $\bar{v}'$ will blur the features in the probability density shown in figs. 6.4c and 6.4d, when it is built up from measurements separated in time. Therefore, we will mostly present the distribution of differences between two consecutive pulse outcomes $\Delta v' = v'_2 - v'_1$, separated by time differences of the order of $T_\mathrm{m}$. As shown in

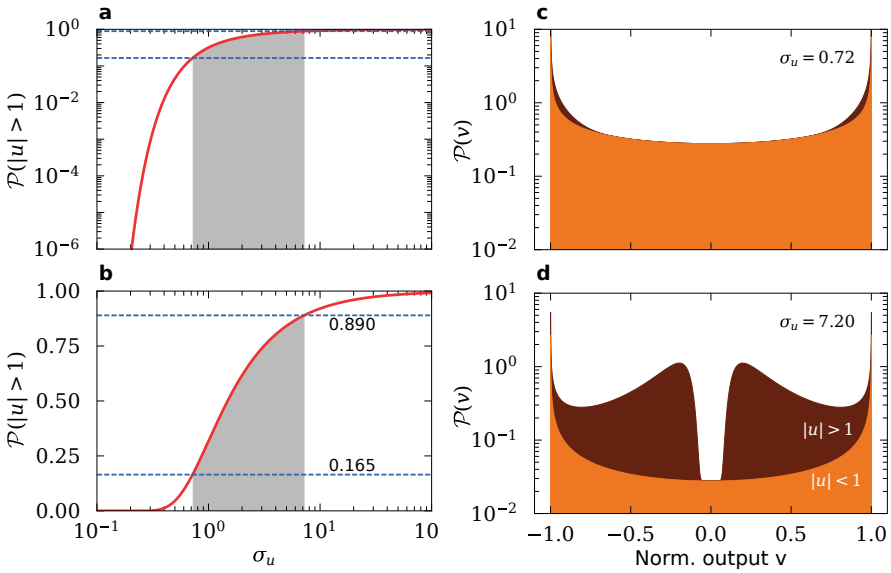


Figure 6.4: (a),(b) Probability of $u = 2Gx/\kappa > 1$, which means the outcome $v$ is on the outer branch ($|u| > 1$). Both panels show the same data, with logarithmic (a) and linear (b) vertical scales. The gray filled area shows the operating regime for the device used in experiments, with the blue dashed lines indicating the minimum and maximum values of $\mathcal{P}(|u| > 1)$, which correspond to operation at 3 K and at 300 K, respectively. (c),(d): probability density of outcomes $v$ expected for our device at 3 K and at room temperature. The contribution of the outer branch ($|u| > 1$) is separately shown (dark filled area), stacked on top of the inner branch ($|u| < 1$) contribution (orange filled area).

fig. 6.2, for a linear measurement, we expect all the resulting distributions to be normally distributed, just like the individual distributions of the quadratures in the thermal state. The nonlinear readout changes this situation.

**Quarter period delay.** After a quarter of a mechanical period ($T_\mathrm{m}/4$), we expect the second relative detuning $u_2$ to be independent from the first, $u_1$. What does this mean for $\mathcal{P}(v_2 - v_1) = \mathcal{P}(v(u_2) - v(u_1))$? In general, the distribution for the difference $\Delta v$ of two independent variables $v_1, v_2$ can be found from the convolution of the individual probability distributions:

$$\mathcal{P}(\Delta v) = \int \mathcal{P}_1(v)\mathcal{P}_2(v + \Delta v)dv \tag{6.28}$$

In our experiment, the two distributions $\mathcal{P}_1(v_1), \mathcal{P}_2(v_2)$ are both given by eq. (6.26). We numerically performed the convolution of this distribution with itself, for $\sigma_u = 0.72$, corresponding to our device at 3 K. The result is shown in fig. 6.5a, together with $\mathcal{P}(v)$ as well as numerically simulated distributions, shown as histograms. These numerical simulations were performed by generating $10^4$ normally distributed relative detunings $u$, with variance $\sigma_u^2$, then calculating

the resulting pulse outcomes $v(u)$. To obtain the distribution of $\mathcal{P}(\Delta v)$, we plotted the distribution of subtracted outcomes $v_2 - v_1$ from separately randomly generated detunings.

As expected from the individual distributions seen in fig. 6.4c, the resulting distribution is strongly influenced by the nonlinear readout and does not resemble the Gaussian distribution that occurs for linear readout. Instead, the convolution of the doubly-peaked function with itself leads to a distribution with a strong peak in the middle, and two weaker peaks near the extremes of its range. As a function of $\sigma_u$, as the individual distributions move from the shape in fig. 6.4c to the one in fig. 6.4d, the convolution will exhibit a broader peak in the middle and less pronounced peaks on the extremes of the range. The expected result of measurement noise such as electronic noise and optical shot noise, is a convolution of a Gaussian noise kernel with the probability distribution shown in fig. 6.5, which will broaden and wash out the features of this distribution. We note that the width of the distribution, at least for the experimental values of $\sigma_u$, gives us a way to calibrate the measured pulse outcomes $v'$ in terms of the normalized values $v$.

**Half period delay.** After a delay of a half period ($T_\mathrm{m}/2$), we expect the second relative detuning to be anticorrelated with the first: $u_2 = -u_1$. Since $v(u)$ is an odd function, this means $v_2 = -v_1$ as well. Therefore we predict $\Delta v = v_2 - v_1 = -2v_1$, which means the probability distribution $\mathcal{P}(\Delta v)$ is doubled in width with respect to $\mathcal{P}(v)$, but is otherwise unchanged. The result is shown in fig. 6.5b, again together with the distribution of individual pulse outcomes $\mathcal{P}(v)$ as well as numerically simulated data. Here, the numerical data was generated in the same way as for the quarter period delay, but the second pulse outcome was set to be $v_2 = -v_1$ to enforce the anticorrelation.

This distribution of $\Delta v_{T_\mathrm{m}/2}$ gives us a direct way to characterize the individual pulse distribution $\mathcal{P}(v)$. Like the distribution for a delay of a quarter period, we can use the width of the distribution as a means to calibrate our measured pulse outcomes $v'$ to the normalized outcomes $v$. Moreover, with the addition of measurement noise, which we expect to result in a distribution convolved with a Gaussian kernel, the distribution will still qualitatively show the double-peaked shape. Therefore we can confirm our prediction of the distribution and potentially even fit the shape of the histogram if we can separately characterize the noise kernel.

**Full period delay.** After a full period ($T_\mathrm{m}$), exactly like in the case for linear readout, the model predicts that we find the same detuning, and therefore the same outcome: $u_2 = u_1; v_2 = v_1$. The measured distribution will therefore be dominated by noise. This could be either intrinsic mechanical noise, such as thermal decoherence or the influence of a second mechanical mode, or measurement noise, such as optical shot noise.

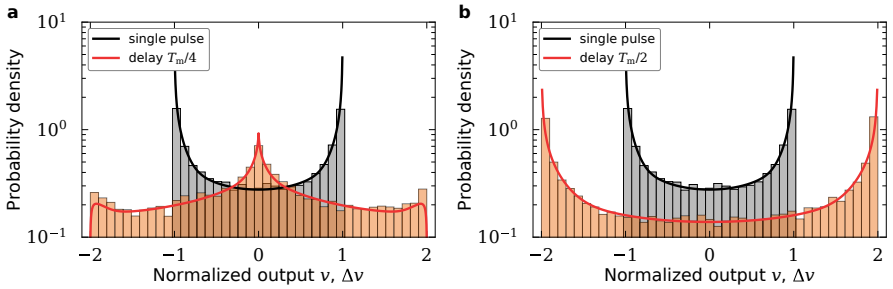


Figure 6.5: Predicted probability density for the difference of two subsequent pulses, without any added noise, shown for delays of (a) a quarter of a mechanical period ($T_\mathrm{m}/4$) and (b) half of a period ($T_\mathrm{m}/2$). The root-mean-square value of relative detunings was taken to be $\sigma_u = 0.72$, corresponding to the total variance due to both mechanical modes of our structure at 3 K. The black solid lines correspond to the probability density $\mathcal{P}(v)$ for the outcome of a single pulse, while the red solid lines show the probability density $\mathcal{P}(\Delta v)$ for the difference of two pulses with the indicated delay. The histograms show the result of a numerical simulation where $10^4$ relative detunings were taken from a normal distribution with variance $\sigma_u^2$.

**Variances of these distributions.** From fig. 6.5 the shape and width of the expected distributions can be evaluated, but not the variance. However, we can directly predict the variance of noise contributions such as the optical shot noise, so it is useful to be able to compare these to the variance of the predicted distributions. For linear readout ($\sigma_u \ll 1$), the variance of the difference between two consecutive pulses $\langle \Delta v^2 \rangle$ is described by eq. (6.10), which for only one mechanical mode results in a sinusoidal dependence. The prediction for linear readout is indicated with a black line in fig. 6.6a, normalized to variance of an individual pulse $\langle v^2 \rangle$. Using the numerical simulation method detailed above, we obtain the expected variance of the distributions for various delays between two pulses in the case of nonlinear readout. To do this, we generate two sets of normally distributed variables to represent the two quadratures of motion, from which we calculate the expected mechanical evolution from the first to the second pulse:

$$\begin{aligned} x_1 &= X_1; \\ x_2 &= X_1 \cos(2\pi\tau/T_\mathrm{m}) + X_2 \sin(2\pi\tau/T_\mathrm{m}). \end{aligned} \tag{6.29}$$

Here $X_1, X_2$ are the two normally distributed quadratures, $T_\mathrm{m}$ is the mechanical period, and $\tau$ represents the delay time between the first and second pulse. The variables $x_1, x_2$ are scaled to relative detunings $u_1, u_2$, such that the variance is $\sigma_u^2 = 0.72^2$, and then we calculate the pulse outcomes $v_1, v_2$ and take their difference. The variance of the resulting distributions is shown in fig. 6.6, normalized to the variance of the first pulse outcome $\langle v_1^2 \rangle$. As expected, at delays of an integer number of periods $\tau = kT_\mathrm{m}$, the variance vanishes. The variance at quarter- and half-periods also follows the expected pattern of $2\langle v^2 \rangle$ and $4\langle v^2 \rangle$, respectively. From the figure, we can see that the variance as a function of delay is hardly changed with respect to the case for linear readout, whereas the shapes of the

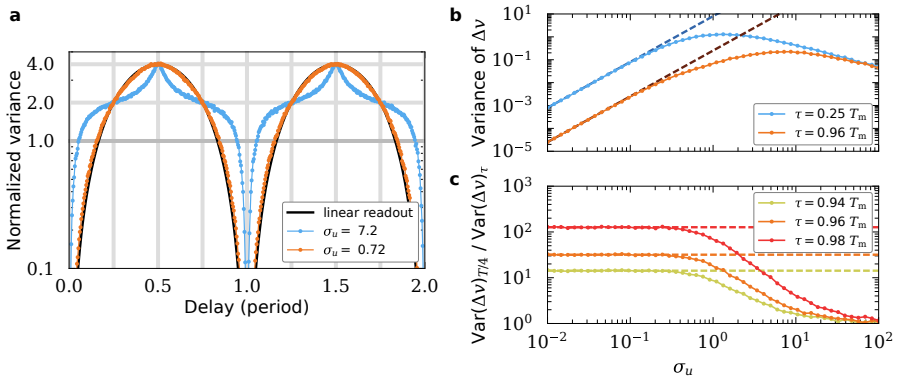


Figure 6.6: (a) Predicted delay dependence of the variance of the difference of two subsequent pulses $\langle \Delta v^2 \rangle$, normalized to the variance of the outcomes of the individual pulses $\langle v^2 \rangle$. The black solid line is the expectation for linear readout (eq. (6.10) with only one mode), while the blue and orange points are numerically simulated results for the thermal variance $\sigma_u$ we expect in our structure at room temperature and 3 K, respectively. (b) Dependence of the variance of $\Delta v$ on the relative detuning fluctuations $\sigma_u$, for different delays $\tau$ in units of the mechanical period $T_\mathrm{m}$. The delay after a quarter period and after 96 % of the period is shown. (c) The ratio of the variance after a quarter period with the variance after 96 % of the period is shown, along with the ratio with the variance after delays of 94 % and 98 % of a period. The dashed lines in (b) and (c) represent the predicted variance if the conversion between displacement and the measured signal would be fully linear, which is a good approximation for $\sigma_u \ll 1$.

distributions shown in fig. 6.5 have significantly changed at this value of $\sigma_u$. The variances are also shown for $\sigma_u = 7.2$, corresponding to a temperature of 300 K, which indicates the expected effects at higher temperatures and larger values of $\sigma_u$.

In figs. 6.6b and 6.6c, we show how the absolute variance of the difference of two subsequent pulses $\langle \Delta v^2 \rangle$ evolves as a function of the variance of the relative detuning $\sigma_u^2$. Both the variance after a quarter period, and the variance after a delay $\tau$ close to a full period, decrease with respect to the linear prediction, due to the nonlinear readout. However, the ratio between the quarter period and almost-full-period variances (panel (c)), shows that the variance after a quarter period decreases faster with respect to the linear prediction than the variance after a full period. We can use this insight to easily find a lower limit for the measurement sensitivity in displacement units from measured variances of pulse outcomes, since the measurement with a quarter period yields a variance that is proportional to the known thermal displacement variance of the structure, and the measurement with a full period delay is dominated by noise. Even if the measurement after with a delay of (almost) a full period is dominated by displacement uncertainty, for example due to the fact that for a second mechanical mode, the delay is not exactly a full period, the nonlinear readout does not invalidate the use of this ratio as a lower limit.

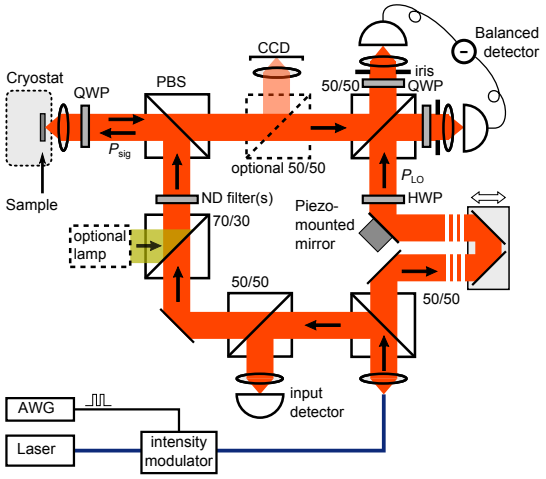


Figure 6.7: Balanced homodyne setup used for the pulsing experiments. Light from a tunable, narrow band laser is modulated using an intensity modulator and then coupled into a Mach-Zehnder interferometer. The light in the signal arm (left) is reflected by the sample, which is located in a closed-cycle cryostat. Light from the two arms of the interferometer is overlapped at a 50/50 beamsplitter (top right) and recorded by a balanced detector. AWG: Arbitrary waveform generator; ND filter: neutral density filter; QWP: quarter-wave plate (at 45°); HWP: half-wave plate (at 45°); PBS: polarizing beamsplitter; CCD: InGaAs infrared camera.

## 6.2. Experimental implementation

### 6.2.1. Optical setup and pulse generation

We use the balanced homodyne interferometer setup described in the previous chapter, with the main difference that we use an intensity modulator to generate pulses in the input laser beam. The setup is shown in detail in fig. 6.7. The intensity modulator is an electro-optic modulator in an integrated Mach-Zehnder interferometer. For some of the data shown, the modulator used was a Thorlabs LN81S (10 GHz bandwidth); for most of the data shown here we switched to a Jenoptik AM1470b (500 ps rise time) which could provide a higher extinction ratio (nominally 30 dB). We drive the intensity modulator with an electronic arbitrary waveform generator (AWG) which has a sample period of 1 ns. With this method, we create square pulses that have a length of 20 ns, with different delays between the pulses, and a resolution of 1 ns. Continuous measurements at relatively low power were used to align the setup and characterize the resonance wavelength of the optical cavity as well as the resonance frequencies of the mechanical resonators. We use the same device as the one described in chapter 5, which has a resonance wavelength at 1458 nm at room temperature, and mechanical resonance frequencies around 3.2 MHz and 3.4 MHz (both the optical and mechanical resonances slowly drift over time when the sample is kept at 3 K for multiple days or weeks).

To characterize the input pulses and record the measurement output, we connect the “input” detector (AC-coupled Femto HCA-S-200M, 200 MHz bandwidth)

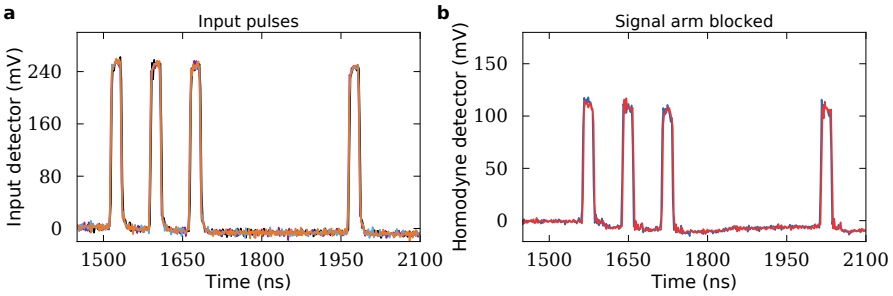


Figure 6.8: (a) Characterization of input pulses using the AC-coupled output of the "input" detector. Three randomly picked traces from a single data set are overlaid. In this case, the four pulses are $20\,\mathrm{ns}$ long and have delays of $75\,\mathrm{ns}$, $75\,\mathrm{ns}$ and $301\,\mathrm{ns}$ (quarter and full period respectively). (b) Characterization of output pulses using the balanced homodyne detector, while the signal arm is blocked. Three randomly picked traces from a single data set are overlaid. Pulse lengths and delays were the same as in (a). The balancing of the intensities on the two detector photodiodes was imperfect here, leading to non-zero output during the pulses.

and the balanced "homodyne" detector (Thorlabs PDB460C, $200\,\mathrm{MHz}$ bandwidth) to a digitizer, which has a sampling period of $2\,\mathrm{ns}$. Figure 6.8a shows a characterization of the pulses in the signal arm. In this case, we create a sequence of four pulses of $20\,\mathrm{ns}$, with delays between the pulses of $75\,\mathrm{ns}$, $75\,\mathrm{ns}$ and $300\,\mathrm{ns}$. Using the specification of this detector and a calibration measurement without pulses, we can relate the voltage shown here to an optical power in the signal and reference arms of the interferometer. We use the maximum available contrast with the combination of modulator and AWG, typically leading to about $1\,\mathrm{mW}$ of optical power in the reference arm ($P_{\mathrm{LO}}$). In the signal arm ($P_{\mathrm{sig}}$), we had up to $150\,\mu\mathrm{W}$ (this is lower than $P_{\mathrm{LO}}$ mainly due to the presence of two beamsplitters), which we then further reduced using neutral density (ND) filters.

### 6.2.2. Data acquisition protocol

In order to perform a pulsed measurement, we need to control several experimental variables. First of all, we need to set the delay times between pulses based on the mechanical resonance frequency of the device. The mechanical resonances that are coupled to the optical cavity resonance can be measured using a continuous optomechanical measurement at low optical power. For this purpose we also connect the output of the "homodyne" balanced detector to an electronic spectrum analyzer (ESA), enabling us to find the resonance frequencies from the peaks in the observed spectrum during a continuous measurement. The wait time between separate pulse sequences is set such that the mechanical modes are completely thermalized. This happens on a timescale set by the damping rates of the mechanical resonances, which we find from the width of the peaks measured on the ESA. For optimum sensitivity, we need to optimize the laser frequency and the homodyne interferometer phase. Like before, we use the continuous measurement on the ESA, which is also optimally sensitive when the laser is resonant

with the optical cavity frequency, and when the homodyne interferometer phase is set such that the homodyne output follows eq. (6.19). Similarly, the continuous measurement can be used to gauge the optimum setting for the "off"-state voltage of the AWG, such that the light is suppressed during the time between pulses, in this case by minimizing the measured signal.

In our experiments, the DC output of the homodyne detector was dominated by slow drift, which did not necessarily coincide with the fluctuations of the interferometer phase. Instead, the drift was likely caused by small fluctuations in alignment leading to a change in the distribution of the local oscillator power on the two diodes of the balanced detector. Instead of using a feedback scheme to control the interferometer phase, we therefore used its passive stability. Judging from the continuous measurements, the interferometer phase was stable within $\lesssim 20\,\%$ over a timescale of a few seconds, which is the time it took to acquire one data set of hundreds of pulse sequences. Suppressing fluctuations by implementing feedback could slightly improve performance, by increasing the average sensitivity. In practice, we optimized the homodyne interferometer phase just before every data set acquisition, and intermittently optimized the laser frequency and the "off"-state voltage on the AWG. The frequency and linewidth of the mechanical resonances was only measured once at the start of each measurement session.

### 6.2.3. Data analysis protocol

Figure 6.8b shows the output of the balanced homodyne detector while the signal arm is blocked. For this measurement, the light in the local oscillator arm was not perfectly balanced on the two detector photodiodes, leading to a non-zero output during the pulses. Figure 6.9a shows the output of the balanced homodyne detector during an on-resonance measurement without blocking the signal path. In fig. 6.9b, the same traces are shown with the mean of the control traces (where the signal arm is blocked, see fig. 6.8b) subtracted. We can see that for these particular traces, the non-zero response of the detector between the pulses is completely accounted for by the subtraction. Small artifacts can be seen at the start and end of some pulses, which could be due to small timing jitter.

Finally, figs. 6.9c to 6.9f show the limits we use for the integration of the pulse outcomes. We sum the subtracted values of $13$ data points (corresponding to $26\,\mathrm{ns}$) to yield a single value for the outcome $v'$ of a single pulse. We perform the same procedure for the input pulses (see fig. 6.8a) to find the total optical power in both arms of the interferometer.

### 6.2.4. Reference measurements and noise sources

To obtain the minimum contribution of noise in our results and characterize its origin, we perform a reference measurement. For this measurement, the laser is detuned far from the optical cavity resonance, but the conditions are otherwise identical to the on-resonance measurements presented below. Here we use sequences of two pulses of $20\,\mathrm{ns}$, separated by a delay of either $75\,\mathrm{ns}$ or $300\,\mathrm{ns}$. We vary $P_{\mathrm{sig}}$, the optical power in the signal arm, by attenuating it with ND fil-

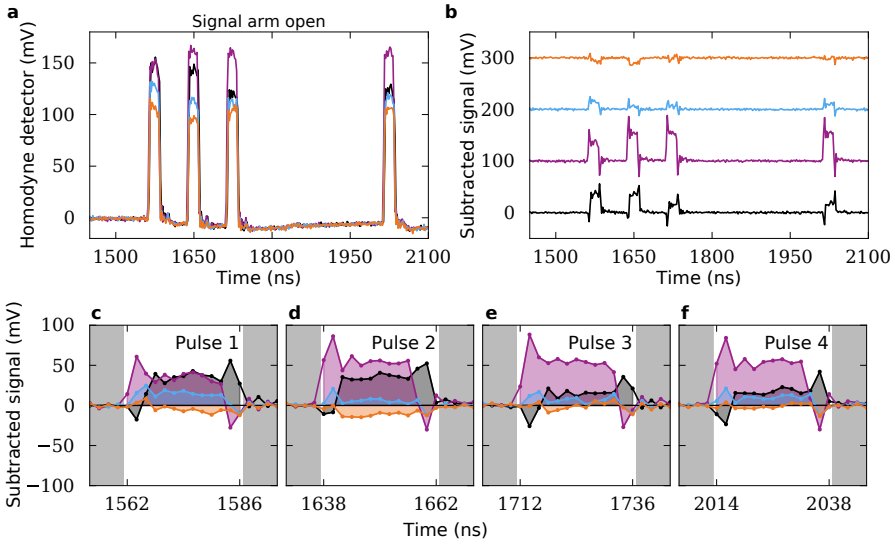


Figure 6.9: (a) Characterization of output pulses using the balanced homodyne detector, while the signal arm is open. Four randomly picked traces from a single data set are shown. The pulse lengths and timings where the same as in fig. 6.8; pulse length was $20\,\mathrm{ns}$ and delays were $75\,\mathrm{ns}$, $75\,\mathrm{ns}$ and $301\,\mathrm{ns}$. (b) The subtracted signal shows the same traces as the raw signal, but with the mean of ten time traces where the signal arm was blocked subtracted (see fig. 6.8b). The subtracted traces are offset by $100\,\mathrm{mV}$ for clarity. (c)–(f) Visual representation of integrating the pulse outcomes. The same four traces are shown as in (a) and (b), where the data points in between the gray shaded areas are all summed to yield a single value per pulse, per trace.

ters. The variance of the differences between two subsequent pulse outcomes $v'$ is shown in Figure 6.10 with black data points. The result is independent of $P_{\mathrm{sig}}$, which is consistent with both electronic noise and the shot noise due to $P_{\mathrm{LO}}$, the light from the reference arm.

We measure the electronic noise by using the recorded voltage in the time trace before the first pulse, and find an expected variance of $\Delta v'$ of $34\,\mathrm{mV}^2$. This value is shown in the figure with the purple horizontal line. As a sanity check, we also calculate the expected variance from the noise equivalent power (NEP), using eq. (6.18), and the conversion factor, both taken from the specification sheet of the detector. The NEP specified for a bandwidth of $10\,\mathrm{MHz}$, together with the provided spectral response for the full detector bandwidth of $200\,\mathrm{MHz}$, yields an expected variance that is approximately $17\,\%$ higher than the measured value.

The contribution of the optical shot noise can be calculated directly from the optical power at the detector using eq. (6.16), combined with the conversion factor of the detector. Using the estimated power of the local oscillator $P_{\mathrm{LO}} = 1.3\,\mathrm{mW}$, we find the variance due to shot noise is $177\,\mathrm{mV}^2$. This value is indicated with the light blue line in fig. 6.10. The sum of the shot noise and the electronic noise is also indicated with the dark blue line. The results from the off-resonance

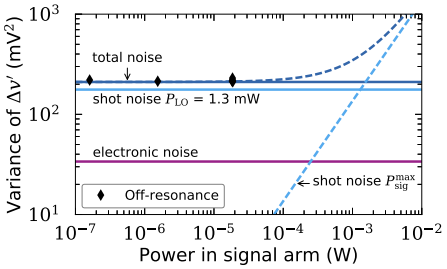


Figure 6.10: Variance of the difference between subsequent pulses in an off-resonance reference measurement, compared to estimates of the contributions from electronic noise and optical shot noise. The electronic noise was determined from the measured variance in the time traces during the time before the first pulse in the pulse sequence, while the optical shot noise was calculated from the optical power in the local oscillator and the conversion efficiency of the detector given by the specifications of the manufacturer.

measurement are very close to this value, which indicates that the noise can be fully explained by these two contributions, and is dominated by the optical shot noise.

In the figure, we also indicated the maximum contribution from the shot noise of the light in the signal arm, if $100\,\%$ of the light incident on the cryostat would reach the homodyne beamsplitter. Even in this extreme case, the noise is dominated by the shot noise from $P_{\mathrm{LO}}$ for all the signal powers we used in the experiment, which was up to $P_{\mathrm{sig}} = 150\,\mu\mathrm{W}$.

## 6.3. Results

### 6.3.1. Signatures of mechanical motion

Figure 6.11 shows the experimental results using $P_{\mathrm{sig}} = 14\,\mu\mathrm{W}$, compared to the reference measurement. In the reference measurement, we used $3000$ sets of two pulses. The data with different delays were obtained in a single data set, by using the pulse sequence shown in fig. 6.8, with two delays of a quarter period ($T_{\mathrm{m}}/4 = 75\,\mathrm{ns}$), followed by a delay of a full period ($T_{\mathrm{m}} = 301\,\mathrm{ns}$). Here, we used $1000$ sets of four pulses, with a delay of $30\,\mathrm{ms}$ between every pulse sequence to ensure every pulse sequence started with a new instance of a thermal state. The gray histograms show the outcomes $v_1', v_2'$, while the colored histograms show the difference $\Delta v'$. To obtain the data with a delay of a half period ($T_{\mathrm{m}}/2 = 150\,\mathrm{ns}$), we take the difference of the first and third pulse in this sequence.

For the data with $T_{\mathrm{m}}/4$ and $T_{\mathrm{m}}/2$ delays, we scale the predicted probability densities shown in fig. 6.5, such that the maximum differences $|\Delta v| = 2$ correspond to the maximum measured differences $\Delta v'$. In both cases, the measured distribution follows the predicted shape. We expect the match can be made even better by including the effect of noise, which can be achieved by convolving the predicted probability density with a Gaussian distribution that has a variance equal to the measured noise variance.

For both the off-resonance (reference) measurements and the data with a full

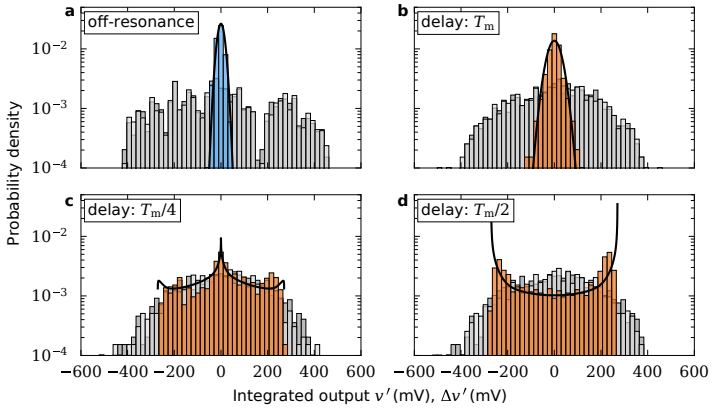


Figure 6.11: Experimentally measured distributions, using the pulse sequence shown in fig. 6.8, with $P_{\text{sig}} = 14\,\mu\text{W}$. The off-resonance data (a) was taken with only two pulses, at $P_{\text{sig}} = 18.5\,\mu\text{W}$. The gray histograms depict the individual outcomes $v'_i, v'_j$ while the colored histograms show the differences $\Delta v' = v'_j - v'_i$. The solid lines in (a) and (b) show a Gaussian fit to the measured distribution, while in (c) and (d) the show the expected distributions (see fig. 6.5) scaled so their bounds coincide with the maximum and minimum measured differences. The total number of pulse sequences was 3000 for the off-resonance measurement (a), and 1000 for the on-resonance data set (b)–(d).

period delay, we plot the normalized Gaussian distribution with the same variance and mean as the measured differences $\Delta v'$. The variance of the data with a full period delay is larger than the reference measurements, which shows that the difference between the pulses is not only determined by the noise. The most likely source of this larger variance is the presence of the second mechanical mode, which has a slightly larger period $T_2 = 313\,\text{ns}$. Using eqs. (6.8) and (6.11), we can calculate

$$\begin{aligned}\frac{\langle \Delta x^2_{T_1}\rangle}{\langle x^2\rangle} &= \frac{2x^2_{\text{zpf},2}\bar{n}_{\text{th},2}\left(1-\cos\frac{2\pi T_1}{T_2}\right)}{\sum_i x^2_{\text{zpf},i}\bar{n}_{\text{th},i}} \\ &\approx 1-\cos\frac{2\pi T_1}{T_2} = 2.7\,\%,\end{aligned} \tag{6.30}$$

where we approximated the two modes to have equal $x_{\text{zpf}}$ and $\bar{n}_{\text{th}}$. According to this equation, we should expect a lower bound on the measured variance after a delay of a full period $T_1$ of a few percent of the thermal variance. To relate this to our measurement result, we first disregard the nonlinear readout. In that case, the measured variances $\langle \Delta v'^2_\tau\rangle$ are linearly related to the displacement variances $\langle x^2_\tau\rangle$. As shown in fig. 6.6, there is also a straightforward relation between these variances at different delays and the thermal variance. The variance with a quarter

period delay ($T_1/4$), again in terms of the thermal variance, is

$$\begin{aligned}\frac{\langle \Delta x^2_{T_1/4}\rangle}{\langle x^2\rangle} &= \frac{2x^2_{\text{zpf},1}\bar{n}_{\text{th},1} + 2x^2_{\text{zpf},2}\bar{n}_{\text{th},2}\left(1-\cos\frac{\pi T_1}{2T_2}\right)}{\sum_i x^2_{\text{zpf},i}\bar{n}_{\text{th},i}} \\ &\approx 2-\cos\frac{\pi T_1}{2T_2} = 1.94,\end{aligned} \tag{6.31}$$

where we again approximated the two modes to have equal $x_{\text{zpf}}$ and $\bar{n}_{\text{th}}$. In the case of linear readout, we therefore expect the variance after a delay of $T_1$ to be $0.027/1.94 = 1.39\,\%$ of the variance after a delay of $T_1/4$.

Finally, we correct both of these variances for nonlinear readout. To do this, we numerically generate four sets of normally distributed displacement quadratures, such that we can simulate two displacement measurements $x_1, x_2$ separated by a delay $\tau$. Using the transduction function (eq. (6.19)), we calculate the resulting normalized outputs $v_1, v_2$, to obtain the variance $\langle \Delta v^2_\tau\rangle_{\text{nonlinear}}$. The correction factor to convert variances between nonlinear and linear readout is found by comparing this quantity to the predicted variance for linear readout $\langle \Delta v^2_\tau\rangle_{\text{linear}} = 4\langle \Delta u^2_\tau\rangle = 16G^2/\kappa^2\langle \Delta x^2_\tau\rangle$. With two modes of equal variance $\langle x^2_i\rangle$ and with the measured ratio of $T_1/T_2 = 0.963$, we find correction factors $C_\tau = \langle \Delta v^2_\tau\rangle_{\text{nonlinear}}/\langle \Delta v^2_\tau\rangle_{\text{linear}}$ of $C_{T_1} = 0.372$ and $C_{T_1/4} = 0.268$. Combining these results with eqs. (6.30) and (6.31), we find

$$\frac{\langle \Delta v^2_{T_1}\rangle_{\text{nonlinear}}}{\langle \Delta v^2_{T_1/4}\rangle_{\text{nonlinear}}} = \frac{C_{T_1}0.027\langle x^2\rangle}{C_{T_1/4}1.94\langle x^2\rangle} = 1.9\,\%. \tag{6.32}$$

For the data set presented in fig. 6.11, we find a value of $4.6\,\%$, or $3.4\,\%$ if we subtract the variance in the off-resonance measurements to account for the noise contribution. The mechanical decoherence due to the presence of the second mechanical mode therefore accounts for more than half of the additional variance in measurements with a delay of a full mechanical period.

In fig. 6.6 we showed the expected variance of the measured difference between pulses as a function of delay, which has a sinusoidal dependence with a period equal to the mechanical resonance period $T_{\text{m}}$. The experimentally measured variance as a function of delay is shown in fig. 6.12. Here we used two pulses, with $P_{\text{sig}} = 15.6\,\mu\text{W}$, and each data point corresponds to a data set with $50$ pulse sequences. We fit the expected sinusoidal curve to the data, shown in the graph with the solid black line. The fit parameters were optimized using differences on a logarithmic scale, and the result was used to plot the gray grid lines in the figure at multiples of a quarter of the fitted period. Just like in the four-pulse data shown in fig. 6.11, the minimum variance, found after a delay of a full mechanical period $T_{\text{m}}$, is larger than the noise variance measured in the off-resonance measurements. We again attribute this to the presence of the second mechanical mode. Using the result in eq. (6.32) and the fitted variance after a quarter period, we plot the predicted variance after a full period delay due to the second mechanical mode with the dash-dotted line, which shows this contribution accounts for

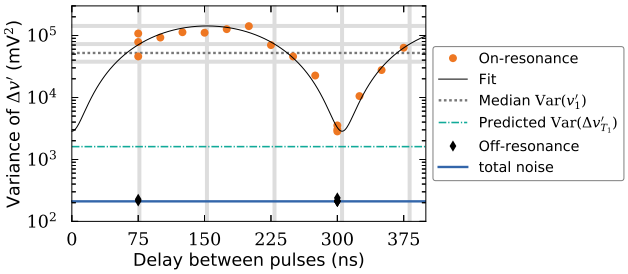


Figure 6.12: Variances of the difference between subsequent pulses $\Delta v' = v'_2 - v'_1$, as a function of the delay between the two pulses. This data was taken with sequences of two pulses at $P_{\text{sig}} = 15.6\,\mu\text{W}$, with a total of $50$ pulse sequences for every data point. The black solid line represents a sinusoidal fit to the data (fitted using the logarithmic scale). The period, offset, and amplitude fit parameters were used to draw the gray grid lines, corresponding to multiples of a quarter period and to the normalized variances at $1$, $2$ and $4$ in fig. 6.6. The lowest horizontal solid line at $4 \times 10^4\,\text{mV}^2$ corresponds to the single pulse outcomes according to the fit parameters, which is slightly lower than the actually measured variance of the single pulse outcomes, as shown with the dotted line. The dash-dotted line shows the expected contribution from the second mechanical mode, at a delay equal to the period of the first mechanical mode ($301\,\text{ns}$). This is calculated from the fitted value for the variance after a quarter period delay, using eq. (6.32). The noise estimate and reference measurements are indicated with the blue solid line and black diamonds, respectively (see fig. 6.10).

a large fraction of the measured minimum variance. The influence of the second mechanical mode is further evidenced by the fact that the fit parameter for the period yielded $306\,\text{ns}$, the average of the mechanical periods of the two modes.

We conclude that we sense mechanical thermal motion of the sliced nanobeam with pulsed optical measurements. While the overall distributions of individual pulse outcomes $\mathcal{P}(v'_1), \mathcal{P}(v'_2)$ are broadened due to slow drift, the differences $\Delta v'$ between two subsequent pulses follow the expected distributions. The periodic behavior of the variance $\langle \Delta v' \rangle$ is a clear signature of the harmonic motion of the mechanical resonator at short timescales. Around a delay of a full period $T_{\text{m}}$, this measurement of $\langle \Delta v'^2 \rangle$ directly represents the uncertainty of our prediction of the second pulse outcome $v'_2$ after a single measurement $v'_1$, which is a first step toward tomography. At other delays, especially around $T_{\text{m}}/2$, to make a good prediction of the second pulse outcome we need to know the pulse outcome $\langle v' \rangle$ corresponding to the equilibrium position $\langle x \rangle$, which is affected by slow drift. However, in the absence of this information, one could argue that our best prediction for any delay would be $v'_2 = v'_1$. In that case, the data in fig. 6.12 represents the uncertainty of that prediction as a function of delay.

### 6.3.2. Noise and sensitivity

We use the variance of $\Delta v'$ with delays of $T_{\text{m}}$ and $T_{\text{m}}/4$ to analyze the noise level and the sensitivity of our measurement. In fig. 6.13, we show these variances in the same graph as the noise estimate and the reference measurements that were presented in fig. 6.10. We include several data sets, shown in orange, red, and light and dark gray. In order to compare the variance as a function of only $P_{\text{sig}}$,

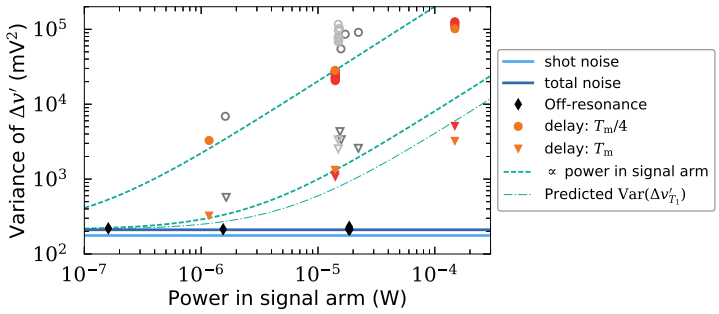


Figure 6.13: Variances of the difference between subsequent pulses $\Delta v' = v'_2 - v'_1$, as a function of the optical power in the signal arm $P_{\text{sig}}$. The circles correspond to variances after a delay of $T_{\text{m}}/4$, triangles to a delay of $T_{\text{m}}$, with the different colors depicting different data sets. Between the gray and orange/red data sets, we switched to a new intensity modulator that allowed better suppression of the light in the "off" state between pulses. The total number of pulse sequences was $50$ per gray data point, $500$ per orange data point, and $1000$ per red data point. The noise estimate and reference measurements are indicated with the blue solid lines and black diamonds, respectively (see fig. 6.10). The dashed lines represent a linear dependence on the power in the signal arm $P_{\text{sig}}$, which includes an offset equal to the "total noise" estimate, and passes through the orange data point at $14\,\mu\text{W}$. The dash-dotted line was calculated from the top dashed line using eq. (6.32) and represents the predicted variance after a delay of a full period due to the presence of the second mechanical mode.

we corrected the data for $P_{\text{LO}}$: $\langle \Delta v'^2 \rangle_{\text{corr}} = \frac{P_{\text{LO,ref}}}{P_{\text{LO}}} \langle \Delta v'^2 \rangle$. The values of $P_{\text{LO}}$ ranged from $1.2\,\text{mW}$ to $1.7\,\text{mW}$. For the data sets shown in orange and red closed symbols, we used an intensity modulator (Jenoptik AM1470b) that allowed a better suppression of the light during the time between pulses than intensity modulator used to obtain the data sets shown in gray open symbols (Thorlabs LN81S). We note that the difference in the measured variances is most likely due to a change in the alignment of the setup, leading to a change in sensitivity.

The variance after a delay of $T_{\text{m}}/4$ (circles) is expected to scale with the sensitivity of the measurement, which means we expect a linear dependence on $P_{\text{sig}}$. In fig. 6.13, we indicated this with a linear function that includes an offset equal to the "total noise" estimate, and with a prefactor such that it passes through the orange data point at $14\,\mu\text{W}$. The variance after a delay of $T_{\text{m}}$ (triangles) also goes up with $P_{\text{sig}}$, which we attribute to the presence of the second mechanical mode. Since the second mechanical mode introduces extra variance of the displacement after a delay of $T_{\text{m}}$, the resulting extra variance of $\Delta v'$ scales with the sensitivity, and therefore with $P_{\text{sig}}$. We also indicated this expected scaling with $P_{\text{sig}}$ in fig. 6.13, again with an offset equal to the "total noise" estimate and a prefactor such that it passes through the orange data point at $14\,\mu\text{W}$. Just like in fig. 6.12, we also use the result in eq. (6.32) to predict the contribution of the second mechanical mode after a delay of a full period, using the variance after a delay of a quarter period (again based on the orange data point at $14\,\mu\text{W}$). This is indicated with a dash-dotted line. The deviation of the data points from the linear trend at $P_{\text{sig}} = 150\,\mu\text{W}$ could be due to a combination of backaction and nonlinear readout and will be discussed in the next section.

To obtain an estimate of the displacement sensitivity of our measurement, we need to calibrate the scale of our results. Once we have a calibrated scale, we can use the variance after a full mechanical period as a limit to how well we can predict the outcome of a measurement. Alternatively, we can use the off-resonance measurements to estimate the imprecision due to the measurement noise, which is dominated by the optical shot noise. In principle, it should be possible to fit the distribution of pulse outcomes with our predicted probability density functions (see fig. 6.11), here we use the simpler approach of using the variances of these distributions and comparing them to the expected value due to the thermal motion of the structure. In essence, we would like to calculate

$$\langle x^2\rangle_{\text{noise}} = \frac{\langle x^2\rangle_{\text{th}}\langle v'^2\rangle_{\text{noise}}}{\langle v'^2\rangle_{\text{th}}}. \tag{6.33}$$

To use the variance of the difference of two pulses, we assume that the noise process limiting our measurement is uncorrelated between the two pulses, which means that $\langle \Delta v'^2\rangle_{\text{noise}} = 2\langle v'^2\rangle_{\text{noise}}$. This leads to

$$\langle x^2\rangle_{\text{noise}} = \frac{\langle \Delta x_\tau^2\rangle_{\text{th}}\langle \Delta v'^2\rangle_{\text{noise}}}{2\langle v_\tau'^2\rangle_{\text{th}}}, \tag{6.34}$$

where we can in principle choose $\tau$ to be any delay except a full period $T_{\text{m}}$ (see fig. 6.12). The thermal displacement variance with delay $\tau$ is given by eq. (6.10), while the other two factors on the right-hand side are experimentally obtained values. For a delay $\tau = T_{\text{m}}/4$, which we choose here, eq. (6.31) showed $\langle \Delta x^2_{T_1/4}\rangle \approx 1.94\langle x^2\rangle_{\text{th}}$.

Equation (6.34) is based on the assumption of a linear transduction from $x$ to $v'$. Without further correction, it provides an upper limit for the imprecision with which we can measure the displacement. This is due to the fact that the average sensitivity only decreases if the spread of relative detunings increases, which can be seen in fig. 6.3b. We note that even if the noise contribution is due to the second mechanical mode, the variance of that second mode at $96\,\%$ of its period is less affected by the nonlinearity than the variance after a quarter period, as we show in fig. 6.6c. This means eq. (6.34) still provides an upper limit for the imprecision. Alternatively, to account for the nonlinearity we can re-use the correction factors $C_\tau$ employed in eq. (6.32) by substituting $\langle \Delta v_\tau'^2\rangle_{\text{corr}} = C_\tau^{-1}\langle \Delta v_\tau'^2\rangle$ into eq. (6.34). The higher sensitivity we find from such a calculation corresponds to the sensitivity to displacement changes for the data where the displacement is small. We note that this higher sensitivity could actually be achieved by post-selection of the data at small displacement.

In the data sets depicted in fig. 6.13, the highest ratio $\mathrm{Var}(\Delta v')_{T_{\text{m}}/4}/\mathrm{Var}(\Delta v')_T$ between variances after $T_{\text{m}}/4$ and after $T_{\text{m}}$ is found at $P_{\text{sig}} = 150\,\mu\text{W}$. However, since the data points at highest power do not follow the expected dependency (and show evidence of backaction, as discussed below), we focus on the lower power at $P_{\text{sig}} = 14\,\mu\text{W}$, where we find a value for this ratio of $22$. The most conservative estimate of the sensitivity based on the data depicted in fig. 6.13 is found by using

this ratio in eq. (6.34), without correcting for the nonlinearity, which leads to $\langle x^2\rangle_{\text{noise}} = (1.94/44)\langle x^2\rangle_{\text{th}} = 0.044\langle x^2\rangle_{\text{th}}$. Using eq. (6.8), and using the fact that both mechanical modes have approximately equal frequencies $\Omega_{\text{m}}$ and zero-point fluctuations $x_{\text{zpf}}$, the thermal displacement variance of the structure is found to be $\langle x^2\rangle = 4x_{\text{zpf}}^2 k_{\text{B}} 3.0\,\text{K}/(h 3.2\,\text{MHz}) = 78\times10^3 x_{\text{zpf}}^2$. We therefore find our most conservative estimate of the sensitivity is $\langle x^2\rangle_{\text{noise}} = 0.044\langle x^2\rangle_{\text{th}} = 3.4\times10^3 x_{\text{zpf}}^2$, which corresponds to a root-mean-square value of $x_{\text{rms}} = \sqrt{\langle x^2\rangle_{\text{noise}}} = 59\,x_{\text{zpf}}$. If we correct both experimental variances $\text{Var}(\Delta v')_{T_{\text{m}}/4}$ and $\text{Var}(\Delta v')_T$ for the nonlinear readout, we find $\langle x^2\rangle_{\text{noise}} = 0.032\langle x^2\rangle_{\text{th}} = 2.5\times10^3 x_{\text{zpf}}^2$, or $x_{\text{rms}} = 50\,x_{\text{zpf}}$.

Finally, we use the off-resonance measurements to estimate the imprecision due to the measurement noise. Using the data set at $P_{\text{sig}} = 14\,\mu\text{W}$ again, $\text{Var}(\Delta v')_{T_{\text{m}}/4}/\,\text{Var}(\Delta v')_{\text{ref}} = 80$. We correct $\text{Var}(\Delta v')_{T_{\text{m}}/4}$ for the nonlinear readout and find $\langle x^2\rangle_{\text{shotnoise}} = 0.0032\langle x^2\rangle_{\text{th}} = 0.25\times10^3 x_{\text{zpf}}^2$, or $x_{\text{rms}}^{\text{shotnoise}} = 16\,x_{\text{zpf}}$.

### 6.3.3. Backaction

**Experimental observation**

Figure 6.13 shows a deviation from the linear trend with $P_{\text{sig}}$ at the highest powers we used. In fig. 6.14, we show one of the data sets taken at this power, in the same format as in fig. 6.11. Apart from the difference in horizontal scale, the most obvious change is the asymmetry in the histogram of differences after a delay of $T_{\text{m}}/4$. We ascribe this to an interplay of backaction and the nonlinear readout: during the first pulse, the light in the cavity exerts a force on the resonator, which changes its momentum. A quarter period later, this change in momentum has translated in a shift in displacement. In the case of linear readout, this would result only in a change of the mean of the output, but would otherwise leave the distribution unchanged. For nonlinear readout however, the shift of the distribution of relative detunings $u$ during the second pulse, can for example move the mean of the distribution toward the relatively insensitive detunings near $u = 1$, which leads to an asymmetric distribution of outputs. In fig. 6.14, the distribution after $T_{\text{m}}/2$ is also changed. This data was obtained by taking the difference between the third and first pulse of the pulse sequence shown in fig. 6.8, which means the backaction of the second pulse could be the main reason for the deviation of the histogram from the expected shape. If the second pulse was not present, we would not expect any backaction to influence the displacement of a single resonator after delays of $T_{\text{m}}/2, T_{\text{m}}$, or any multiple of $T_{\text{m}}/2$. However, since in our case there is a second mechanical mode, the backaction on that mode could still show up in the measurement, since the mechanical periods are not exactly the same.

**Estimated effect of backaction**

To support our hypothesis that the deviations from the predictions at higher power are due to backaction, we calculate the expected change is detuning $u$ after a

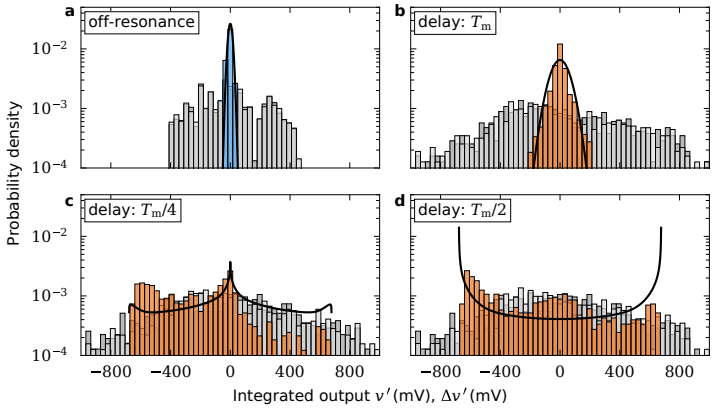


Figure 6.14: Experimentally measured distributions, using the pulse sequence shown in fig. 6.8, with $P_{\text{sig}} = 150\,\mu\text{W}$ (approximately 10 times more than in fig. 6.11). The off-resonance data (a) is the same as in fig. 6.11, taken with only two pulses, at $P_{\text{sig}} = 18.5\,\mu\text{W}$. Grey histograms: individual outcomes $v'_a, v'_b$; colored histograms: differences $\Delta v' = v'_b - v'_a$. Solid lines: Gaussian fit to the measured distribution (a,b), and scaled expected distributions (c,d). The total number of pulse sequences was 3000 for the off-resonance measurement (a), and 1000 for the on-resonance data set (b–d).

quarter period, due to a single optical pulse.

The radiation pressure force can be expressed using the optomechanical coupling $G = g_0/x_{\text{zpf}}$ as

$$F_{\text{rad}} = \frac{\hbar G n_c^{\max}}{1+u^2}, \tag{6.35}$$

where $u \equiv \frac{2}{\kappa}(\Delta_0 + Gx)$ with $\Delta_0$ the average detuning between the laser and cavity frequency, and

$$n_c^{\max} = \frac{4\eta}{\kappa}\frac{P_{\text{in}}}{\hbar\omega_{\text{c}}} \tag{6.36}$$

is the maximum number of photons in the cavity when it is driven at resonance. The maximum possible force, when the cavity is at resonance, is therefore

$$F_{\text{rad}}^{\max} = \hbar G n_c^{\max} = \frac{4\hbar\eta G}{\kappa}\frac{P_{\text{in}}}{\hbar\omega_{\text{c}}}. \tag{6.37}$$

We apply this force for a very short period of time, which will change the momentum of the mechanical resonator:

$$F = \frac{\mathrm{d}p}{\mathrm{d}t}, \quad \text{so} \quad \Delta p = \int F\mathrm{d}t = F\Delta t, \tag{6.38}$$

where we assumed in the last step that we apply a constant force during a time interval with length $\Delta t$, which is much shorter than the mechanical period.

A quarter period later, the change in momentum $\Delta p$ will be translated to a change in displacement

$$\begin{aligned}\Delta x &= \frac{\Delta p}{m\Omega_{\mathrm{m}}} = \frac{\hbar G n_c^{\max} \Delta t}{m\Omega_{\mathrm{m}}} \frac{P_{\mathrm{in}}}{\hbar\omega_{\mathrm{c}}} \\ &= 2g_0 x_{\mathrm{zpf}} n_c^{\max} \Delta t,\end{aligned} \tag{6.39}$$

which can be directly related to a change in optical frequency

$$\Delta\omega_{\mathrm{c}} = G\Delta x = 2g_0^2 n_c^{\max}\Delta t = \frac{8g_0^2\eta}{\kappa}\frac{P_{\mathrm{in}}}{\hbar\omega_{\mathrm{c}}}\Delta t. \tag{6.40}$$

If we use the experimental parameters for one of the mechanical modes, with $g_0/2\pi = 25\,\mathrm{MHz}$, $\eta = 0.02$, $\kappa/2\pi = 20\,\mathrm{GHz}$, $\omega_{\mathrm{c}} = 200\,\mathrm{THz}$, $P_{\mathrm{in}} = 150\,\mu\mathrm{W}$, and $\Delta t = 20\,\mathrm{ns}$, we find $\Delta\omega_{\mathrm{c}}/2\pi = 113\,\mathrm{GHz}$, which is more than five times larger than the optical linewidth. This power $P_{\mathrm{in}}$ corresponds to the highest-power measurements shown in fig. 6.13. Accounting for the second mechanical mode, the frequency shift can even be up to twice as large. As shown in eq. (6.40), this effect scales directly with the used optical power, so even at $P_{\mathrm{in}} \approx 15\,\mu\mathrm{W}$, the shift can be of the order of the optical linewidth.

We conclude that the maximum change in cavity frequency due to the backaction of a single optical pulse can indeed strongly influence the measured output a quarter period later at the highest power we used. Based on this calculation, also at the lower optical powers the induced frequency change can be of the same order of magnitude as the optical linewidth. While the distributions in fig. 6.11 don't show evidence of this, like fig. 6.14, the effect could be observed in future tomography experiments.

## 6.4. Discussion and outlook

### 6.4.1. Factors limiting sensitivity

At the start of this chapter, we introduced the idea of using pulsed measurements to characterize the quantum state of a mechanical resonator. Essentially, the state of the resonator encodes our knowledge of the outcomes of future measurements of the system. We discuss the factors that limit our ability to use a pulsed measurement to predict the outcome of a second measurement, one mechanical period later. Ideally, both measurements have the same outcome, because they both probe the same quadrature of the motion of the resonator.

The dominant contribution limiting the measurement is the presence of a second mechanical mode, which leads to non-zero displacement variance after a full period delay for the other mode, since the two modes have different periods. This effect does not scale with the optical power used to do the measurement, $P_{\mathrm{sig}}$, since both the "signal" (thermal variance) and the "noise" (residual variance due to second mode) directly influence the *displacement* variance, which is transduced in the same way.

A second contribution is the optical shot noise. The signal-to-noise ratio for a shot-noise limited measurement scales with $P_{\mathrm{sig}}$. We have characterized the noise

with an off-resonance measurement and expect that a measurement with only a single mechanical mode would be shot-noise limited, all else being equal.

The effect on the nonlinear readout is more complex, since the sensitivity depends on the displacement. However, this can be partially mitigated, by post-selecting only the measurements where the displacement was small, and consequently the sensitivity was high.

Finally, we found evidence of backaction affecting our measurements. The optical force scales with $P_{\mathrm{sig}}$, therefore this effect limits the amount of optical power we can use for the measurement. For shot-noise limited measurements, this directly limits the obtainable sensitivity.

### 6.4.2. Improvements to reach quantum-limited sensitivity

The most important improvements necessary to obtain a measurement uncertainty near the quantum limit follow from the sensitivity-limiting factors above.

First, it is necessary to deal with the two mechanical modes. A possible strategy is changing the design of the structure, to either (partly) immobilize one of the half-beams or couple the motion of the two half-beams stronger to each other, such that the two modes successfully hybridize to an odd and even mode. In the latter case, one of the modes will not couple to the optical cavity mode because it does not change the gap size, while the other mode couples more strongly (see section 3.2.3). This corresponds to a difference in the zero-point fluctuation amplitudes $x_{\mathrm{zpf},i}$. To achieve $\langle \Delta x^2_{T_i} \rangle < 2x^2_{\mathrm{zpf},i}$, we find from eq. (6.11) that we need

$$2\frac{x^2_{\mathrm{zpf},j}}{x^2_{\mathrm{zpf},i}}\bar{n}_{\mathrm{th},j}\left(1-\cos\frac{2\pi\Omega_j}{\Omega_i}\right) < 1, \tag{6.41}$$

where indeed the left-hand side is smallest if we can achieve strongly hybridized modes with $x_{\mathrm{zpf},j} \ll x_{\mathrm{zpf},i}$. Assuming we don't change the frequency and temperature, we would need a mode asymmetry of $x_{\mathrm{zpf},j}/x_{\mathrm{zpf},i} < 0.031$. Another strategy could be to couple the motion of one half-beam to the other through optical feedback [163]. If the coupling is stronger than the frequency difference between the modes, we again expect hybridization to an odd and even mode. Perhaps the simplest strategy to deal with the two mechanical modes would be to modify the measurement scheme, such that we gain information about both mechanical modes, in analogy to Ockeloen-Korppi *et al.* [164], who characterize a quadrature defined at the difference frequency in continuous measurements. This method is limited by the backaction introduced by extra pulses, or by thermal decoherence during relatively long wait times between pulses, which is necessary when measuring at the difference frequency instead of at the individual mechanical resonance frequencies.

The backaction effect we observe, through the nonlinear readout, can only be avoided by limiting the amount of light in the cavity. The sensitivity of a measurement that corresponds to that intracavity power scales with the measurement efficiency, which is currently limited by the rather low cavity coupling rate $\eta \approx 1.3\,\%$. The coupling to the cavity can be improved by optimizing the design

of the cavity for outcoupling at normal incidence (see section 3.3.4), by using waveguide coupling (either by coupling to on-chip waveguides which are in turn coupled to free-space or optical fibers, or by using a dimpled tapered fiber to directly couple to the cavity), or maybe by employing wavefront shaping to improve the mode matching between the optical cavity mode and the free-space propagating light. Finally, strategies for post-selection of data to mitigate the nonlinear readout should be developed, as well as models to predict the resulting sensitivity.

### 6.4.3. Conclusion

In conclusion, we demonstrate pulsed optical measurements of displacement in a nanoscale cavity optomechanical system. We resolve thermal motion at cryogenic temperatures with single pulsed measurements and analyze the influence of nonlinear readout on the measurement results. We find an upper limit for the imprecision at $x_{\text{rms}} = 59\, x_{\text{zpf}}$, which is mainly limited by the presence of a second mechanical mode coupled to the optical cavity. With only a single mode, we expect to reach a shot-noise limited displacement imprecision of $x_{\text{rms}} = 16 x_{\text{zpf}}$. With improvements to the cavity outcoupling rate $\eta$, it should be possible to achieve $x_{\text{rms}} < x_{\text{zpf}}$. With such resolution, mechanical quantum state reconstruction is possible. At the same time, this would enable protocols to (conditionally) prepare the mechanical resonator in a near-minimum uncertainty state—cooling by measurement—and even in a squeezed state. Other interesting possibilities include studying the decoherence of the mechanical resonator, implementing feedback based on the pulsed measurement outcomes by using the radiation pressure force of an additional pulse to change the state of the resonator, or coupling the mechanical resonator to two-level systems, for example to see if it is possible to do tomography on the quantum states of such a hybrid system.

# A

# Nonlinear cavity response

In this appendix, we estimate the size of nonlinear effects in a silicon photonic crystal cavity similar to the devices we describe in this thesis. Barclay, Srinivasan & Painter [49] modeled the processes that occur in silicon photonic crystal cavities at wavelengths near $1500\,\mathrm{nm}$ and found that two-photon absorption generates free carriers, which increases the absorption at higher optical powers. Additionally, the absorbed light leads to local heating of the cavity, which in turn shifts the cavity frequency since the refractive index of the material depends on temperature. Finally, temperature gradients can drive motion of the mechanical resonator through thermo-elastic forces, leading to dynamical photo-thermal effects.

## A.1. Two-photon and free-carrier absorption

We first consider the processes leading to higher absorption. The two-photon absorption (TPA) at position $\mathbf{r}$ is given by

$$\gamma_{\text{TPA}} = \beta'(\mathbf{r}) w_E(\mathbf{r}) \tag{A.1}$$

where $\beta' = (c/n)^2\beta$ is the material parameter which is related to the two-photon absorption coefficient $\beta$ and $w_E(\mathbf{r}) = (1/2)\varepsilon_0 n^2(\mathbf{r}) E^2(\mathbf{r})$ is the local energy density of the electric field, with $\varepsilon_0$ is the permittivity of free space, $n(\mathbf{r})$ is the local refractive index, and $E(\mathbf{r}) = \langle|\mathbf{E}(\mathbf{r})|\rangle$ is the cycle-averaged amplitude of the electric field of the resonant mode of the cavity. The total TPA rate for the cavity mode can be found by computing the weighted average of $\gamma_{\text{TPA}}$. As a simple approximation, if we assume a fraction $\xi$ of the total stored energy $U = \hbar\omega_{\text{L}}|a|^2$ is homogeneously distributed in a volume $V$ inside of the silicon material, we find

$$\bar{\gamma}_{\text{TPA}} \approx \xi \beta'_{\text{Si}} U/V. \tag{A.2}$$

Free-carrier absorption (FCA) is given by the rate

$$\gamma_{\text{FCA}} = \sigma'(\mathbf{r}) N(\mathbf{r}), \tag{A.3}$$

where $\sigma'(\mathbf{r}) = (c/n)\sigma$ is the material parameter related to the free carrier cross sections for electrons and holes via $\sigma = \sigma_\mathrm{e} + \sigma_\mathrm{h}$, and $N(\mathbf{r})$ quantifies the number of electron-hole pairs. We ignore the small background population of carriers and approximate the density of free carriers generated by the TPA process as

$$N(\mathbf{r}) = \frac{\tau \gamma_\mathrm{TPA}(\mathbf{r}) w_E(\mathbf{r})}{2\hbar\omega_\mathrm{L}}. \tag{A.4}$$

Here, $\tau$ represents the carrier lifetime and $\gamma_\mathrm{TPA}(\mathbf{r})w_E(\mathbf{r})$ is the local absorbed power density due to two-photon absorption. The total free-carrier absorption rate for the cavity mode can again be found by computing a weighted average over $\gamma_\mathrm{FCA}$, combining eqs. (A.3) and (A.4). As with the TPA rate, we use the simple approximation of a homogeneous field inside the silicon material of the cavity to find

$$\bar{\gamma}_\mathrm{FCA} \approx \frac{\xi \beta'_\mathrm{Si} \sigma'_\mathrm{Si} \tau U^2}{2\hbar\omega_\mathrm{L} V^2}. \tag{A.5}$$

To estimate the optical powers in the cavity for which the nonlinear response will start to play a significant role, we now calculate the limit of the stored energy $U$ such that the added absorption amounts to $10\,\%$ of the intrinsic losses of the cavity, that is, $\bar{\gamma}_\mathrm{TPA,FCA} \leq 0.1\kappa$. We take a resonance wavelength of $1.5\,\mu\mathrm{m}$ and an optical quality factor of $10^4$, and we assume that the mode is totally confined ($\xi = 1$) to a mode volume of a cubic wavelength in silicon ($V = (\lambda/n_\mathrm{Si})^3$). Using the material parameters also used by Barclay, Srinivasan & Painter [49] and a conservative estimate for the carrier lifetime of $\tau = 100\,\mathrm{ns}$, we find

$$\frac{U_\mathrm{TPA}}{\hbar\omega_\mathrm{L}} \leq 1.2 \times 10^5, \tag{A.6}$$

$$\frac{U_\mathrm{FCA}}{\hbar\omega_\mathrm{L}} \leq 1.2 \times 10^3. \tag{A.7}$$

From this we conclude that if we use less than $\sim 10^3$ photons in the cavity, two-photon absorption and free-carrier absorption do not play a significant role.

## A.2. Thermo-optic tuning

While the nonlinear effects on the linewidth of the cavity are dominated by the free-carrier absorption, the cavity frequency mainly shifts due to the thermo-optic effect. The light absorbed by the cavity causes a local increase in the cavity temperature, which changes the refractive index as $\Delta n(\mathbf{r}) = (\mathrm{d}n/\mathrm{d}T)\Delta T(\mathbf{r})$. The total shift of the mode can be found by considering the weighted average of the relative refractive index change, which for a cavity with a fraction $\xi$ of the energy in the silicon yields

$$\Delta\omega_\mathrm{c} = \omega_\mathrm{c}\xi\Delta n/n = \frac{\omega_\mathrm{c}\xi}{n}\frac{\mathrm{d}n}{\mathrm{d}T}\Delta T. \tag{A.8}$$

We can approximate the temperature increase using the thermal resistance of the structure $R_\mathrm{th}$ and the total absorbed power in the cavity $P_\mathrm{abs} = U\kappa_\mathrm{abs}$, such that

$$\Delta T = R_\mathrm{th} U \kappa_\mathrm{abs}. \tag{A.9}$$

We now calculate the energy in the cavity which will lead to a shift of $10\,\%$ of the linewidth of the cavity, that is, $\Delta\omega_\mathrm{c} \leq 0.1\kappa$. We again use a cavity with wavelength $1.5\,\mu\mathrm{m}$ and $Q = 10^4$, and set $\xi$ to 1. The thermal resistance is taken from the work of Deotare *et al.* [16], who successfully modeled the response of their double nanobeam cavity. With $\omega_\mathrm{c}/\kappa_\mathrm{abs} = 10^6$, also from Deotare *et al.* [16], and the room-temperature value of $\mathrm{d}n/\mathrm{d}T = 1.8 \times 10^{-4}\,\mathrm{K}^{-1}$ for silicon [165], we find $U_\mathrm{th}/\hbar\omega_\mathrm{c} \leq 9.9 \times 10^2$. At low temperature, the thermo-optic coefficient of silicon is much lower, with $\mathrm{d}n/\mathrm{d}T = 1.0 \times 10^{-8}\,\mathrm{K}^{-1}$ at a temperature of $5\,\mathrm{K}$ [165]. This leads to a much higher power corresponding to a shift of $10\,\%$ of the cavity linewidth, $U_{\mathrm{th},5\,\mathrm{K}}/\hbar\omega_\mathrm{c} \leq 1.8 \times 10^7$. We conclude that the thermo-optic tuning, like the nonlinear absorption effects discussed above, will not have a significant effect for cavity occupancies below $\sim 10^3$ photons.

## A.3. Photo-thermal dynamical effects

Like the static effect of increased temperature discussed in appendix A.2, heating of the cavity can also have dynamical effects. The temperature increase of the cavity will react to the cavity modulations in the same way as the radiation pressure force, since both depend on the intracavity power. In addition to thermo-optic tuning of the cavity, there is also a thermo-elastic force acting on the mechanical resonator due to the temperature gradients in the structure. While the optical force discussed in section 1.4.2 acts with a delay due to the cavity lifetime $\sim \kappa^{-1}$, these thermal effects are governed by the thermal response time of the structure, which is much longer.

We can include these effects into the equations of motion by introducing the thermo-optic frequency detuning $\Delta_\mathrm{to}(a,t)$ and the thermo-elastic force $F_\mathrm{te}(a,t)$ in the equations for the optical cavity and the mechanical resonator, respectively. In both of these terms, the response to a change of optical intensity is not instantaneous, which can be modeled by a convolution with a thermal response function [13]. The equations of motion then read

$$\dot{a} = \left(i\left[\Delta + Gx + \Delta_\mathrm{to}(a,t)\right] - \frac{\kappa}{2}\right)a + \sqrt{\eta_\mathrm{in}\kappa}s_\mathrm{in}, \tag{A.10}$$

$$\ddot{x} = -\Omega_\mathrm{m}^2 x - \Gamma_\mathrm{m}\dot{x} + \frac{\hbar G|a|^2}{m} + \frac{F_\mathrm{te}(a,t)}{m} + \frac{F_\mathrm{ext}}{m}. \tag{A.11}$$

In section 1.4.1 we already compared the optomechanical frequency shift to the thermo-optic tuning $\Delta_\mathrm{to}$ for a constant intracavity field $a$, and found the optomechanical shift is ten times larger for the cavity parameters we considered, with an even larger difference when the cavity is cooled to cryogenic temperatures. This comparison also holds for the dynamical effects due to the radiation pressure force and due to thermo-optic tuning, where the latter might actually be further attenuated if the thermal response time of the structure is so large that it cannot follow the mechanical motion. The thermo-elastic force is difficult to estimate quantitatively, since it requires modeling of the complex interplay between the thermal gradient set up by absorption of the light in the cavity mode and the shape of the mechanical mode. The thermo-elastic force was found to be an im-

portant factor in experiments involving reflective cantilevers [9, 166], where the multi-layered nature of the devices provides a clear mechanism for strong thermo-elastic effects, and it was found to play a minor role in a microtoroid experiment [13]. In reported experiments with photonic crystal cavities, the thermo-elastic force was not found to have a dominant role. However, the larger time constant associated with the thermal response with respect to the radiation pressure force means that even if the magnitude of the thermo-elastic force is much smaller, it could have a larger effect on the mechanical linewidth for cavities with a large optical linewidth ($\kappa \gg \Omega_{\mathrm{m}}$).

# Bibliography


1. Braginsky, V. B., Khalili, F. Y. & Thorne, K. S. *Quantum Measurement* (Cambridge University Press, Cambridge, 1992).
2. Wiseman, H. M. & Milburn, G. J. *Quantum Measurement and Control* (Cambridge University Press, Cambridge, 2009).
3. Binnig, G., Quate, C. F. & Gerber, C. Atomic Force Microscope. *Physical Review Letters* **56,** 930–933 (1986).
4. LIGO Scientific Collaboration & VIRGO Collaboration. Observation of gravitational waves from a binary black hole merger. *Physical Review Letters* **116,** 061102 (2016).
5. Kepler, J. *De cometis libelli tres* (Andrea Apergeri, Augsburg, 1619).
6. Ashkin, A. Acceleration and Trapping of Particles by Radiation Pressure. *Physical Review Letters* **24,** 156–159 (1970).
7. Aspelmeyer, M., Kippenberg, T. J. & Marquardt, F. Cavity optomechanics. *Reviews of Modern Physics* **86,** 1391–1452 (2014).
8. Cohadon, P. F., Heidmann, A. & Pinard, M. Cooling of a Mirror by Radiation Pressure. *Physical Review Letters* **83,** 3174–3177 (1999).
9. Metzger, C. H. & Karrai, K. Cavity cooling of a microlever. *Nature* **432,** 1002–1005 (2004).
10. LIGO Scientific Collaboration. Observation of a kilogram-scale oscillator near its quantum ground state. *New Journal of Physics* **11,** 073032 (2009).
11. Ding, L., Baker, C., Senellart, P., Lemaitre, A., Ducci, S., Leo, G. & Favero, I. Wavelength-sized GaAs optomechanical resonators with gigahertz frequency. *Applied Physics Letters* **98,** 113108 (2011).
12. Balram, K. C., Davanço, M., Lim, J. Y., Song, J. D. & Srinivasan, K. Moving boundary and photoelastic coupling in GaAs optomechanical resonators. *Optica* **1,** 414–420 (2014).

13. Verhagen, E., Deléglise, S., Weis, S., Schliesser, A. & Kippenberg, T. J. Quantum-coherent coupling of a mechanical oscillator to an optical cavity mode. *Nature* **482,** 63–67 (2012).

14. Teufel, J. D., Donner, T., Castellanos-Beltran, M. A., Harlow, J. W. & Lehnert, K. W. Nanomechanical motion measured with an imprecision below that at the standard quantum limit. *Nature Nanotechnology* **4,** 820–823 (2009).

15. Chan, J., Alegre, T. P. M., Safavi-Naeini, A. H., Hill, J. T., Krause, A., Gröblacher, S., Aspelmeyer, M. & Painter, O. Laser cooling of a nanomechanical oscillator into its quantum ground state. *Nature* **478,** 89–92 (2011).

16. Deotare, P. B., Bulu, I., Frank, I. W., Quan, Q., Zhang, Y., Ilic, R. & Lončar, M. All optical reconfiguration of optomechanical filters. *Nature Communications* **3,** 846 (2012).

17. Safavi-Naeini, A. H., Gröblacher, S., Hill, J. T., Chan, J., Aspelmeyer, M. & Painter, O. Squeezed light from a silicon micromechanical resonator. *Nature* **500,** 185–189 (2013).

18. Safavi-Naeini, A. H., Hill, J. T., Meenehan, S., Chan, J., Gröblacher, S. & Painter, O. Two-Dimensional Phononic-Photonic Band Gap Optomechanical Crystal Cavity. *Physical Review Letters* **112,** 153603 (2014).

19. Gomis-Bresco, J., Navarro-Urrios, D., Oudich, M., El-Jallal, S., Griol, A., Puerto, D., Chavez, E., Pennec, Y., Djafari-Rouhani, B., Alzina, F., Martínez, A. & Torres, C. S. A one-dimensional optomechanical crystal with a complete phononic band gap. *Nature Communications* **5,** 4452 (2014).

20. Schneider, K. & Seidler, P. Strong optomechanical coupling in a slotted photonic crystal nanobeam cavity with an ultrahigh quality factor-to-mode volume ratio. *Optics Express* **24,** 13850–13865 (2016).

21. Zobenica, Z., van der Heijden, R., Petruzzella, M., Pagliano, F., Leijssen, R., Xia, T., Midolo, L., Cotrufo, M., Cho, Y., van Otten, F., Verhagen, E. & Fiore, A. Fully integrated nano-opto-electro-mechanical wavelength and displacement sensor. in *Advanced Photonics 2016 (IPR, NOMA, Sensors, Networks, SPPCom, SOF)* (OSA, Washington, D.C., 2016), paper SeW2E.4.

22. Thijssen, R., Kippenberg, T. J., Polman, A. & Verhagen, E. Plasmomechanical Resonators Based on Dimer Nanoantennas. *Nano Letters* **15,** 3971–3976 (2015).

23. Anetsberger, G., Gavartin, E., Arcizet, O., Unterreithmeier, Q. P., Weig, E. M., Gorodetsky, M. L., Kotthaus, J. P., Kippenberg, T. J. & Verlot, P. Measuring nanomechanical motion with an imprecision below the standard quantum limit. *Physical Review A* **82,** 061804 (2010).

24. Murch, K. W., Moore, K. L., Gupta, S. & Stamper-Kurn, D. M. Observation of quantum-measurement backaction with an ultracold atomic gas. *Nature Physics* **4,** 561–564 (2008).

25. Purdy, T. P., Peterson, R. W. & Regal, C. A. Observation of Radiation Pressure Shot Noise on a Macroscopic Object. *Science* **339,** 801–804 (2013).

26. Teufel, J. D., Donner, T., Li, D., Harlow, J. W., Allman, M. S., Cicak, K., Sirois, A. J., Whittaker, J. D., Lehnert, K. W. & Simmonds, R. W. Sideband cooling of micromechanical motion to the quantum ground state. *Nature* **475,** 359–363 (2011).

27. Wilson, D. J., Sudhir, V., Piro, N., Schilling, R., Ghadimi, A. & Kippenberg, T. J. Measurement-based control of a mechanical oscillator at its thermal decoherence rate. *Nature* **524,** 325–329 (2015).

28. Brooks, D. W. C., Botter, T., Schreppler, S., Purdy, T. P., Brahms, N. & Stamper-Kurn, D. M. Non-classical light generated by quantum-noise-driven cavity optomechanics. *Nature* **488,** 476–480 (2012).

29. Purdy, T. P., Yu, P.-L., Peterson, R. W., Kampel, N. S. & Regal, C. A. Strong Optomechanical Squeezing of Light. *Physical Review X* **3,** 031012 (2013).

30. Wollman, E. E., Lei, C. U., Weinstein, A. J., Suh, J., Kronwald, A., Marquardt, F., Clerk, A. A. & Schwab, K. C. Quantum squeezing of motion in a mechanical resonator. *Science* **349,** 952–955 (2015).

31. Pirkkalainen, J.-M., Damskägg, E., Brandt, M., Massel, F. & Sillanpää, M. A. Squeezing of Quantum Noise of Motion in a Micromechanical Resonator. *Physical Review Letters* **115,** 243601 (2015).

32. Lecocq, F., Clark, J. B., Simmonds, R. W., Aumentado, J. & Teufel, J. D. Quantum Nondemolition Measurement of a Nonclassical State of a Massive Object. *Physical Review X* **5,** 041037 (2015).

33. Palomaki, T. A., Teufel, J. D., Simmonds, R. W. & Lehnert, K. W. Entangling Mechanical Motion with Microwave Fields. *Science* **342,** 710–713 (2013).

34. Palomaki, T. A., Harlow, J. W., Teufel, J. D., Simmonds, R. W. & Lehnert, K. W. Coherent state transfer between itinerant microwave fields and a mechanical oscillator. *Nature* **495,** 210–214 (2013).

35. Reed, A. P., Mayer, K. H., Teufel, J. D., Burkhart, L. D., Pfaff, W., Reagor, M., Sletten, L., Ma, X., Schoelkopf, R. J., Knill, E. & Lehnert, K. W. Faithful conversion of propagating quantum information to mechanical motion, preprint at arXiv:1703.02548 (2017).

36. Riedinger, R., Hong, S., Norte, R. A., Slater, J. A., Shang, J., Krause, A. G., Anant, V., Aspelmeyer, M. & Gröblacher, S. Non-classical correlations between single photons and phonons from a mechanical oscillator. *Nature* **530,** 313–316 (2016).

37. Sudhir, V., Schilling, R., Fedorov, S. A., Schuetz, H., Wilson, D. J. & Kippenberg, T. J. Quantum correlations of light due to a room temperature mechanical oscillator for force metrology, preprint at arXiv:1608.00699 (2016).

38. Purdy, T. P., Grutter, K. E., Srinivasan, K. & Taylor, J. M. Quantum correlations from a room-temperature optomechanical cavity. *Science* **356,** 1265–1268 (2017).

39. Kampel, N. S., Peterson, R. W., Fischer, R., Yu, P.-L., Cicak, K., Simmonds, R. W., Lehnert, K. W. & Regal, C. A. Improving Broadband Displacement Detection with Quantum Correlations. *Physical Review X* **7,** 021008 (2017).

40. Bowen, W. P. & Milburn, G. J. *Quantum Optomechanics* (CRC Press, Boca Raton, FL, 2015).

41. Genes, C., Vitali, D., Tombesi, P., Gigan, S. & Aspelmeyer, M. Ground-state cooling of a micromechanical oscillator: Comparing cold damping and cavity-assisted cooling schemes. *Physical Review A* **77,** 033804 (2008).

42. Eichenfield, M., Camacho, R., Chan, J., Vahala, K. J. & Painter, O. A picogram- and nanometre-scale photonic-crystal optomechanical cavity. *Nature* **459,** 550–555 (2009).

43. Gavartin, E., Braive, R., Sagnes, I., Arcizet, O., Beveratos, A., Kippenberg, T. J. & Robert-Philip, I. Optomechanical Coupling in a Two-Dimensional Photonic Crystal Defect Cavity. *Physical Review Letters* **106,** 203902 (2011).

44. Chan, J., Safavi-Naeini, A. H., Hill, J. T., Meenehan, S. & Painter, O. Optimized optomechanical crystal cavity with acoustic radiation shield. *Applied Physics Letters* **101,** 081115 (2012).

45. Fan, S., Suh, W. & Joannopoulos, J. D. Temporal coupled-mode theory for the Fano resonance in optical resonators. *Journal of the Optical Society of America A* **20,** 569–572 (2003).

46. Haus, H. A. *Waves and fields in optoelectronics* (Prentice-Hall, Englewood Cliffs, NJ, 1984).

47. Galli, M., Portalupi, S. L., Belotti, M., Andreani, L. C., O'Faolain, L. & Krauss, T. F. Light scattering and Fano resonances in high-Q photonic crystal nanocavities. *Applied Physics Letters* **94,** 071101 (2009).

48. Fano, U. Effects of configuration interaction on intensities and phase shifts. *Physical Review* **124,** 1866–1878 (1961).

49. Barclay, P. E., Srinivasan, K. & Painter, O. Nonlinear response of silicon photonic crystal micresonators excited via an integrated waveguide and fiber taper. *Optics Express* **13,** 801–820 (2005).

50. Clerk, A. A., Marquardt, F. & Harris, J. G. E. Quantum Measurement of Phonon Shot Noise. *Physical Review Letters* **104,** 213603 (2010).

51. Clerk, A. A., Marquardt, F. & Jacobs, K. Back-action evasion and squeezing of a mechanical resonator using a cavity detector. *New Journal of Physics* **10,** 095010 (2008).

52. Gorodetsky, M. L., Schliesser, A., Anetsberger, G., Deleglise, S. & Kippenberg, T. J. Determination of the vacuum optomechanical coupling rate using frequency noise calibration. *Optics Express* **18,** 23236–23246 (2010).

53. Lvovsky, A. I. & Raymer, M. G. Continuous-variable optical quantum-state tomography. *Reviews of Modern Physics* **81,** 299–332 (2009).

54. Bachor, H.-A. & Ralph, T. C. *A Guide to Experiments in Quantum Optics* (Wiley-VCH, Weinheim, 2004).

55. Van Thourhout, D. & Roels, J. Optomechanical device actuation through the optical gradient force. *Nature Photonics* **4,** 211–217 (2010).

56. Johnson, S. G., Ibanescu, M., Skorobogatiy, M. A., Weisberg, O., Joannopoulos, J. D. & Fink, Y. Perturbation theory for Maxwell's equations with shifting material boundaries. *Physical Review E* **65,** 066611 (2002).

57. Rakich, P. T., Davids, P. & Wang, Z. Tailoring optical forces in waveguides through radiation pressure and electrostrictive forces. *Optics Express* **18,** 14439–14453 (2010).

58. Suh, W., Yanik, M. F., Solgaard, O. & Fan, S. Displacement-sensitive photonic crystal structures based on guided resonance in photonic crystal slabs. *Applied Physics Letters* **82,** 1999–2001 (2003).

59. Notomi, M., Taniyama, H., Mitsugi, S. & Kuramochi, E. Optomechanical Wavelength and Energy Conversion in High-Q Double-Layer Cavities of Photonic Crystal Slabs. *Physical Review Letters* **97,** 023903 (2006).

60. Lu, T.-W. & Lee, P.-T. Ultra-high sensitivity optical stress sensor based on double-layered photonic crystal microcavity. *Optics Express* **17,** 1518–1526 (2009).

61. Povinelli, M. L., Lončar, M., Ibanescu, M., Smythe, E. J., Johnson, S. G., Capasso, F. & Joannopoulos, J. D. Evanescent-wave bonding between optical waveguides. *Optics Letters* **30,** 3042–3044 (2005).

62. Povinelli, M. L., Johnson, S. G., Lončar, M., Ibanescu, M., Smythe, E. J., Capasso, F. & Joannopoulos, J. D. High-Q enhancement of attractive and repulsive optical forces between coupled whispering-gallery-mode resonators. *Optics Express* **13,** 8286–8295 (2005).

63. Rakich, P. T., Popović, M. A., Soljačić, M. & Ippen, E. P. Trapping, corralling and spectral bonding of optical resonances through optically induced potentials. *Nature Photonics* **1,** 658–665 (2007).

64. Li, M., Pernice, W. H. P., Xiong, C., Baehr-Jones, T., Hochberg, M. & Tang, H. X. Harnessing optical forces in integrated photonic circuits. *Nature* **456,** 480–484 (2008).

65. Li, M., Pernice, W. H. P. & Tang, H. X. Ultrahigh-frequency nanooptomechanical resonators in slot waveguide ring cavities. *Applied Physics Letters* **97,** 183110 (2010).

66. Bagheri, M., Poot, M., Li, M., Pernice, W. P. H. & Tang, H. X. Dynamic manipulation of nanomechanical resonators in the high-amplitude regime and non-volatile mechanical memory operation. *Nature Nanotechnology* **6,** 726–732 (2011).

67. Rosenberg, J., Lin, Q. & Painter, O. Static and dynamic wavelength routing via the gradient optical force. *Nature Photonics* **3,** 478–483 (2009).

68. Wiederhecker, G. S., Chen, L., Gondarenko, A. & Lipson, M. Controlling photonic structures using optical forces. *Nature* **462,** 633–636 (2009).

69. Deotare, P. B., McCutcheon, M. W., Frank, I. W., Khan, M. & Lončar, M. Coupled photonic crystal nanobeam cavities. *Applied Physics Letters* **95,** 031102 (2009).

70. Leijssen, R. & Verhagen, E. Strong optomechanical interactions in a sliced photonic crystal nanobeam. *Scientific Reports* **5,** 15974 (2015).

71. Eichenfield, M., Chan, J., Camacho, R. M., Vahala, K. J. & Painter, O. Optomechanical crystals. *Nature* **462,** 78–82 (2009).

72. Safavi-Naeini, A. H., Alegre, T. P. M., Winger, M. & Painter, O. Optomechanics in an ultrahigh-Q two-dimensional photonic crystal cavity. *Applied Physics Letters* **97,** 97–99 (2010).

73. Zheng, J., Sun, X., Li, Y., Poot, M., Dadgar, A., Shi, N. N., Pernice, W. H. P., Tang, H. X. & Wong, C. W. Femtogram dispersive L3-nanobeam optomechanical cavities: design and experimental comparison. *Optics Express* **20,** 26486–26498 (2012).

74. Sun, X., Zheng, J., Poot, M., Wong, C. W. & Tang, H. X. Femtogram Doubly Clamped Nanomechanical Resonators Embedded in a High-Q Two-Dimensional Photonic Crystal Nanocavity. *Nano Letters* **12,** 2299–2305 (2012).

75. Roh, Y.-G., Tanabe, T., Shinya, A., Taniyama, H., Kuramochi, E., Matsuo, S., Sato, T. & Notomi, M. Strong optomechanical interaction in a bilayer photonic crystal. *Physical Review B* **81,** 121101 (2010).

76. Midolo, L., van Veldhoven, P. J., Dündar, M. A., Nötzel, R. & Fiore, A. Electromechanical wavelength tuning of double-membrane photonic crystal cavities. *Applied Physics Letters* **98,** 211120 (2011).

77. Midolo, L., Pagliano, F., Hoang, T. B., Xia, T., van Otten, F. W. M., Li, L. H., Linfield, E. H., Lermer, M., Höfling, S. & Fiore, A. Spontaneous emission control of single quantum dots by electromechanical tuning of a photonic crystal cavity. *Applied Physics Letters* **101,** 091106 (2012).

78. Petruzzella, M., Xia, T., Pagliano, F., Birindelli, S., Midolo, L., Zobenica, Z., Li, L. H., Linfield, E. H. & Fiore, A. Fully tuneable, Purcell-enhanced solid-state quantum emitters. *Applied Physics Letters* **107,** 141109 (2015).

79. Petruzzella, M., La China, F., Intonti, F., Caselli, N., De Pas, M., van Otten, F. W. M., Gurioli, M. & Fiore, A. Nanoscale mechanical actuation and near-field read-out of photonic crystal molecules. *Physical Review B* **94,** 115413 (2016).

80. Midolo, L., Yoon, S. N., Pagliano, F., Xia, T., van Otten, F. W. M., Lermer, M., Höfling, S. & Fiore, A. Electromechanical tuning of vertically-coupled photonic crystal nanobeams. *Optics Express* **20,** 19255–19263 (2012).

81. Van Laer, R., Kuyken, B., Van Thourhout, D. & Baets, R. Analysis of enhanced stimulated Brillouin scattering in silicon slot waveguides. *Optics Letters* **39,** 1242–1245 (2014).

82. Almeida, V. R., Xu, Q., Barrios, C. A. & Lipson, M. Guiding and confining light in void nanostructure. *Optics Letters* **29,** 1209–1211 (2004).

83. Robinson, J. T., Manolatou, C., Chen, L. & Lipson, M. Ultrasmall Mode Volumes in Dielectric Optical Microcavities. *Physical Review Letters* **95,** 143901 (2005).

84. Midolo, L. *Electromechanical Tuning of Photonic Crystal Cavities.* PhD thesis (Eindhoven University of Technology, 2013).

85. Westendorp, S. *Cavity optomechanics in vertically-coupled photonic crystal nanobeams and membranes.* Master's thesis (Eindhoven University of Technology, 2014).

86. Ramos, D., Frank, I. W., Deotare, P. B., Bulu, I. & Lončar, M. Non-linear mixing in coupled photonic crystal nanobeam cavities due to cross-coupling opto-mechanical mechanisms. *Applied Physics Letters* **105,** 181121 (2014).

87. Quan, Q. & Lončar, M. Deterministic design of wavelength scale, ultra-high Q photonic crystal nanobeam cavities. *Optics Express* **19,** 18529–18542 (2011).

88. Joannopoulos, J. D., Johnson, S. G., Winn, J. N. & Meade, R. D. *Photonic Crystals: Molding the Flow of Light* (Princeton University Press, Princeton, NJ, 2008).

89. Krause, A. G., Blasius, T. D. & Painter, O. Optical read out and feedback cooling of a nanostring optomechanical cavity, preprint at arXiv:1506.01249 (2015).

90. Tao, Y., Boss, J. M., Moores, B. A. & Degen, C. L. Single-crystal diamond nanomechanical resonators with quality factors exceeding one million. *Nature Communications* **5,** 3638 (2014).

91. Cleland, A. N. *Foundations of Nanomechanics* (Springer-Verlag, Berlin, Heidelberg, 2003).

92. Ryckman, J. D. & Weiss, S. M. Low mode volume slotted photonic crystal single nanobeam cavity. *Applied Physics Letters* **101,** 071104 (2012).

93. Seidler, P., Lister, K., Drechsler, U., Hofrichter, J. & Stoferle, T. Slotted photonic crystal nanobeam cavity with an ultrahigh quality factor-to-mode volume ratio. *Optics Express* **21,** 32468–32483 (2013).

94. Wang, C., Quan, Q., Kita, S., Li, Y. & Lončar, M. Single-nanoparticle detection with slot-mode photonic crystal cavities. *Applied Physics Letters* **106,** 261105 (2015).

95. Englund, D., Fushman, I. & Vučković, J. General recipe for designing photonic crystal cavities. *Optics Express* **13,** 5961–5975 (2005).

96. Minkov, M. & Savona, V. Automated optimization of photonic crystal slab cavities. *Scientific Reports* **4,** 5124 (2014).

97. Freisem, L. *Low-loss photonic nanocavities with strong optomechanical interactions.* Master's thesis (University of Amsterdam, 2015).

98. Chan, J. *Laser cooling of an optomechanical crystal resonator to its quantum ground state of motion.* PhD thesis (California Inititute of Technology, 2012).

99. Bonato, C., Hagemeier, J., Gerace, D., Thon, S. M., Kim, H., Andreani, L. C., Petroff, P. M., van Exter, M. P. & Bouwmeester, D. Far-field emission profiles from L3 photonic crystal cavity modes. *Photonics and Nanostructures - Fundamentals and Applications* **11,** 37–47 (2013).

100. Tran, N.-V.-Q., Combrié, S., Colman, P., De Rossi, A. & Mei, T. Vertical high emission in photonic crystal nanocavities by band-folding design. *Physical Review B* **82,** 075120 (2010).

101. Rousseau, I., Sánchez-Arribas, I., Carlin, J.-F., Butté, R. & Grandjean, N. Far-field coupling in nanobeam photonic crystal cavities. *Applied Physics Letters* **108,** 201104 (2016).

102. Olynick, D. L., Cord, B., Schipotinin, A., Ogletree, D. F. & Schuck, P. J. Electron-beam exposure mechanisms in hydrogen silsesquioxane investigated by vibrational spectroscopy and in situ electron-beam-induced desorption. *Journal of Vacuum Science & Technology B* **28,** 581–587 (2010).

103. Van Delft, F. C. M. J. M. Delay-time and aging effects on contrast and sensitivity of hydrogen silsesquioxane. *Journal of Vacuum Science & Technology B* **20,** 2932–2936 (2002).

104. Legtenberg, R. Anisotropic Reactive Ion Etching of Silicon Using $SF_6/O_2/CHF_3$ Gas Mixtures. *Journal of The Electrochemical Society* **142,** 2020–2028 (1995).

105. Jansen, H., de Boer, M., Wensink, H., Kloeck, B. & Elwenspoek, M. The black silicon method. VIII. A study of the performance of etching silicon using $SF_6/O_2$-based chemistry with cryogenical wafer cooling and a high density ICP source. *Microelectronics Journal* **32,** 769–777 (2001).

106. Wahlbrink, T., Mollenhauer, T., Georgiev, Y., Henschel, W., Efavi, J., Gottlob, H., Lemme, M., Kurz, H., Niehusmann, J. & Bolivar, P. H. Highly selective etch process for silicon-on-insulator nano-devices. *Microelectronic Engineering* **78-79,** 212–217 (2005).

107. Tuda, M., Shintani, K. & Ootera, H. Profile evolution during polysilicon gate etching with low-pressure high-density $Cl_2/HBr/O_2$ plasma chemistries. *Journal of Vacuum Science & Technology A* **19,** 711–717 (2001).

108. Selvaraja, S. K., Bogaerts, W. & Van Thourhout, D. Loss reduction in silicon nanophotonic waveguide micro-bends through etch profile improvement. *Optics Communications* **284,** 2141–2144 (2011).

109. Grigorescu, A. E., van der Krogt, M. C. & Hagen, C. W. Sub-10-nm structures written in ultra-thin HSQ resist layers using electron-beam lithography. in *Proceedings of SPIE* **6519** (2007), 65194A.

110. Georgiev, Y. M., Henschel, W., Fuchs, A. & Kurz, H. Surface roughness of hydrogen silsesquioxane as a negative tone electron beam resist. *Vacuum* **77,** 117–123 (2005).

111. Yamashita, D., Takahashi, Y., Asano, T. & Noda, S. Raman shift and strain effect in high-Q photonic crystal silicon nanocavity. *Optics Express* **23,** 3951–3959 (2015).

112. Iwase, E., Hui, P.-C., Woolf, D., Rodriguez, A. W., Johnson, S. G., Capasso, F. & Lončar, M. Control of buckling in large micromembranes using engineered support structures. *Journal of Micromechanics and Microengineering* **22,** 065028 (2012).

113. Hu, S. & Weiss, S. M. Design of Photonic Crystal Cavities for Extreme Light Concentration. *ACS Photonics* **3,** 1647–1653 (2016).

114. Choi, H., Heuck, M. & Englund, D. Self-Similar Nanocavity Design with Ultrasmall Mode Volume for Single-Photon Nonlinearities. *Physical Review Letters* **118,** 223605 (2017).

115. Vanner, M. R., Pikovski, I. & Kim, M. S. Towards optomechanical quantum state reconstruction of mechanical motion. *Annalen der Physik* **527,** 15–26 (2015).

116. Vanner, M. R., Hofer, J., Cole, G. D. & Aspelmeyer, M. Cooling-by-measurement and mechanical state tomography via pulsed optomechanics. *Nature Communications* **4,** 2295 (2013).

117. Gavartin, E., Verlot, P. & Kippenberg, T. J. A hybrid on-chip optomechanical transducer for ultrasensitive force measurements. *Nature Nanotechnology* **7,** 509–514 (2012).

118. Poggio, M., Degen, C. L., Mamin, H. J. & Rugar, D. Feedback Cooling of a Cantilever's Fundamental Mode below 5 mK. *Physical Review Letters* **99,** 017201 (2007).

119. Vanner, M. R., Pikovski, I., Cole, G. D., Kim, M. S., Brukner, C., Hammerer, K., Milburn, G. J. & Aspelmeyer, M. Pulsed quantum optomechanics. *Proceedings of the National Academy of Sciences of the United States of America* **108,** 16182–16187 (2011).

120. Gong, Y., Rundquist, A., Majumdar, A. & Vučković, J. Low power resonant optical excitation of an optomechanical cavity. *Optics Express* **19,** 1429–1440 (2011).

121. McCutcheon, M. W., Rieger, G. W., Cheung, I. W., Young, J. F., Dalacu, D., Frédérick, S., Poole, P. J., Aers, G. C. & Williams, R. L. Resonant scattering and second-harmonic spectroscopy of planar photonic crystal microcavities. *Applied Physics Letters* **87,** 221110 (2005).

122. Anetsberger, G., Arcizet, O., Unterreithmeier, Q. P., Rivière, R., Schliesser, A., Weig, E. M., Kotthaus, J. P. & Kippenberg, T. J. Near-field cavity optomechanics with nanomechanical oscillators. *Nature Physics* **5,** 909–914 (2009).

123. Metzger, C., Favero, I., Ortlieb, A. & Karrai, K. Optical self cooling of a deformable Fabry-Perot cavity in the classical limit. *Physical Review B* **78,** 035309 (2008).

124. Lin, Q., Rosenberg, J., Jiang, X., Vahala, K. J. & Painter, O. Mechanical Oscillation and Cooling Actuated by the Optical Gradient Force. *Physical Review Letters* **103,** 103601 (2009).

125. Cohen, J. D., Meenehan, S. M. & Painter, O. Optical coupling to nanoscale optomechanical cavities for near quantum-limited motion transduction. *Optics Express* **21,** 11227–11236 (2013).

126. Doolin, C., Hauer, B. D., Kim, P. H., MacDonald, A. J. R., Ramp, H. & Davis, J. P. Nonlinear optomechanics in the stationary regime. *Physical Review A* **89,** 053838 (2014).

127. Brawley, G. A., Vanner, M. R., Larsen, P. E., Schmid, S., Boisen, A. & Bowen, W. P. Nonlinear optomechanical measurement of mechanical motion. *Nature communications* **7,** 10988 (2016).

128. Hauer, B., Maciejko, J. & Davis, J. Nonlinear power spectral densities for the harmonic oscillator. *Annals of Physics* **361,** 148–183 (2015).

129. Quan, Q., Deotare, P. B. & Lončar, M. Photonic crystal nanobeam cavity strongly coupled to the feeding waveguide. *Applied Physics Letters* **96,** 203102 (2010).

130. Thijssen, R., Kippenberg, T. J., Polman, A. & Verhagen, E. Parallel Transduction of Nanomechanical Motion Using Plasmonic Resonators. *ACS photonics* **1,** 1181–1188 (2014).

131. Heinrich, G., Ludwig, M., Qian, J., Kubala, B. & Marquardt, F. Collective Dynamics in Optomechanical Arrays. *Physical Review Letters* **107,** 043603 (2011).

132. Nunnenkamp, A., Børkje, K. & Girvin, S. M. Single-Photon Optomechanics. *Physical Review Letters* **107,** 063602 (2011).

133. Rabl, P. Photon blockade effect in optomechanical systems. *Physical Review Letters* **107,** 063601 (2011).

134. Yeo, I., de Assis, P.-L., Gloppe, A., Dupont-Ferrier, E., Verlot, P., Malik, N. S., Dupuy, E., Claudon, J., Gérard, J.-M., Auffèves, A., Nogues, G., Seidelin, S., Poizat, J.-P., Arcizet, O. & Richard, M. Strain-mediated coupling in a quantum dot-mechanical oscillator hybrid system. *Nature Nanotechnology* **9,** 106–110 (2013).

135. Bokaian, A. Natural frequencies of beams under compressive axial loads. *Journal of Sound and Vibration* **126,** 49–65 (1988).

136. Leijssen, R., La Gala, G. R., Freisem, L., Muhonen, J. T. & Verhagen, E. Nonlinear cavity optomechanics with nanomechanical thermal fluctuations. *Nature Communications* **8,** 16024 (2017).

137. Lemonde, M.-A., Didier, N. & Clerk, A. A. Enhanced nonlinear interactions in quantum optomechanics via mechanical amplification. *Nature Communications* **7,** 11338 (2016).

138. Khosla, K. E., Vanner, M. R., Bowen, W. P. & Milburn, G. J. Quantum state preparation of a mechanical resonator using an optomechanical geometric phase. *New Journal of Physics* **15,** 043025 (2013).

139. Bennett, J. S., Khosla, K., Madsen, L. S., Vanner, M. R., Rubinsztein-Dunlop, H. & Bowen, W. P. A quantum optomechanical interface beyond the resolved sideband limit. *New Journal of Physics* **18,** 053030 (2016).

140. Kippenberg, T. J., Rokhsari, H., Carmon, T., Scherer, A. & Vahala, K. J. Analysis of Radiation-Pressure Induced Mechanical Oscillation of an Optical Microcavity. *Physical Review Letters* **95,** 033901 (2005).

141. Marquardt, F., Harris, J. G. E. & Girvin, S. M. Dynamical multistability induced by radiation pressure in high-finesse micromechanical optical cavities. *Physical Review Letters* **96,** 103901 (2006).

142. Vahala, K., Herrmann, M., Knünz, S., Batteiger, V., Saathoff, G., Hänsch, T. W. & Udem, T. A phonon laser. *Nature Physics* **5,** 682–686 (2009).

143. Krause, A. G., Hill, J. T., Ludwig, M., Safavi-Naeini, A. H., Chan, J., Marquardt, F. & Painter, O. Nonlinear Radiation Pressure Dynamics in an Optomechanical Crystal. *Physical Review Letters* **115,** 233601 (2015).

144. Carmon, T., Cross, M. & Vahala, K. Chaotic Quivering of Micron-Scaled On-Chip Resonators Excited by Centrifugal Optical Pressure. *Physical Review Letters* **98,** 167203 (2007).

145. Wu, J., Huang, S.-W., Huang, Y., Zhou, H., Yang, J., Liu, J.-M., Yu, M., Lo, G., Kwong, D.-L., Duan, S. & Wei Wong, C. Mesoscopic chaos mediated by Drude electron-hole plasma in silicon optomechanical oscillators. *Nature Communications* **8,** 15570 (2017).

146. Navarro-Urrios, D., Capuj, N. E., Colombano, M. F., García, P. D., Sledzinska, M., Alzina, F., Griol, A., Martínez, A. & Sotomayor-Torres, C. M. Nonlinear dynamics and chaos in an optomechanical beam. *Nature Communications* **8,** 14965 (2017).

147. Meenehan, S. M., Cohen, J. D., MacCabe, G. S., Marsili, F., Shaw, M. D. & Painter, O. Pulsed Excitation Dynamics of an Optomechanical Crystal Resonator near Its Quantum Ground State of Motion. *Physical Review X* **5,** 041002 (2015).

148. Schilling, R., Schütz, H., Ghadimi, A. H., Sudhir, V., Wilson, D. J. & Kippenberg, T. J. Near-Field Integration of a SiN Nanobeam and a $SiO_2$ Microcavity for Heisenberg-Limited Displacement Sensing. *Physical Review Applied* **5,** 054019 (2016).

149. Brennecke, F., Ritter, S., Donner, T. & Esslinger, T. Cavity Optomechanics with a Bose-Einstein Condensate. *Science* **322,** 235–238 (2008).

150. Thompson, J. D., Zwickl, B. M., Jayich, A. M., Marquardt, F., Girvin, S. M. & Harris, J. G. E. Strong dispersive coupling of a high-finesse cavity to a micromechanical membrane. *Nature* **452,** 72–75 (2008).

151. Miao, H., Danilishin, S., Corbitt, T. & Chen, Y. Standard Quantum Limit for Probing Mechanical Energy Quantization. *Physical Review Letters* **103,** 100402 (2009).

152. Paraïso, T. K., Kalaee, M., Zang, L., Pfeifer, H., Marquardt, F. & Painter, O. Position-Squared Coupling in a Tunable Photonic Crystal Optomechanical Cavity. *Physical Review X* **5,** 041024 (2015).

153. Kaviani, H., Healey, C., Wu, M., Ghobadi, R., Hryciw, A. & Barclay, P. E. Nonlinear optomechanical paddle nanocavities. *Optica* **2,** 271–274 (2015).

154. Jacobs, K., Tian, L. & Finn, J. Engineering Superposition States and Tailored Probes for Nanoresonators via Open-Loop Control. *Physical Review Letters* **102,** 057208 (2009).

155. Vanner, M. R. Selective Linear or Quadratic Optomechanical Coupling via Measurement. *Physical Review X* **1,** 021011 (2011).

156. Gröblacher, S., Hill, J. T., Safavi-Naeini, A. H., Chan, J. & Painter, O. Highly efficient coupling from an optical fiber to a nanoscale silicon optomechanical cavity. *Applied Physics Letters* **103,** 181104 (2013).

157. Olivero, J. & Longbothum, R. Empirical fits to the Voigt line width: A brief review. *Journal of Quantitative Spectroscopy and Radiative Transfer* **17,** 233–236 (1977).

158. Giovannetti, V. & Vitali, D. Phase-noise measurement in a cavity with a movable mirror undergoing quantum Brownian motion. *Physical Review A* **63,** 023812 (2001).

159. Braginsky, V. B., Vorontsov, Y. I. & Thorne, K. S. Quantum Nondemolition Measurements. *Science* **209,** 547–557 (1980).

160. Braginsky, V. B., Vorontsov, Y. I. & Khalili, F. Y. Optimal quantum measurements in detectors of gravitation radiation. *JETP Letters* **27,** 276–280 (1978).

161. Hertzberg, J. B., Rocheleau, T., Ndukum, T., Savva, M., Clerk, A. A. & Schwab, K. C. Back-action-evading measurements of nanomechanical motion. *Nature Physics* **6,** 213–217 (2010).

162. Suh, J., Weinstein, A. J., Lei, C. U., Wollman, E. E., Steinke, S. K., Meystre, P., Clerk, A. A. & Schwab, K. C. Mechanically detecting and avoiding the quantum fluctuations of a microwave field. *Science* **344,** 1262–1265 (2014).

163. Shkarin, A. B., Flowers-Jacobs, N. E., Hoch, S. W., Kashkanova, A. D., Deutsch, C., Reichel, J. & Harris, J. G. E. Optically Mediated Hybridization between Two Mechanical Modes. *Physical Review Letters* **112,** 013602 (2014).

164. Ockeloen-Korppi, C. F., Damskägg, E., Pirkkalainen, J.-M., Clerk, A. A., Woolley, M. J. & Sillanpää, M. A. Quantum Backaction Evading Measurement of Collective Mechanical Modes. *Physical Review Letters* **117,** 140401 (2016).

165. Komma, J., Schwarz, C., Hofmann, G., Heinert, D. & Nawrodt, R. Thermo-optic coefficient of silicon at 1550 nm and cryogenic temperatures. *Applied Physics Letters* **101,** 041905 (2012).

166. Gigan, S., Böhm, H. R., Paternostro, M., Blaser, F., Langer, G., Hertzberg, J. B., Schwab, K. C., Bäuerle, D., Aspelmeyer, M. & Zeilinger, A. Self-cooling of a micromirror by radiation pressure. *Nature* **444,** 67–70 (2006).

# List of common symbols

| Notation | Description |
|---|---|
| $a$ | optical field amplitude inside the optical cavity *(chapters 1, 4 and 5 and appendix A)* |
| $a$ | period of the photonic crystal patterning of the nanobeam *(chapters 2 to 4)* |
| $c$ | speed of light in vacuum *(chapter 2)* |
| $c$ | amplitude of nonresonant scattering from the input channel to the output channel *(chapters 1, 2 and 4)* |
| $C_0$ | cooperativity, $C_0 \equiv 4g_0^2/\kappa\Gamma_\mathrm{m}$ |
| $C_\mathrm{q}$ | quantum cooperativity, $C_\mathrm{q} \equiv 4g_0^2 n_\mathrm{c}/\kappa\Gamma_\mathrm{m}\bar{n}_\mathrm{th}$ |
| $d$ | width of the gap in the sliced nanobeam |
| $\Delta$ | detuning of the incident laser with respect to the optical resonance frequency, $\Delta \equiv \omega_\mathrm{L} - \omega_\mathrm{c}$ |
| $\eta$ | overal coupling efficiency to the optical cavity, $\eta \equiv \sqrt{\eta_\mathrm{in}\eta_\mathrm{out}}$ |
| $\eta_\mathrm{in}$ | coupling efficiency from the input channel to the optical cavity |
| $\eta_\mathrm{out}$ | coupling efficiency from the output channel to the optical cavity |
| $F_\mathrm{opt}$ | optical (radiation pressure) force acting on the mechanical resonator |
| $\varphi$ | phase of nonresonant scattering from the input channel to the output channel |
| $G$ | optomechanical coupling rate, $G \equiv -\partial\omega_\mathrm{c}/\partial x$ |
| $g_0$ | optomechanical photon-phonon coupling rate, $g_0 \equiv G x_\mathrm{zpf}$ |
| $\Gamma_\mathrm{m}$ | loss rate of the mechanical resonator |
| $h$ | quantum efficiency for detection of the optical field in the output channel of the optical cavity |

| Notation | Description |
|---|---|
| $\hbar$ | reduced Planck constant |
| $h_{\mathrm{s}}$ | size of the holes in the nanobeam at the side of the "support" |
| $h_{\mathrm{t}}$ | size of the holes in the nanobeam at the side of the "teeth" |
| $k_{\mathrm{B}}$ | Boltzmann constant |
| $k_{\parallel}$ | parallel component of the wavevector of light |
| $\kappa$ | loss rate of the optical cavity |
| $m$ | effective motional mass of the mechanical resonator |
| $n_{\mathrm{c}}$ | average photon occupancy of the optical cavity |
| $\bar{n}_{\mathrm{th}}$ | average thermal phonon occupancy of the mechanical resonator, $\bar{n}_{\mathrm{th}} \equiv k_{\mathrm{B}}T/\hbar\Omega_{\mathrm{m}}$ |
| $P$ | optical power |
| $Q$ | quality factor of the resonator or cavity, $Q_{\mathrm{m}} = \Omega_{\mathrm{m}}/\Gamma_{\mathrm{m}}$ and $Q_{\mathrm{c}} = \omega_{\mathrm{c}}/\kappa$ |
| $R$ | reflectivity of the optical cavity |
| $s$ | width of the "support", the narrowest part of the nanobeam next to the holes |
| $s_{\mathrm{channel}}$ | optical field amplitude in the labeled channel |
| $S_{xx}$ | power spectral density of the variable $x$ |
| $t$ | thickness of the nanobeam *(chapters 2 and 3)* |
| $t$ | time *(chapters 1 and 4 to 6 and appendix A)* |
| $T$ | temperature |
| $T_{\mathrm{m}}$ | resonance period of the mechanical resonator |
| $\theta$ | interferometer angle / phase *(chapters 1, 5 and 6)* |
| $\theta$ | mixing angle describing the hybridization of two coupled mechanical modes *(chapters 3 and 4)* |
| $u$ | relative detuning (dimensionless), $u \equiv 2\Delta/\kappa$ |
| $v$ | normalized output of the transduction function linking relative detuning $u$ to the measurement outcome |
| $w$ | width of the nanobeam |
| $x$ | position or displacement of a mechanical resonator |
| $x_{\mathrm{zpf}}$ | root-mean-square amplitude of the zero-point fluctuations of the mechanical resonator |
| $\langle x^2 \rangle$ | variance of the variable $x$ |
| $\zeta$ | quantum efficiency for detection of the optical field in the optical cavity, $\zeta \equiv h\eta_{\mathrm{out}}$ |
| $\omega_{\mathrm{c}}$ | resonance frequency of the optical cavity |
| $\omega_{\mathrm{L}}$ | frequency of the laser beam incident on the optical cavity |
| $\Omega_{\mathrm{m}}$ | resonance frequency of the mechanical resonator |

# Measuring mechanical motion using light confined at the nanoscale


## Summary

Optical measurements of motion are widely used in sensitive measurement techniques, for example in atomic force microscopes, where a sharp tip on a cantilever is moved across a surface and light is used to measure the deflection of the cantilever due to variations in height of the surface. One of the main advantages of optical measurements is that laser beams can carry information with very low levels of noise. In fact, using high-quality laser sources and optical techniques like interferometry, it is possible to perform measurements of motion with levels of uncertainty close to the fundamental quantum limit. A natural way to increase the measurement sensitivity of an optical measurement of motion is to trap light in an optical cavity to make it interact longer with the moving object, and to make the interaction stronger by confining the light in a small volume at or near it. The interaction of light and motion in such a system, where an optical cavity interacts with a moving object, is studied in the field of *cavity optomechanics*. In systems ranging from clouds of atoms to suspended mirrors with kilogram-scale mass, the optomechanical interaction leads to the possibility of extremely sensitive measurements of motion as well as effects on the mechanical motion due to optical forces.

The performance of an optomechanical device depends on the strength of the interaction between light and motion, described by the optomechanical (photon-phonon) coupling rate. This should be compared to the loss rates of the optical and mechanical degrees of freedom, which describe how strongly the system is damped. The optical loss rate is larger than the optomechanical coupling rate for all systems demonstrated so far, such that they operate in the weak-coupling

regime. The coupling rates of different systems have been improved over time, in the hope of eventually reaching the single-photon strong-coupling regime, meanwhile improving the performance in the weak-coupling regime and enabling experimental demonstrations of many interesting phenomena. In this thesis, we develop and study optomechanical systems in which the optomechanical coupling rate is especially large. To achieve this, we create photonic crystal nanobeam cavities in which light is highly confined between two beams exhibiting flexural motion, such that the interaction between light and motion is enhanced.

In chapter 1 we introduce the formalism we use to describe the optomechanical interaction. We discuss the effects of optical forces as well as the sensitivity of optical displacement measurements. For devices in the bad-cavity limit (where the mechanical resonance frequency is smaller than the optical loss rate), the strongest effect of optical forces is the *optical spring effect*, that is, the change of the mechanical frequency due to an incident laser beam that is slightly detuned from the optical resonance. Displacement measurements can be performed by direct measurements of the reflected intensity or by an interferometric measurement of the reflected light field using a balanced homodyne interferometer. The latter technique can in principle reach the ultimate limit to the precision of a continuous displacement measurement, which is given by the standard quantum limit. In practice, the measurement sensitivity is set by the amount of light in the optical cavity and the measurement efficiency.

The optomechanical interaction in coupled nanobeam systems is discussed in chapter 2. Optically, such systems resemble a slotted waveguide, whose guided modes can have high electric fields at the interfaces defining the gap. This enhances the effect of the moving boundary on the mode frequency. These considerations for waveguides also predict the performance for photonic crystal nanobeam cavities, whose resonant modes are derived from the waveguide modes. We find that the strongest optomechanical interaction is achieved for the smallest gaps, with the electric field oriented across the gap (perpendicular to the material interfaces), for geometries which concentrate the field close to the gap by not having high-refractive-index material far away from the gap. However, the choice of geometry and gap size can be restricted by other considerations such as fabrication limitations, and we find that modes with the field oriented along the gap can have more robust performance for somewhat larger gaps.

In the second part of chapter 2, we show optomechanical measurements of the thermal motion of a vertically coupled nanobeam system. We fit the optical frequency dependence of the sensitivity of displacement measurements and the magnitude of the optical spring effect with a model and obtain the parameters of the optomechanical system. The optomechanical coupling rates for the fundamental flexural modes of the nanobeams are found to be on par with state-of-the-art optomechanical devices, even though the gap between the nanobeams is larger than in other coupled-nanobeam systems.

We develop the design of a horizontally-coupled nanobeam cavity system in chapter 3. The *sliced nanobeam* design contains a small gap in the middle, with the electric field oriented across the gap. To find a design that combines large

optomechanical interactions with low optical losses, we explore the parameter space with finite-element simulation and engineer a Gaussian profile of the field confinement, which helps to reduce cavity radiation losses. The resulting cavity designs reach simulated quality factors on par with state-of-the-art photonic crystal nanobeam cavities, while the optomechanical coupling rate can be larger by an order of magnitude or more.

Chapter 4 details the experimental implementation and characterization of the sliced nanobeam system. Here we use a simple defect cavity, which leads to a relatively large optical bandwidth. We show that despite this, the device allows sensitive detection of the mechanical motion. This is due to the large optomechanical photon-phonon coupling rate, which is indeed improved by an order of magnitude with respect to other state-of-the-art optomechanical systems.

The thermal motion of the device leads to frequency fluctuations of the optical cavity through the optomechanical interaction, which for the measurements in chapter 4 amount to a few percent of the optical linewidth. This leads to observable nonlinear transduction of the motion, which is well-described by an order-by-order approximation. In chapter 5, we consider the behavior of devices with designs optimized for lower optical losses, in which case the thermal motion at room temperature causes frequency fluctuations of the cavity which are larger than its intrinsic linewidth. Thus, the optical cavity response is dominated by the thermomechanical fluctuations over a wide range of temperatures. Additionally, the transduction of motion becomes highly nonlinear, such that the order-by-order approximation breaks down. We show that the nonlinear transduction can in fact be used to perform nonlinear measurements of the displacement.

In chapter 6 we present pulsed optomechanical measurements of the sliced nanobeam device. In contrast to the continuous measurements employed in the other chapters of this thesis, here we use short optical pulses with which we resolve the instantaneous displacement of the device in a time much shorter than the mechanical resonance period. With sufficient resolution, this approach could enable evasion of measurement backaction and tomography of the quantum state of the mechanical resonator. At the same time, protocols using pulsed measurements can potentially be used for measurement-based control of the mechanical resonator. We measure the thermal motion at cryogenic temperatures and find the displacement imprecision is mainly limited by the presence of a second mechanical mode. Without the second mode, we expect the displacement imprecision of our pulsed measurement needs to be improved by only a factor of $16$ to be able to resolve displacements of the scale of the zero-point fluctuations, which could enable reconstruction and manipulation of the quantum state of the mechanical resonator.

# Mechanische beweging meten met licht opgesloten op de nanoschaal

## Samenvatting

Optische metingen van beweging worden gebruikt bij vele gevoelige meettechnieken. Een voorbeeld zijn *atomic force microscopes*, tastmicroscopen waarbij een scherpe naaldpunt over een oppervlak wordt bewogen en licht wordt gebruikt om de beweging van de naald te meten die ontstaat door de hoogtevariaties in het oppervlak. Eén van de belangrijkste voordelen van optische metingen is dat licht informatie kan dragen met een zeer lage hoeveelheid ruis. Met goede lasers en optische technieken zoals interferometrie is het zelfs mogelijk om metingen van beweging te doen met meetonzekerheden nabij de fundamentele quantumlimiet. Om de meetgevoeligheid van een optische meting van beweging te vergroten kan men de interactie tussen licht en beweging langer laten duren door licht vast te houden in een optische trilholte, en sterker maken door licht op te sluiten in een klein volume, daar waar de beweging plaatsvindt. In het onderzoeksveld genaamd *cavity optomechanics* (trilholte-optomechanica) wordt de interactie tussen licht en beweging bestudeerd in de systemen die ontstaan als een optische trilholte gecombineerd wordt met een bewegend object. In systemen die variëren van wolkjes koude atomen tot opgehangen spiegels met massa's in de orde van een kilogram leidt de optomechanische interactie steeds tot de mogelijkheid om extreem gevoelige metingen van mechanische beweging te doen en tot beïnvloeding van de beweging door optische krachten.

De prestaties van een optomechanisch systeem hangen af van de sterkte van de interactie tussen licht en beweging, die wordt aangeduid door de optomechanische (foton-fonon) koppelingsconstante. Deze moet worden vergeleken met de demping van de optische en mechanische vrijheidsgraden. De optische verlies-

constante is groter dan de optomechanische koppelingsconstante in alle tot nu toe gedemonstreerde systemen, waardoor zij in het regime van zwakke koppeling opereren. In de loop van de tijd zijn de koppelingsconstantes van verschillende systemen verbeterd, in de hoop uiteindelijk het regime van sterke koppeling voor een enkel foton te bereiken. In de tussentijd verbeteren de prestaties in het regime van zwakke koppeling, wat onderzoekers in staat heeft gesteld vele interessante fenomenen experimenteel aan te tonen. In dit proefschrift ontwikkelen en onderzoeken we optomechanische systemen waarin de optomechanische koppelingsconstante zeer groot is. Om dit te bereiken creëren we nanobalktrilholtes gebaseerd op een fotonisch kristal. Hierin is het licht sterk opgesloten tussen twee buigbare silicium balkjes, waardoor de interactie tussen licht en beweging wordt versterkt.

In hoofdstuk 1 introduceren we het formalisme dat we gebruiken om de optomechanische interactie te beschrijven. We behandelen zowel de effecten van optische krachten als de gevoeligheid van optische metingen van verplaatsing. Voor systemen in de slechte-trilholte-limiet (waar de mechanische resonantiefrequentie kleiner is dan de optische verliesconstante) is het sterkste effect van optische krachten het *optische-veer-effect*: de verandering van de mechanische frequentie door een inkomende laserstraal die net verstemd is ten opzichte van de optische resonantie. Metingen van verplaatsing kunnen worden uitgevoerd door directe metingen van de gereflecteerde intensiteit of door een interferometrische meting van het gereflecteerde lichtveld met een gebalanceerde *homodyne* interferometer. Deze laatstgenoemde techniek kan in principe de ultieme limiet voor de precisie van een continue meting van verplaatsing bereiken, gegeven door de standaard quantum limiet. In de praktijk is de meetgevoeligheid afhankelijk van de hoeveelheid licht in de trilholte en van de meetefficiëntie.

De optomechanische interactie in gekoppelde-nanobalksystemen wordt behandeld in hoofdstuk 2. Optisch gezien lijken zulke systemen op een golfgeleider met een sleuf, waarin de geleide modes hoge elektrische velden kunnen bevatten bij de oppervlakken aan de rand van de sleuf. Dit versterkt het effect van de bewegende materiaalgrens op de frequentie van de modes. Deze overwegingen voor golfgeleiders voorspellen ook de prestaties voor fotonisch-kristal-nanobalktrilholtes, waarvan de resonante modes afgeleid zijn van de geleide modes in de golfgeleider. We zien dat de sterkste optomechanische interactie plaatsvindt bij de smalste sleuven, met het elektrische veld loodrecht gericht ten opzichte van het de sleuf, vooral in structuren met meer hogebrekingsindex-materiaal vlakbij de sleuf waardoor het elektrische veld daar sterk geconcentreerd wordt. De keus voor de geometrie en de grootte van de sleuf kan beperkt worden door andere factoren zoals de limieten van fabricagetechnieken, en we observeren dat de modes met het elektrisch veld gericht langs de sleuf betere prestaties kunnen hebben voor bredere sleuven.

In het tweede deel van hoofdstuk 2 laten we optomechanische metingen zien van de thermische (Brownse) beweging van een verticaal gekoppeld nanobalksysteem. We fitten de golflengte-afhankelijkheid van de gevoeligheid van verplaatsingsmetingen en de grootte van het optische-veer-effect met een model en vinden

zo de parameters van het optomechanische systeem. De optomechanische koppelingsconstantes voor de fundamentele resonante modes van de nanobalken blijken even groot te zijn als die van de beste optomechanische systemen, ondanks het feit dat de sleuf tussen de nanobeams groter is dan die in sommige andere gekoppelde-nanobalk-systemen.

We ontwikkelen het ontwerp van een horizontaal gekoppeld nanobalk-trilholte-systeem in hoofdstuk 3. De *sliced nanobeam* (gespleten nanobalk) structuur heeft een sleuf in het midden, met het elektrisch veld gericht loodrecht op de sleuf. Om een ontwerp te vinden dat grote optomechanische interactiesterkte met lage optische verliezen combineert, verkennen we eerst de parameterruimte met numerieke *finite element* simulaties. Vervolgens proberen we een Gaussisch profiel van de veldsterkte te bereiken, wat helpt om de stralingsverliezen van de trilholte te beperken. De trilholtes die we op deze manier ontwerpen bereiken gesimuleerde verliezen vergelijkbaar met de beste fotonisch-kristal-nanobalktrilholtes, terwijl de optomechanische koppelingsconstante (meer dan) een ordegrootte groter kan zijn.

Hoofdstuk 4 beschrijft de experimentele realisatie en karakterisatie van de *sliced nanobeam* structuur. We gebruiken hier een trilholte gebaseerd op een simpel defect in het fotonisch kristalrooster, wat leidt tot een relatief grote optische bandbreedte. We laten zien dat het systeem desondanks gevoelige metingen van de mechanische beweging toelaat. Dit komt door de grote optomechanische foton-fonon koppelingsconstante, die inderdaad verbeterd is met een orde van grootte ten opzichte van andere *state-of-the-art* optomechanische systemen.

De thermische beweging van de structuur leidt tot frequentiefluctaties van de optische trilholte via de optomechanische interactie, die voor de metingen in hoofdstuk 4 enkele procenten van de optische lijnbreedte bedragen. Hierdoor kunnen we niet-lineaire transductie van de beweging waarnemen, die goed beschreven kan worden met een benadering waarbij elke hogere orde los behandeld wordt. In hoofdstuk 5 bestuderen we het gedrag van systemen waarbij het ontwerp is geoptimaliseerd voor lage optische verliezen. In dat geval veroorzaakt de thermische beweging bij kamertemperatuur frequentiefluctuaties van de trilholte die groter zijn dan de intrinsieke lijnbreedte. De optische respons van de trilholte wordt dan gedomineerd door de thermomechanische fluctuaties over een groot bereik van temperaturen. Daarnaast wordt de transductie van beweging zeer niet-lineair, waardoor de eerder genoemde benadering niet meer werkt en we een numerieke berekening met een volledig model van de transductie nodig hebben om de meetresulaten te verklaren. We laten zien dat de niet-lineaire transductie ook gebruikt kan worden om niet-lineaire metingen van de verplaatsing te doen.

In hoofdstuk 6 presenteren we gepulste optomechanische metingen van het *sliced nanobeam* systeem. In tegenstelling tot de continue metingen toegepast in de andere hoofdstukken gebruiken we hier korte optische pulsen, waarmee we de instantane verplaatsing van de structuur detecteren in een tijd die veel korter is dan de mechanische resonante trillingstijd. Met voldoende meetresolutie zou deze methode gebruikt kunnen worden voor het ontwijken van quantum meetverstoring (*measurement backaction*) en voor tomografie van de quantumtoestand van

de mechanische resonator. Daarnaast kan de quantumtoestand van een mechanische resonator mogelijk beheerst worden door middel van protocollen gebaseerd op gepulste metingen. We meten de thermische beweging van de structuur bij lage temperatuur en vinden dat de meetonzekerheid van de verplaatsing vooral wordt beperkt door de aanwezigheid van een tweede mechanische resonantie. Zonder die tweede resonantie verwachten we dat de meetonzekerheid van onze gepulste metingen slechts met een factor $16$ verbeterd hoeft te worden om verplaatsingen te meten ter grootte van de nulpuntsfluctuaties, wat bovengenoemde reconstructie en manipulatie van de quantumtoestand van de mechanische resonator mogelijk kan maken.

# Acknowledgments

When I started in December 2012, the Photonic Forces lab was still empty (the delivery of optical tables was delayed because the shipping company lost them in a warehouse) and the group consisted of only four people: the group leader, a technician, one PhD student and one master student. Looking back to that, the difference with the present is astonishing. The group has grown, measurement setups were built, and theoretical and practical challenges were attacked. This thesis shows some of the results of that. Scientific research is a collective affair, not an individual effort, and here I would like to thank the people that have made this thesis possible.

First and foremost Ewold, thank you for placing your trust in me while you were just starting your group. In just a few years we have gone from an empty lab to nice results. I am also grateful for the many interesting discussions we had, as well as for your help in presenting and writing down our results. I greatly admire your enthusiasm and dedication.

I would also like to thank all the other members of the Photonic Forces group for the nice atmosphere, constructive feedback and interesting discussions. I appreciated the lunch breaks, group meetings, conferences, and of course group outings where we spend time together. Freek, you've almost caught up with me in writing your thesis, although you joined months later. It was great to be able to share our frustrations with theory, coding, fab or experiments. Nikhil, I always appreciate your input in discussions and you have a great eye for style. Giada, you're not afraid to ask questions and challenge assumptions, which I appreciate a lot. Thank you for being my paranymph! Juha, it's great to share an office and a measurement setup with you, always ready to discuss some weird data or random questions. John, it was fun to teach you a bit about nanobeams, and I appreciate your sense of humor. Robin, the most recent addition to the team, you were always ready for a discussion about anything over lunch, helping me relax from writing some chapter or worrying about the planning of the defense. There were also students that joined the group for a limited period for an internship or master's research project. Lars, you created our first high-$Q$ sliced nanobeams,

and your work was the basis for the results in chapter 3. Thijs, the interferometer you built was essential to obtain all the results in chapters 5 and 6. Hugo, Ruud, Aloys, Randy, thanks for being great group members during your stay at AMOLF.

The support that researchers receive at AMOLF is incredible. In particular I'd like to thank our group technicians, first Mohamed and now Jan Bonne. To design parts of my setup, Iliya at the mechanical design department was invaluable, as well as the people at the workshop who actually produced the vacuum chamber, sample mounts, etc. Fabricating the sliced nanobeams would not have been possible without the cleanroom technicians. I'd like to thank Hans, Dimitry, Andries, Peter and Bob for their help in the cleanroom, getting me started and helping me diagnose problems in the fabrication process. I'm also grateful to our software support, Luc, to Duncan and Ronald at the electronics department, and to the IT department, in particular Wiebe, all of whom were always ready to help and answer questions. I'd also like to thank all the people that made administrative tasks painless, especially the purchasing department that had to handle all the purchases to fill our empty lab.

The AMOLF Center for Nanophotonics weekly meetings were a great way to discuss ideas and learn about the research being done by others at AMOLF. I am grateful to everyone that contributed to these, and especially to the group leaders organizing them over the years I was here: Albert Polman, Kobus Kuipers, Jaime Gomez Rivas, Femius Koenderink, Erik Garnett, Bruno Ehrler and Esther Alarcon Llado. I also enjoyed the weekly journal club that we organized with the members of the groups of Femius and Ewold. Trying to understand (and criticizing) a variety of published articles was a great learning experience, both for the actual content of the articles, and for what not to do when writing a paper.

I thank everyone that made AMOLF a fun place to work over the past years, the members of the PV who organized outings, Christmas and Easter lunches, and other activities; Mark, Benjamin, Hinke, Wouter, Sophie and Verena who took part in our weekly running group; Giorgios who was a great office mate; and the many, many other colleagues that I interacted with, including (but not limited to) Clara, Felipe, Lutz, Sander, Ruben, Rutger, Ruben, Marie Anne, Boris, Anouk, Cocoa, Lorenzo, Dolfine, Kevin, Ruslan, Isabelle, Annemarie, and Christiaan.

I also thank my collaborators from the Technical University of Eindhoven: Tian Xia, who fabricated the samples used in chapter 2, and Sybren, who came to Amsterdam with the samples and helped to obtain the measurement results. I also enjoyed spending a few days with Zarko in his lab in Eindhoven. Finally, thanks to Andrea who agreed to be my promotor and provided useful comments on the text of this thesis.

Ik wil ook graag de leden van Klarinetensemble Lignum bedanken voor alle mooie muziek die we samen gemaakt hebben de afgelopen jaren. Daarnaast ben ik dankbaar voor mijn vrienden. In het bijzonder Rick, bedankt dat je mijn paranimf wil zijn!

Ik bedank ook mijn ouders voor hun steun en interesse. Mam, bedankt voor het schilderij dat nu op de omslag van dit proefschrift prijkt! Ten slotte bedank ik Inge, die mijn leven zoveel leuker maakt.

# About the author

Rick Leijssen was born in 1988 in Weert. He studied physics at Leiden University, obtaining a Bachelor's degree in 2009 with a final research project on AFM and optical measurements on photonic-crystal slabs. He went on to obtain a Master's degree from the same university in 2012. Here, the first research project was about the optical properties of DNA-encapsulated silver clusters. For a second project, he spent six months at Harvard University in the group of Professor Lončar to study mid-infrared photonic crystal cavities in silicon. During his studies in Leiden, Rick was active in the student-run *Rino foundation*, where he regularly performed physics shows at secondary schools throughout The Netherlands and also served as a board member for two years.

In 2012, Rick started as a PhD researcher in the newly started Photonic Forces research group of Professor Verhagen at the AMOLF research institute in Amsterdam. The results are presented in this thesis. Rick also presented his work at several national and international conferences. He won the poster prize at the annual NNV AMO Lunteren meeting in 2013 and was one of the recipients of the Emil Wolf outstanding student paper award at the OSA Frontiers in Optics conference in 2016.